Generalized Lorenz-Mie theory

Application to scattering and resonances of photonic complexes

Thèse

Denis Gagnon

Doctorat en physique
Philosophiæ doctor (Ph.D.)

Québec, Canada

Résumé

Les structures photoniques complexes permettent de façonner la propagation lumineuse à l'échelle de la longueur d'onde au moyen de processus de diffusion et d'interférence. Cette fonctionnalité à l'échelle nanoscopique ouvre la voie à de multiples applications, allant des communications optiques aux biosenseurs.

Cette thèse porte principalement sur la modélisation numérique de structures photoniques complexes constituées d'arrangements bidimensionnels de cylindres diélectriques. Deux applications sont privilégiées, soit la conception de dispositifs basés sur des cristaux photoniques pour la manipulation de faisceaux, de même que la réalisation de sources lasers compactes basées sur des molécules photoniques. Ces structures optiques peuvent être analysées au moyen de la théorie de Lorenz-Mie généralisée, une méthode numérique permettant d'exploiter la symétrie cylindrique des diffuseurs sous-jacents.

Cette dissertation débute par une description de la théorie de Lorenz-Mie généralisée, obtenue des équations de Maxwell de l'électromagnétisme. D'autres outils théoriques utiles sont également présentés, soit une nouvelle formulation des équations de Maxwell-Bloch pour la modélisation de milieux actifs appelée SALT (*steady state ab initio laser theory*). Une description sommaire des algorithmes d'optimisation dits *métaheuristiques* conclut le matériel introductif de la thèse.

Nous présentons ensuite la conception et l'optimisation de dispositifs intégrés permettant la génération de faisceaux d'amplitude, de phase et de degré de polarisation contrôlés. Le problème d'optimisation combinatoire associé est solutionné numériquement au moyen de deux métaheuristiques, l'algorithme génétique et la recherche tabou.

Une étude théorique des propriétés de micro-lasers basés sur des molécules photoniques – constituées d'un arrangement simple de cylindres actifs – est finalement présentée. En combinant la théorie de Lorenz-Mie et SALT, nous démontrons que les propriétés physiques de ces lasers, plus spécifiquement leur seuil, leur spectre et leur profil d'émission, peuvent être affectés de façon non-triviale par les paramètres du milieu actif sous-jacent. Cette conclusion est hors d'atteinte de l'approche établie qui consiste à calculer les états méta-stables de l'équation de Helmholtz et leur facteur de qualité. Une perspective sur la modélisation de milieux photoniques désordonnés conclut cette dissertation.

Abstract

Complex photonic media mold the flow of light at the wavelength scale using multiple scattering and interference effects. This functionality at the nano-scale level paves the way for various applications, ranging from optical communications to biosensing.

This thesis is mainly concerned with the numerical modeling of photonic complexes based on two-dimensional arrays of cylindrical scatterers. Two applications are considered, namely the use of photonic-crystal-like devices for the design of integrated beam shaping elements, as well as active photonic molecules for the realization of compact laser sources. These photonic structures can be readily analyzed using the 2D Generalized Lorenz-Mie theory (2D-GLMT), a numerical scheme which exploits the symmetry of the underlying cylindrical structures.

We begin this thesis by presenting the electromagnetic theory behind 2D-GLMT. Other useful frameworks are also presented, including a recently formulated stationary version of the Maxwell-Bloch equations called *steady-state ab initio laser theory* (SALT). Metaheuristics, optimization algorithms based on empirical rules for exploring large solution spaces, are also discussed.

After laying down the theoretical content, we proceed to the design and optimization of beam shaping devices based on engineered photonic-crystal-like structures. The combinatorial optimization problem associated to beam shaping is tackled using the genetic algorithm (GA) as well as tabu search (TS). Our results show the possibility to design integrated beam shapers tailored for the control of the amplitude, phase and polarization profile of the output beam.

A theoretical and numerical study of the lasing characteristics of photonic molecules – composed of a few coupled optically active cylinders – is also presented. Using a combination of 2D-GLMT and SALT, it is shown that the physical properties of photonic molecule lasers, specifically their threshold, spectrum and emission profile, can be significantly affected by the underlying gain medium parameters. These findings are out of reach of the established approach of computing the meta-stable states of the Helmholtz equation and their quality factor. This dissertation is concluded with a research outlook concerning the modeling of disordered photonic media.

Contents

List of Figures

List of Tables

Glossary

Notation	Description
C	Cavity region.
c	Speed of light in vacuum.
$\mathrm{Corr}(U,V)$	Pearson correlation coefficient.
D_0	Pump parameter.
$\mathfrak{D}$	Population inversion.
D	Normalized population inversion.
$\mathbf{E}$	Electric field.
f_i	Objective function used in the beam shaping problem normalized with respect to a heuristic upper bound, i.e. $f_i = g_i / g_i^{\max}$.
g_i	Objective functions used in beam shaping problems.
$\mathbf{H}$	Magnetic field.
$H_l^{(+)}(z)$	Hankel function of the first kind.
$J_l(z)$	Bessel function of the first kind.
K	Eigenvalue of a constant-flux state.
k	Wavevector.
N	Number of cylinders in an array. Equivalently, number of binary optimization variables.
n	Refractive index ($n = \sqrt{\epsilon}$).

Notation	Description
$\mathbf{P}$	Polarization field.
p_c, p_m	Crossover and mutation probabilities (specific to the genetic algorithm).
$\mathscr{P}$	Degree of polarization.
Q	Quality factor.
R	Polarization ratio between orthogonal components.
$\mathbf{R}_i = (X_i, Y_i)$	Cartesian coordinates of the center of scatterer i.
r_i	Radius of cylinder i (equivalent to u_i).
r_s	Complex-source beam argument.
$\mathbf{T}$	Transfer matrix (specific to 2D-GLMT).
u_i	Radius of cylinder i (equivalent to r_i).
w_0	Half-width of beam, waist diameter.
x_R	Rayleigh distance (or Rayleigh range) of a beam.
α_i	Relative weights used in the aggregation method.
χ_e	Electric susceptibility.
ϵ	Relative dielectric permittivity.
η	Power transmission efficiency.
γ	Relaxation rate.
ω	Frequency.
φ	Wavefunction (either E_z or H_z).
$\phi_{\mathrm{nn}'}$	Angular position of scatterer n' in the frame of reference of scatterer n.
ρ, θ	Cylindrical coordinates.
Υ	Solution space of an optimization problem, i.e. $v \in \Upsilon$.
v	Solution to an optimization problem.

Acronyms

Notation	Description
2D-GLMT	Two-dimensional generalized Lorenz-Mie theory.
ARC	Asymmetric resonating cavity.
BEM	Boundary element method.
CF	Constant-flux.
CSB	Complex-source beam.
EP	Exceptional point.
FDTD	Finite-difference time-domain.
FEM	Finite element method.
GA	Genetic algorithm.
GB	Gaussian beam.
HIS	Holes-in-slab.
MOP	Multiobjective optimization problem.
PhC	Photonic crystal.
PM	Photonic molecule.
PTS	Parallel tabu search.
PW	Plane wave.
QB	Quasi-bound.

Notation	Description
RIA	Rods-in-air.
RSS	Root sum of squares.
RWA	Rotating wave approximation.
SALT	Steady-state ab initio laser theory.
TE	Transverse electric.
TLM	Threshold lasing mode.
TM	Transverse magnetic.
TS	Tabu search.

List of contributions

Peer-reviewed journals

1. **Denis Gagnon**, Joey Dumont and Louis J. Dubé
   Beam shaping using genetically optimized two-dimensional photonic crystals
   J. Opt. Soc. Am. A, Vol. 29, pp. 2673–2678 (2012) [44]
   Inserted in chapter 4
2. **Denis Gagnon**, Joey Dumont and Louis J. Dubé
   Multiobjective optimization in integrated photonics design
   Optics Letters, Vol. 38, pp. 2181–2184 (2013) [46]
   Inserted in chapter 5
3. **Denis Gagnon**, Joey Dumont, Jean-Luc Déziel and Louis J. Dubé
   Optimization of integrated polarization filters [43]
   Optics Letters, Vol. 39, pp. 5768–5771 (2014)
   Inserted in chapter 6
4. **Denis Gagnon**, Joey Dumont, Jean-Luc Déziel and Louis J. Dubé
   Ab initio investigation of lasing thresholds in photonic molecules
   J. Opt. Soc. Am. B, Vol. 31 pp. 1867–1873 (2014) [42]
   Inserted in chapter 7

International conferences

(Name of the presenting author is underlined)

1. **Denis Gagnon**, Joey Dumont and Louis J. Dubé
   Optimization in optical systems revisited: Beyond genetic algorithms
   44th Annual DAMOP Meeting (poster session), Quebec, Canada (2013)
2. **Denis Gagnon**, Joey Dumont and Louis J. Dubé
   Coherent beam shaping using two-dimensional photonic crystals
   15th International Conference on Transparent Optical Networks, Cartagena, Spain (2013)

3. Guillaume Painchaud-April, Joey Dumont, **Denis Gagnon**, and Louis J. Dubé
   S and Q Matrices Reloaded: applications to open, inhomogeneous, and complex cavities
   15th International Conference on Transparent Optical Networks, Cartagena, Spain (2013)
4. **Denis Gagnon**, Joey Dumont, Jean-Luc Déziel and Louis J. Dubé
   Adding SALT to Coupled Microcavities: the making of active photonic molecule lasers (invited)
   16th International Conference on Transparent Optical Networks, Graz, Austria (2014)

Remerciements

Pour reprendre les propos de Carl Sagan, « la science est, à la base, une entreprise humaine ». Il apparaît donc naturel, dans ces quelques lignes, de remercier ceux qui ont contribué à la rédaction de cette thèse, que ce soit au niveau du contenu scientifique ou du support moral. Je tiens d'abord remercier mon directeur de recherche, le Professeur Louis J. Dubé, pour son mentorat constant, ses opinions éclairées et son soutien inconditionnel depuis 2009. J'ai grandement apprécié la latitude offerte à ses étudiants gradués lors de cette période importante de leur cheminement académique. Je remercie également le Professeur Alain Hertz pour ses judicieux conseils sur les métaheuristiques, en particulier l'introduction à la recherche tabou.

J'ai été privilégié de connaître l'ensemble des membres du groupe de recherche de M. Dubé, en qui j'ai trouvé des collaborateurs, mais surtout de bons amis. Je garderai un excellent souvenir du travail scientifique accompli (et des albums de Ayreon écoutés) en collaboration avec les gars de lumière: Joey Dumont et Jean-Luc Déziel. J'aimerais également saluer les gars de réseaux pour les litres de caféine absorbés en leur compagnie: Antoine Allard, Edward Laurence, Jean-Gabriel Young. Quelques anciens membres du groupe méritent également d'être mentionnés: Dr. Pierre-André Noël et Dr. Guillaume Painchaud-April. Vous côtoyer pendant l'ensemble de mes études graduées fut un privilège.

Je voudrais également remercier mes compagnons d'armes du temps du baccalauréat: Francis Lajeunesse, Laurent Hébert-Dufresne, Vincent Marceau et Éric Poulin. J'espère que nos soirées au Victor demeureront une tradition pour bien des années à venir.

À travers leur support moral, plusieurs autres parents et amis, trop nombreux pour être mentionnés ici, ont contribué à l'aboutissement de cette thèse. Je ne peux toutefois pas passer sous silence l'apport de mes proches: mes parents France et Yves, pour l'éveil de la curiosité, l'encouragement et la générosité; mon frère Charles, pour les rires et l'inspiration; et finalement Catherine, pour être la plus grande partisane de ma carrière scientifique.

Avant-propos

Cette thèse présente mes travaux de doctorat effectués entre septembre 2011 et août 2014. Quatre articles publiés dont je suis le premier auteur sont insérés dans le corps du texte et constituent l'essentiel du contenu de cette thèse. J'ai effectué l'ensemble des travaux de nature numérique contenus dans ces articles au moyen de codes développés en grande partie par moi-même.

Trois des contributions de recherche insérées dans cette thèse concernent la manipulation de faisceaux au moyen de structures optiques bidimensionnelles composées d'arrangements de cylindres diélectriques (chapitres 4 à 6). Le principal outil numérique développé afin de réaliser ce projet de recherche est basé sur la théorie de Lorenz-Mie généralisée, une méthode de solution des équations de Maxwell centrale à cette thèse. Comme le problème de manipulation de faisceaux considéré dans cette thèse est en fait un problème d'optimisation combinatoire, j'ai également programmé deux algorithmes d'optimisation dits *méta-heuristiques*, soit l'algorithme génétique et la recherche tabou.

La première contribution (D. Gagnon, J. Dumont et L. J. Dubé, J. Opt. Soc. Am. A, Vol. 29, pp. 2673–2678) date de 2012 et est insérée au chapitre 4. On y définit le problème de manipulation de faisceaux de même que les méthodes numériques utilisées pour sa solution, soit la méthode de Lorenz-Mie et l'algorithme génétique.

La seconde contribution (D. Gagnon, J. Dumont et L. J. Dubé, Optics Letters, Vol. 38, pp. 2181–2184) a été publiée quelques mois plus tard en 2013 et est insérée au chapitre 5. La nouveauté de cette publication, présentée sous forme de lettre, est la manipulation de la phase du faisceau (seule l'amplitude était optimisée dans le travail précédent). Par ailleurs, en 2013, j'ai développé un code d'optimisation plus performant utilisant la recherche tabou plutôt que l'algorithme génétique. Ce code est utilisé pour la première fois dans cette publication.

La troisième et dernière contribution concernant la manipulation de faisceaux (D. Gagnon, J. Dumont, J.-L. Déziel et L. J. Dubé, Optics Letters, Vol. 39, pp. 5768–5771) est insérée au chapitre 6. Cette lettre porte plutôt sur l'optimisation du degré de polarisation des faisceaux de sortie en plus de leur profil d'amplitude.

La quatrième contribution de recherche (D. Gagnon, J. Dumont, J.-L. Déziel et L. J. Dubé, J. Opt. Soc. Am. B, Vol. 31 pp. 1867–1873) a été publiée en 2014 et est insérée au chapitre 7. Elle concerne

plutôt la modélisation de molécules photoniques, une réalisation possible de sources laser microscopiques. Ce travail est effectué au moyen de la théorie de Lorenz-Mie généralisée développée dans le cadre de mes travaux parallèles sur la manipulation de faisceaux. Par conséquent, l'article inséré au chapitre 7 est indépendant des trois autres. Cette publication a été écrite avant la troisième sur la manipulation de faisceaux, mais elle est insérée à la toute fin de la thèse afin d'assurer une certaine cohérence thématique de la présentation.

Bien que les quatre publications insérées soient indépendantes, trois chapitres introductifs et une conclusion ont été ajoutés à cette thèse. Le chapitre 1 se veut une introduction de nature pédagogique permettant de situer mes contributions dans le contexte plus global des structures photoniques complexes, un champ de recherche en plein essor. Le chapitre 2 présente de façon détaillée les développements théoriques associés à mes publications. L'emphase est placée sur la méthode de Lorenz-Mie généralisée – sujet principal de cette thèse – mais aussi sur une théorie du laser récemment développée intitulée SALT, acronyme de « steady state ab initio laser theory ». Le chapitre 3 présente de façon sommaire les algorithmes dits *méta-heuristiques*, des algorithmes d'optimisation qui constituent un sujet de recherche à part entière. L'emphase de ce chapitre est placée sur l'implémentation numérique des méta-heuristiques utilisées dans cette thèse, soit l'algorithme génétique et la recherche tabou. Le chapitre 8 contient un résumé des conclusions de chacune de nos contributions, un aperçu d'autres algorithmes de modélisation électromagnétique (§8.2) et une perspective sur les milieux photoniques désordonnés (§8.3).

À l'exception du résumé, des remerciements, de l'avant-propos et de résumés individuels avant chaque publication insérée, cette thèse est rédigée entièrement en anglais. Il s'agit d'un choix fait par souci de cohérence entre le texte des chapitres introductifs et le texte anglais des publications insérées. Ce texte est aussi près que possible des originaux publiés à l'exception de la mise en forme, de quelques ajustements visant à harmoniser la notation utilisée dans ce document et de la correction de quelques coquilles mineures. L'utilisation de l'anglais vise également à faciliter la diffusion de ces travaux auprès de la communauté scientifique.

Foreword

This dissertation contains a synthesis of my doctoral work, performed between September 2011 and August 2014. Four articles of which I am the first author are inserted in the body of this thesis and constitute the bulk of its content. I have carried out the totality of the numerical work contained in these articles using programs developed in-house.

Three of the contributions inserted in this thesis are concerned with beam shaping using two-dimensional (2D) photonic-crystal-like structures (chapters 4 to 7). The numerical tool central to this research project is based on the 2D generalized Lorenz-Mie theory (2D-GLMT), a method for solving Maxwell's equations in cylindrically symmetrical geometries. Since the beam shaping problem tackled in this thesis is in fact a combinatorial optimization problem, I have also implemented two so-called *metaheuristic* optimization algorithms, specifically the genetic algorithm and tabu search.

The first contribution (D. Gagnon, J. Dumont and L. J. Dubé, J. Opt. Soc. Am. A, Vol. 29, pp. 2673–2678) was published in 2012 and is inserted in chapter 4. The beam shaping problem is defined in this paper, as well as the numerical methods used for its solution, namely 2D-GLMT and the genetic algorithm.

The second contribution (D. Gagnon, J. Dumont and L. J. Dubé, Optics Letters, Vol. 38, pp. 2181–2184) was published a few months later in 2013 and is inserted in chapter 5. The novel aspect of this publication, presented in letter form, is the shaping of the phase front of the output beam (amplitude shaping only was considered in the 2012 article). Also in 2013, I have developed a more efficient optimization routine based on tabu search rather than the genetic algorithm. This code is used for the first time in this publication.

The third and final contribution on beam shaping (D. Gagnon, J. Dumont, J.-L. Déziel and L. J. Dubé, Optics Letters, Vol. 39, pp. 5768–5771) is inserted in chapter 6. This letter is concerned with the optimization of the degree of polarization of the output beams in addition to their amplitude profile.

The fourth research contribution (D. Gagnon, J. Dumont, J.-L. Déziel and L. J. Dubé, J. Opt. Soc. Am. B, Vol. 31 pp. 1867–1873) was published in 2014 and is inserted in chapter 7. It is concerned with the numerical modeling of photonic molecules, possible realizations of wavelength-scale

laser sources. This study is carried out using the 2D-GLMT approach used in my parallel works on beam shaping. Consequently, the article inserted in chapter 7 is mostly independent from the three others. This publication was written before the latest one on beam shaping, but it is inserted at the end of the dissertation in order to keep the presentation thematically coherent.

Although the four publications inserted in this thesis are completely self-contained, three introductory chapters and a conclusion complete them. Chapter 1 is a pedagogical introduction, the goal of which is to show the connection of my contributions with the broader and very active research field of complex photonic media. Chapter 2 details the theoretical aspects of my contributions. The emphasis is placed on 2D-GLMT – the central topic of this thesis – and also on a recently formulated laser theory called "steady-state ab initio laser theory", or SALT. Chapter 3 contains a summary of *metaheuristics*, optimization algorithms which constitute a full-fledged research field. The emphasis of this chapter is placed on the numerical implementations used in this thesis, specifically the genetic algorithm and tabu search. To conclude, chapter 8 contains a summary of the main findings of each of my contributions, as well as a survey of alternative numerical methods (§8.2) and a research outlook on disordered photonic media (§8.3).

This thesis is for the most part written in English, with the exception of the Acknowledgements section being solely written in French. It was decided to write all the scientific content in English to ensure cohesion of the presentation. The text of the inserted publications is as close as possible to the original source material, with some minor notation and formatting adjustments. The use of English is also intended to facilitate the dissemination of this work to other researchers.

Chapter 1

Introduction

This chapter introduces the scope of this thesis within the research field of complex photonic media, optical materials which are imbued with functionalities at the wavelength-scale level. The goal of this chapter is to give a pedagogical, hands-on introduction to the subject, leaving the theoretical and numerical aspects of the electromagnetic theory to chapter 2, as well as the algorithmic details of combinatorial optimization to chapter 3. The main objectives of this doctoral work are summarized in section 1.2, which also contains a plan of the dissertation.

1.1 Background: Photonic complexes

Traditional optical media, such as lenses and beam-splitters, are often called "macroscopically homogeneous", in the sense that the characteristic scale of their variation, or inhomogeneities, is much smaller than the wavelength of light [102]. On the other hand, optical geometries characterized by wavelength-scale inhomogeneities are called *complex photonic media*. Some typical examples of complex photonic media are photonic crystals [27], metamaterials [24] and disordered photonic materials [120, 167]. Photonic crystals can be viewed as composite optical materials characterized by spatial periodicities on the order of the wavelength of light, similar to Bragg gratings. Controlling the flow of light on the micro- and nano-scale level is one of the main technological breakthroughs enabled by the use of complex photonic media [102, 120]. Although this description suggests that complex photonic media are passive, they can also be composed of *active* optical material, making possible the fabrication of wavelength-scale *laser sources*.

One of the key objectives of this thesis work is to develop numerical tools for the modeling of complex photonic media. This is intrinsically challenging, since novel media often involve rich underlying physical phenomena, such as bandgaps [7], resonances [89] and Anderson localization of light [120, 165]. Counter-intuitive effects such as slow light [9] and negative refraction [95] can also take place in complex photonic media. Moreover, some of the tools typically taught in graduate courses in optics, such as the paraxial approximation and $ABCD$ matrices, are often incompatible with complex optical geometries. In short, numerical modeling tools for complex photonic me-

dia must often compose with the full vectorial nature of the electromagnetic field (described by Maxwell's equations), potentially active or nonlinear media and non-trivial boundary conditions.

Although the engineering of photonic materials allows a great level of control on the propagation of light, one important issue is how to integrate these materials on photonic circuits. This is crucial to the deployment of innovative optical elements onto existing technological platforms, for instance silicon-on-insulator wafers [27, 121] or plastic substrates [83]. One way to achieve integration is by effectively confining light propagation in two dimensions using planar waveguides, in which wavelength-scale structures are written using micro-fabrication technology [167]. In this thesis, we are mostly concerned with optical structures based on cylindrical scatterers introduced in the form of holes in a dielectric waveguide core [27]. Structures based on pillars are also possible [27]. The geometric properties of arrays of scatterers found in recent studies vary widely, ranging from periodic to aperiodic [25, 155] or completely disordered [39, 120, 167]. Throughout this thesis, we shall refer generically to these 2D wavelength-scale arrays of cylinders as *photonic complexes*.

An effectively 2D geometry defines two privileged propagation directions, namely the direction parallel to the scatterers' axis and the direction perpendicular to this axis. For modeling purposes, this allows one to uncouple the polarization of the electromagnetic field in two components commonly termed "TM" and "TE". The TM polarization corresponds to the electric field component parallel to the scatterers' or holes' axis, and the TE polarization is defined as the orthogonal component. This terminology shall be useful for the remainder of this section, in which we introduce the two kinds of photonic complexes that will be thoroughly studied in this thesis. In section 1.1.1, we briefly introduce photonic-crystal-like periodic arrangements of cylindrical scatterers. The emphasis is placed on the definition of a *bandgap*, an important wave effect that lies outside the reach of classical optics. Photonic-crystal inspired devices are the main topic of chapter 4 to 6 of this thesis. In section 1.1.2, we introduce the so-called *photonic atoms and molecules*, defined as simple arrangements of *optically active* cylinders. Photonic atoms and molecules often exhibit highly confined *resonances*, which suggests that they may be used as wavelength-scale laser sources. This is the main topic of chapter 7 of this thesis.

1.1.1 Photonic crystals

Photonic crystals (PhCs), defined as engineered periodic structures that exhibit photonic functionality at the material level [7], are a prime example of photonic complexes. This research field has been active since the seminal 1987 paper by Yablonovitch [172]. In this early work, the author observed that multiple scattering in a PhC could slow down the group velocity of light to the point of completely inhibiting propagation. The frequency interval in which waves cannot propagate in a PhC is called the *bandgap*. Bandgap effects can be predicted from the computation of the Bloch modes of photonic crystals, in essence solutions of Maxwell's equations in a periodic potential [140].

In this dissertation, we are mostly concerned with 2D PhCs, periodic in a plane and homogeneous in the perpendicular dimension [7]. As an example, a 2D square lattice of dielectric rods placed in air can possess a complete bandgap for the TM polarization if the refractive index contrast between the rods and the surrounding medium is sufficiently large. This means that a light wave characterized by a polarization parallel to the cylinders axis cannot propagate in such a crystal. An example of this bandgap phenomenon can be seen from in Fig. 1.1e. This band diagram shows the first two TM-polarized Bloch modes of the crystal are separated by a frequency interval which corresponds to the bandgap. Analogously, a 2D triangular lattice of air holes in a dielectric core can exhibit a complete bandgap for the TE polarization [7]. This means that the in-plane polarization component cannot propagate in this PhC geometry. This can be seen from Fig. 1.1f. In this thesis, computational analysis of the band structure of PhCs is carried out using the plane wave expansion method [73, 140]. The main hypothesis behind this numerical scheme [1] is that the Bloch modes of photonic crystals – periodic functions in space – can be expanded in terms of Fourier series or, in other words, plane waves [140, p. 132].

PhC inspired optical elements can readily be fabricated using micro-fabrication methods such as UV [171], holographic [140] or electron beam [27, 120] lithography. This relative ease of fabrication has enabled the realization of various integrated optical elements based on bandgap effects. Notable instances are Mach-Zehnder interferometers [104, 114], waveguides [72, 169], mirrors [114], polarization beam-splitters [114] and all-optical switches [64]. One of the main contributions of this thesis is to use PhC inspired integrated optical elements to achieve *beam shaping*, which is broadly defined as redistributing the irradiance and phase of an input beam into an output beam with pre-defined amplitude, phase and polarization characteristics [30].

In most of the practical applications described above, including beam shaping, the pillars or holes arrangements considered are often finite and irregular. This means the Bloch modes analysis does not strictly hold, since the arrangement of holes and pillars are neither infinite nor periodic. For this reason, this thesis is mostly concerned with numerical methods able to deal with non-periodic, finite PhCs. However, the Bloch modes analysis sometimes proves to be a useful design tool for integrated devices since it allows one to determine at which frequencies scattering is stronger, and how the two orthogonal polarization directions are affected by the presence of 2D scatterers.

1.1.2 Photonic atoms and molecules

The term "photonic crystal" is often defined by analogy with atomic and molecular structures, the photonic bandgap being the counterpart to the electronic bandgap. Following this analogy, the building blocks of photonic crystals – basically wave scatterers – are sometime called *photonic atoms and molecules*. Photonic atoms are often understood as composed of a single scatterer, while more than one of these building blocks coupled together constitutes a photonic molecule

1. The free and open-source software package MIT PHOTONIC BANDS, developed by S. G. Johnson, is a readily available implementation of the plane wave expansion method [73].

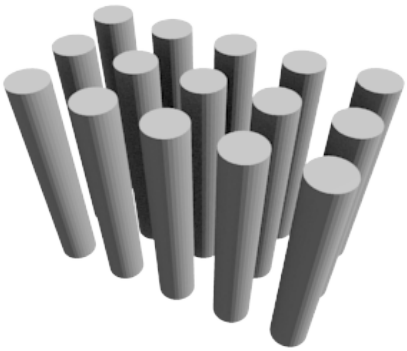

(a) Square lattice

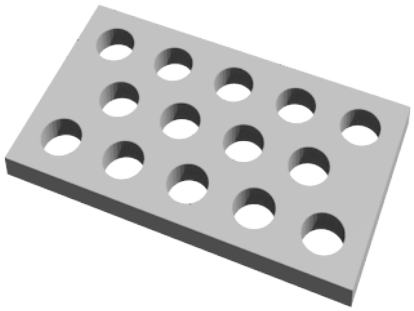

(b) Triangle lattice

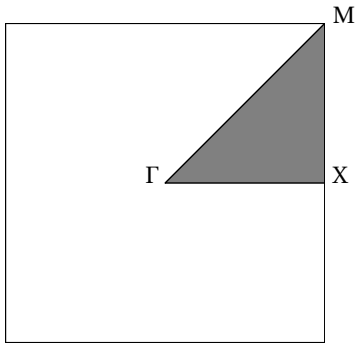

(c) First Brillouin zone (reciprocal space)

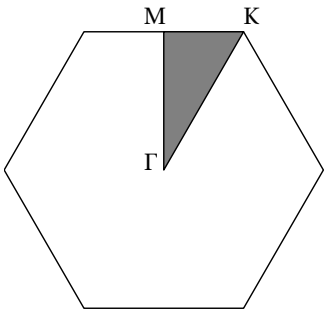

(d) First Brillouin zone (reciprocal space)

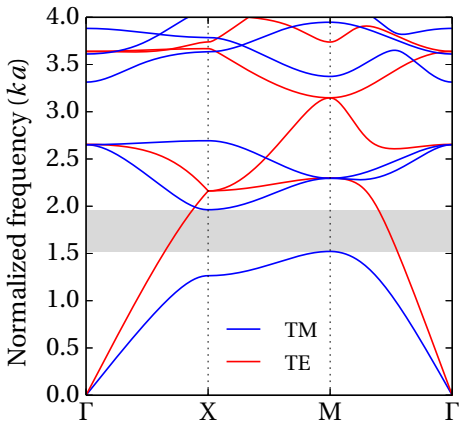

(e) Band diagram

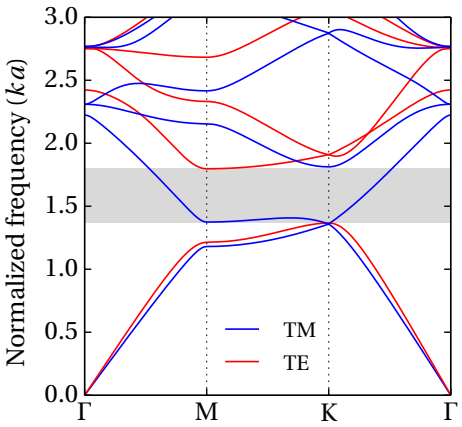

(f) Band diagram

Figure 1.1 – Two usual 2D photonic crystal geometries. (a) Photonic crystal based on rods in air. (b) Photonic crystal based on holes in a planar waveguide core. The refractive index of the dielectric materials is set to $n = 3.3$, and the aspect ratio between the cylinders (or holes) and the lattice constant is set to 0.3. (c-d) Irreducible first Brillouin zones (shaded) with an identification of high symmetry points. Plotting the Bloch mode frequencies along the irreducible zone is sufficient to establish the presence of a bandgap [140]. (e-f) Band diagrams along the irreducible first Brillouin zones, computed using the MIT PHOTONIC BANDS software package [73]. Shaded areas indicate complete bandgaps for either polarization (e: TM , f: TE).

(PM) [12, 13]. They are most often composed of a high refractive index dielectric medium in which the electromagnetic radiation can be trapped by means of total internal reflection, forming a *cavity*. This gives rise to various *resonances*, or *eigenmodes*. Cavity eigenmodes are inherently lossy, since they constitute physical systems open to the outside environment. Low losses are associated to a high quality factor (Q-factor), which is proportional to the number of round-trips a photon makes in the cavity in a given time interval. A high Q-factor also implies a narrow resonance. The most common shapes of individual photonic atoms include 3D geometries such as spheres [18] and tori [96], as well as effectively 2D geometries such as disks [85], rings [86] and stadium-shaped cavities [80, 82]. Additionally, mass production of photonic atoms and molecules is in principle possible since they can be integrated on a chip using standard photo-lithographic techniques [156].

The optical properties of microcavities and PMs, in particular their resonant behavior, make them useful for a variety of applications [153]. The detection of biological molecules, for instance proteins, is one application of microresonators that has emerged in the last decade [6, 156, 157]. In a typical biosensing experiment, the resonant spectrum of a microresonator is continuously monitored using a tunable laser. After a certain amount of time, the molecule to be detected attaches itself on the surface of the resonator, which is functionalized with appropriate binding agents [156]. The attachment event results in a shift of the resonance spectrum, the signature of the presence of the target molecule. This biomedical application is successful because microcavities are characterized by very narrow resonances, making attachment events easy to detect [6]. In other words, the high Q-factor of typical microresonators comes with a high sensitivity to outside perturbations [156].

Another privileged application of photonic atoms and molecules is the development of novel compact laser sources [98, 153]. Various active materials have been used to realize these small-scale lasers, including silica glass [18], semiconductors [47] and chalcogenide [154]. While silica glass is the preferred material used for sensing applications because of the very low associated losses [156], chalcogenide is particularly interesting for laser applications because of its very high Raman gain [154] and ease of integration on plastic substrates [83]. Indeed, pump thresholds as low as 13 μW have been reported in a spherical chalcogenide Raman microlaser operating at a wavelength of $\lambda = 1550$ nm [154]. These conspicuously low threshold values are a direct consequence of the low mode volume and high Q-factors typical of photonic atoms and molecules. Other applications that stem from the high Q-factor of microresonators include filters in optical communications [57] and frequency combs [28].

Keeping laser applications in mind, much work has been devoted to the achievement of directional emission from photonic atoms and molecules [54, 58, 61, 74, 81, 110, 125, 126, 144, 160]. Directional emission is defined as a far-field profile concentrated in a few preferential directions, and is usually achieved by breaking the geometric symmetry of a resonator, since symmetrical resonators are non-directional. There are two possible ways to realize this symmetry breaking.

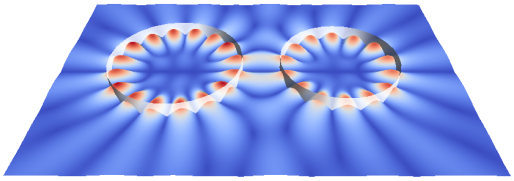

(a) Diatomic photonic molecule

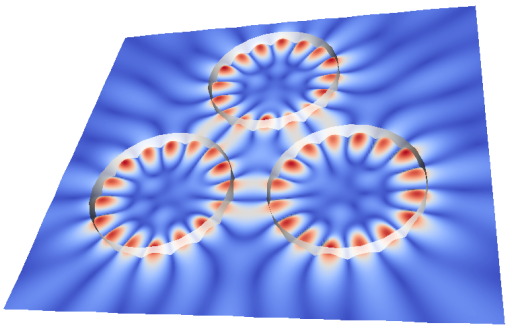

(b) Triangular photonic molecule

Figure 1.2 – Two representative photonic molecules and associated resonances. The colormap is in arbitrary units of irradiance and the cylinders are schematically represented, with an arbitrary height for visualization purposes. (a) Representation of the result of Fig. 7.2a. (b) Representation of the result of Fig. 7.11a.

The originally proposed approach is to consider a photonic atom with an irregular boundary, for instance smooth deformations of a circular cavity [58, 82, 144, 160]. Another approach that has emerged in recent years is to couple several symmetrical photonic atoms to form a directionally emitting PM [125, 126].

In this thesis, we are mostly concerned with the numerical modeling of PMs as compact laser sources. Although the coupling of several irregular individual photonic atoms is possible, we restrict our attention to PMs composed of a few coupled symmetric, or cylindrical cavities. Two possible realizations of this geometry are shown in Fig. 1.2, namely a diatomic PM composed of two active cylinders of different radii, and another one composed of three identical cylinders arranged on the vertices of an equilateral triangle.

1.2 Objectives and organization of this thesis

As stated in section 1.1, there exist two notable realizations of photonic complexes composed of coupled cylindrical structures. The first one is a passive arrangement of dielectric scatterers forming a so-called “finite PhC”, and the second one is the coupling of several active cylinders forming a PM. The key topic of this thesis is the study of these coupled structures using a numerical method that exploits the circular symmetry of the individual scatterers. These schemes are usually referred to as *Generalized Lorenz-Mie theories* [56]. Different schemes that can deal either with individual or coupled symmetrical scatterers such as spheres and cylinders are available in the literature [56]. Since this thesis primarily deals with the modeling of coupled cylindrical structures, the numerical scheme we use in this thesis can be referred to as *2D Generalized Lorenz-Mie theory*, or 2D-GLMT. Its objective is to obtain non-paraxial solutions to Maxwell’s equations in passive or active media, yielding the full electromagnetic field for both the TM and TE polarizations.

The specific research objectives of this thesis are as follows:

1. The design and optimization of integrated optical elements dedicated to beam shaping, which convert a given input beam into another one with pre-defined, amplitude, phase and polarization characteristics. The basic design procedure for these elements consists in optimizing the spatial arrangement of cylindrical scatterers on a photonic lattice. An integral part of this optimization procedure is to compute the field transmitted by the beam shaping elements using 2D-GLMT, which we generically refer to as *scattering computations*.

2. The numerical investigation of the physical properties of PM lasers. This is achieved via the determination of the *resonances* of coupled active cylinders using 2D-GLMT. More specifically, the objective is to better understand the effect of the underlying gain media on the lasing thresholds, lasing frequencies and emission patterns of photonic molecule lasers.

In order to achieve these two objectives, a numerical implementation of 2D-GLMT able to deal both with scattering and resonances of photonic complexes is presented in this dissertation. Besides 2D-GLMT, additional computational and theoretical tools are needed for both objectives. The first research objective (beam shaping) involves the solution of a hard optimization problem, which means that it is not practical to systematically enumerate its solutions. Consequently, this thesis is partly concerned with optimization algorithms called *metaheuristics*, robust methods that involve searching for optimal solutions in an empirical, albeit guided way. As for the second research objective (PMs), it involves dealing with optically active media. In order to obtain an accurate description of gain transitions, we choose to combine 2D-GLMT with the recently formulated *steady-state ab initio laser theory* (SALT).

This dissertation is organized as follows:

Chapter 2 – Methods I: Electromagnetic theory. This chapter contains a summary of the electromagnetic theory behind our research contributions. In section 2.1, a derivation of the vector and scalar Helmholtz equation for generic 2D geometries is presented, starting from Maxwell's equations. The difference between scattering and resonances of photonic complexes is discussed in section 2.1.1. The concept of *quasi-bound* states, a common definition of a resonance, is also introduced in this section.

Section 2.2 contains a discussion of the so-called *steady-state ab initio laser theory* (SALT), which is central to our contributions on PM lasers. The main features of SALT are also briefly discussed, specifically the introduction of new classes of resonant states.

Finally, section 2.3 contains a theoretical description of 2D-GLMT, the numerical scheme central to this thesis. The main hypotheses of the theory are stated, following by a description of how to apply it to scattering and eigenstates of arrays of coupled cylinders. Limitations and possible extensions of the methods are discussed in section 2.3.6.

Chapter 3 – Methods II: Metaheuristics for combinatorial optimization in photonics design. This chapter contains a summary of *metaheuristics*, broadly defined as optimization algorithms dedicated to the solution of "hard" optimization problems. In section 3.1, the definition of a "hard" combinatorial optimization problem is first presented. This is followed by a brief overview of the two algorithms that are used in this thesis, namely tabu search (§3.2.1) and the canonical genetic algorithm (§3.2.2).

Chapter 4 – Beam shaping using genetically optimized 2D photonic crystals. This chapter contains our first original research contribution concerning beam shaping. More specifically, we design integrated amplitude beam shapers using a combination of the 2D-GLMT approach presented in chapter 2 and the genetic algorithm (GA) presented in chapter 3. We show that it is possible to use optimized photonic lattice configurations to generate different orders of Hermite-Gauss profiles, while maintaining reasonable losses and tolerance to variations in the input beam and the slab refractive index. Detailed characterization of the optimized configurations are presented in supplement 4.6.

This chapter is the reproduction of a peer-reviewed article published in 2012 [44]. On a side note, the GA is used in this contribution mainly for historical reasons, as it was quickly replaced by tabu search for reasons that shall become clear in chapter 5.

Chapter 5 – Multiobjective optimization in integrated photonics design. This chapter contains a second original contribution concerning beam shaping, and can be viewed as a "sequel" to the previous one. While the beam shaping devices proposed in chapter 4 were designed to control solely the amplitude profile of the output beam, this contribution addresses the control of the phase profile as well (coherent beam shaping). The phase control represents another objective function to optimize in addition to the amplitude-related objective function. Consequently, the optimization problem to be solved becomes more computationally intensive. To alleviate this increased computational cost, we propose the use of an alternative metaheuristic called *parallel tabu search* (PTS). Using this improved algorithm, the coherent beam shaping problem can be solved more efficiently as illustrated by the generation of Hermite-Gauss beams of controlled phase profile, leading to a better beam collimation.

This chapter is the reproduction of a peer-reviewed article published in 2013 [46]. One of the take-home messages of this work is to propose the use of PTS as a possible alternative to the GA for combinatorial optimization problems in photonics design. Indeed, while the GA is part of the lore of the photonics research community, PTS is not as well-known and is seldom used in this field. Additional results concerning self-collimation in photonic crystals and the tolerance of beam shaping devices to fabrication imperfections are presented in appendices of this chapter.

Chapter 6 – Optimization of integrated polarization filters. This chapter is the last of our trilogy on beam shaping. In this contribution, we optimize integrated optical devices that combine two

functionalities, specifically beam shaping and logical polarization filtering. The basic geometry and optimization procedure are similar to those used in chapter 5. Using a rods-in-air lattice as a basis for a TE filter and a holes-in-slab lattice for the analogous TM filter, we show the possibility to generate Gaussian beams with a degree of polarization of up to 98 %, while maintaining a transmission efficiency greater than 75 %.

This chapter is the reproduction of an article published in 2014. While we restrict the discussion to Gaussian beams in the main contribution, the generation of arbitrarily shaped polarized beams is possible. This is hinted at by the results found in supplement 6.5.1. This chapter also suggests a possible application of the beam shaping devices proposed in this dissertation, since polarization is a physical dimension of light that can be exploited to increase the transmission rate of optical networks [113, 168].

Chapter 7 – Ab initio investigation of lasing thresholds in photonic molecules. This chapter is concerned with another application of 2D-GLMT, the computation of resonances in PMs. It begins with a discussion of how the usual method of computing the quasi-bound (or meta-stable) resonances falls short of giving accurate quantitative predictions of the lasing thresholds in laser resonators. Indeed, the gain medium parameters – such as the gain transition central frequency and its linewidth – are not taken into account in the theory leading to quasi-bound states. To improve this description, we use 2D-GLMT to compute the *threshold lasing modes* of a simple PM, a new kind of eigenstate central to the SALT theory. We then proceed to extract the value of the lasing thresholds from these modes and show that they depend non-trivially on the gain medium parameters, a result that is out of reach of the usual quasi-bound states approach.

This chapter is the reproduction of a peer-reviewed article published in 2014 [42]. The aim of this contribution is to show the importance of using SALT to accurately describe the lasing characteristics of photonic atoms and molecules, especially lasing thresholds. In addition, supplement 7.6 shows how the gain medium parameters can affect the emission profiles, thereby yielding an additional control parameter for the achievement of directionally emitting compact laser sources.

Chapter 8 – Conclusion This chapter summarizes the main findings of this doctoral work and presents a research outlook on disordered photonic media. Alternative modeling tools for complex photonic media are also briefly discussed.

Reading guide. As this dissertation is composed of 3 introductory chapters (1 to 3) followed by 4 chapters containing peer-reviewed contributions (4 to 7), there are several possible ways to read it in a self-consistent manner, as explained in Fig. 1.3.

The application of 2D-GLMT to beam scattering (§2.3.4) and chapter 3 on combinatorial optimization are necessary only to the peer-reviewed contributions concerning beam shaping. For the reader mostly interested in these contributions, the sections on SALT (§2.2) and eigenmode

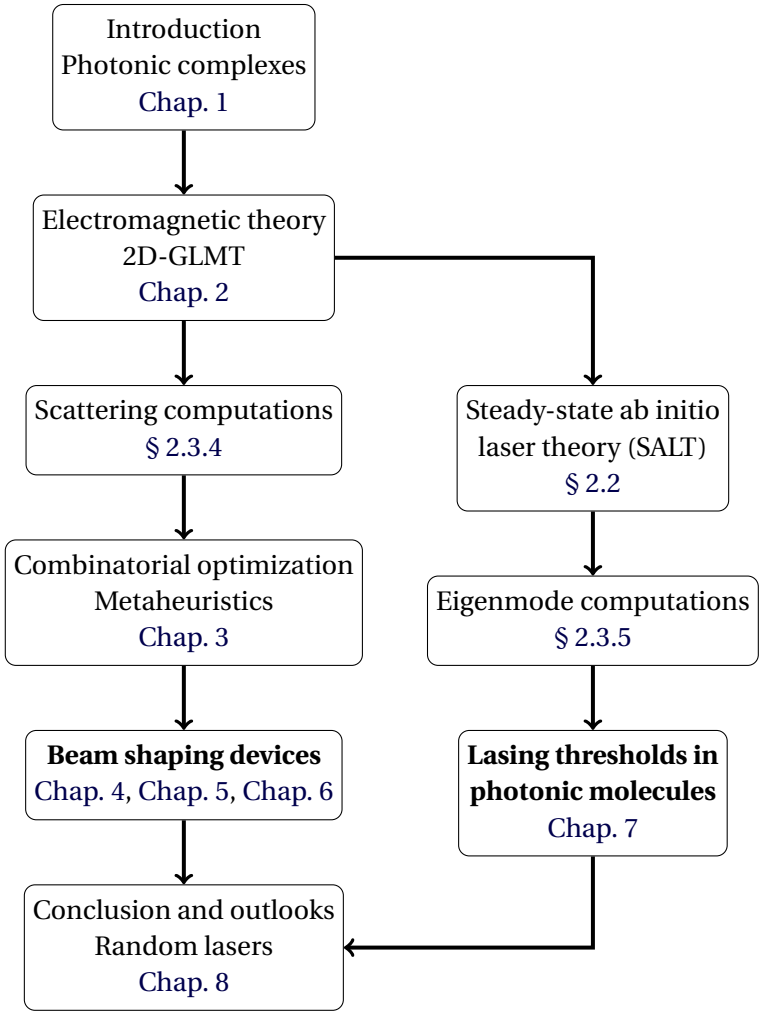

Figure 1.3 – Flowchart of this thesis. In chap. 2, a branching point exists between research contributions on beam shaping (left track) and contributions on PMs (right track), although the thesis can still be read continuously. The nodes labeled in **bold** indicate peer-reviewed contributions reproduced in this dissertation.

computations (§2.3.5) can be skipped, as well as chapter 7. This corresponds to the left track in Fig. 1.3.

Similarly, the SALT theory (§2.2) and eigenmode computations (§2.3.5) are reused chiefly in chapters 7 and 8 of the thesis. Consequently, all of these sections are independent from chapters 3 to 6. This corresponds to the right track on Fig. 1.3, which can be followed by readers mostly interested in the parts of this thesis concerned with microcavities and PMs. Despite this apparent disconnection of the two topics (scattering and eigenmode computations), we attempt to present a coherent, natural progression from passive to active complex photonic media, both within chapter 2 and throughout the dissertation.

Chapter 2

Methods I: Electromagnetic theory

In a theory which has given results like these, there must certainly be a great deal of truth.

H. A. Lorentz

In this chapter, we summarize the electromagnetic theory used in this thesis. We begin by deriving the vector and scalar Helmholtz equations for 2D geometries, starting from Maxwell's equations (§2.1). While the derivation of the Helmholtz equation for linear optical media is straightforward, the approach must be modified to take active optical media into account. This can be achieved using a stationary formulation of the Maxwell-Bloch equations called *steady-state ab initio laser theory* (SALT). This recently formulated approach, as well as the new kind of optical eigenmodes it introduces, are described in section 2.2.

After these derivations of the basic equations for passive and active 2D geometries, we move on to a description of the central modeling tool behind this thesis, the two-dimensional generalized Lorenz-Mie theory (2D-GLMT, §2.3). This theory is in fact a numerical method used to compute the interaction of light with arrays of cylindrical scatterers. This is achieved via the expansion of the electromagnetic field in a basis of cylindrical waves centered on each individual scatterer.

The electromagnetic theory presented here is a prelude to our contributions described in chapters 4 to 7. The problem of beam shaping using passive two-dimensional structures is approached using 2D-GLMT in chapters 4 to 6. Finally, 2D-GLMT is combined with the SALT theory in chapter 7 to investigate the lasing behavior of coupled active cavities.

2.1 Electromagnetic theory

The starting point for the electromagnetic theory presented in this chapter are Maxwell's equations. In a non-magnetic medium (unitary magnetic permeability, or $\mu = 1$), these equations take

the following form [2]

$$\nabla \cdot \mathbf{D} = \rho, \tag{2.1.1a}$$

$$\nabla \cdot \mathbf{H} = 0, \tag{2.1.1b}$$

$$\nabla \times \mathbf{E} = -\frac{1}{c}\frac{\partial \mathbf{H}}{\partial t}, \tag{2.1.1c}$$

$$\nabla \times \mathbf{H} = \frac{1}{c}\frac{\partial \mathbf{D}}{\partial t} + \frac{\mathbf{J}}{c}. \tag{2.1.1d}$$

These equations relate the four fundamental vector fields of electromagnetism – the electric field **E**, the magnetic field **H**, the current density **J** and the electric displacement field **D** – as well as two scalar quantities – the volume charge density ρ and the speed of light in vacuum c. We are chiefly concerned by obtaining rigorous solutions of Maxwell's equations in regions of space that contain no free charges and no free currents, that is [15]

$$\rho = 0, \tag{2.1.2a}$$

$$\mathbf{J} = 0. \tag{2.1.2b}$$

However, since we are also interested in solutions of Maxwell's equations in active media, we suppose the following relation between the displacement field **D** and the electric field **E** [15, 29]

$$\mathbf{D} = \mathbf{E} + \mathbf{P}, \tag{2.1.3}$$

where **P** is the nonlinear polarization field. It contains both a contribution from the linear response of the medium (basically the optical density, or refractive index) and the nonlinear response. Under these conditions, Maxwell's equations take the following form

$$\nabla \cdot \mathbf{D} = 0, \tag{2.1.4a}$$

$$\nabla \cdot \mathbf{H} = 0, \tag{2.1.4b}$$

$$\nabla \times \mathbf{E} = -\frac{1}{c}\frac{\partial \mathbf{H}}{\partial t}, \tag{2.1.4c}$$

$$\nabla \times \mathbf{H} = \frac{1}{c}\frac{\partial \mathbf{E}}{\partial t} + \frac{1}{c}\frac{\partial \mathbf{P}}{\partial t}. \tag{2.1.4d}$$

Taking the curl of (2.1.4c) and (2.1.4d), one obtains the following wave equations

$$\nabla \times \nabla \times \mathbf{E} + \frac{1}{c^2}\frac{\partial^2 \mathbf{E}}{\partial t^2} + \frac{1}{c^2}\frac{\partial^2 \mathbf{P}}{\partial t^2} = 0, \tag{2.1.5a}$$

$$\nabla \times \nabla \times \mathbf{H} + \frac{1}{c^2}\frac{\partial^2 \mathbf{H}}{\partial t^2} - \frac{1}{c}\frac{\partial}{\partial t}\big[\nabla \times \mathbf{P}\big] = 0. \tag{2.1.5b}$$

These two fundamental equations for **E** and **H** can be further reduced if the response of the optical media is assumed to be linear. In the remainder of this section, we shall suppose it is indeed the case and continue the discussion for nonlinear and/or active media in section 2.2.

2. Without loss of generality, the system of Heaviside-Lorentz electromagnetic units is used throughout this work except where indicated. In this system of units, the SI constants are fixed to $\mu_0 = \epsilon_0 = 1$, which leaves only the fundamental constant c in the equations. This definition also implies that the units of **E** and **H** are the same. Details of the conversion between Heaviside-Lorentz and other systems, i.e. SI or Gaussian units, can be found in [29].

In the case of a linear response of the medium, we suppose that the polarization field is a linear function of the electric field, more specifically

$$\mathbf{P} = \chi_e \mathbf{E}, \tag{2.1.6}$$

where χ_e is the electric susceptibility of the medium, i.e. $\chi_e = 0$ in free space. The substitution of the Ansatz (2.1.6) in (2.1.5a) and (2.1.5b) yields the linear wave equations

$$\nabla \times \nabla \times \mathbf{E} + \frac{\epsilon}{c^2}\frac{\partial^2 \mathbf{E}}{\partial t^2} = 0, \tag{2.1.7a}$$

$$\nabla \times \nabla \times \mathbf{H} + \frac{1}{c^2}\frac{\partial^2 \mathbf{H}}{\partial t^2} - \frac{1}{c}\frac{\partial}{\partial t}\big[\nabla \times (\chi_e \mathbf{E})\big] = 0, \tag{2.1.7b}$$

where we have redefined $\epsilon \equiv 1 + \chi_e$, the frequently used *relative dielectric permittivity*. Using a few vector identities, these wave equations can be recast as

$$\nabla(\nabla \cdot \mathbf{E}) - \nabla^2 \mathbf{E} + \frac{\epsilon}{c^2}\frac{\partial^2 \mathbf{E}}{\partial t^2} = 0, \tag{2.1.8a}$$

$$\nabla(\nabla \cdot \mathbf{H}) - \nabla^2 \mathbf{H} + \frac{\epsilon}{c^2}\frac{\partial^2 \mathbf{H}}{\partial t^2} - \frac{1}{c}\frac{\partial}{\partial t}\big[\mathbf{E} \times \nabla \chi_e\big] = 0. \tag{2.1.8b}$$

In the case where $\epsilon(\mathbf{r})$ is a continuous function of space, these equations can not be further simplified. However, in most cases of interest for this thesis, $\epsilon(\mathbf{r})$ will be a piecewise constant function, meaning that the photonic structures of interest to this work are composed of constant relative permittivity regions separated by well defined interfaces, where the value of $\epsilon(\mathbf{r})$ is discontinuous. It is therefore possible to solve the equations under the assumption that $\nabla\epsilon(\mathbf{r}) = 0$ and $\nabla\chi_e(\mathbf{r}) = 0$, and then connect the solutions at the interfaces using appropriate electromagnetic boundary conditions. In other terms, it can be assumed that most of the time there is no refractive index gradient in the photonic structures we consider. This excludes graded index media, for instance.

Under these circumstances, $\nabla \cdot \mathbf{E} = 0$, as can be shown from (2.1.4a). Expanding the divergence operator yields

$$\nabla \cdot \mathbf{D} = \nabla \cdot [\epsilon \mathbf{E}] = \epsilon \nabla \cdot \mathbf{E} + \mathbf{E} \cdot \nabla \epsilon = 0. \tag{2.1.9}$$

Since, $\nabla\epsilon(\mathbf{r}) = 0$, one concludes that $\nabla \cdot \mathbf{E} = 0$. The substitution of these results in (2.1.8a) and (2.1.8b) finally yields the vector Helmoltz equations

$$\nabla^2 \mathbf{E} - \frac{\epsilon}{c^2}\frac{\partial^2 \mathbf{E}}{\partial t^2} = 0, \tag{2.1.10a}$$

$$\nabla^2 \mathbf{H} - \frac{\epsilon}{c^2}\frac{\partial^2 \mathbf{H}}{\partial t} = 0. \tag{2.1.10b}$$

These equations are more conveniently solved in the frequency domain, using the following substitution for temporal derivatives

$$\frac{\partial^2}{\partial t^2} \leftarrow -\omega^2. \tag{2.1.11}$$

This is equivalent to assuming a harmonic time-dependence of the electromagnetic field, i.e. $\mathbf{E} = \mathbf{E}(\mathbf{r})e^{-i\omega t}$ and $\mathbf{H} = \mathbf{H}(\mathbf{r})e^{-i\omega t}$. This yields

$$\nabla^2\mathbf{E} + \epsilon(\mathbf{r})k^2\mathbf{E} = 0, \tag{2.1.12a}$$

$$\nabla^2\mathbf{H} + \epsilon(\mathbf{r})k^2\mathbf{H} = 0, \tag{2.1.12b}$$

where we have used the definition of the wavenumber $k \equiv \omega/c$.

The vector Helmholtz equation is a general description of wave propagation in fully three-dimensional, linear media of piecewise constant refractive index. This covers a wide range of optical geometries, such as optical fibers and waveguides [106], dielectric cavities such as spheres and tori [153] and three-dimensional photonic crystals [7, 92, 140]. Since the scope of this thesis is mostly two-dimensional structures, an additional symmetry can be further used to reduce the vector Helmholtz equation to a scalar form [41].

Two dimensional geometries usually suggest two privileged polarization directions. Formally, it is possible to uncouple the electromagnetic field in two orthogonal polarization components if variations of the relative permittivity $\epsilon(\mathbf{r})$ are restricted to a plane, say the (x, y) plane, meaning

$$\epsilon(\mathbf{r}) = \epsilon(x, y). \tag{2.1.13}$$

Under this condition, the electromagnetic field can be uncoupled in a transverse-electric (TE) component (**E** field component parallel to the x, y plane, **H** field component normal to the x, y plane) and a transverse magnetic (TM) component (**H** field component parallel to the x, y plane, **E** field component normal to the x, y plane). Under this condition, (2.1.12a) and (2.1.12b) can be recast in a single *scalar Helmholtz equation*, that is

$$\boxed{\nabla^2\varphi(x, y) + \epsilon(x, y)k^2\varphi(x, y) = 0,} \tag{2.1.14}$$

where φ stands for either the E_z or H_z field component, and the ω dependence is dropped. As described in section 2.3, the scalar Helmholtz equation (2.1.14) is particularly suitable for modeling dielectric cylinders. Indeed, as with (2.1.12a) and (2.1.12b), the scalar form of the equation means that the eigenfunctions of the Helmholtz equation are of similar form for both polarizations, with the boundary conditions however differing (see for instance §2.3.3).

2.1.1 Scattering vs resonances: Quasi-bound states

The linear Helmholtz equation (2.1.14) may be used for two kinds of computations, namely (1) wave scattering and (2) resonances. As will be discussed in section 2.3.4, scattering computations are straightforward and consist in computing the response of a given optical system to an incident excitation. The incident and scattered waves are expanded on a suitable basis of the Helmholtz equation, and the expansion coefficients of the scattered wave are deduced from the expansion coefficients of the incident excitation. Thus, wave scattering problems are analogous to solving a linear system of equations.

On the other hand, resonance computations are more subtle than scattering computations since they are analogous to solving a homogeneous linear system, in other words finding the *eigenvalues* of a system of equations. The associated solutions of the Helmholtz equation are consequently termed *eigenmodes*. Computing the eigenmodes usually implies searching for complex k values ($k = \mathrm{Re}[k] + i\,\mathrm{Im}[k]$) satisfying a *resonance condition*. Complex k values with $\mathrm{Im}[k] < 0$ result in exponential decay of the total energy of the optical system. According to the harmonic hypothesis $\varphi(\mathbf{r}, t) = \varphi(\mathbf{r})e^{-i\omega t}$, the total electromagnetic energy of the system is proportional to

$$|\varphi(\mathbf{r}, t)|^2 = |\varphi(\mathbf{r})|^2 e^{-t/\tau}, \tag{2.1.15}$$

where $|\varphi(\mathbf{r})|^2$ is the field profile of the eigenmode and τ the characteristic decay time (or half-life) of the system energy. It is given by

$$\tau = -\frac{1}{2c\,\mathrm{Im}[k]}. \tag{2.1.16}$$

This delay can be readily interpreted as the characteristic residency time of a photon trapped in an optical resonator. Since these modes are inherently leaky, they are usually called *meta-stable* or *quasi-bound* (QB) states, by opposition to bound states which are characteristic of closed quantum systems. This analogy stems from the similarity between the Schrödinger equation and the Helmholtz equation [41].

Although useful for modeling active cavities, QB states come with an important shortcoming. This stems from the fact that the solutions to (2.1.14) are assumed to be stationary inside the cavity, although resonant wavefunctions of open systems cannot by definition be stationary (their energy must decay in time) [58]. Since $\epsilon(\mathbf{r})$ is real everywhere, the only way to obtain a decaying energy is by means of the imaginary part of the eigenfrequency k. However, this imaginary part has the net effect of introducting an artificial gain in the whole space domain. Consequently, QB states grow exponentially towards infinity, which is not physically realistic [49, 152]. Strictly speaking, these states are not even regular functions because of this blow-up behavior [58]. In section 2.2, we introduce a recently formulated theory that overcomes this shortcoming by taking into account the active medium *ab initio*, instead of the *a posteriori* introduction of gain associated with QB states [49].

2.2 Optically active media: Steady-state ab initio laser theory

In the previous section, we have derived the scalar Helmholtz equation (2.1.14) for 2D geometries. The main hypothesis behind the derivation is the linear response of the optical media. In the presence of an active medium, for instance a pumped laser cavity, the derivation is rather different. However, as discussed in section 2.1.1, it is still possible to use the linear Helmholtz equation to model two-dimensional active media using QB states. This description has two main shortcomings, specifically (1) the exponential growth of QB states outside the resonator and (2) the conspicuous absence of the gain medium parameters in the linear Helmholtz equation (2.1.14).

To improve on these shortcomings, this thesis makes use of a recent formulation called *steady-state ab initio laser theory* (SALT). The term *ab initio* refers to the fact that SALT only requires the distribution of $\epsilon(\mathbf{r})$ of the passive cavity, or resonator, and a number of parameters describing the gain medium. The theory is stationary, meaning it works in the frequency domain, and is intended to bridge the gap between the simplified QB states approach described in section 2.1.1 and time-domain simulations using dynamical theories, for instance the Maxwell-Bloch or Schrödinger-Bloch theories [49, 58, 152]. Moreover, as described in section 2.3.5, the Lorenz-Mie theory central to this thesis is mostly compatible with SALT [4].

The goal of this section is to highlight the meaningful features of this theory as well as derive the main SALT equations from Maxwell's equations. [3]

2.2.1 Basic equations and threshold lasing modes

In this section, we derive the basic equations of SALT using the electromagnetic theory presented in section 2.1 and the Maxwell-Bloch equations for a two-level atomic system. For convenience, only the derivation for a TM polarized wave in a 2D geometry is presented here. The first step is to introduce a non-linear polarization term of the following form

$$\mathbf{P} = \chi_e \mathbf{E} + \mathbf{P}_{\mathrm{NL}}, \tag{2.2.1}$$

in (2.1.5a), which yields

$$\nabla \times \nabla \times \mathbf{E} + \frac{\epsilon}{c^2}\frac{\partial^2 \mathbf{E}}{\partial t^2} + \frac{1}{c^2}\frac{\partial^2 \mathbf{P}_{\mathrm{NL}}}{\partial t^2} = 0. \tag{2.2.2}$$

We then assume a TM polarized wave, use the notation $E \equiv E_z, P \equiv (P_{\mathrm{NL}})_z$ and suppose a piecewise constant refractive index in order for the $\nabla \cdot \mathbf{E}$ term to drop. Under these assumptions, (2.2.2) becomes

$$\nabla^2 E - \frac{\epsilon}{c^2}\frac{\partial^2 E}{\partial t^2} - \frac{1}{c^2}\frac{\partial^2 P}{\partial t^2} = 0. \tag{2.2.3}$$

Under the rotating wave approximation (RWA), one can expand the electric and polarization fields in a positive frequency part and a negative frequency part, i.e. $E = E^+ + E^-$ and $P = P^+ + P^-$. [4] This allows to rewrite (2.2.3) only for the positive frequency field component, keeping in mind that the negative frequency component satisfies a similar equation

$$\nabla^2 E^+ - \frac{\epsilon}{c^2}\frac{\partial^2 E^+}{\partial t^2} - \frac{1}{c^2}\frac{\partial^2 P^+}{\partial t^2} = 0. \tag{2.2.4}$$

3. The steady-state ab initio laser theory was initially developed by H. Türeci, A. Stone and B. Collier in 2006, and was originally called *ab initio self-consistent laser theory*, or AISC [152]. It was this seminal paper that first introduced the constant-flux (CF) states central to the *ab initio* approach. Derivations in this section of the thesis are mostly drawn from the work of L. Ge, who worked on generalizing the theory after it was renamed SALT [48, 49].

4. The RWA consists in only keeping the difference-frequency terms in nonlinear equations, discarding the sum-frequency parts (for example, a E^+P^+ term would be dropped from the equations, while a E^+P^- term would be kept)

The SALT theory is based on the Maxwell-Bloch equations for a two-level atomic system:

$$\frac{\partial P^+}{\partial t} = -(i\omega_a + \gamma_\perp)P^+ + \frac{g^2}{i\hbar}E^+\mathfrak{D}, \tag{2.2.5}$$

$$\frac{\partial \mathfrak{D}}{\partial t} = \gamma_\parallel(\mathfrak{D}_0(\mathbf{r}) - \mathfrak{D}) - \frac{2}{i\hbar}[E^+(P^+)^* + P^+(E^+)^*]. \tag{2.2.6}$$

This set of equations relates the electric and polarization field with the spatially varying population inversion $\mathfrak{D}(\mathbf{r})$ and the pump profile $\mathfrak{D}_0(\mathbf{r})$. The gain central frequency ω_a and linewidth (or polarization relaxation rate) $\gamma_\perp$ appear in (2.2.5). Other constants are the population relaxation rate $\gamma_\parallel$ and the dipole matrix element g. For convenience, we renormalize the population inversion in the following way

$$D \equiv \frac{g^2\mathfrak{D}}{\gamma_\perp\hbar}, \tag{2.2.7}$$

so that D is dimensionless. This yields the following Maxwell-Bloch equations

$$\frac{\partial P^+}{\partial t} = -(i\omega_a + \gamma_\perp)P^+ - i\gamma_\perp E^+ D, \tag{2.2.8}$$

$$\frac{1}{\gamma_\parallel}\frac{\partial D}{\partial t} = (D_0(\mathbf{r}) - D) - \kappa[E^+(P^+)^* + P^+(E^+)^*], \tag{2.2.9}$$

where the coupling constant κ is defined as [5]

$$\kappa \equiv \frac{2g^2}{\gamma_\parallel\gamma_\perp\hbar^2}. \tag{2.2.10}$$

As shall become clear later, this coupling coefficient governs the strength of the spatial-hole burning effect, that is interaction between lasing modes above threshold.

The next step in the derivation is to assume a multi-mode Ansatz as presented in Ref. [49]. More specifically, we suppose the following harmonic expansions of the electric and polarization field

$$E^+ = \sum_\mu \varphi_\mu(\mathbf{r})e^{-i\omega_\mu t}, \tag{2.2.11a}$$

$$P^+ = \sum_\mu p_\mu(\mathbf{r})e^{-i\omega_\mu t}, \tag{2.2.11b}$$

where the indices μ label the different lasing modes of the system and ω_μ are the (real) lasing frequencies. Substituting this Ansatz in (2.2.4) and (2.2.8) yields the following equations

$$\nabla^2\varphi_\mu + k_\mu^2[\epsilon\varphi_\mu + p_\mu] = 0, \tag{2.2.12}$$

$$p_\mu = \frac{\gamma_\perp D(\mathbf{r})}{\omega_\mu - \omega_a + i\gamma_\perp}\varphi_\mu. \tag{2.2.13}$$

where $k_\mu = \omega_\mu/c$. Upon inserting (2.2.13) in (2.2.12), one obtains the main equation of SALT

$$\left\{\nabla^2 + \left[\epsilon(\mathbf{r}) + \frac{\gamma_a D(\mathbf{r})}{k - k_a + i\gamma_a}\right]k^2\right\}\varphi(\mathbf{r}) = 0, \tag{2.2.14}$$

5. A side note on units: The Heaviside-Lorentz units are dimensionally equivalent to Gaussian units, so that (2.2.8) has units of electric field over time, (2.2.9) is dimensionless and κ has inverse units of E^2. As a reminder, electric, magnetic and polarization fields are dimensionally equivalent in Heaviside-Lorentz and Gaussian units.

where we have dropped the μ indices and redefined $k_a = \omega_a / c$ and $\gamma_a = \gamma_\perp / c$. This equation contains all the relevant *ab initio* information on the lasing system. Indeed, it is analogous to the linear Helmholtz equation (2.1.14) with a complex effective dielectric function which depends on the gain medium parameters k_a, γ_a, as well as on the inversion profile $D(\mathbf{r})$ which in turns depends nonlinearly on the field φ as dictated by (2.2.9).

The only question that remains at this point of the derivation is how to fix the value of $D(\mathbf{r})$. For conciseness, we shall only summarize the main results and refer the reader to Ref. [48] for a detailed discussion. The main hypothesis that yields a convenient expression for $D(\mathbf{r})$ is the *stationary inversion approximation*, which implies $\frac{\partial D}{\partial t} = 0$. In short, this approximation implies that the population inversion of the two-level system remains constant in time. This approximation is valid in the single-mode regime, as well as in the multi-mode regime under the condition $\gamma_\perp \gg \gamma_\parallel$, in other words if the characteristic time scale of the inversion dynamics is larger than that of the polarization dynamics. Under these conditions, the dependence of $D(\mathbf{r})$ on the set of lasing modes φ_μ can be worked out from (2.2.9), and one obtains

$$D(\mathbf{r}) = \frac{D_0 F(\mathbf{r})}{1 + \kappa h(\mathbf{r})}, \tag{2.2.15}$$

where D_0 is the dimensionless pump strength, $F(\mathbf{r})$ is the pump profile and h is the modal interaction term, or *spatial hole-burning* term, given by [49]

$$h(\mathbf{r}) \equiv \sum_\nu \Gamma_\nu |\varphi_\nu(\mathbf{r})|^2, \tag{2.2.16}$$

where

$$\Gamma_\nu = \frac{\gamma_a^2}{(k_\nu + k_a)^2 + \gamma_a^2}. \tag{2.2.17}$$

In the single-mode regime or when the electromagnetic fields are small with respect to the coupling coefficient κ, the hole-burning effects can be neglected. In that case, the lasing modes are governed by the following equation

$$\boxed{\left\{\nabla^2 + \left[\epsilon(\mathbf{r}) + \frac{\gamma_a D_0 F(\mathbf{r})}{k - k_a + i\gamma_a}\right] k^2\right\}\varphi(\mathbf{r}) = 0.} \tag{2.2.18}$$

The eigenmodes governed by this equation are usually called *threshold lasing modes* (TLMs) since they paint an accurate picture of the emission profile of the laser at threshold. Unlike the modes described by (2.2.14), the TLMs only depend on the gain medium parameters k_a, γ_a, the pump strength D_0 and the spatial pump profile $F(\mathbf{r})$. Moreover in the absence of pumping ($F(\mathbf{r}) = 0$), for instance outside the laser resonator, the modes satisfy a linear Helmholtz equation (2.1.14) with real frequency k. This allows a more realistic description of the lasing modes than the QB states approach since the gain medium is introduced as an effective permittivity instead of an artificial imaginary part of the wavenumber [49].

The determination of TLMs can be achieved using various numerical schemes including the Lorenz-Mie approach described in section 2.3 or the finite element method described in [84]. For a given

combination of $\epsilon(\mathbf{r})$, $F(\mathbf{r})$, k_a and γ_a, the problem consists in finding the value of the lasing frequencies k_μ, thresholds D_0^μ and the field distributions φ_μ. However, for a given choice of exterior real frequency k, the value of D_0^μ is in general complex. Consequently, the TLM must satisfy an additional reality condition on the threshold value, since a complex-valued D_0^μ does not correspond to a physically realistic lasing mode [49]. In short, one must map the evolution of D_0^μ as a function of k, and when the former crosses the real axis at $k = k_\mu$, obtain a pair of *real* numbers (k_μ, D_0^μ) defining the TLM lasing frequency and lasing threshold, respectively. The first lasing mode is therefore the TLM with the smallest threshold D_0^μ [49].

2.2.2 Constant-flux states

One of the defining features of SALT is the introduction of new eigenstates, such as the TLMs described in the previous section. The theory also introduces another kind of eigenstate called a constant-flux (CF) state [49, 58, 152]. CF states are useful because they are straightforward to compute and can be used as a basis to expand the lasing modes of SALT described by (2.2.14). CF states are parametrized by real wavenumbers outside the laser resonator, and are thus physically meaningful. The basis of CF states satisfy the following modified Helmholtz equation

$$[\nabla^2 + \epsilon(\mathbf{r})K^2(k)]\varphi = 0, \qquad \mathbf{r} \in C, \tag{2.2.19a}$$

$$[\nabla^2 + \epsilon(\mathbf{r})k^2]\varphi = 0, \qquad \mathbf{r} \notin C, \tag{2.2.19b}$$

where C is the *cavity region*, defined as the union of all optically active regions. The eigenvalues K are complex and depend on the *exterior frequency* k, which is always real. This formulation ensures that the total electromagnetic flux outside the cavity is conserved [48].

In the special case of a uniform pumping inside the cavity region, i.e. $F(\mathbf{r}) = 1$ for $\mathbf{r} \in C$ and $F(\mathbf{r}) = 0$ for $\mathbf{r} \notin C$ and a uniform refractive index distribution $\epsilon(\mathbf{r}) = \epsilon_c$ for $\mathbf{r} \in C$, the TLMs can be trivially expanded in the basis of CF states. By comparing (2.2.18) and (2.2.19a), one obtains the relation

$$\frac{\gamma_a D_0}{k - k_a + i\gamma_a} = \epsilon_c \left(\frac{K^2}{k^2} - 1 \right). \tag{2.2.20}$$

In other terms, if the active medium is uniformly pumped, one can simply compute the CF states of the geometry, given the value of ϵ_c, and extract the complex values D_0 of the associated TLMs using (2.2.20).

2.2.3 Circular cavity: QB vs CF states

This section wraps up the description of QB and CF states by giving their explicit expressions for the simplest 2D geometry, a circular cavity. Consider a dielectric circle of refractive index $n_c = \sqrt{\epsilon_c}$ and radius r placed in a medium of refractive index n_0. We suppose that the cavity is centered on the origin of a "global" cylindrical coordinate system. Under these conditions, the QB states of the

circular cavity, solutions of Eq. (2.1.14), are [41]

$$\varphi_l(\rho,\theta) = \begin{cases} A_l J_l(n_c k\rho), & \rho < r, \\ B_l H_l^{(+)}(n_0 k\rho), & \rho > r, \end{cases} \tag{2.2.21}$$

where l is the angular quantum number of the solution, J_l is a Bessel function of the first kind and $H_l^{(+)}$ is a Hankel function of the first kind. Analogously, the CF states of the circular cavity, solutions of Eq. (2.2.19), are [48, p. 52]

$$\varphi_l(\rho,\theta) = \begin{cases} A_l J_l(n_c K(k)\rho), & \rho < r, \\ B_l H_l^{(+)}(n_0 k\rho), & \rho > r. \end{cases} \tag{2.2.22}$$

One can see the CF eigenvalue $K(k)$ explicitly appearing in the solution for $\rho < r$.

There exists an infinite set of QB and CF states for any cavity. In the case of the circular cavity, both types of states can be characterized by a pair of quantum numbers (l, j), corresponding to the number of angular and radial lobes of the eigenmode, respectively. Moreover, the expressions given by Eqs. (2.2.21) and (2.2.22) satisfy an outgoing boundary condition outside the resonator, sometimes called *Sommerfeld radiation condition*. This condition ensures a net flow of the electromagnetic energy of the eigenstate towards infinity, and is mathematically given by

$$\lim_{\rho\to\infty} \varphi(\rho,\theta) = \varphi(\theta)\frac{e^{ik\rho}}{\sqrt{k\rho}}. \tag{2.2.23}$$

In order to determine the eigenvalues of QB states, one must find non-trivial solutions to a homogeneous linear system relating the unknown coefficients A_l and B_l. This linear system, obtained via the application of electromagnetic boundary conditions [6] at $\rho = r$ is given by

$$\begin{pmatrix} J_l(n_c kr) & -H_l^{(+)}(n_0 kr) \\ \varsigma_n n_c J_l'(n_c kr) & -\varsigma_0 n_0 H_l^{(+)\prime}(n_0 kr) \end{pmatrix} \begin{pmatrix} A_l \\ B_l \end{pmatrix} = 0, \tag{2.2.24}$$

where $\varsigma_i = 1\ (1/n_i^2)$ for a TM (TE) polarized wave. These factors account for the polarization of the mode. In short, one must find eigenvalues $k = k_{\mathrm{QB}}$ such that the determinant of the coefficient matrix in Eq. (2.2.24) is zero. Once this is done, the A_l and B_l coefficients are readily obtained from the linear system. A similar system of equations can be obtained for the CF states of the circular cavity

$$\begin{pmatrix} J_l(n_c Kr) & -H_l^{(+)}(n_0 kr) \\ \varsigma_n n_c K J_l'(n_c Kr) & -\varsigma_0 n_0 k H_l^{(+)\prime}(n_0 kr) \end{pmatrix} \begin{pmatrix} A_l \\ B_l \end{pmatrix} = 0. \tag{2.2.25}$$

In that case, one must find eigenvalues $K(k)$ for a fixed exterior frequency k.

For comparison purposes, a QB state of this circular cavity and the associated CF state are plotted in Fig. 2.1. Both modes are characterized by the pair of quantum numbers $(l, j) = (10, 3)$. Since we

6. These boundary conditions are detailed in section 2.3.3

chose the exterior frequency of the CF state near the real part of the QB eigenvalue $\mathrm{Re}[k_{\mathrm{QB}}]$, the field profile inside the cavity ($\rho < r$) is similar for both eigenstates. However, one clearly sees that the CF state remains bounded outside the cavity, whereas the QB state begins to grow exponentially roughly beyond $\rho = 1.5r$. This behavior is consistent with the Sommerfeld radiation condition. Indeed, if one injects a complex k value in Eq. (2.2.23) with $\mathrm{Im}[k] < 0$, the solution clearly blows up at infinity. However, CF states are always characterized by real wavenumbers outside the cavity region, which ensures the solution remains bounded. This example of the circular cavity thus serves two purposes. First, it shows that QB and CF states can be uniquely mapped one onto another using the quantum numbers (actually, this mapping is also possible in the case of coupled cavities, as discussed in chapter 7). It also serves to highlight the unphysical behavior of the usual QB states at infinity, a behavior which can be corrected using the formulation of CF states.

To conclude this section on SALT, a summary of the main features of the three kinds of eigenstates (QB states, CF states and TLMs) presented in this chapter is contained in Table 2.1.

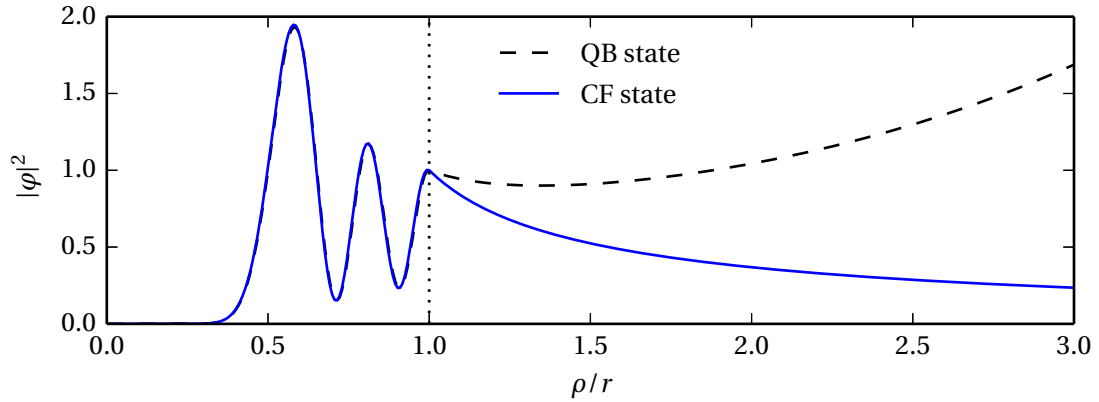

Figure 2.1 – Comparison of the field profile of a QB and a CF state of a circular cavity of refractive index $n_c = 1.5$ embedded in a medium of refractive index $n_0 = 1$. (TM polarization, arbitrary normalization). The eigenmodes are characterized by the quantum numbers $(l, j) = (10, 3)$. The QB state eigenvalue is $k_{\mathrm{QB}} = 13.521 - 0.442i$. The CF state eigenvalue is $K = 13.558 - 0.440i$ (exterior frequency $k = 13.52$).

Table 2.1 – Comparison of the three kinds of eigenstates used in this thesis. Outside the cavity region, all eigenstates are governed by the linear Helmholtz equation (2.1.14). The defining features listed in this table assume that the refractive index distribution $\epsilon(\mathbf{r})$ is a real function.

Name	Acronym	Governing equation inside cavity region	Defining features
Quasi-bound state	QB	$[\nabla^2 + \epsilon(\mathbf{r})k^2]\varphi(\mathbf{r}) = 0$	Grows exponentially at infinity
Constant-flux state	CF	$[\nabla^2 + \epsilon(\mathbf{r})K^2(k)]\varphi(\mathbf{r}) = 0$	Remains bounded at infinity (Real frequency outside of the cavity region)
Threshold lasing mode	TLM	$\left\{\nabla^2 \left[\epsilon(\mathbf{r}) + \dfrac{\gamma_a D_0 F(\mathbf{r})}{k - k_a + i\gamma_a}\right] k^2\right\}\varphi(\mathbf{r}) = 0$	+ Includes a description of the pump and gain medium

2.3 2D Generalized Lorenz-Mie Theory

In this section, we describe the theoretical framework which we refer to as 2D Generalized Lorenz-Mie theory [7]. According to Gouesbet and Lock, the expression "generalized Lorenz-Mie theories" (GLMTs) is used to generically denote a set of light-scattering theories describing the interaction between an illuminating electromagnetic beam and a discrete scattering particle (or array of particles) provided that the scatterers possess enough symmetry, allowing one to solve the problem using the method of separation of variables [56]. The framework used here indeed involves the method of separation of variables, plus the application of Graf's addition theorem. Since we are concerned with cylinders, we shall refer to the aforementioned theoretical framework as 2D-GLMT [8].

The goal of this section is to present our "reference implementation" of the 2D-GLMT and its application to electromagnetic modeling of two-dimensional arrays of cylinders. The organization of this part of the thesis is as follows.

The first sections (§2.3.1 to §2.3.3) are concerned with the basic theoretical treatment of 2D-GLMT. In section 2.3.1, we state Graf's addition theorem for cylindrical functions since it is at the heart of 2D-GLMT. Section 2.3.2 is concerned with the basic equations and the main hypothesis of 2D-GLMT, specifically the expansion of the electromagnetic fields in a basis of cylindrical waves. To isolate the unknown expansion coefficients, electromagnetic boundary conditions must be enforced as described in section 2.3.3.

The next sections (§2.3.4 to §2.3.5) are concerned with two privileged applications of 2D-GLMT studied in this thesis. These applications are:

1. **Scattering computations**. As shown in section 2.3.4, 2D-GLMT is an ideal tool to compute the field scattered by a finite array of cylindrical scatterers. We show how this formalism is compatible not only with the scattering of plane waves, but also of Gaussian beams. Scattering computations are central to the research contributions detailed in chapters 4 to 6 of this thesis.
2. **Eigenmode computations**. The 2D-GLMT framework can also be used to compute lasing modes of an array of cylinders, as described in section 2.3.5. More specifically, we are interested in the computation of the usual quasi-bound (QB) states, but also the constant-

7. The derivations are mostly drawn from references [33, 36, 103, 105]. Similar derivations are also found in a variety of other published works including [4, 99]

8. This theoretical framework based on cylindrical wave expansions has been referred to by a certain number of names in the past, including "multipole method" or "fast multipole method" in Refs. [4, 158]. On a historical note, it should be mentioned that neither Ludvig Lorenz nor Gustav Mie were involved in the solution of Maxwell's equations in coupled cylinders. The solution of Maxwell's equations in cylindrical geometries is more often associated to Lord Rayleigh [88], thus some authors prefer the term "Rayleigh scattering" for cylinders instead of "Lorenz-Mie scattering" or "Mie scattering" which usually deals with spheres [56]. However, we are not fond of the term "Rayleigh scattering" because it is most often used to refer to scattering by particles much smaller than the wavelength of the incident light, which is not a condition used for the framework exposed here.

flux (CF) states which are central to the SALT theory. An equivalent method for computing modes of random lasers has been summarily described in Ref. [4] under the name "multipole method". Eigenmodes computations using 2D-GLMT are central to chapter 7 of this thesis.

2.3.1 Graf's addition theorem

We state Graf's addition theorem [1, Eq. 9.1.79] since it is central to the derivation of the main equations of 2D-GLMT. This addition formula allows one to displace one cylindrical system of coordinates into another using a Bessel function expansion. Let $\mathscr{F}$ denote $J, Y, H^{(+)}, H^{(-)}$ or any linear combination of these functions. The following identity holds

$$\mathscr{F}_\nu(W)e^{i\nu\chi} = \sum_{m=-\infty}^{\infty} \mathscr{F}_{\nu+m}(U)J_m(V)e^{im\alpha}, \tag{2.3.1}$$

where $|Ve^{\pm i\alpha}| < |U|$ and

$$\begin{aligned} W^2 &= U^2 + V^2 - 2UV\cos\alpha, \\ U - V\cos\alpha &= W\cos\chi, \\ V\sin\alpha &= W\sin\chi. \end{aligned} \tag{2.3.2}$$

The branches must be chosen such that $W \to U$ and $\chi \to 0$ as $V \to 0$. The restriction $|Ve^{\pm i\alpha}| < |U|$ is unnecessary if $\mathscr{F} = J$ because the Bessel function of the first kind and integer order is an entire function. If U, V, W are real numbers, they can be interpreted as edges of a triangle as shown in Fig. 2.2. The theorem nevertheless holds for complex-valued arguments.

2.3.2 Basic equations

Consider an array of N cylindrical scatterers of radii r_n and relative permittivity ϵ_n. Let also $\mathbf{r}_n = (\rho_n, \theta_n)$ be the cylindrical coordinate system local to the n^{th} scatterer, whose center is located at $\mathbf{R}_n = (X_n, Y_n)$. For modeling purposes, we suppose that every cylinder (hole) is infinite along the

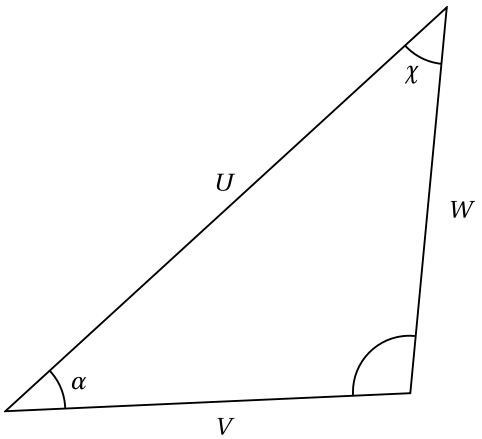

Figure 2.2 – Graf's addition theorem

axial z direction. We also suppose that cylinders do not overlap. The field outside the cylinders satisfies the following Helmholtz equation

$$[\nabla^2 + k_0^2]\varphi(x,y) = 0, \tag{2.3.3a}$$

with $k_0 = \sqrt{\epsilon_0}k$, whereas the field inside the n^{th} scatterer satisfies the following Helmholtz equation

$$[\nabla^2 + k_n^2]\varphi(\rho_n,\theta_n) = 0, \qquad \rho_n < r_n. \tag{2.3.3b}$$

For generality, we do not suppose any relation between k_n and ϵ_n at this point. This will allow the derivations presented here to be compatible both with passive and active media, as described in section 2.2.

The central hypothesis of 2D-GLMT is that the field outside the scatterers φ^E can be written as the superposition of an arbitrary incident beam and the sum of the field scattered by each individual scatterer. The fields can be expanded in a basis of outgoing cylindrical functions, that is

$$\varphi^E(\mathbf{r}) = \varphi_i(\mathbf{r}) + \varphi_s(\mathbf{r}), \tag{2.3.4}$$

with

$$\varphi_i(\mathbf{r}) = \sum_{l=-\infty}^{\infty} a_{nl}^0 J_l(k_0\rho_n)e^{il\theta_n}, \tag{2.3.5a}$$

$$\varphi_s(\mathbf{r}) = \sum_{n=1}^{N}\sum_{l'=-\infty}^{\infty} b_{nl'} H_{l'}^{(+)}(k_0\rho_n)e^{il'\theta_n}. \tag{2.3.5b}$$

The coefficients $\{a_{nl}^0\}$ are the *beam-shape coefficients*, used to parametrize the incident field in the frame of reference of the n^{th} scatterer.

Inside the n^{th} scatterer, the field can be written as

$$\varphi_n^I(\mathbf{r}) = \sum_{l=-\infty}^{\infty} c_{nl} J_l(k_n\rho_n)e^{il\theta_n}. \tag{2.3.6}$$

In order to apply electromagnetic boundary conditions at the interface of the n^{th} scatterer, one must find an expression for $\varphi^E(\mathbf{r})$ containing only cylindrical harmonics centered on the n^{th} scatterer, that is

$$\varphi_n^E(\mathbf{r}) = \sum_{l=-\infty}^{\infty}\left[a_{nl}J_l(k_0\rho_n) + b_{nl}H_l^{(+)}(k_0\rho_n)\right]e^{il\theta_n}. \tag{2.3.7}$$

This can be achieved via the application of Graf's addition theorem for cylindrical functions, which allows a translation from the frame of reference of scatterer n' to the frame of reference of scatterer n. We apply Graf's addition theorem using the following change of variables (see Fig. 2.2 for the definition of angles)

$$\begin{aligned} U &= k_0 R_{nn'}, \\ V &= k_0\rho_n, \\ W &= k_0\rho_{n'}, \end{aligned} \tag{2.3.8}$$

The theorem states that

$$H_{l'}^{(+)}(k_0\rho_{n'})e^{il'\theta_{n'}} = \sum_{l=-\infty}^{\infty} e^{i(l'-l)\phi_{nn'}} H_{l-l'}^{(+)}(k_0 R_{nn'}) J_l(k_0\rho_n) e^{il\theta_n}, \tag{2.3.9}$$

where $R_{nn'}$ is the center-to-center distance between scatterers n and n' and $\phi_{nn'}$ is the angular position of scatterer n' in the frame of reference of scatterer n. Substituting (2.3.9) in (2.3.5) yields

$$\begin{aligned}\varphi_n^E(\mathbf{r}) = &\sum_{l=-\infty}^{\infty} a_{nl}^0 J_l(k_0\rho_n)e^{il\theta_n} + \sum_{l=-\infty}^{\infty} b_{nl} H_l^{(+)}(k_0\rho_n)e^{il\theta_n} \\ &+ \sum_{l=-\infty}^{\infty}\sum_{n'\neq n}\sum_{l'=-\infty}^{\infty} b_{n'l'} e^{i(l'-l)\phi_{nn'}} H_{l-l'}^{(+)}(k_0 R_{nn'}) J_l(k_0\rho_n) e^{il\theta_n}.\end{aligned} \tag{2.3.10}$$

The comparison of (2.3.7) with (2.3.10) yields the following relation between the $\{a_{nl}\}$ and $\{b_{nl}\}$ coefficients

$$a_{nl} = a_{nl}^0 + \sum_{n'\neq n}\sum_{l'=-\infty}^{\infty} e^{i(l'-l)\phi_{nn'}} H_{l-l'}^{(+)}(k_0 R_{nn'}) b_{n'l'}. \tag{2.3.11}$$

2.3.3 Electromagnetic boundary conditions

The relation (2.3.11) is one of the central results of 2D-GLMT. It accounts for the mutual influence of all individual scatterers. In order to obtain the $\{a_{nl}\}$, $\{b_{nl}\}$ and $\{c_{nl}\}$ for a given set of beam-shape coefficients $\{a_{nl}^0\}$, one must apply electromagnetic boundary conditions to (2.3.6) and (2.3.7) at $\rho_n = r_n$. For a TM polarized wave, the first condition is the continuity of E_z across the cylinder interface at $\rho_n = r_n$. The second condition is the continuity of the component of **H** parallel to the interface (H_{θ_n} component). From (2.1.1c), one obtains

$$H_{\theta_n} = -\frac{i}{k}[\nabla\times\mathbf{E}]_{\theta_n} = -\frac{i}{k}\frac{\partial E_z}{\partial\rho_n}. \tag{2.3.12}$$

For a TE polarized wave, the first condition is rather the continuity of H_z across the cylinder interface at $\rho_n = r_n$. Similarly, the second condition is the continuity of the component of **E** parallel to the interface (E_{θ_n} component). From (2.1.1d), one obtains

$$E_{\theta_n} = \frac{i}{\epsilon k}[\nabla\times\mathbf{H}]_{\theta_n} = \frac{i}{\epsilon k}\frac{\partial H_z}{\partial\rho_n}. \tag{2.3.13}$$

The two conditions (2.3.12) and (2.3.13) can be rewritten as

$$\varphi_n^I(r_n) = \varphi_n^E(r_n), \tag{2.3.14a}$$

$$\varsigma_n \frac{\partial\varphi_n^I}{\partial\rho_n}\Big|_{r_n} = \varsigma_0 \frac{\partial\varphi_n^E}{\partial\rho_n}\Big|_{r_n}. \tag{2.3.14b}$$

Again, the ς_i factors account for polarization. Specifically, we have $\varsigma_i = 1$ $(1/\epsilon_i)$ for a TM (TE) polarized wave. Thus, applying this boundary condition to (2.3.6) and (2.3.7), one obtains

$$c_{nl}J_l(k_n r_n) = a_{nl}J_l(k_0 r_n) + b_{nl}H_l^{(+)}(k_0 r_n), \tag{2.3.15a}$$

$$c_{nl}\varsigma_n k_n J_l'(k_n r_n) = a_{nl}\varsigma_0 k_0 J_l'(k_0 r_n) + b_{nl}\varsigma_0 k_0 H_l^{(+)\prime}(k_0 r_n). \tag{2.3.15b}$$

Eliminating c_{nl} from those equations, we obtain the relation $b_{nl} = a_{nl} s_{nl}$, with

$$s_{nl}(k_0, k_n) = -\frac{J_l'(k_0 r_n) - \Gamma_{nl} J_l(k_0 r_n)}{H_l^{(+)\prime}(k_0 r_n) - \Gamma_{nl} H_l^{(+)}(k_0 r_n)}, \tag{2.3.16}$$

where

$$\Gamma_{nl} = \xi_{n0} \frac{k_n J_l'(k_n r_n)}{k_0 J_l(k_n r_n)}, \tag{2.3.17}$$

and

$$\xi_{ij} = 1 \qquad \left(\frac{\epsilon_j}{\epsilon_i}\right), \tag{2.3.18}$$

for a TM (TE) polarized wave.

Substituting $b_{nl} = a_{nl} s_{nl}$ in (2.3.11) yields

$$b_{nl} - s_{nl} \sum_{n' \neq n} \sum_{l'=-\infty}^{\infty} e^{i(l'-l)\phi_{nn'}} H_{l-l'}^{(+)}(k_0 R_{nn'}) b_{n'l'} = s_{nl} a_{nl}^0. \tag{2.3.19}$$

This relation between the $\{a_{nl}^0\}$ and $\{b_{nl}\}$ coefficients can be rewritten in matrix form as

$$\mathbf{T}\mathbf{b} = \mathbf{a}_0, \tag{2.3.20}$$

with

$$\mathbf{T}_{nn'}^{ll'} = \delta_{nn'}\delta_{ll'} - (1 - \delta_{nn'}) e^{i(l'-l)\phi_{nn'}} H_{l-l'}^{(+)}(k_0 R_{nn'}) s_{nl}, \tag{2.3.21}$$

and

$$\mathbf{a}_0 = \left\{ s_{nl} a_{nl}^0 \right\} \qquad , \qquad \mathbf{b} = \left\{ b_{nl} \right\}. \tag{2.3.22}$$

Matrix $\mathbf{T}$ is typically constructed by truncating the series expansions to order $l_{\max}$. It is composed of $N \times N$ blocks of dimension $2l_{\max} + 1$, where the truncation order $l_{\max}$ is sufficiently large to ensure convergence of the cylindrical function expansions. As a representative example, the transfer matrix for an array of three identical ($\epsilon_c = 4$) coupled dielectric cylinders arranged on the vertices of an equilateral triangle is shown in Fig. 2.3b. This matrix is clearly composed of 3×3 blocks of dimension $2l_{\max} + 1$, where we have used the prescription $l_{\max} = 3kr_1$ to set the truncation order [33, 36]. More details on this prescription can be found in section 2.3.6.

2.3.4 Scattering of arbitrary beams

The interaction of an arbitrary beam with an array of cylindrical scatterers can be readily modeled using 2D-GLMT. Given a set of beam-shape coefficients $\{a_{nl}^0\}$, the scattered coefficients $\{b_{nl}\}$ can be directly computed by solving the system of linear equations (2.3.20). In fact, as stated by Gouesbet and Lock, the main difficulty behind Lorenz-Mie theories is usually the computation of the beam-shape coefficients [56]. In section 2.3.4.1, we present the analytic derivation of the beam-shape coefficients for an incident plane wave. In section 2.3.4.2, we show how to compute the beam-shape coefficients for a focused input beam parametrized by the complex-source beam (CSB) technique.

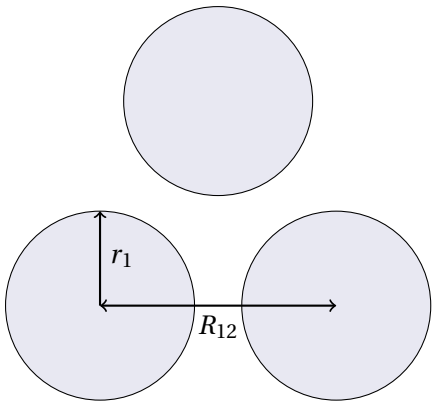

(a) Cylinder array ($R_{12} = 2.5r_1$)

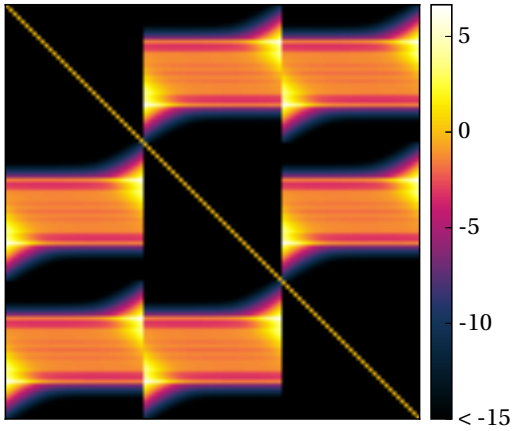

(b) Magnitude of $\log|\mathbf{T}|$

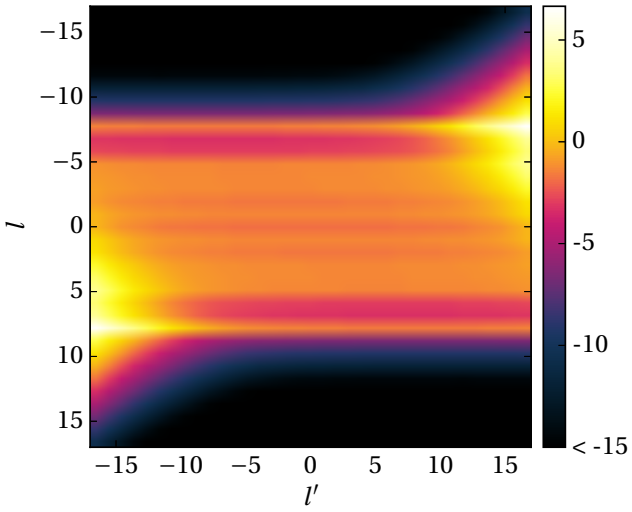

(c) Sub-matrix view of one off-diagonal block

Figure 2.3 – Transfer matrix for three identical coupled cylinders arranged on the vertices of an equilateral triangle ($\epsilon_c = 4, kr_1 = 5.3779$). The truncation order of the matrix is chosen as $l_{\max} = \text{ceil}[3kr_1] = 17$.

2.3.4.1 Beam-shape coefficients for a plane wave

Consider the following incident field (plane wave) on the scatterer array

$$\varphi_i(\mathbf{r}) = \varphi_0 e^{i\mathbf{k}\cdot\mathbf{r}}. \tag{2.3.23}$$

The incident wavevector $\mathbf{k}$ is defined by a modulus $k_0 = k\sqrt{\epsilon_0}$ and an angle of incidence Θ. The position vector $\mathbf{r}$ is defined with respect to the origin of a global coordinate system. In the frame of reference of the n^{th} scatterer, one can write

$$\varphi_i(\rho_n, \theta_n) = \varphi_0 e^{i\mathbf{k}\cdot(\mathbf{R}_n+\mathbf{r}_n)} = \varphi_0 e^{i\mathbf{k}\cdot\mathbf{R}_n} e^{ik_0\rho_n[\cos(\theta_n-\Theta)]}. \tag{2.3.24}$$

Using the Jacobi-Anger expansion [163], one can rewrite

$$e^{ik_0\rho_n[\cos(\theta_n-\Theta)]} = \sum_{l=-\infty}^{\infty} i^l J_l(k_0\rho_n) e^{il(\theta_n-\Theta)}. \tag{2.3.25}$$

The substitution of (2.3.25) in (2.3.24) and comparison with (2.3.5) yields the following beam-shape coefficients, similar to those found in [33, 103]

$$\boxed{a_{nl}^0 = \varphi_0 e^{i\mathbf{k}\cdot\mathbf{R}_n} i^l e^{-il\Theta}.} \tag{2.3.26}$$

2.3.4.2 Beam-shape coefficients for a complex-source beam

The basic form of a two-dimensional Gaussian beam (GB) propagating along the x axis, which satisfies the paraxial 2D Helmholtz equation, is given by

$$\varphi_g(x,y) = \sqrt{\frac{2}{\pi k_0(x-x_{\text{R}})}} \exp\left\{ik_0\left(x + \frac{1}{2}\frac{y^2}{x-ix_{\text{R}}}\right)\right\}. \tag{2.3.27}$$

The parameter x_{R} is the Rayleigh distance of the GB and is proportional to the coherence length of the beam. The beam waist is located in the $x = 0$ plane. The physical appeal and usefulness of the Gaussian beam is well established. Indeed, it is compatible with semi-analytical approaches such as ray-transfer (or $ABCD$) matrices and leads to a closed form solution of the Fresnel-Kirchhoff integral [127]. A Gaussian beam is also a good approximation of the radiation pattern of the fundamental mode of a rectangular waveguide [106, pp. 43–46] or of an optical fiber [93]. However, in the cases of interest for this thesis, the Gaussian beam solution suffers from two main drawbacks. First, it is an approximate solution of the Helmholtz equation. Indeed, one must use the *paraxial approximation* to obtain (2.3.27) from (2.1.14). Second, computing the beam-shape coefficients for the canonical Gaussian beam solution is not easily accomplished.

To circumvent these two drawbacks, we shall use the complex-source beam (CSB) solution of the 2D Helmholtz equation as a closed-form incident field. This solution has been proposed in order to extend the validity of the GB beyond the paraxial zone and exhibits the required cylindrical symmetry [65]. Using the Green's function of the inhomogeneous Helmholtz equation for a point

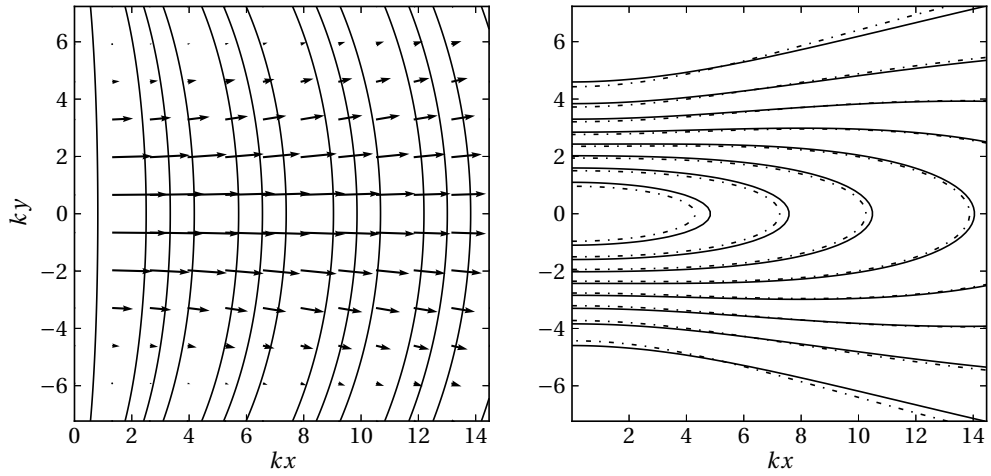

Figure 2.4 – (Left) Phase fronts and Poynting vectors of the free-space CSB solution described by Eq. (2.3.28). (Right) Amplitude contours of the CSB solution and comparison with the canonical Gaussian beam (dashed). The normalized Rayleigh distance is set to $k_0 x_R = 9.65$, the same value used in chapter 4.

source located in complex space at coordinates $x' = i x_R$ and $y' = 0$, one obtains the CSB solution [91]

$$\varphi_i(\mathbf{r}) = H_0^{(+)}(k_0 r_s), \tag{2.3.28}$$

with

$$r_s \equiv [(y-y')^2 + (x-x')^2]^{1/2} = [y^2 + (x - i x_R)^2]^{1/2}. \tag{2.3.29}$$

This solution is continuous everywhere in the real plane except across the branch cut connecting the two singularities at $(x,y) = (0, x_R)$ and $(x,y) = (0, -x_R)$. The waist plane is thus located in the branch cut [9]. The CSB solution reduces, up to a multiplicative constant, to a canonical Gaussian beam in the paraxial zone $x \gg y$. To show this, one can rewrite r_s in the following way

$$r_s = \pm(x - i x_R)\sqrt{1 + \frac{y^2}{(x - i x_R)^2}}, \qquad x \gtrless 0, \tag{2.3.30}$$

and use the binomial approximation [65] to write

$$r_s \sim \pm\left[(x - i x_R) + \frac{1}{2}\frac{y^2}{x - i x_R}\right], \qquad x \gtrless 0. \tag{2.3.31}$$

Moreover, using the asymptotic expansion of Hankel functions for large arguments, one can write [1]

$$\begin{aligned} \varphi_i(x,y) &\sim \sqrt{\frac{2}{\pi k_0 r_s}} \exp i\left(k_0 r_s + \frac{\pi}{4}\right) \\ &\sim \sqrt{\frac{2}{\pi k_0 (x - i x_R)}} \exp\left[i k_0 \left(x + \frac{1}{2}\frac{y^2}{x - i x_R}\right)\right] e^{\frac{i\pi}{4}} e^{k_0 x_R}, \qquad x > 0, \end{aligned} \tag{2.3.32a}$$

9. In order to obtain a regular solution in that plane, one can combine linearly independent CSB solutions as described in [91].

$$\varphi_i(x,y) \sim \sqrt{\frac{2}{\pi k_0 (x - i x_\mathrm{R})}} \exp\left[-i k_0 \left(x + \frac{1}{2}\frac{y^2}{x - i x_\mathrm{R}}\right)\right] e^{\frac{i\pi}{4}} e^{-k_0 x_\mathrm{R}}, \qquad x < 0. \tag{2.3.32b}$$

Eq. (2.3.32) and Fig. 2.4 clearly show the transverse Gaussian profile of the CSB in the paraxial zone. The next step is to expand the CSB on a basis of cylindrical waves centered on each individual scatterer to obtain the beam-shape coefficients. To obtain this expansion, one can rewrite (2.3.28) as

$$\varphi_i(\rho_n, \theta_n) = H_0^{(+)}(k_0 |\mathbf{r}_n - \mathbf{r}_{sn}|), \tag{2.3.33}$$

where $\mathbf{r}_n = (\rho_n, \theta_n)$ and $\mathbf{r}_{sn}$ is the vector pointing from the center of the n^{th} scatterer to the complex source point. We apply Graf's addition theorem using the following change of variables

$$\begin{aligned} U &= k_0 r_{sn}, \\ V &= k_0 \rho_n, \\ W &= k_0 |\mathbf{r}_n - \mathbf{r}_{sn}|, \end{aligned} \tag{2.3.34}$$

where $\rho_n = |\mathbf{r}_n|$ and $r_{sn} = |\mathbf{r}_{sn}|$ (geometric norms). In accordance with [105], we write

$$-\mathbf{r}_{sn} = (X_n - i x_\mathrm{R})\hat{\mathbf{e}}_x + Y_n \hat{\mathbf{e}}_y, \tag{2.3.35a}$$

$$r_{sn} = \sqrt{(X_n - i x_\mathrm{R})^2 + Y_n^2}, \tag{2.3.35b}$$

thus

$$\mathbf{r}_n - \mathbf{r}_{sn} = (x_n + X_n - i x_\mathrm{R})\hat{\mathbf{e}}_x + (y_n + Y_n)\hat{\mathbf{e}}_y, \tag{2.3.36a}$$

$$|\mathbf{r}_n - \mathbf{r}_{sn}| = \sqrt{(x_n + X_n - i x_\mathrm{R})^2 + (y_n + Y_n)}, \tag{2.3.36b}$$

where (x_n, y_n) are Cartesian coordinates centered on the n^{th} scatterer. Using (2.3.2), one obtains

$$\cos(\alpha_n + \pi) = \cos\mu_n \cos\theta_n + \sin\mu_n \sin\theta_n = \cos(\theta_n - \mu_n), \tag{2.3.37}$$

where

$$\cos\mu_n = \frac{X_n - i x_\mathrm{R}}{r_{sn}} \quad , \quad \sin\mu_n = \frac{Y_n}{r_{sn}}, \tag{2.3.38a}$$

$$\cos\theta_n = \frac{x_n}{\rho_n} \quad , \quad \sin\theta_n = \frac{y_n}{\rho_n}. \tag{2.3.38b}$$

Using those substitutions, the expansion can be written

$$\varphi_i(\rho_n, \theta_n) = \sum_{l=-\infty}^{\infty} H_l^{(+)}(k_0 r_{sn}) J_l(k_0 \rho_n) e^{i l \alpha_n}, \tag{2.3.39}$$

and substituting $\alpha_n = \theta_n - \mu_n - \pi$, one obtains the beam-shape coefficients for a CSB

$$\boxed{a_{nl}^0 = (-1)^l H_l^{(+)}(k_0 r_{sn}) e^{-i l \mu_n},} \tag{2.3.40}$$

where r_{sn} is given by (2.3.35b) and μ_n by (2.3.38a).

The expansion (2.3.39) is similar to Eq. (3) in reference [105], with the difference that the condition $|Ue^{\pm i\alpha_n}| < |V|$ is required in the said reference (because the source is located inside a circular reflector), whereas our form requires $|Ve^{\pm i\alpha_n}| < |U|$. In accordance with this condition, the convergence of (2.3.39) is limited to a disk not intersecting or touching the branch cut between $(x, y) = (0, x_R)$ and $(x, y) = (0, -x_R)$. In other words, scatterers must not intersect or touch the branch cut for the expansion to hold.

2.3.5 Eigenmode computations

In the previous section, it was shown that the scattering wavefunctions can be computed by solving the linear system of equations (2.3.20). Eigenmodes computations rather involve a homogeneous version of this linear system. Generally, this system is of the form

$$\mathbf{T}(\lambda)\mathbf{b} = 0. \tag{2.3.41}$$

In short, the computation of lasing states is a non-linear eigenvalue problem. One must compute the discrete set of (generally complex) eigenvalues λ and eigenvectors $\mathbf{b}$ for which $\det(\mathbf{T}) = 0$. Since the eigenvalue is usually a complex frequency or wavenumber, this problem amounts to finding the resonant frequencies associated to an *infinite* scattered amplitude in presence of a *finite* amplitude incident wave. Algorithms for solving the non-linear eigenvalue problem are described in [122, 165].

In this section, we show that (2.3.41) can be readily adapted for the computation of the classical QB states of an array of cylinders, and of the CF states described in section 2.2.2. The QB states of an array of dielectric scatterers satisfy the following Helmholtz equation

$$[\nabla^2 + \epsilon_0 k^2]\varphi(\rho_n, \theta_n) = 0, \qquad \text{(Outside all cylinders)} \tag{2.3.42a}$$

$$[\nabla^2 + \epsilon_n k^2]\varphi(\rho_n, \theta_n) = 0, \qquad \rho_n < r_n. \tag{2.3.42b}$$

Consequently, the matrix equation describing the quasi-bound modes is simply

$$\mathbf{T}(k)\mathbf{b} = 0, \tag{2.3.43}$$

with the substitution $k_n \leftarrow k\sqrt{\epsilon_n}$ in (2.3.16).

As stated in section 2.2, QB states cannot accurately describe the steady-state lasing behavior of an array of active cylinders, even near threshold [49]. This is due to the QB eigen-frequencies being complex everywhere outside the cylinders, resulting in exponential growth of the electromagnetic energy at infinity [49]. To enable a more realistic treatment of eigenmodes, we have introduced a new kind of eigenstate central to SALT, the CF state, in section 2.2.2. One of the appealing features of CF states is that they are readily computed using the Lorenz-Mie approach described here, under the assumption that the cavity region is composed of a subset of the cylinder array. In other words, the medium surrounding all cylinders is passive, and some cylinders may also be passive.

Accordingly, the wavevector is complex only inside active cylinders. The CF states therefore satisfy

$$[\nabla^2 + \epsilon_0 k^2]\varphi = 0, \qquad \text{(Outside all cylinders)} \tag{2.3.44a}$$

$$[\nabla^2 + \epsilon_n k^2]\varphi = 0, \qquad \text{(Inside passive cylinders)} \tag{2.3.44b}$$

$$[\nabla^2 + \epsilon_n K(k)^2]\varphi = 0, \qquad \text{(Inside active cylinders).} \tag{2.3.44c}$$

The matrix equation describing the CF states is

$$\mathbf{T}(K)\mathbf{b} = 0, \tag{2.3.45}$$

with the substitution $k_n \leftarrow K\sqrt{\epsilon_n}$ in (2.3.16) if the n^{th} cylinder is active, and $k_n \leftarrow k\sqrt{\epsilon_n}$ otherwise. Note that, as always, the complex eigenfrequency K associated to the CF states depends on the value of the exterior frequency k.

In summary, 2D-GLMT can be used to compute the eigenstates of arrays of coupled active cylinders, possibly all different in size and refractive indices. The method works equally well for the computation of the eigenfunctions and eigenfrequencies of QB states, meta-stable solutions of the 2D Helmholtz equation, and for the computation of CF states. These "improved" eigenstates central to the SALT theory are more physically realistic solutions to the Helmholtz equation in the sense that they remain bounded at infinity, unlike QB states. Using CF states also enables the computation of resonances of photonic complexes in the case where some cylinders are active and other remain passive. This is incompatible with QB states computations, which amount to an active medium extending to the whole spatial domain.

2.3.6 Limitations and extensions of the method

Although the usefulness of 2D-GLMT has been demonstrated in the literature for a wide variety of applications, two important limitations of the method are noteworthy. The first limitation is that the size of the transfer matrix described by (2.3.21) scales like N^2, where N is the number of cylinders considered. In this work, we perform computations with arrays ranging from $N = 2$ (chapter 7) to $N = 372$ (§5.8). In the latter case, the memory and processor requirements of the method are kept low by the fact that we consider cylinder dimensions of the order of the operating wavelength. This allows us to perform fast computations and combine 2D-GLMT with metaheuristics, optimization algorithms described in chapter 3. Since these algorithms imply a large number of scattering computations, the speed of 2D-GLMT is a critical issue. However, the method can become time and memory consuming either if we consider cylinders much larger than the operating wavelength, or a very large number of scatterers as in section 8.3. In that case, alternative methods might be more practical than 2D-GLMT, for instance the finite element method discussed in section 8.2 [39, 84].

A second limitation of the 2D-GLMT approach presented in this chapter is that the underlying matrix equation (2.3.20) cannot be truncated at an arbitrary order to provide convergence [99, 143].

This can be demonstrated by using the asymptotic form of cylindrical functions for large positive order [1, p. 365]

$$\lim_{l\to\infty} J_l(z) = \frac{1}{\sqrt{2\pi l}}\left(\frac{ez}{2l}\right)^l, \tag{2.3.46a}$$

$$\lim_{l\to\infty} H_l^{(+)}(z) = \lim_{l\to\infty} iY_l(z) = -i\sqrt{\frac{2}{\pi l}}\left(\frac{2l}{ez}\right)^l. \tag{2.3.46b}$$

In other terms, Bessel functions of the first kind decay exponentially for large orders, while Hankel functions of the first kind grow exponentially in similar situations. Combining these results with (2.3.21), one obtains the following asymptotic forms for large values of l'

$$\lim_{|l'|\to\infty} \mathbf{T}_{nn'}^{ll'} = \delta_{nn'}\delta_{ll'} - (1-\delta_{nn'})e^{i(l'-l)\phi_{nn'}} s_{nl} \lim_{|l'|\to\infty} H_{-l'}^{(+)}(k_0 R_{nn'}). \tag{2.3.47}$$

The limit can be computed using (2.3.46b)

$$\lim_{|l'|\to\infty} H_{-l'}^{(+)}(k_0 R_{nn'}) = \begin{cases} i(-1)^{l'+1}\sqrt{\dfrac{2}{\pi l'}}\left(\dfrac{2l'}{ek_0 R_{nn'}}\right)^{l'}, & l'>0, \\ -i\sqrt{\dfrac{2}{\pi|l'|}}\left(\dfrac{2|l'|}{ek_0 R_{nn'}}\right)^{|l'|}, & l'<0. \end{cases} \tag{2.3.48}$$

This result means that for large values of $|l'|$, the elements of the off-diagonal blocks of $\mathbf{T}_{nn'}^{ll'}$ grow exponentially. As for large values of l, one can readily compute the following asymptotic dependence

$$\lim_{|l|\to\infty} s_{nl} \sim \left(\frac{1}{2|l|}\right)^{2|l|}. \tag{2.3.49}$$

Overall, this results in an exponential decay of the matrix elements with respect to l, specifically

$$\lim_{|l|\to\infty} \mathbf{T}_{nn'}^{ll'} \sim \left(\frac{1}{2|l|}\right)^{|l|}. \tag{2.3.50}$$

The net result is that, for small values of $|l-l'|$, the elements of the off-diagonal blocks remain bounded, as the exponential growth with respect to $|l'|$ is compensated by the exponential decay with respect to $|l|$. On the other hand, for large values of $|l-l'|$, the matrix elements quickly blow up. This exponential growth can be clearly seen in Fig. 2.3c for off-diagonal elements.

The consequences are important, since it is theoretically not possible to minimize the error of 2D-GLMT by solving arbitrarily large matrices because it would require storing arbitrarily large numbers in memory. In this work, we attempted to avoid numerical instabilities by applying the usual rule of using "not too large" truncation orders. For a given cylinder array, the prescription we use to choose the truncation order $l_{\max}$ is usually [33, 36]

$$l_{\max} \sim 3kr_{\max}, \tag{2.3.51}$$

where $r_{\max}$ is the radius of the largest cylinder comprised in the array. Using this rule, we did not encounter any numerical instabilities in the computations presented in chapters 4 to 7.

Despite the fact that we were satisfied with the arbitrary prescription described above, we recently became aware of a method that can guarantee the convergence of the matrix equations to an arbitrary truncation order. The main idea is to re-normalize the beam shape coefficients a^0_{nl} and the unknowns b_{nl} using the formulas [99]

$$\begin{aligned} a^0_{nl} &= \hat{a}^0_{nl} J_l(k_0 r_n), \\ b_{nl} &= \hat{b}_{nl} J_l(k_0 r_n), \end{aligned} \tag{2.3.52}$$

and solve the linear system for the new unknowns $\hat{b}_{nl}$. Substituting this form in (2.3.19) yields

$$\hat{b}_{nl} - s_{nl} \sum_{n' \neq n} \sum_{l'=-\infty}^{\infty} e^{i(l'-l)\phi_{nn'}} H^{(+)}_{l-l'}(k_0 R_{nn'}) \frac{J_{l'}(k_0 r_{n'})}{J_l(k_0 r_n)} \hat{b}_{n'l'} = s_{nl} \hat{a}^0_{nl}. \tag{2.3.53}$$

The modified matrix equation is therefore

$$\hat{\mathbf{T}}\hat{\mathbf{b}} = \hat{\mathbf{a}}_0, \tag{2.3.54}$$

with

$$\hat{\mathbf{T}}^{ll'}_{nn'} = \delta_{nn'}\delta_{ll'} - (1-\delta_{nn'}) e^{i(l'-l)\phi_{nn'}} H^{(+)}_{l-l'}(k_0 R_{nn'}) \frac{J_{l'}(k_0 r_{n'})}{J_l(k_0 r_n)} s_{nl}. \tag{2.3.55}$$

The net effect of this re-normalization is that, for large $|l'|$, the additional factor exponentially decays and compensates the exponential growth of the Hankel function with respect to that index. Conversely, for large $|l|$, the additional factor exponentially grows and compensates the exponential decay with respect to that index. After this rescaling, it can be shown from the Fredholm theorem of operator analysis that a truncated version of (2.3.54) converges to the exact solution of the scattering/eigenmode problem for $l_{\max} \to \infty$ [99]. This was not the case for the original system (2.3.20).

A final remark on this re-normalization approach is to be made. Although convergence of the truncated matrix equation is guaranteed, the computation of matrix elements using (2.3.55) implies computing the product of an exponentially large cylindrical function with an exponentially small one, which can imply some numerical difficulties. Nevertheless, this more robust re-normalization approach should be useful in the case of problems requiring a great precision on the scattering wavefunctions or eigenfrequencies [10]. An example problem is the computation of modes of random lasers, which is the topic of section 8.3.

10. We have recently been successful in the implementation of this renormalization technique for the computation of eigenmodes of photonic crystal lasers. This will be the object of a future publication.

Chapter 3

Methods II: Metaheuristics for combinatorial optimization in photonics

Premature optimization is the root of all evil.

D. E. Knuth [75]

This chapter is chiefly concerned with a discussion of *metaheuristics*, algorithms used in this thesis for beam shaping computations. Metaheuristics are broadly defined as optimization algorithms allowing the exploration of large solution spaces using empirical rules. The key objective of metaheuristics is to obtain acceptable solutions to "hard" optimization problems in a reasonable amount of time. As a trade-off, metaheuristics imply no guarantee of finding the global optimum of a given problem, unlike exact methods [149]. The goal of this chapter is not to give an exhaustive lecture about metaheuristics, but rather to review in a "hands-on" way the basic concepts that will be of use in subsequent chapters, which deal with optical engineering [11].

This chapter begins with a general description of the optimization problems tackled in this thesis (§3.1). These problems are almost exclusively combinatorial in nature, meaning that they have a countable (albeit large) number of solutions. After discussing "hard" combinatorial optimization problems, we proceed with a general description of metaheuristics (§3.2). We then review the difference between algorithms based on iterating a single solution (type S) and algorithms based on iterating populations or ensembles of solutions (type P). Once this distinction is made, we proceed to a more specific description of the two algorithms used in this thesis, namely the canonical genetic algorithm (§3.2.2) and the parallel tabu search (§3.2.1).

Most of the discussion in this chapter is dedicated to the optimization of a single objective function. However, *multiobjective optimization* is also an important part of this thesis. For instance,

11. The main references used in this section are Talbi's book on metaheuristics in general [149], Glover's book on Tabu search [53] and Whitley's tutorial on the canonical genetic algorithm [164].

one might want to optimize the profile of the beam emitted by an optical device while maintaining its degree of polarization, as we seek to achieve in chapter 6. There are additional subtleties associated with the optimization of multiple non-independent objective functions. In that case, the optimized solution is not a single one but rather a set of possible compromises between the two (or more) optimization objectives. Consequently, multiobjective optimization is discussed in section 3.3.

3.1 Combinatorial optimization

The range of optimization problems approached in this thesis can be formalized as follows. Suppose a solution space corresponding to a set of N optimization (or decision) variables v^i defining, for instance, geometric parameters of an optical system. This ensemble of variables can be represented using a vector of length N, where each component is a discrete or continuous variable

$$v = \{v^1, v^2, \cdots, v^N\}. \tag{3.1.1}$$

The domain of $v \in \Upsilon$ is called *solution space*, and contains all possible values of v. An optimization problem consists in assigning a value to every decision variable v^i in order to fulfill one or more predefined optimization targets. These targets can be mathematically expressed using a set of M *objective functions* , for instance

$$G(v) = \{g_1(v), g_2(v), \cdots, g_M(v)\}. \tag{3.1.2}$$

If $M = 1$, the optimization problem can be termed *monoobjective*. The case $M \geq 2$, further discussed in section 3.3, corresponds to *multiobjective optimization* [32]. Without loss of generality a single objective function, i.e. $G(v) = g_1(v)$, is assumed in the following two sections.

In most cases of interest, $G(v)$ depends nonlinearly on v, which implies that it is not possible to isolate the effect of every independent variable v^i [164]. This excludes approaching the problem using exact optimization algorithms such as linear programming [149]. A key issue for the design of an optimization algorithm is the estimation of the computational cost associated to one evaluation of $G(v)$. This is especially important if the size of the solution space of a problem is large, meaning that solving the optimization problem implies a large number of evaluations of $G(v)$.

This thesis mainly deals with combinatorial problems. More specifically, in beam shaping problems, a single decision variable denotes the presence or the absence of a single cylindrical scatterer part of a larger design. A consequence of this binary nature of the optimization variables is that solutions can be directly encoded using vectors of binary variables [149, 164]. For instance, a possible solution to a "model" binary problem with $N = 8$ could be encoded using the following representation

$$v = \{01011001\}. \tag{3.1.3}$$

Since it is assumed that the effect of the individual binary variables cannot be isolated, the size of the search space of this model problem is 2^N and forms a $N-$dimensional hypercube [164]. This

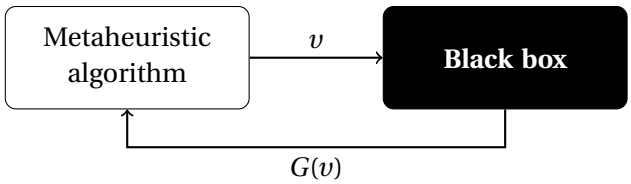

Figure 3.1 – Black box interpretation of metaheuristics [149]

model problem therefore belongs to the NP (non-polynomial) complexity class, since its complexity is exponential [12]. This means no polynomial-time algorithm can solve it [149]. In the worst case scenario, $G(v)$ must be computed for every possible value of $v \in \Upsilon$. Since the size of Υ grows exponentially with N, the time needed to carry out this brute-force procedure also increases with N. Accordingly, problems belonging to this NP complexity class are often termed *intractable*, or *hard* optimization problems.

3.2 Metaheuristics

Optimization problems belonging to the NP complexity class are often approached using metaheuristics. According to Glover's definition, a metaheuristic is defined as "a master strategy that guides and modifies other heuristics to produce solutions beyond those which are normally generated in a quest for local optimality" [53, p. 17]. In other terms, metaheuristics can be broadly defined as optimization algorithms which do not depend on the specific problem to be solved. This independence can be interpreted using the "black box" picture seen in Fig. 3.1. Metaheuristics only require the knowledge of the solution space v and a "black box" to compute values of $G(v)$. The box can represent a more or less costly simulation, the details of which are not available to the metaheuristic [149]. Moreover, metaheuristics are contrasted with algorithms oriented towards local optimality, in that most of the former implement some mechanism allowing to escape from local optima in the search space.

As seen in Fig. 3.2, metaheuristics are a sub-category of approximate algorithms, in other words algorithms which do not guarantee convergence to the global optimum (if it exists) of an optimization problem. Since there is no guarantee to find an optimal solution, metaheuristics basically search for acceptable solutions until a user-specified *stopping criterion* is met. Two popular criteria typically used when implementing metaheuristics are:

1. **Static stopping criterion:** Achieving a predetermined number of iterations. One might only have a small computation time available to perform the optimization, so the number of objective function evaluations is be set to a predetermined value. This is the simplest criterion [149].
2. **Dynamic stopping criterion:** Achieving a given value of $G(v)$. This requires an estimation of what is considered an "acceptable" solution. The optimization is then stopped when this

12. Using the "big-oh" notation, one would say the complexity of this model problem is $\mathcal{O}(2^N)$.

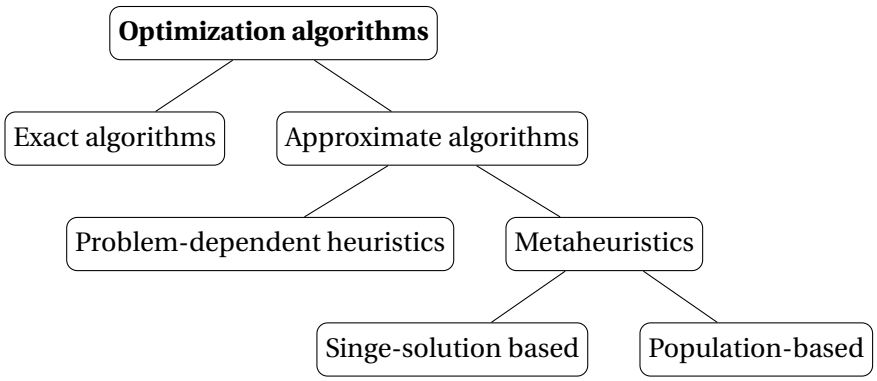

Figure 3.2 – A possible taxonomy of metaheuristics [149].

threshold is met [149]. However, since the convergence of metaheuristics is never guaranteed, it is impossible to know in advance the number of iterations required to achieve this threshold, if it is ever met. As a safeguard against possible infinite loops, an additional criterion normally used is the achievement of a predetermined number of iterations without improving the best encountered objective function value [149].

There are many possible ways to classify the different metaheuristics available in the literature. In this work, we choose to use the number of solutions carried over from iteration to iteration as a distinguishing feature [53]. This allows to make a distinction between metaheuristics based on iterating a single-solution (type S) and those based on the evolution of populations of solutions (type P). This taxonomy is shown in Fig. 3.2.

The general template of type S metaheuristics is show in algorithm 3.2.1. Type S algorithms work by generating an ensemble containing number of candidate solutions $\mathscr{C}(v_t)$ using the current solution v_t. A choice is then made for v_{t+1} using some predetermined rules. They can be viewed as "walks", or trajectories covering the search space using some empirical rules [149]. The exact method for generating $\mathscr{C}(v_t)$ and then moving to the next iteration is what distinguishes one type S algorithm from another. Some well known S-metaheuristics include the widely used simulated annealing based on stochastic methods for generating $\mathscr{C}(v_t)$ [115, 149]. Other methods include variable neighborhood search and tabu search, an algorithm which is the topic of section 3.2.1.

Algorithm 3.2.1 : High-level template for single-solution-based metaheuristics (type S) [149]

Initial solution v_0
$t := 0$;
while *No stopping criterion met* **do**
    Generate candidate solutions $\mathscr{C}(v_t)$;
    Choose a solution v_{t+1} among all candidate solutions $\mathscr{C}(v_t)$;
    $t := t + 1$;
end
Output : Final solution v_t

Algorithm 3.2.2 : High-level template for population-based metaheuristics (type P) [149]

Initial population $P_0 = \{v_n\}$
$t := 0$;
while *No stopping criterion met* **do**
    Generate new population P_{t+1};
    Choose a new population from members of $(P_t \cup P_{t+1})$;
    $t := t + 1$;
end
Output : Final population P_t

In contrast with S-metaheuristics, P-metaheuristics are based on ensembles of solutions which are called "populations". P-metaheuristics can be viewed as procedures that allow iterative improvement of a population. As shown in algorithm 3.2.2, this improvement begins with a *generation phase*, during which a new population of candidate solutions is generated. Then follows a *replacement phase*, during which the individuals (another word for solutions) that are to "survive" in the next generation are selected. Well-known P-metaheuristics include evolutionary algorithms such as the genetic algorithm, which is the topic of section 3.2.2. Other popular nature-inspired P-metaheuristics include particle swarm optimization and ant colonies [149].

In designing and implementing a metaheuristic for a given optimization problem, two desirable features must be taken into account, namely *diversification* and *intensification* [149]. Diversification is the capability of the metaheuristic to explore wide regions of the solution space Υ, while intensification is the capability to exploit promising regions (i.e. regions with interesting values of $G(v)$) of the solution space. Diversification is a global process, whereas intensification acts locally. Since these features are somewhat contradictory, a good metaheuristic will usually offer a compromise between the two. Keeping these requirements in mind, we now proceed to the description of the two metaheuristics used in this thesis, namely tabu search (§3.2.1) and the standard genetic algorithm (§3.2.2).

3.2.1 Tabu search

Tabu search (TS) is a type S metaheuristic first proposed by F. Glover in the late 1980s [13]. The defining feature of TS is that it uses an adaptive memory – called the *tabu list* – to escape from local minima in the solution space [53, 149]. TS is a *deterministic* local search algorithm, meaning that it "walks" through the solution space using systematic rules.

Before going into the specifics of tabu search, we begin by giving a definition of the distance between solutions. Let v_i and v_j be two solutions comprised in the solution space Υ of an optimization problem. The distance $d(v_i, v_j)$ between these solutions is defined as the minimal number of applications of a "move" operator needed to obtain one of the solutions starting from the other

13. On a historical note, the term "meta-heuristic" was coined by F. Glover in the same article that introduced the "tabu search" terminology [53, p. 17].

[149]. In the case of a binary problem, the move operator works by flipping individual bits, and the distance $d(v_i, v_j)$ is simply the number of non-equal bits between v_i and v_j.

As shown in algorithm 3.2.1, an iteration of a S-metaheuristic begins with the generation of a set of candidate solutions $\mathscr{C}(v_t)$ from the current solution v_t. In the simplest case $\mathscr{C}(v_t)$ is composed of the nearest neighbors of v_t, i.e. all solutions located at a distance $d = 1$ from the current solution. In the case of a binary encoding of solutions, each of the N bits of the solution are flipped in an subsequently independent way to generate N neighbors. Going back to the example of the following binary chain ($N = 8$)

$$v = (01011001), \tag{3.2.1}$$

the first degree neighborhood of v is composed of the following solutions

$$\mathscr{C}(v) = \begin{pmatrix} 11011001 \\ 00011001 \\ 01111001 \\ 01001001 \\ 01010001 \\ 01011101 \\ 01011011 \\ 01011000 \end{pmatrix}. \tag{3.2.2}$$

Once this neighborhood is generated, the objective function G is evaluated for every member of $\mathscr{C}(v)$. The last step of a tabu search iteration is then a move to the best possible solution found in $\mathscr{C}(v)$. However, to prevent cyclic trajectories in the search space, a number of past moves are kept in a short-term memory. These moves remain forbidden for a certain number of iterations L, called the *tabu tenure* [149]. This short-term memory is called the *tabu list*, since the moves it contains are tabu (forbidden). The choice of the tabu list length L is crucial to the convergence of the algorithm. Indeed, if the tabu list is rotated with the last L moves, cycles in the solution space of length at most L are prevented. The value of L may be kept fixed for all iterations, or dynamically changed. The iteration continue until a user-defined stopping criterion is met. A high-level template of TS corresponding to this description is shown in Fig. 3.3.

Despite these general rules, additional precautions must be taken in order to avoid missing good solutions [53]. For instance, the algorithm should accept tabu moves if they result in a better value of $G(v)$ than all other solutions considered during the search. This important condition is called an *aspiration criterion* [149]. Other possible refinements of TS include considering medium and long-term memories, as well as multiple tabu lists [149].

In this thesis, we use a simple version of TS that is characterized by a static list length and a single tabu list corresponding to the last L moves applied to the current solution. However, in order to improve the quality of optimized solutions, we use a multi-threaded version of TS which we call *parallel tabu search*, or PTS [23, 53]. This procedure allows to consider broader areas of the search

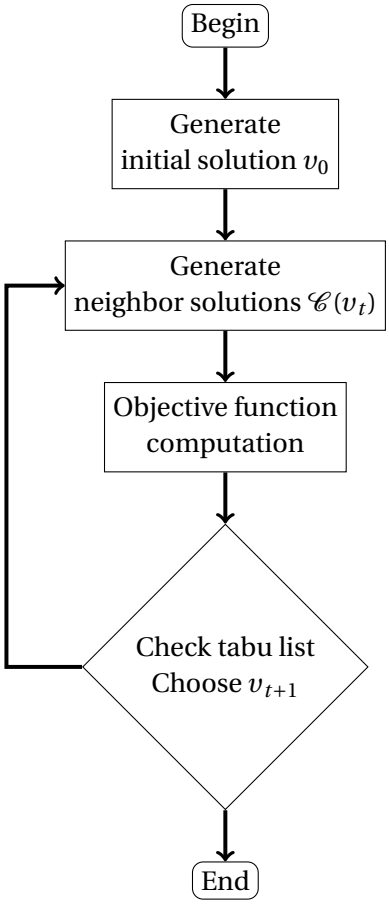

Figure 3.3 – High-level template of tabu search [149].

space and, for a given number of iterations, may be more effective than a sequential search using a single processor [149]. Therefore, using a parallel computer, better and more diverse solutions to a combinatorial optimization problem can be obtained than using a single-thread computer running for the same amount of time. As noted by Glover, if there is no communication between each thread, this approach is equivalent to restarting the search after a stopping criterion is met, each time using a different initial solution, thereby introducing diversity in the final solutions found.

The main idea behind the parallel implementation we use in this thesis is to launch multiple TS instances each working in a different area of the solution space, as shown in Fig. 3.4. In order to cover the solution space efficiently, we use a procedure called *sequential diversification* [149]. In the case of a binary problem, this procedure works as follows. Let $\{v_0\}$ be the set of initial solutions, initially composed of only one randomly generated bit sequence. Every new solution added to $\{v_0\}$ must be located at a minimal distance $d = d_{\min}$ of all members of $\{v_0\}$. In this work, we choose to fix this number using the following rule

$$d_{\min} = \text{ceil}(0.3N), \tag{3.2.3}$$

where N is the number of binary variables considered, and ceil(z) is the ceiling function, returning

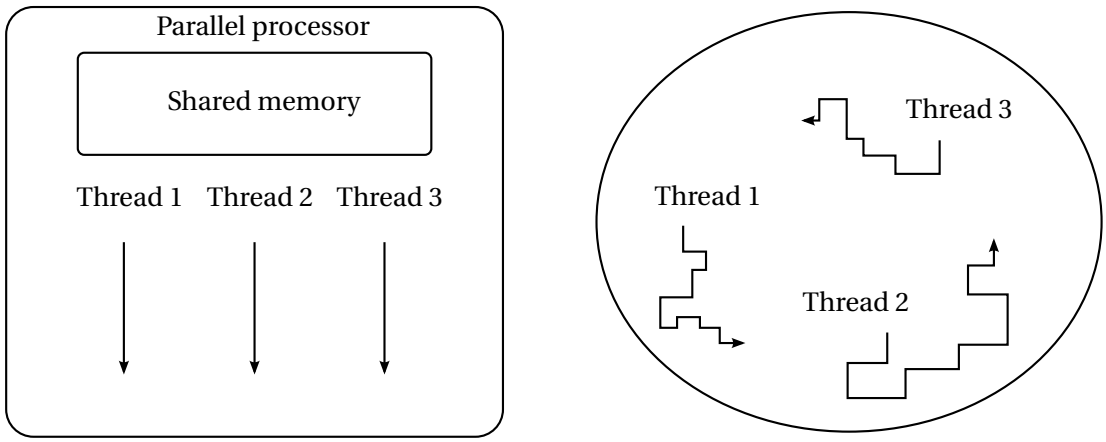

(a) Multi-threaded approach

(b) Worker threads in solution space Υ

Figure 3.4 – Schematic representation of the multiple threads of a parallel tabu search process. Inspired by [149].

the smallest integer larger or equal to z. In other terms, to ensure that the cloud of initial solutions is well scattered in the solution space (see Fig. 3.4b), every initial solution must be characterized by at least $d_{\min}$ bits differing from every other initial solution.

In summary, TS is a local search metaheuristic well suited for intensification – concentrating the search in the neighborhood of the best solutions found – and retains a mechanism to escape from local minima, the tabu list. As stated earlier, a metaheuristic should ideally combine search intensification and diversification. The parallel implementation of TS presented in this section (PTS) adds this diversification dimension by considering different regions of the search space simultaneously.

3.2.2 Genetic algorithm

In this section, we briefly discuss one of the best known metaheuristics, the genetic algorithm (GA). The goal of this section is to present the canonical implementation of the GA that is used in chapter 4. For reasons that shall become clear later, the use of the GA was progressively abandoned during this research project in favor of the PTS algorithm described earlier (§3.2.1). Moreover, since the application of evolutionary techniques to optical engineering problems has been exhaustively documented in previous studies [35, 40, 79, 94, 130, 158], we shall only present a brief description of the GA here and refer the reader to Refs. [149, 164] for more details.

The GA is part of a broader class of P-metaheuristics called *evolutionary algorithms*. Evolutionary algorithms are mostly *stochastic* techniques inspired by biological evolution. Solutions to optimization problems are often called "individuals" in the metaphor of evolutionary techniques, and the objective function $G(v)$ is used to assign a "fitness" value to each individual. For instance, if we wish to maximize $G(v)$, the fitness value $F(v)$ can be simply assigned as $F(v) = G(v)$. If $G(v)$ is

to be minimized, one can use the choices $F(v) = 1/G(v)$ or $F(v) = -G(v)$. Populations of individuals are then generated and evolved using nature-inspired operators such as mutations and natural selection.

The term "genetic algorithm" usually denotes a specialization of evolutionary techniques based on probabilistic natural selection rules and using a binary encoding of solutions. We specifically use the canonical GA, the template of which corresponds to algorithm 3.2.3. After generating an initial population using the sequential diversification procedure described in section 3.2.1, this population is evolved (iterated) using sequential applications of four operators: selection, crossover, mutation and elitism. While most implementations of the GA follow this template, there are many ways to define each of these operators. Consequently, we shall give details about each of the four in this section.

Algorithm 3.2.3 : High-level template for the canonical genetic algorithm [164]

Input : Initial population $P_0 = \{v_i\}$
$t = 0$;
while *No stopping criterion met* **do**
    $P' :=$ Selection (P_t) ; `// Apply selection operator using` $F(v)$ `values`
    $P' :=$ Crossover (P') ; `// Apply crossover operator`
    $P' :=$ Mutation (P') ; `// Apply mutation operator`
    $P_{t+1} :=$ Elitism (P_t, P') ; `// Keep elite(s) in subsequent generation`
end
Output : Final population P_t

3.2.2.1 Selection

The selection operation in evolutionary algorithms is based on the principle of "survival of the fittest". The higher the fitness of an individual member of the population, the better is his chance of being propagated in subsequent generation. The flavor of selection operator we use in this work is called "stochastic universal sampling". Let $P_t = \{v_i\}$ be a population containing n individuals. A selection probability p_i can be assigned to every member of the population using the fitness values of the individuals $F(v_i)$

$$p_i = \frac{F(v_i)}{\sum_{j=1}^{n} F(v_j)}. \tag{3.2.4}$$

Stochastic universal sampling can be viewed as laying down a pie chart with n sectors proportional to the probabilities p_i. A "roulette wheel" with n equally spaced pointers is then spun using a single random number generation, and the pointers directly select which individuals are to survive in the subsequent population [149, pp. 206–207].

3.2.2.2 Crossover

Once the selection operator has been applied to the current population P_t, the intermediate population P' contains a number of "parent" individuals, which are used to generate "offspring" individ-

uals. The goal of this step is to propagate desirable characteristics of the parents to the offsprings. More specifically, we use uniform crossover (or recombination), which consists in randomly assigning bits of the children from those of the parents. Going back to the example of binary chains of length $N = 8$, consider the following two parents

$$\begin{pmatrix} v_1 \\ v_2 \end{pmatrix} = \begin{pmatrix} 01011001 \\ 01000111 \end{pmatrix}. \tag{3.2.5}$$

Assuming an equal probability of inheriting characteristics of v_1 and v_2, the following two children are a possible realization of a single application of the uniform crossover operator

$$\begin{pmatrix} v_1' \\ v_2' \end{pmatrix} = \begin{pmatrix} 01010011 \\ 01001101 \end{pmatrix}. \tag{3.2.6}$$

Notice that bits that are equal for both parents (e.g the first three and the last one) are necessarily propagated in the encoding of the children. This uniform crossover operator is applied on randomly chosen pairs of parents with a *crossover probability* p_c, which we keep static during the optimization procedure [14]. The most commonly used crossover probabilities are in the interval $p_c \in [0.45, 0.95]$, which means that crossover is roughly applied to more than half the individuals of the population. The parents that are chosen are then replaced by their children in the next intermediate generation, a procedure called generational replacement.

3.2.2.3 Mutation

Mutation operators are stochastic operators acting on single individuals. The main objective of a mutation operator is to introduce diversity in the population [63]. In the case of a binary encoding of solutions, the definition of the mutation operator is straightforward. First, a small mutation probability p_m is defined, typically betwen 10^{-3} and 10^{-2}. Then, for every bit of every individual, a pseudo-random number in the interval $[0, 1]$ is generated. If the pseudo-random number is smaller than p_m, the bit is flipped. This means that roughly one in 1000 bits will be changed if $p_m = 10^{-3}$.

3.2.2.4 Elitism

Elitism is an operator which ensures that the best solution found is always part of the next generation in order not to lose any ground during the search. In this work, we use an implementation that chooses a random solution from P' and replaces it by the current elite individual, in other words the best solution found to this point in the search.

3.2.3 Concluding remarks

In general, the performance of a metaheuristic algorithm is strongly dependent on the landscape of the objective functions considered [149, p. 179]. Consequently, the question "which metaheuristic algorithm should be used for a given problem?" does not have a definitive answer. In chapter

14. As discussed in Ref. [145] adaptive probabilities are also possible.

4, we "solved" the problem of amplitude-only beam shaping using the GA. However, by the time we decided to tackle the coherent beam shaping problem (amplitude and phase shaping), the existence of TS was brought to our attention. Using the amplitude-only problem, we compared the performance of GA and PTS, and found that PTS yielded better results on average than the GA for a similar computational time (see §5.2). We subsequently turned to PTS for the remainder of the optimization runs performed in this thesis.

There is one possible way to explain this improvement. As described earlier, the GA is a stochastic algorithm with a strong emphasis on using crossover and random mutations to introduce diversity in the populations. While the population-based nature of the GA makes it inherently good for diversification, it tends to spend a lot of time sampling useless solutions because of its stochastic nature. By contrast, TS is a local method dedicated to the intensification of solutions, and is conceptually simpler since one does not need to manage the probabilities p_m and p_c associated with the GA. Since parallel computers are nowadays more available, using a multi-threaded implementation (PTS) allows us to combine the intensification and diversification dimensions in a more straightforward, deterministic algorithm.

While PTS fares better than the GA for our combinatorial optimization problems, these findings do not mean that the GA is necessarily to be avoided. Indeed, it is possible to introduce intensification into the GA by means of local search methods, yielding a *hybrid metaheuristic* [149]. Moreover, the cost of evaluating the objective functions considered in this dissertation is quite low. Combined with the fact that the neighborhood sizes N considered are between 50 and 100, this makes the use of TS appealing. However, because TS systematically searches the neighborhood of promising solutions, problems characterized by very large neighborhoods can become time-consuming. On the other hand, the GA does not sample the whole neighborhood at every iteration, because of its limited population size. This may be appealing when considering very large neighborhoods.

3.3 Multiobjective optimization

Many real-world design problems are multiobjective in nature. For instance, in chapter 6, we are concerned with generating polarized Gaussian beams. We are thus faced with optimizing an objective function related to the beam profile, and another related to its degree of polarization at the same time. Compared to a monoobjective one, a multiobjective optimization problem (MOP) is inherently more difficult to solve since every solution to a monoobjective problem is a necessary solution of the associated n-objective problem. Moreover, there is no commonly accepted definition of the "global" optimum of a MOP, which means characterization of the solutions must be done *a posteriori* by the decision-maker in order to choose which solutions to retain as "optimal".

In this section, we begin by introducing the concept of Pareto dominance, which allows one to order the solutions of a MOP. The solution of a multiobjective problem is not a single solution, but rather a set of solutions which form the *Pareto set* of the problem. The location of this ensemble

of solutions, called *Pareto front*, must be determined using metaheuristic algorithms. This can be achieved using various methods, the simpler of which is the *aggregation method*.

Before defining the Pareto set, the concept of *Pareto dominance* must be defined [149, p. 311]. Without loss of generality, suppose a multiobjective minimization problem. Let $G = \{g_1, \ldots, g_n\}$ and $H = \{h_1, \ldots, h_n\}$ be two objective function vectors. G is said to dominate H (denoted by $G \prec H$) if and only if no component of H is smaller than the corresponding component of G, and at least one component of G is strictly smaller. In other words, G dominates H if it corresponds to equal or better values of the objective functions. Pareto optimality stems directly from the concept of Pareto dominance. Suppose a set of solutions to a MOP, which we denote $\{v_1, \ldots v_m\}$. A solution v_i is said to be Pareto optimal if

$$\forall i \neq j : \qquad G(v_j) \not\prec G(v_i), \tag{3.3.1}$$

where G is the vector containing the values of all objective functions. In other words, a solution can be termed Pareto optimal if its corresponding objective function vector is not dominated by that of any other solution. Another way to state this is that, for a Pareto optimal solution, it is not possible to improve the value of an objective function g_i without deteriorating at least one other.

While searching for the solution to a monoobjective optimization problem, one usually retains the solution characterized by the smallest value of $G(v)$. However, in the case of a multiobjective problem, all Pareto optimal solutions are possible solutions and form the *Pareto set* of the problem. The location of this set of solutions in the objective function space is called *Pareto front*. An example Pareto front for a biobjective minimization problem is shown in Fig. 3.5. This typical shape shows that the two objective functions g_1 and g_2 are not independent, which means that improving one of the two is usually detrimental to the other.

In short, a multiobjective optimization algorithm samples the location of the Pareto front via a combination of monoobjective problems, each using an appropriate objective function. The simplest way to construct this objective function is the aggregation, or weighted sum method [32, 149]. In short, one defines the following aggregate objective function

$$\min_{v \in Y} \sum_{i=1}^{n} \alpha_i f_i(v), \tag{3.3.2}$$

where $f_i = g_i / g_i^{\max}$ and $g_i^{\max}$ is a heuristic upper bound. This normalization aims to ensure that all objective functions are commensurate. Once this function is defined, the problem is reduced to a monoobjective problem which can be tackled using the metaheuristics described in this chapter, for instance PTS or GA. Multiple monoobjective problems can be solved in parallel using different values of the weights α_i. Varying the relative weights enables to explore different sections of the Pareto front, although the same Pareto optimal solution may be generated by using different weights.

We conclude this section with a remark about multiobjective optimization. Most of the time, the multiple objective functions associated to a MOP represent different physical dimensions of the

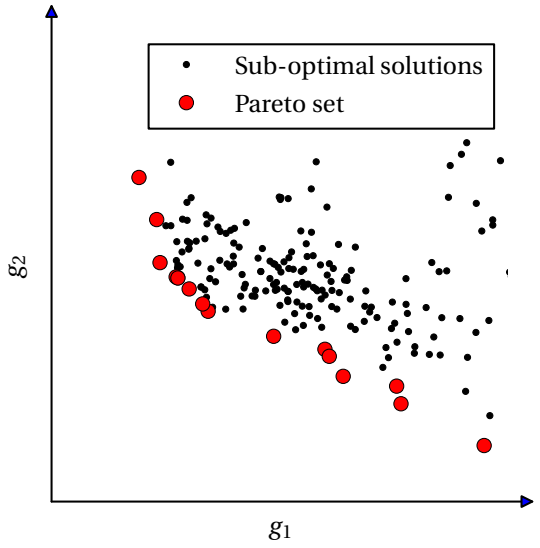

Figure 3.5 – Typical Pareto front of a biobjective optimization problem. Black dots indicated dominated solutions, as for each of these solutions, there exists a solution characterized by a better value of both g_1 and g_2. Real data taken from Fig. 5.11.

problem. Thus, it is not possible for the decision maker to determine *a priori* the exact required compromise between the multiple objectives. In other terms, it is not generally possible to decide which values of the α_i will give an aggregate objective function representing this compromise. In this thesis, we use an *a posteriori* approach. We use a limited knowledge of the MOP (for instance the results of an associated monoobjective problem) to establish a set of values for the weights α_i, then sample the location of the Pareto front. The obtained values of g_i are then examined, and if needed optimization is performed again using other values of α_i to reach more Pareto optimal solutions. In summary, solving a MOP amounts to obtaining the best possible sampling of the Pareto front of the problem in order to provide the decision maker a wider variety of "optimal" solutions to choose from.

Chapter 4

Beam shaping using genetically optimized two-dimensional photonic crystals

Denis Gagnon, Joey Dumont and Louis J. Dubé

Département de physique, de génie physique et d'optique
Faculté des Sciences et de Génie, Université Laval, Québec G1V 0A6, Canada

Journal reference: J. Opt. Soc. Am. A, Vol. 29, pp. 2673–2678 (2012)

URL: http://dx.doi.org/10.1364/JOSAA.29.002673
ePrint: http://arxiv.org/abs/1204.5380

Résumé

Nous proposons l'utilisation de cristaux photoniques bidimensionnels possédant des défauts optimisés comme méthode de manipulation de faisceaux. Cette méthode permet la transfromation d'un faisceau d'entrée focalisé en un faisceau de sortie de profil arbitraire. Le développement en harmoniques cylindriques de faisceaux de type « source complexe » est présenté et utilisé pour calculer la fonction d'onde diffusée d'un cristal 2D fini à l'aide d'un algorithme de diffusion multiple. Le problème de manipulation de faisceaux est ensuite solutionné au moyen d'un algorithme génétique. Nous illustrons cette procédure via la génération de deux différents faisceaux de profil Hermite-Gauss. Les pertes et la robustesse des configurations obtenues aux variations des paramètres du faisceau d'entrée sont finalement caractérisées.

Abstract

We propose the use of two-dimensional photonic crystals with engineered defects for the generation of an arbitrary-profile beam from a focused input beam. The cylindrical harmonics expansion of complex-source beams is derived and used to compute the scattered wavefunction of a 2D photonic crystal via the multiple scattering method [15]. The beam shaping problem is then solved using a genetic algorithm. We illustrate our procedure by generating different orders of Hermite-Gauss profiles, while maintaining reasonable losses and tolerance to variations in the input beam and the slab refractive index.

4.1 Introduction

Laser beam shaping, defined as redistributing the irradiance and phase of a beam, is of great interest for many applications such as image processing and holography [30], atom guiding [97], materials processing [31] and controlling random laser emission [10]. Shaping can be achieved using various optical apparatus, such as binary holograms [17], conical lenses [31, 62], solid state lasers [78], and spatial light modulators [10]. Beam shaping using anisotropic photonic crystals has also been reported [134, 119, 135]. Moreover, the generation of self-healing, limited-diffraction Bessel-Gauss beams by 2D axicon-shaped photonic crystals has recently been demonstrated by Kurt and Turduev [76, 77]. These promising results highlight the potential of photonic crystal engineering for the generation of beams of *arbitrary* profiles. However, few solutions are available for robust integration of optical elements dedicated to beam shaping on planar lightwave circuits. One of those is the use of a heterogeneous refractive index maps to convert a Gaussian beam to a Bessel-Gauss profile [128]. Nevertheless, planar-waveguide based photonic crystal slabs, consisting of air holes in a high index core, retain immense potential for fabrication of integrated optical elements [9, 27, 38, 114].

15. The name "multiple scattering" was used in this article as we were not yet settled on the name "2D-GLMT".

The aim of this paper is to show that two-dimensional photonic crystals (PhC) can be engineered to achieve *any* specific beam profile required for a given application, while maintaining relatively low scattering losses. Theoretical PhC engineering involves selecting a number of adjustable geometric parameters and performing parametric optimization of a cost function related to the irradiance distribution of the scattered beam. Since the use of more adjustable parameters (usually) results in more diverse output profiles, a fast and accurate numerical method is needed to compute the field scattered by the PhC device. The speed of the method is critical since a large number of configurations must be tested. Consequently, resource-heavy finite-difference time-domain (FDTD) computations [77] are not suited for our purpose. We rather use the typically faster multiple scattering computations [33, 103]. The first part of this paper is concerned with a description of the scattering approach. We present a derivation of the cylindrical harmonics expansion of focused beams used to parametrize the wave incident on the PhC. This expansion is required by the multiple scattering formalism.

In the latter part of this paper, we detail the proposed PhC devices and the optimization scheme used. Like Vukovic *et al.* [158], we choose a basic photonic lattice configuration and allow individual scatterers to be present or absent as the only adjustable parameters, thereby enabling a binary encoding of the configuration space and the use of the standard genetic algorithm (GA) to find the configuration best suited to our purpose [35, 139]. Our results show that the optimization strategies presented in [158] can be advantageously used to design an integrated beam shaping device. To illustrate this, we present engineered configurations allowing the generation of two different Hermite-Gauss beam profiles with great accuracy, and discuss the power conversion efficiency of the proposed devices.

4.2 Scattering of complex-source beams by PhCs

This section establishes the theoretical framework used to compute the field scattered by a finite PhC slab. A generic two-dimensional PhC consists of an array of air holes in a planar dielectric waveguide, with a lattice constant of the order of the operation wavelength [9, 140]. Since our goal is to engineer the geometric properties of the PhC to achieve a given beam profile, we only consider finite-size slabs. For modeling purposes, we suppose that every cylinder (hole) is infinite along the axial z direction. The field scattered by the cylinder array is then given by the solution of the 2D Helmholtz equation

$$[\nabla^2 + k^2(x,y)]\varphi(x,y) = 0, \tag{4.2.1}$$

where a harmonic time dependence $\exp(-i\omega t)$ is assumed and $k = k_0 n(x,y)$, where n is the refractive index. Both TM ($\varphi \equiv E_z$) and TE ($\varphi \equiv H_z$) polarized waves can be considered. The wavefunction outside the scatterers can be written as a superposition of an incident and a scattered wave, $\varphi(x,y) = \varphi_i(x,y) + \varphi_s(x,y)$. We then seek the scattered wavefunction $\varphi_s(x,y)$ in the case where $\varphi_i(x,y)$ is a focused beam with a Gaussian shape in the paraxial zone. For this purpose, the incident

wavefunction is represented by a complex-source beam (CSB). This solution has been proposed in order to extend the validity of the Gaussian beam (GB) beyond the paraxial zone [37, 65].

Using the Green's function of the inhomogeneous Helmholtz equation for a point source located in the complex plane at coordinates $x' = ix_R$ and $y' = 0$, one obtains the CSB solution

$$\varphi_i(x,y) = H_0^{(1)}(kr_s), \tag{4.2.2}$$

where $H_0^{(1)}$ is a Hankel function of the first kind. The complex distance r_s is given by

$$r_s \equiv [(y-y')^2 + (x-x')^2]^{1/2} = [y^2 + (x-ix_R)^2]^{1/2}. \tag{4.2.3}$$

The complex point-source yields a directional field radiating away from the beam waist ($x = 0$). The CSB is continuous everywhere in the real plane except across the branch cut connecting the two singularities at $(x,y) = (0,x_R)$ and $(x,y) = (0,-x_R)$. For the purposes of this paper, we shall restrict our attention to scatterers located in the positive x plane, referring the reader to [91] for regularization strategies in the waist plane. Since the $H_0^{(1)}$ function converges rapidly to a complex exponential, one can readily show that, for $x > 0$,

$$\varphi_i(x,y) \sim \varphi_g(x,y)\exp(kx_R + i\pi/4), \tag{4.2.4}$$

where

$$\varphi_g(x,y) = \sqrt{\frac{2}{\pi k(x-ix_R)}}\exp\left\{ik\left(x + \frac{1}{2}\frac{y^2}{x-ix_R}\right)\right\}. \tag{4.2.5}$$

In other words, the CSB reduces to a GB of Rayleigh distance x_R propagating along the x axis in the paraxial zone. Moreover, since the CSB is an analytical solution of the Helmholtz equation exhibiting the cylindrical symmetry characteristic of the multiple scattering method, it is the ideal parametrization of a focused non-paraxial GB incident on an array of cylindrical scatterers.

4.2.1 Expansion of complex-source beams in cylindrical harmonics

To compute the scattered wavefunction via the multiple scattering method, one needs to expand the incident field on a basis of cylindrical waves centered on each individual scatterer. This section is dedicated to the analytic expansion of the aforementioned CSB into cylindrical harmonics. Let (ρ_n,θ_n) be the cylindrical coordinate system local to the n^{th} scatterer, whose center is located at (X_n, Y_n). We seek a series expansion to rewrite the incident beam in the following fashion

$$\varphi_i(\rho_n,\theta_n) = \sum_{l=-\infty}^{\infty} a_{nl}^0 J_l(k\rho_n)e^{il\theta_n}. \tag{4.2.6}$$

On can rewrite eq. (4.2.2) as

$$\varphi_i(\rho_n,\theta_n) = H_0^{(1)}(k|\boldsymbol{r}_n - \boldsymbol{r}_{sn}|), \tag{4.2.7}$$

where $\boldsymbol{r}_n = (\rho_n,\theta_n)$ and $\boldsymbol{r}_{sn}$ is the vector pointing from the center of the n^{th} scatterer to the complex source point at coordinates $(x,y) = (ix_R,0)$. To uncouple $\boldsymbol{r}_n$ and $\boldsymbol{r}_{sn}$ in the argument of Bessel

functions, we apply Graf's addition theorem [1]. This leads to the following expansion coefficients, similar to those found in [105]

$$a_{nl}^0 = (-1)^l H_l(kr_{sn})e^{-il\mu}, \tag{4.2.8}$$

where

$$r_{sn} = \sqrt{(X_n - ix_\mathrm{R})^2 + Y_n^2}, \tag{4.2.9}$$

$$\cos\mu = \frac{X_n - ix_\mathrm{R}}{r_{sn}}. \tag{4.2.10}$$

For comparison, the expansion coefficients for a plane wave (PW) incident from the $-x$ axis are given by

$$a_{nl}^0 = i^l e^{ikX_n}. \tag{4.2.11}$$

The sole knowledge of the a_{nl}^0 expansion coefficients of the incident beam allows the use of the multiple scattering method. In a nutshell, one writes the scattered field as a sum of cylindrical waves centered on each individual scatterer

$$\varphi_s(x,y) = \sum_n \sum_l b_{nl} H_l^{(1)}(k\rho_n)e^{il\theta_n}. \tag{4.2.12}$$

The matrix equation connecting the expansion coefficients can be written as $s_{nl}a_{nl}^0 = T_{nn'}^{ll'}b_{n'l'}$, with

$$T_{nn'}^{ll'} = \delta_{nn'}\delta_{ll'} - (1-\delta_{nn'})e^{i(l'-l)\phi_{nn'}}H_{l-l'}^{(1)}(kR_{nn'})s_{nl}, \tag{4.2.13}$$

where $R_{nn'}$ is the center-to-center distance between scatterers n and n', $\phi_{nn'}$ is the angular position of scatterer n' in the frame of reference of scatterer n and s_{nl} is a constant resulting from the application of electromagnetic boundary conditions. Further details are given in [33, 103].

Remarkably, except for the computation of a cylindrical function, no supplementary numerical cost is involved in computing the scattered wavefunction in the case of an incident CSB rather than an incident PW. Indeed, the core operation of the multiple scattering method involves computing the b_{nl} coefficients via a matrix inversion, whose computation scales as the square of the number of scatterers N, regardless of the shape of the incident beam. However, a simple analysis shows that the convergence of (4.2.8) is limited to a disk not intersecting or touching the branch cut between $(x,y) = (0, x_\mathrm{R})$ and $(x,y) = (0, -x_\mathrm{R})$. In other words, scatterers must not intersect or touch the branch cut for the expansion to be used in scattering computations. This restriction is not present in the case of an incident PW. It does not restrict the scope of our computations since we position all scatterers in the $+x$ half plane.

4.3 Beam shaping computations

4.3.1 Problem definition

The objective is to find a PhC configuration which, when illuminated with a CSB, produces a scattered wavefunction that matches a desired irradiance profile in a given plane. Let $\bar{\varphi}(x,y)$ be the

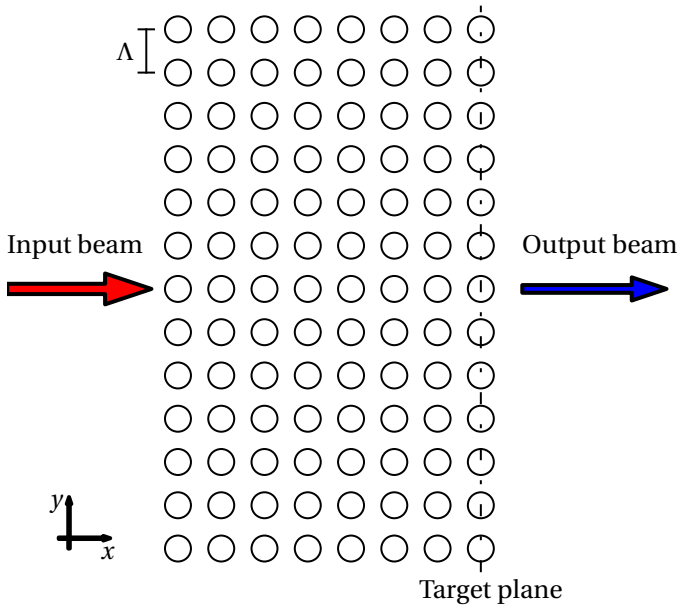

Figure 4.1 – Basic photonic lattice configuration ($N = 104$). To generate a desired beam profile, defects can be present or absent. We impose a vertical mirror symmetry, resulting in 2^{56} possible configurations. The dotted line indicates the plane used for the computation of the desired beam profile.

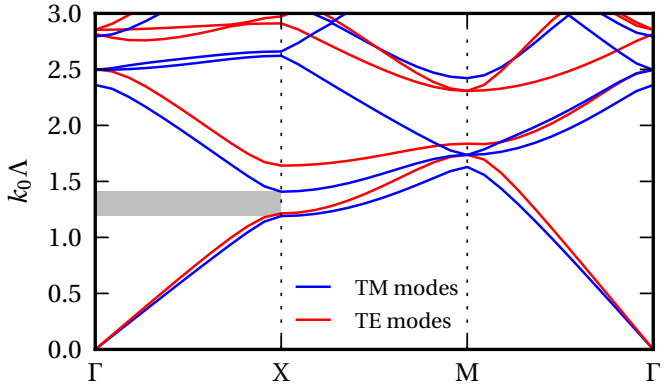

Figure 4.2 – Band structure for a square lattice of air holes of radius $r = 0.3\Lambda$ in a dielectric medium with refractive index 2.76. The location of the partial bandgap is shaded. Eigenmodes were computed using the MIT PHOTONIC BANDS software package [73].

desired output wavefunction. The beam shaping problem can be formulated as the minimization of the following integral

$$g_1(x_0) = \frac{\int ||\varphi(x_0, y)|^2 - |\bar{\varphi}(x_0, y)|^2| dy}{\int |\bar{\varphi}(x_0, y)|^2 dy}, \tag{4.3.1}$$

where x_0 is the location of the target plane. This is equivalent to minimizing the root sum of squares (RSS) of irradiance variations at a set of points of the target plane [30]. It is worth noting that we do not take into account the phase of the output beam, only the amplitude. This increases the number of "acceptable" configurations in the problem space, at the cost of losing information about the collimation of the output beam in the optimization process. Large variations in the output phase front may result in large output beam divergences, although this is not critical for applications such as materials processing [30, 31]. Moreover, since backscattering losses are mostly unavoidable in PhC devices, imposing a peak irradiance value is too severe a condition for the optimization algorithm. We rather seek a normalized irradiance profile, and evaluate backscattering losses *a posteriori*.

The basic scatterer geometry (Fig. 4.1) is a variation of that presented in [158, 169], i.e. part of a square lattice of air holes embedded in a medium of index $n = 2.76$. The radius of all holes is set to $r = 0.3\Lambda$, where Λ is the lattice constant. The infinite counterpart of this photonic lattice exhibits a partial photonic bandgap for both polarizations in the $\Gamma - X$ direction (see Fig. 4.2). Although the strong confinement associated with a full photonic bandgap is exploited in the case of waveguide design [169], it is not mandatory for beam shaping purposes. Indeed, the purpose of the finite PhC slab is not to act as a Bragg reflector, but rather to redistribute the incident beam irradiance via multiple scattering. We shall therefore concentrate on operating wavelengths near the partial bandgap to ensure relatively strong scattering.

For definiteness, we prescribe our incident beam as a TM-polarized CSB given by (4.2.2) with a half-width $w_0 = 2.5\Lambda$ and a wavenumber $k_0 = 1.76/\Lambda$ for a Rayleigh distance $x_R = k_0 w_0^2/2 = 5.48\Lambda$. Although the desired output beam and target plane can be arbitrary, for illustrative purposes we have chosen to generate Hermite-Gauss beam profiles of half-width w at the device output, that is

$$|\bar{\varphi}_m(x_0, y)|^2 = [\mathscr{H}_m(\xi)]^2 \exp\left(-\xi^2\right), \tag{4.3.2}$$

where $\xi = \sqrt{2}y/w$ and $\mathscr{H}_m(\xi)$ is a Hermite polynomial. The first two orders are

$$\begin{aligned} \mathscr{H}_1(\xi) &= 2\xi, \\ \mathscr{H}_2(\xi) &= 4\xi^2 - 2, \end{aligned} \tag{4.3.3}$$

while $\mathscr{H}_0(\xi) = 1$. For simplicity, we require further that the half-width w of the desired beam profile be identical to w_0.

We use a genetic algorithm (GA) to find the configuration best suited to the generation of a given beam profile [35, 158]. The problem encoding is binary, with each configuration being assigned a "genotype" of length equal to the number of available scatterer sites. For the purpose of demonstration, we have targeted symmetric beam shapes and have explicitly imposed mirror symmetry

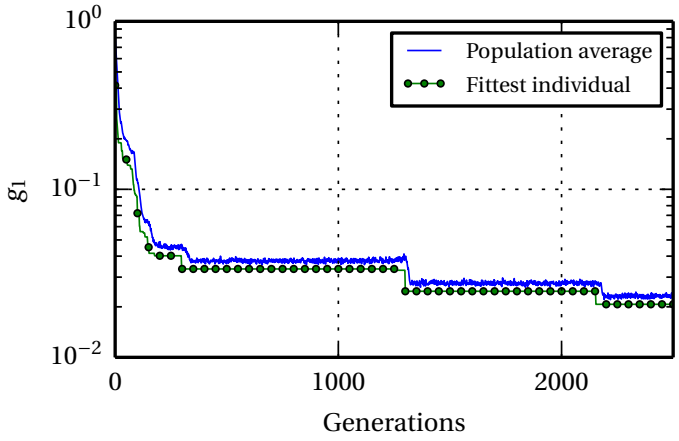

Figure 4.3 – Convergence of the standard GA used to find the configuration shown on Fig. 4.4. The fitness value reached is $1/g_1 \sim 47.6$.

of the scatterers about the y-axis. This effectively reduces the problem space dimension, but the method is equally efficient for asymmetric beam shapes. Each trial configuration is assigned a fitness value inversely proportional to g_1. Populations of 200 individuals are generated and evolution takes place until an optimum is reached, typically within a few thousand generations (see Fig. 4.3). We use the standard GA evolutionary operators: roulette wheel sampling, mutation probability $p_m = 0.002$, uniform crossover with probability $p_c = 0.2$ and elitism. It is noteworthy that the computation of the fitness function, which implies a matrix inversion and field evaluation via the multiple scattering method, takes only a few seconds for one generation (200 configurations).

4.3.2 Generation of beam profiles and tolerance of configurations

In this section, we present the best configurations found for order 1 and 2 Hermite-Gauss beam profiles, exhibiting a zero and a maximum on the propagation axis, respectively. Results shown on Figs. 4.4 and 4.5 highlight the possibility to generate order 1 and 2 Hermite-Gauss beam profiles with great accuracy ($g_1 < 0.05$) and are representative of a number of calculations that we have performed. For comparison, the error on the amplitude profile for the PhC device reported in Ref. [119] is around 10 %, while the error of the integrated device proposed in Ref. [128] is around 5 %. This shows that our designs perform equally well or better than recently proposed integrated beam shaping solutions with respect to the profile accuracy. We also stress that the method used is not limited to a single lattice nor to a specific output beam profile. For example, we have obtained profiles with similar accuracy using a triangular lattice with the same refractive index.

Since our primary goal is to obtain an accurate normalized profile via GA optimization, the best configurations found do not necessarily exhibit low backscattering losses. To quantify these losses, we compute the efficiency η of the best designs by evaluating the ratio between the electromag-

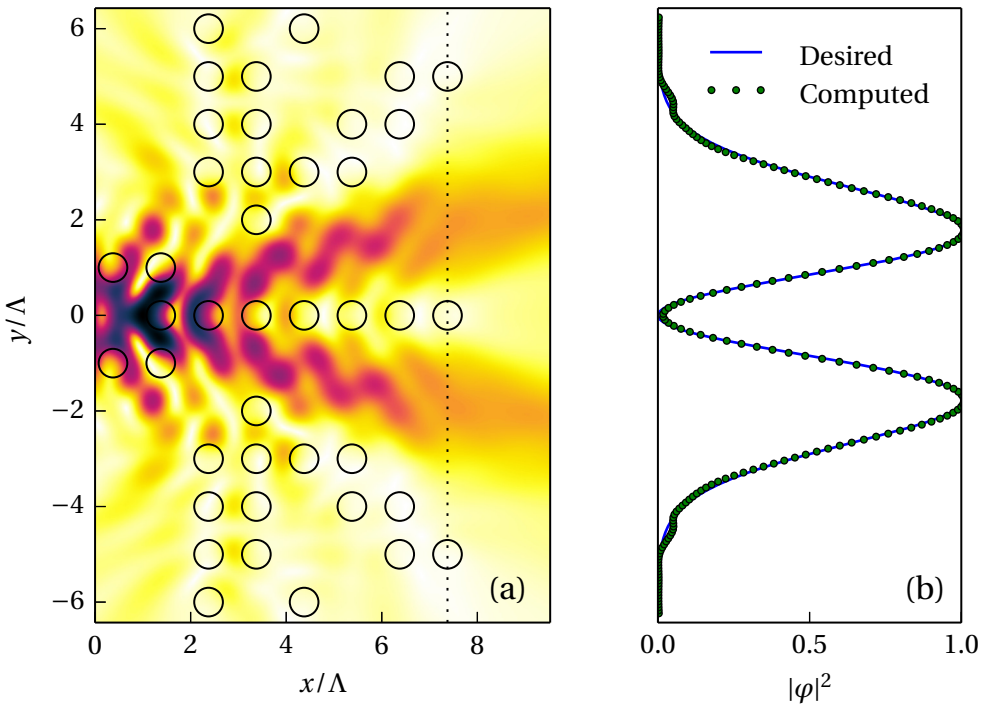

Figure 4.4 – Generation of order 1 Hermite-Gauss beam. (a) Optimized configuration and field profile ($N = 41$). The target plane is indicated by a dashed line. (b) Comparison of computed irradiance along target plane and desired profile (arbitrary units). This design is characterized by $g_1 = 0.021, \eta = 0.705$.

netic power transmitted in the target plane and the total incident power; that is

$$\eta = \frac{\int_{-\infty}^{\infty} \langle S_x(x_0, y)\rangle dy}{\int_{-\infty}^{\infty} \langle S_x(x_{\text{in}}, y)\rangle dy}, \tag{4.3.4}$$

where x_{in} is the location of the input plane and $\langle S_x\rangle$ is the x component of the time-averaged Poynting vector [103]. The computation of η is achieved via numerical quadrature. As our computations show, efficiencies of optimized configurations typically fall between 70 % and 80 %. These numbers are only 10-20 % smaller than proposed integrated beam shaping devices *specifically* tailored for high efficiencies: Refs. [119, 128] report efficiencies of ~ 90 %. It is therefore quite rewarding that our final configurations not only provide a high profile accuracy, but also a low loss design. Of course, if a higher efficiency is critical to a given application, it is always possible to alter the fitness function of the GA to optimize for efficiency as well.

It is instructive to examine the tolerance of optimized PhC configurations to variations of the design parameters. In experimental situations, the Rayleigh distance may vary if the input beam focusing is more or less controlled. On the other hand, the slab refractive index may be fixed using the effective index approximation [116]. To assess the tolerance to variations of these two parameters, we have computed the RSS integral g_1 for various values of x_{R}/Λ and n around the design values, while maintaining all others parameters fixed (Fig. 4.6). Results show that varying the value

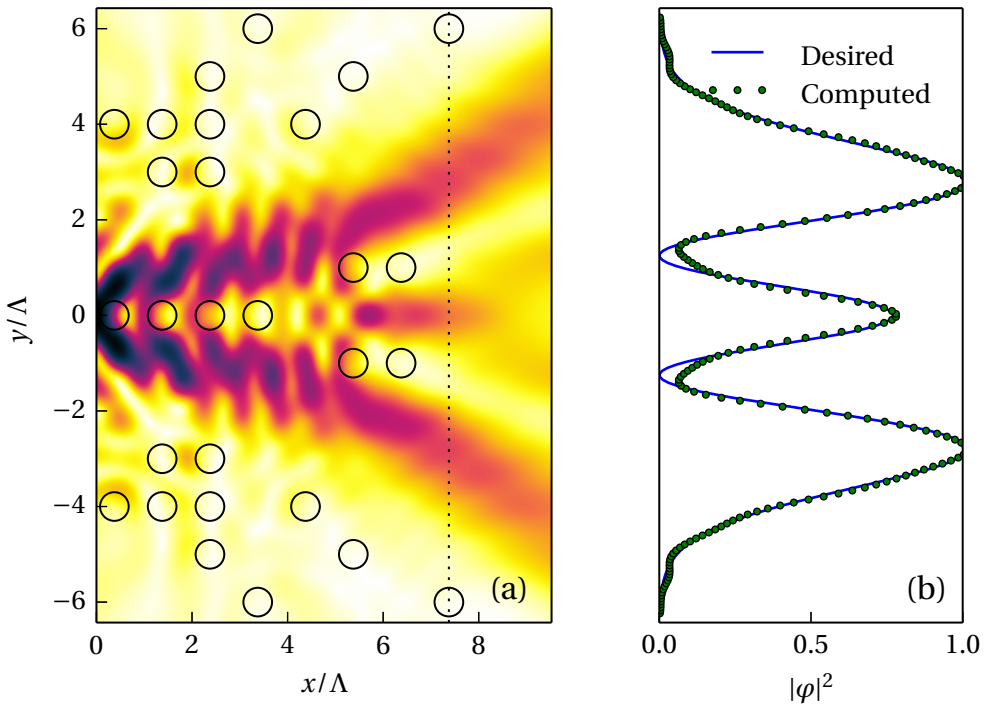

Figure 4.5 – Generation of order 2 Hermite-Gauss beam. (a) Optimized configuration and field profile ($N = 28$). The target plane is indicated by a dashed line. (b) Comparison of computed irradiance along target plane and desired profile (arbitrary units). This design is characterized by $g_1 = 0.044, \eta = 0.785$.

of x_R/Λ by ± 1, one full lattice spacing, preserves the low value of g_1 (under 0.10), especially in the case of the order 1 Hermite-Gauss beam profile. The PhC configurations presented are also robust with respect to the parameter n. It is possible to draw two observations from these computations. First, it is not necessary to run a GA search over a wide range of parameters to keep the fitness of the PhC designs within acceptable limits of performance even if some parameters are only approximately known in experimental applications. Second, the results show that the fabrication of a PhC based integrated beam shaper operating in the infrared ($\lambda_0 \sim 1500$ nm, $\Lambda \sim 500$ nm) is well within reach of current fabrication techniques. Indeed, devices operating in that regime have been successfully fabricated in silicon-on-insulator material using UV lithography [9, 27, 38, 114].

4.4 Conclusion

In this paper, we have presented a general design method based on a genetic algorithm for beam shaping using integrated two-dimensional photonic crystals. Parametrization of the incident Gaussian-like beam was achieved using the CSB solution of the Helmholtz equation. The cylindrical harmonics expansion of the incident CSB allows for the use of the multiple scattering method to compute the field scattered by the PhC slab. This method enables fast computation of the ampli-

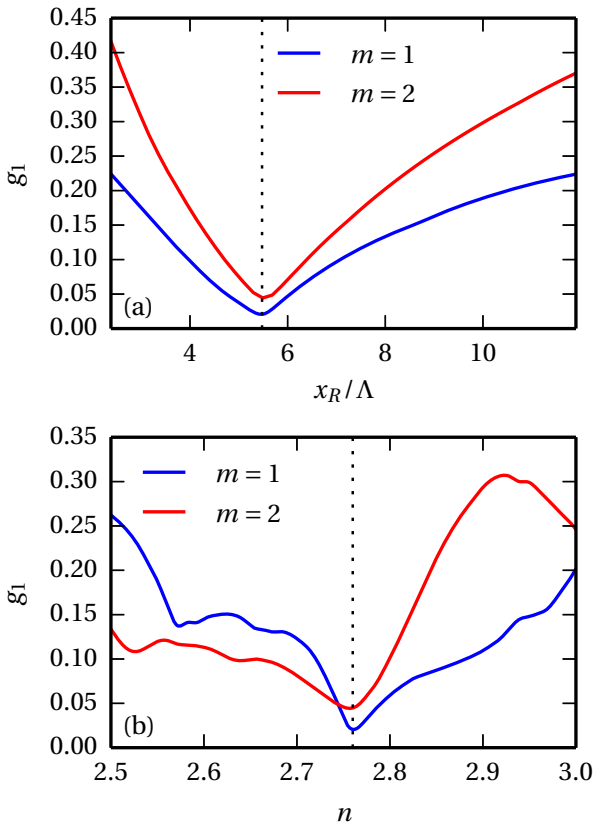

Figure 4.6 – Tolerance of PhC lattice configurations to (a) variations of the Rayleigh distance of the input beam and (b) group refractive index of the slab. The design values are indicated by a dotted line.

tude profile of the beam scattered by individual photonic lattice configurations.

Using this design method, we have tailored photonic crystal devices for the conversion of a CSB to order 1 and 2 Hermite-Gauss beam profiles. The associated beam shaping error (< 5%) compares advantageously to other known integrated solutions. We also found that over 70 % of the input beam power was channeled to the output beam. Although we have used a square lattice and required a Hermite-Gauss profile, different lattices and output beam profiles can be accommodated at will.

We have also evaluated the sensitivity of the output beam to variations in the depth of focus of the input beam and the slab refractive index. Our results show that integrated amplitude beam shapers may very well be fabricated using current technology.

4.5 Authors' contributions

DG designed the study, carried out the analysis, wrote the numerical codes, performed the computations and wrote the first version of the manuscript. All authors have contributed to the analysis and have been instrumental in bringing the original manuscript to a publishable research contribution.

4.6 Supplement: Excerpts of supplemental material

This section gives more details on the data presented in the article, including parameter sweeps of the correlation coefficient and the efficiency. The Pearson correlation coefficient is another way of evaluating the "goodness" of a configuration. Let U and V be two real vectors of length n. The correlation coefficient between the two vectors is given by

$$\mathrm{Corr}(U,V) = \frac{\sum_{i=1}^{n}(U_i-\bar{U})(V_i-\bar{V})}{\sqrt{\sum_{i=1}^{n}(U_i-\bar{U})^2}\sqrt{\sum_{i=1}^{n}(V_i-\bar{V})^2}}. \tag{4.6.1}$$

In the present case, we shall use $U = |\varphi(x,y)|^2$ and $V = |\bar{\varphi}(x,y)|^2$. Although there is no mapping from g_1 to $\mathrm{Corr}(|\varphi|^2,|\bar{\varphi})|^2$, the minimal value $g_1 = 0$ necessarily implies $\mathrm{Corr}(|\varphi|^2,|\bar{\varphi}|^2) = 1$.

In the companion piece, we evaluated the robustness of two "optimal" configurations. In short, we plotted the variation in the value of g_1 to variations of the Rayleigh distance of the input beam and group refractive index of the slab. We chose those two plots as the most relevant. The remaining plots are presented in Fig. 4.7. We considered η and $\mathrm{Corr}(|\varphi|^2,|\bar{\varphi}|^2)$ as additional "dependent" variables, as well as k_0 as an additional "independent" variable.

The study of tolerance to variations in the scatterers' geometry (fabrication imperfections) is further detailed in section 5.9.

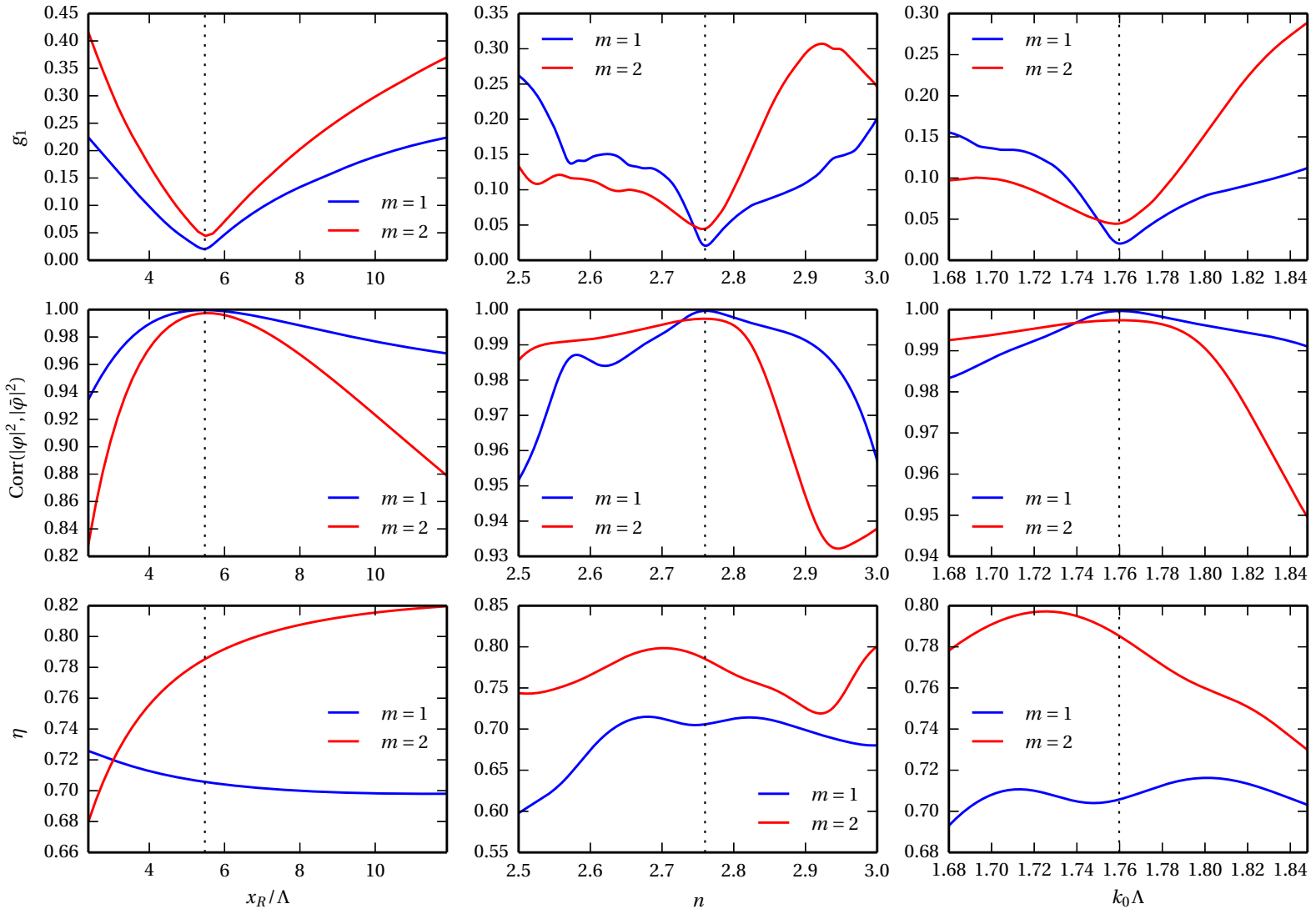

Figure 4.7 – Robustness of "optimal" PhC lattice configurations to variations of the Rayleigh distance of the input beam, the group refractive index of the slab and the free-space wavenumber. The design values are indicated by a dotted line. The configurations are those of Figs. 4.4 and 4.5.

Chapter 5

Multiobjective optimization in integrated photonics design

Denis Gagnon, Joey Dumont and Louis J. Dubé

Département de physique, de génie physique et d'optique
Faculté des Sciences et de Génie, Université Laval, Québec G1V 0A6, Canada

Journal reference: Optics Letters, Vol. 38, pp. 2181–2184 (2013)

URL: http://dx.doi.org/10.1364/OL.38.002181
ePrint: http://arxiv.org/abs/1305.5455

Résumé

Nous proposons l'utilisation de la recherche tabou parallèle pour la solution de problèmes inverses combinatoires en optique-photonique. Afin d'évaluer le potentiel de cet algorithme, nous considérons le problème de manipulation de faisceaux au moyen d'un arrangement bidimensionnel de diffuseurs diélectriques. La performance de la recherche tabou parallèle est comparée à celle de l'algorithme génétique, une des méthodes d'optimisation les plus usitées en optique-photonique. La recherche tabou parallèle produit des solutions optimisées comparables ou supérieures à l'algorithme génétique, tout en nécessitant moins de temps de calcul et un plus petit nombre de paramètres ajustables. En utilisant le problème cohérent de manipulation de faisceaux comme étalon, nous montrons comment la recherche tabou parallèle permet de solutionner efficacement des problèmes d'optimisation à plusieurs objectifs. Cet algorithme représente ainsi une alternative robuste à l'algorithme génétique dans le cas de problèmes en optique-photonique.

Abstract

We propose the use of the parallel tabu search algorithm (PTS) to solve combinatorial inverse design problems in integrated photonics. To assess the potential of this algorithm, we consider the problem of beam shaping using a two-dimensional arrangement of dielectric scatterers. The performance of PTS is compared to one of the most widely used optimization algorithms in photonics design, the genetic algorithm (GA). We find that PTS can produce comparable or better solutions than the GA, while requiring less computation time and fewer adjustable parameters. For the coherent beam shaping problem as a case study, we demonstrate how PTS can tackle multiobjective optimization problems and represent a robust and efficient alternative to GA.

5.1 Introduction

Silicon integrated optical chips offer enormous potential for practical applications. The capability to design and manufacture various planar integrated photonics components such as waveguides [38], beam-splitters [114] and slow-light devices [9] has increased considerably in recent years. This broad spectrum of functionalities is enabled by the interplay of in-plane reflection and interference processes caused by the presence of scattering elements such as an arrangement of holes in a two-dimensional pattern. The arrangements can range from periodic – for instance in 2D photonic crystals – to aperiodic [25, 155] or even completely disordered [167]. A frequently arising design issue in integrated photonics is to determine the scatterers' configuration required to achieved a given functionality. This class of NP-hard inverse design problems is often approached using *metaheuristics*, optimization algorithms based on empirical rules for exploring large solution spaces [149].

The genetic algorithm (GA), a nature-inspired evolutionary method, is perhaps the most widely

used metaheuristic in the field of optics and photonics [14, 94, 129, 130, 158, 162]. Some defining features of the canonical GA are that it uses stochastic transition rules, not deterministic ones, and has no memory of past solutions [52]. The escape from local minima is then achieved using the application of a random mutation operator. For large-scale optimization problems in integrated photonics (for instance a large number of parameters, or the simultaneous optimization of multiple objective functions), this results in many instances in slow convergence. Common approaches for speeding up convergence include breaking the solution space in several pieces [158], or using a combination of GA and local search algorithms [52].

The aim of this letter is to show that purely deterministic metaheuristics can very well be applied to large-scale photonics design problems. The optimization algorithm chosen is the parallel tabu search (PTS), a deterministic algorithm which involves fewer adjustable parameters than the GA. The performance of PTS is compared to the standard GA for a case study, namely the inverse problem of beam shaping using a two-dimensional arrangement of dielectric scatterers [44]. As a further illustration, we show that this algorithm is also well suited to inverse problems involving the simultaneous optimization of more than one attribute. More specifically, we apply PTS to the *coherent beam shaping* problem, in other words the generation of a beam of controlled phase and amplitude profile.

We will address a model inverse problem, namely beam shaping using a photonic crystal lattice. Consider a finite-size arrangement of air holes in a high-index dielectric core. The problem consists in finding a lattice configuration which, when illuminated with an arbitrary input beam, produces a scattered field that matches a desired profile in a given plane. In two dimensions, the beam shaping problem can be formulated as the minimization of the following objective function [30]

$$g_1 = \frac{\int ||\varphi(x_0, y)|^2 - |\bar{\varphi}(x_0, y)|^2| dy}{\int |\bar{\varphi}(x_0, y)|^2 dy}, \tag{5.1.1}$$

where x_0 is the location of the target plane, $\varphi(x_0, y)$ is the computed EM field on the target plane, $\bar{\varphi}(x_0, y)$ is the desired beam at the device output (the $x-$axis is the beam propagation axis). The parameters to optimize can be defined as the geometry of the scatterers' arrangement. A given combination of scatterers is termed a *solution*, or a *configuration*. For a given configuration, the resulting beam $\varphi(x_0, y)$ can be computed using a generalized Lorenz-Mie theory [103]. For definiteness, we set a basic lattice geometry and only allow the scatterers to be present or absent. Consequently, the optimization problem is a combinatorial one. This means individual solutions can be encoded via vectors of bits, the length of each vector being equal to the number of available scattering sites [130, 158].

This beam shaping problem was recently tackled using a standard implementation of the GA [44]. In this previous work, the basic geometry is a 13×8 square grid of scatterers with mirror symmetry, resulting in 2^{56} possible configurations (see fig. 5.1). While the GA is successful in finding very acceptable solutions to this inverse problem, the minimization of g_1 does not take into account the phase profile of the beam, only the amplitude, or irradiance distribution. As a result, the opti-

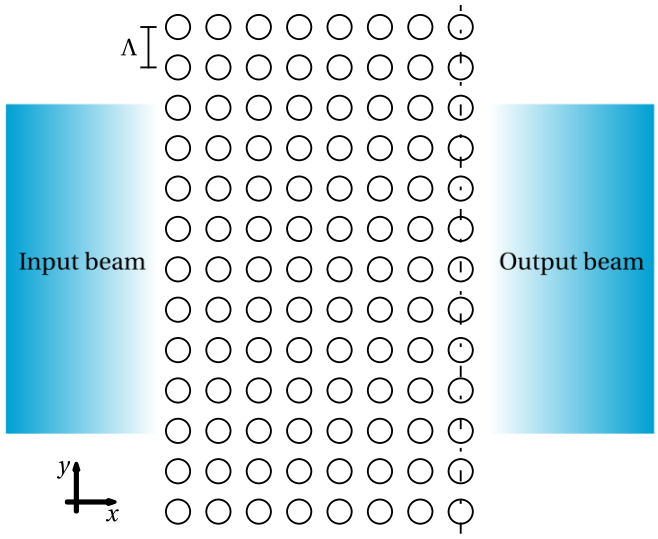

Figure 5.1 – Basic photonic lattice configuration for the beam shaping problem. The dotted line indicates the plane used for the computation of the desired beam profile.

mized beams sometimes exhibit large transverse phase fluctuations, which in turn result in a poor field depth. This is a major impediment to applications such as atom guiding [97] and microscopy [107], where beams with large field depths (low divergence) are needed. In order to achieve *coherent beam shaping*, we must define another objective function related to phase fluctuations of the transverse profile. Consider the following integral

$$g_2 = \frac{\int |\mathrm{Im}[\varphi(x_0,y)e^{-i\phi(x_0,0)}]|^2 dy}{\int |\bar{\varphi}(x_0,y)|^2 dy}, \tag{5.1.2}$$

where $\tan\phi(x,y) = \mathrm{Im}[\varphi(x,y)]/\mathrm{Re}[\varphi(x,y)]$. The value of g_2 is zero for a collimated beam (plane phase front), and increases with the number of oscillations in the phase front. The set of attributes g_1 and g_2 constitutes a *multiobjective optimization problem* (MOP), which must be solved by sampling the set of optimal solutions, commonly known as the Pareto set [149].

The main computational difficulty associated with MOPs lies in the fact that all Pareto solutions of a $p-$objective problem are necessarily solutions of the same problem with a larger number of objectives [149]. Consequently, the number of objective function evaluations needed to solve a MOP is significantly greater than in the single-objective case. Because of that higher computation cost, it is beneficial to use a metaheuristic algorithm that yields better solutions than the GA for a given number of objective function evaluations. However, one would want to preserve the innate ability of the GA to sample broad areas of the solution space. In light of this observation, we propose the use of the parallel tabu search (PTS) consisting in an ensemble of individual tabu search processes exploring the solution space in a parallel fashion [23].

5.2 Performance assessment of PTS

The tabu search is a deterministic local search algorithm first proposed by Glover in the late 1980s [51, 149]. One iteration of a tabu search process begins with the evaluation of the objective function in the *neighborhood* of the current solution. The algorithm then proceeds to the best possible neighbor (best possible value of the objective function) that is not prohibited by the *tabu list*. This list of forbidden moves constitutes the short-term memory of the algorithm and prevents a cyclic search in the solution space. Its length L may be kept constant or dynamically adjusted as the algorithm progresses. In our parallel implementation of the tabu method, we begin by generating a diverse "population" of solutions using a method known as simple sequential inhibition [149]. An individual tabu search process then begins working on a member of the initial "population" until a stopping criterion is met (typically a fixed number of iterations). Since each process acts in a local and deterministic way, the goal of the parallel implementation is to provide a broad sampling of the solution space, as does the GA.

To compare the performance of PTS versus the GA, we apply both algorithms to the incoherent beam shaping problem mentioned earlier. We only optimize for g_1 (see eq. 5.1.1) using the basic scatterer geometry shown in Fig. 5.1. The radius of all air holes holes is set to $r = 0.3\Lambda$, where Λ is the lattice constant. We use an effective index $n = 2.76$, corresponding to a thin silicon slab at $\lambda \sim 1.5$ µm [22]. Although the input and output beams may be arbitrary, we prescribe our incident beam as a TM-polarized non-paraxial Gaussian beam with a half-width $w_0 = 2.5\Lambda$ and a wavenumber $k_0 = 1.76/\Lambda$. Moreover, a mirror symmetry across the x axis is taken into account, resulting in 2^{56} possible solutions, or $\sim 7 \times 10^{16}$. The generalized Lorenz-Mie method used to compute the scattered field $\varphi(x, y)$ is detailed in Refs. [44, 103].

The parameters of the canonical GA are set following the guidelines of Vukovic *et al.* [158]. More specifically, we use roulette wheel sampling, random mutations with probability $p_m = 0.002$, uniform crossover with probability $p_c = 0.2$, and elitism. The generation size is set to 200 individuals. On the other hand, the only PTS parameter to be specified by the user is the tabu list length L. In this work, we use a fixed length of $L = 2.5\sqrt{N_n}$, where N_n is the number of neighbors of a given solution. In this case, N_n is also equal to the number of available scattering sites. We launched 100 GA processes and 100 parallel tabu search processes, each for 5000 iterations (or generations). Since PTS is deterministic, each iteration implies no more than $N_n = 56$ objective function evaluations, whereas we found that each generation of the GA implied an average of 60 objective function evaluations (we keep the values for the best solution in memory). This means that the run-time of each algorithm is similar given our choice of parameters. The minimal values of g_1 for each optimization algorithm are presented in Fig. 5.2. The results show that the solutions found by PTS are more optimal on average for an equivalent computation time. Moreover, some solutions found by PTS were inaccessible to the GA. Therefore, for combinatorial optimization in integrated photonics, PTS may be a better choice. This is similar to the performance gain of tabu search when applied to timetable scheduling problems [21]. PTS is also appealing because it involves very few

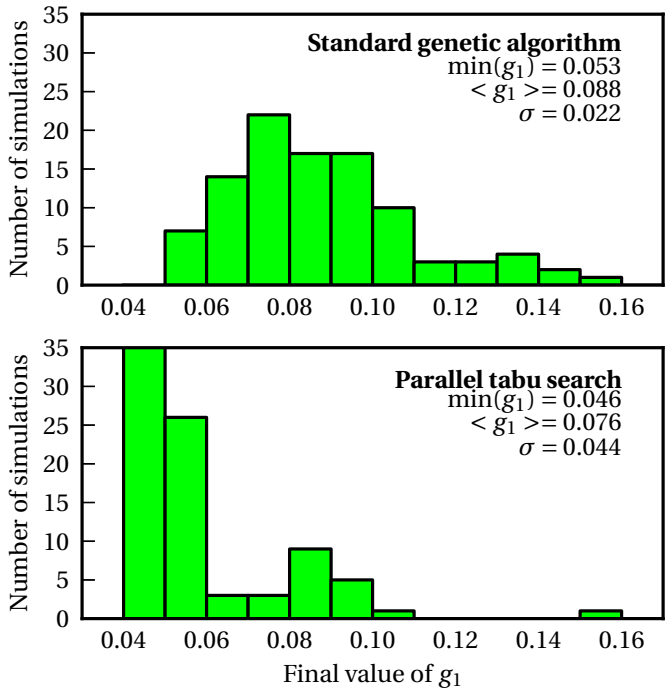

Figure 5.2 – Comparison of the GA and PTS algorithms applied to the incoherent beam shaping problem. Each simulation represents 5000 generations/iterations, with a similar computational cost. 100 simulations are shown for each algorithm.

adjustable parameters and its implementation is more straightforward than that of the GA.

Furthermore, and remarkably, the configurations computed via PTS exhibit a power conversion efficiency ranging from 70 % to 80 %, similar to those obtained with the GA, and merely 10–20 % lower than arrangements *specifically* designed for high efficiency. Additional discussion and comparison to other integrated devices can be found in Ref. [44] (chapter 4 of this dissertation).

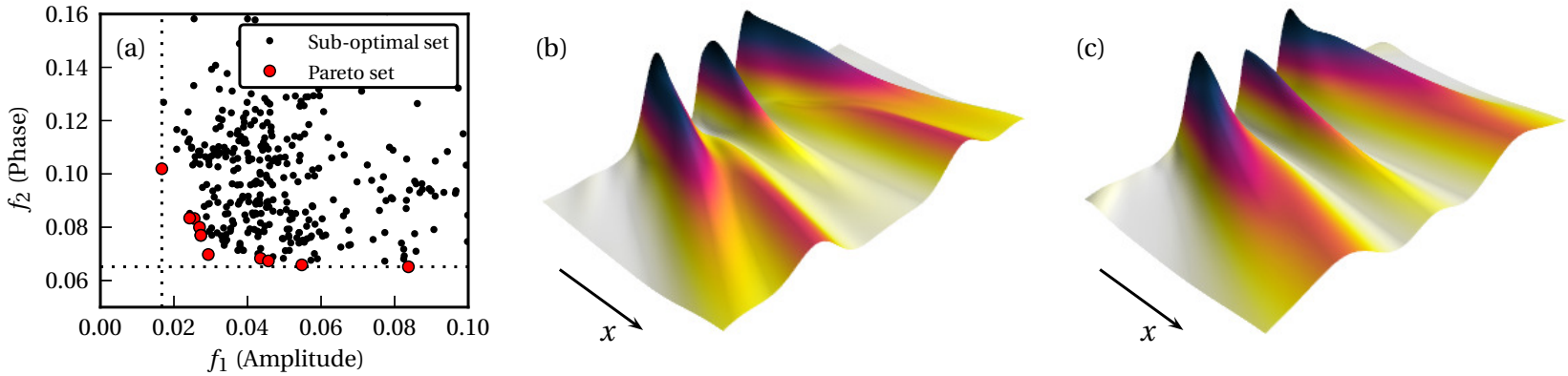

Figure 5.3 – Multiobjective optimization results. (a) Sampling of the Pareto front for the coherent beam shaping problem. The dotted lines indicate the best possible value for each of the two objectives separately. (b) Hermite-Gauss beam profile with the lowest possible value of f_1 ($f_1 = 0.0167, f_2 = 0.1019$). (c) Best possible trade-off between the two objectives ($f_1 = 0.0255, f_2 = 0.0833$). Since the phase is controlled, the Hermite-Gauss profile shape is preserved over a greater propagation distance. This can be seen in the number of ridges in the transverse profile (arbitrary intensity units). The lattice configurations producing these beams are made of $N = 56$ (b) and $N = 52$ (c) scattering sites whose explicit positions can be found in [45] (and in supplement 5.6).

5.3 Multiobjective results and discussion

Having assessed the potential of the PTS optimization algorithm, we now center our attention on the solution of the MOP described by the two objective functions g_1 and g_2. The solution to a MOP is not a single solution, but rather a set of solutions called *Pareto optimal*. A solution is Pareto optimal if it is not possible to improve a given objective without deteriorating at least another [32]. MOPs arise in various areas of engineering and science, such as microprocessor design [133], medical physics [68], chaotic systems [150] and accelerator physics [67]. The simplest way to solve a MOP is the weighted-sum method (or aggregation method). Basically, one recasts a $p-$objective problem into a single-objective one in the following way [32]

$$\min_{v\in\Upsilon} \sum_{i=1}^{p} \alpha_i f_i(v), \tag{5.3.1}$$

where v is a solution, Υ is the solution space, and $f_i = g_i / g_i^{\max}$. Objective functions must be normalized with respect to a heuristic upper bound $g_i^{\max}$ to ensure that all objectives are commensurate. The Pareto front (location of the set of optimal solutions) is then sampled by solving several different single-objective problems using different values of the weights α_i. This has the effect of increasing or decreasing the relative importance of each objective, thereby steering the search towards different regions of the Pareto front [32, 149]. In our case, this implies running several PTS processes using different values of the relative weights α_i.

Using the weighted-sum method, we perform the simultaneous optimization of the amplitude and the phase of a order 2 Hermite-Gauss beam. The geometry used is the same as described above, except that the square lattice is somewhat larger, 13×10 scatterers, for a total of 130 possible scattering sites. Accounting for symmetry, this results in 2^{70} possible solutions, or $\sim 10^{21}$. We set the values $g_1^{\max} = 1$, $g_2^{\max} = 10$ and the restriction $\alpha_1 + \alpha_2 = 1$. The sampling of the Pareto front is performed using 7 different values of $\alpha_2 \in [0.0, 0.425]$. For each of those values, 48 tabu search processes are performed in parallel. This set of search processes yields a number of final solutions, out of which we extract the Pareto optimal set (i.e. those solutions for which there is no solution found that is characterized by a lower value of both g_1 and g_2). The resulting Pareto front is shown in Fig. 5.3a.

Once the Pareto front is sampled, the "optimality" of the solutions is to be evaluated *a posteriori* depending on the preferred application. In other words, it is up to the end-user, or decision maker, to determine what is the best trade-off between the predefined objectives. In our case, we are interested in generating beams with a large field depth. As illustration, the configuration in Fig. 5.3b offers the most accurate reproduction of a Hermite-Gauss beam profile (smallest obtained value of f_1). However, the non-uniformity of the phase front results in a poor field depth. On the other hand, the configuration in Fig. 5.3c exhibits a better field depth, keeping a Hermite-Gaussian profile over a greater distance. This solution would likely have been "missed" in the single-objective case. This last point is crucial in the optimization problem. In selecting a multi-objective versus a

single-objective calculation, one must keep in mind that the former offers a much greater diversity and density of solutions. For instance, we found that replacing the integrand of the single-objective function g_1 by $|\varphi(x_0, y) - \bar{\varphi}(x_0, y)|^2$ for the coherent problem, we could only reach a much smaller and less optimal subset of solutions.

5.4 Conclusion

In summary, we propose the use of the PTS algorithm for combinatorial optimization problems in integrated photonics. We show that PTS finds some optimal solutions faster than the standard GA for the specific problem of beam shaping using a 2D photonic lattice. Moreover, the tabu method involves fewer adjustable parameters, allowing for a straightforward implementation. Using this improved algorithm, we have reported the possibility to control the coherent profile (amplitude and phase) of the output beam. Our results show that multiobjective optimization in integrated photonics design is within reach and that a PTS algorithm offers an efficient alternative to the standard GA.

5.5 Authors' contributions

DG designed the study, carried out the analysis, wrote the numerical codes, performed the computations and wrote the first version of the manuscript. All authors have contributed to the analysis and have been instrumental in bringing the original manuscript to a publishable research contribution.

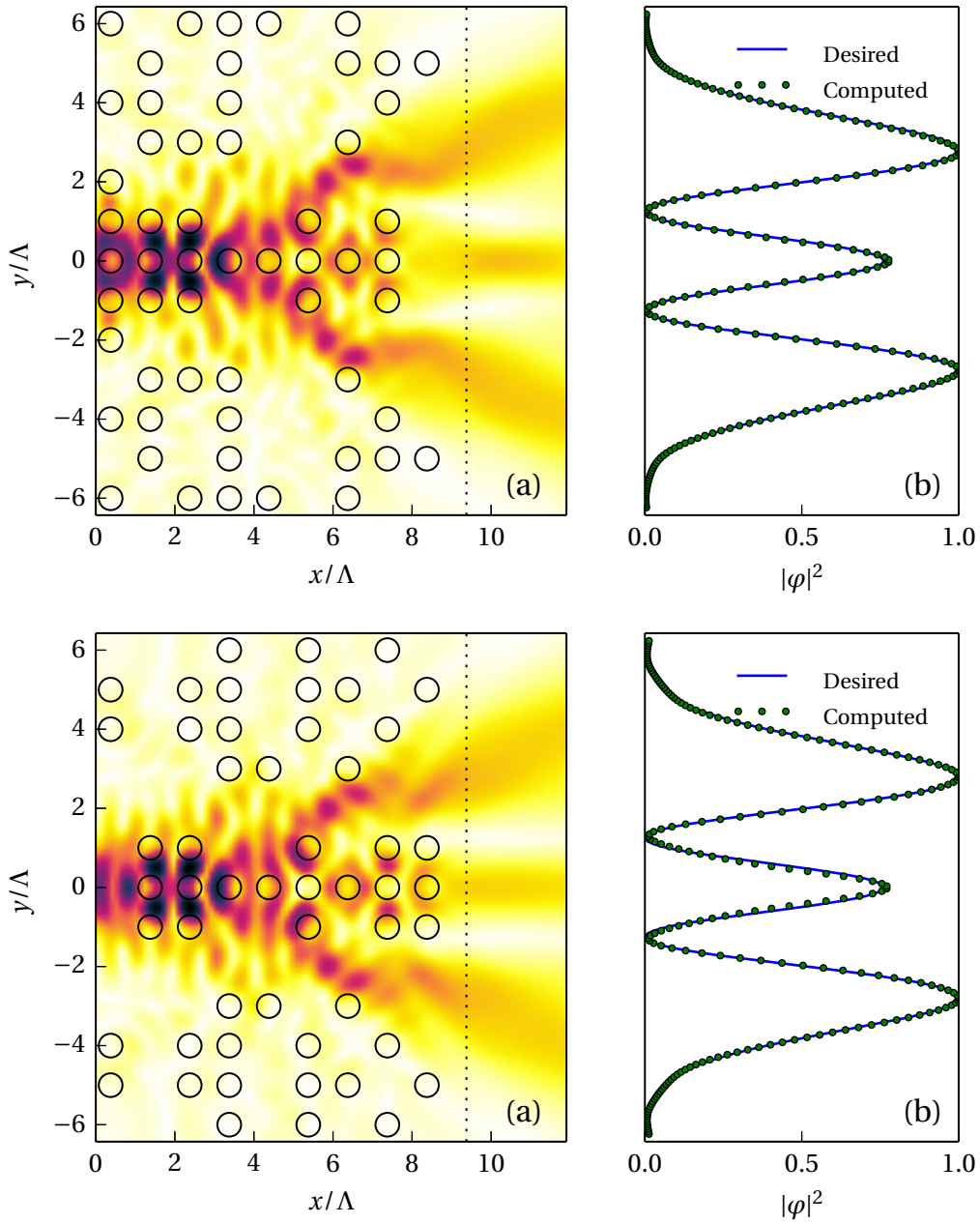

Figure 5.4 – Generation of coherent order 2 Hermite-Gauss beam. The target plane is indicated by a dashed line. Arbitrary intensity units. (Top) Optimized configuration characterized by (f_1 = 0.0167, f_2 = 0.1019, η = 0.836, N = 56). (Bottom) Optimized configuration characterized by (f_1 = 0.0255, f_2 = 0.0833, η = 0.842, N = 52).

5.6 Supplement I: Lattice configurations

In the companion piece, only the output beam profiles were given in Fig. 5.3 because of space constraints. For convenience, the configurations and full amplitude profiles are reproduced in Fig. 5.4.

5.7 Supplement II: Multiobjective optimization with wider beams

This supplement contains additional results concerning multiobjective optimization using photonic lattices. Specifically, additional computations are carried out in the same wavelength regime as the main contribution, but for less divergent input and target beams. The main goal is to use more realistic beams in the computations, since the largely non-paraxial beams used in the main contribution may be hard to produce in the laboratory [16].

5.7.1 New geometry and input beam

The angle of divergence θ of a GB is related to its wavelength λ and waist diameter w_0 by the following relation

$$\theta = \frac{\lambda}{\pi w_0}. \tag{5.7.1}$$

The consequence of this definition is that, in order to reduce the beam divergence at a given wavelength, its waist diameter, or width, must be increased. In the following supplement, we attempt to reduce this divergence angle by doubling the width of the incident beam, as well as requiring a similarly wide target beam. The angle of divergence of a GB is also related to its Rayleigh distance x_R by [127]

$$\theta = \sqrt{\frac{2}{k x_\mathrm{R}}}. \tag{5.7.2}$$

Consequently, in 2D-GLMT computations, reducing the divergence angle by a factor 2 amounts to quadrupling the Rayleigh range of the incident complex-source beam (CSB). In order to accommodate the increased beam width, we use a somewhat larger grid in our computations. Figure 5.5a shows the geometry used for multiobjective computations in the main contribution. The grid used in this supplement is shown in Fig. 5.5b. Taking a mirror symmetry into account, the size of the solution space accordingly increases from 2^{70} to 2^{90} possible solutions.

Before performing the usual multiobjective optimization procedure, we assess the performance of PTS when applied to this larger space by performing single-objective optimization. Figure 5.6 shows that PTS needs more iterations to explore this rather large solution space, on the order of 60 000 iterations. In comparison, the "small grid" only required about 20 000 iterations to converge to acceptable values of (g_1, g_2). The objective function distribution of a set of 48 parallel tabu processes after 65 000 iterations is shown on Fig. 5.7.

Having assessed the performance of PTS, we now center our attention on generating beams with larger field depths. We perform multiobjective optimization, requiring a Hermite-Gauss beam profile of order 2 with twice the width used in the main contribution ($w_0 = 5\Lambda$). To improve the overall quality of solutions, the configurations found after 45 000 monoobjective tabu iterations (amplitude-only) are used as starting points for multiobjective runs. Four different values of the

16. However, the possibility to generate beams characterized by very small beam waists using a cleaved integrated waveguide is discussed in section 5.9.

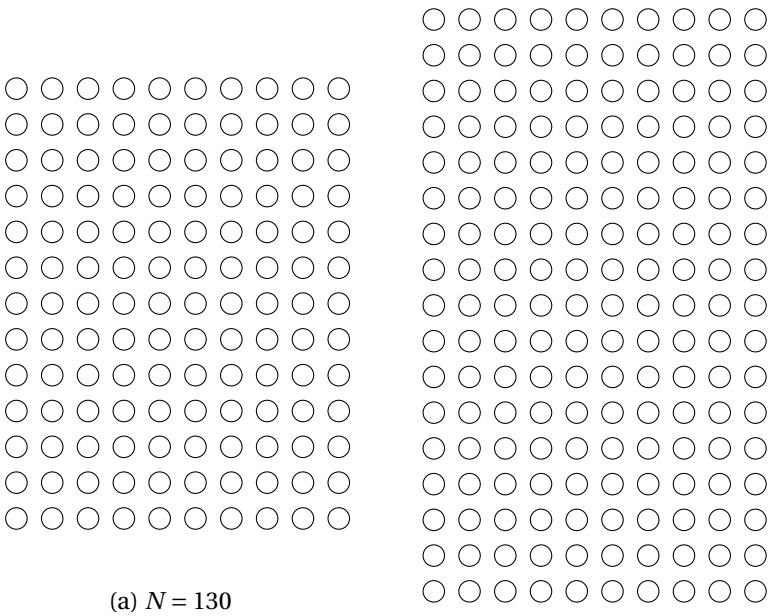

(a) $N = 130$

(b) $N = 170$

Figure 5.5 – Basic photonic lattice configurations used for beam shaping computations. (a) Configuration used in our previous work for multiobjective optimization in the main contribution. (b) Configuration used in this supplement to accommodate the wider incident beam.

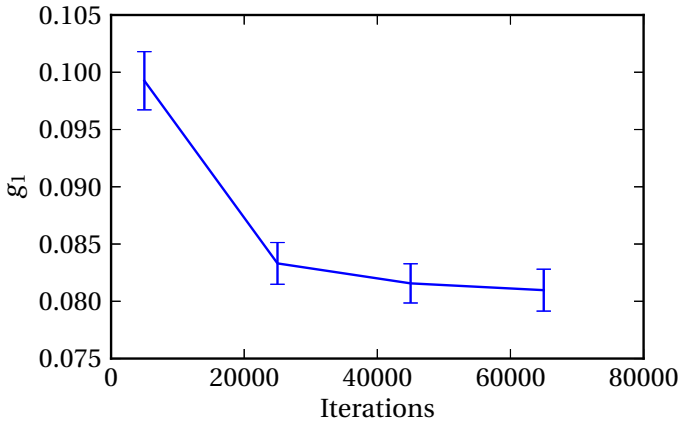

Figure 5.6 – Assessment of the convergence of a set of 48 PTS processes, using the wider grid (Fig. 5.5b). For this specific problem, the computational cost is about 18 hours (860 CPU hours) per 10 000 iterations.

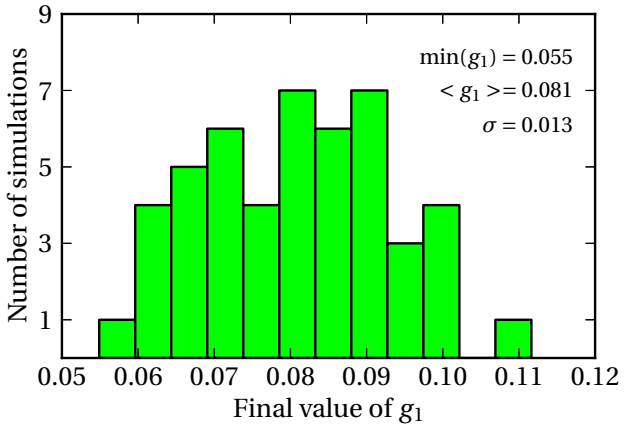

Figure 5.7 – Distribution of the final value of g_1 for a set of 48 PTS processes after 65 000 iterations, using the wider grid (Fig. 5.5b).

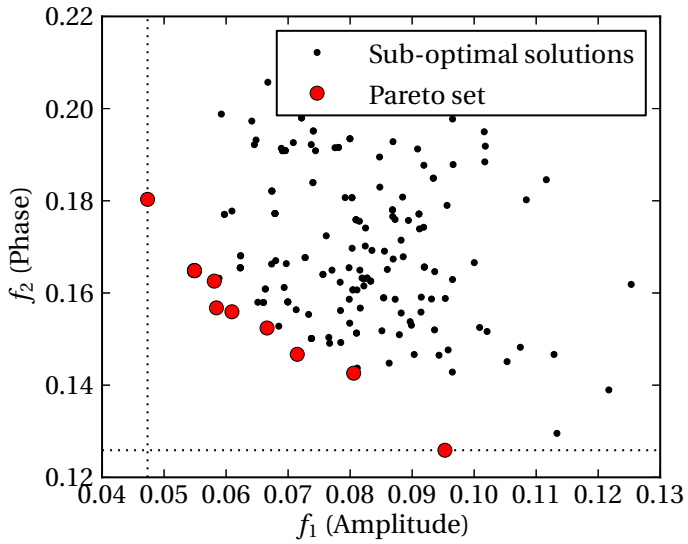

Figure 5.8 – Sampling of the Pareto front of the multiobjective problem for the wider grid (Fig. 5.5b).

relative weights are used in PTS runs involving 48 parallel processes. This represents about 9000 CPU hours (~ 1 core-year). The resulting Pareto front is shown in Fig. 5.8. The number of solutions found is similar to that composing the Pareto front shown in Fig. 5.3. However, the final values of f_2 are higher by a factor of 2 in the case of the wider input beam.

The output beams generated by the configurations forming the Pareto front are plotted in Fig. 5.9. The higher values of f_2 translate into oscillations in the phase front. This results in substantial deterioration of the transverse profile as the beam propagates, as compared to the main contribution. This can be seen in the large number of ridges appearing in the transverse profile after propagation over a few units of Λ. The appearance of an effective "focal point" can also be seen in the output profiles. An attempt is made to explain this focusing effect in the next section (§5.7.2).

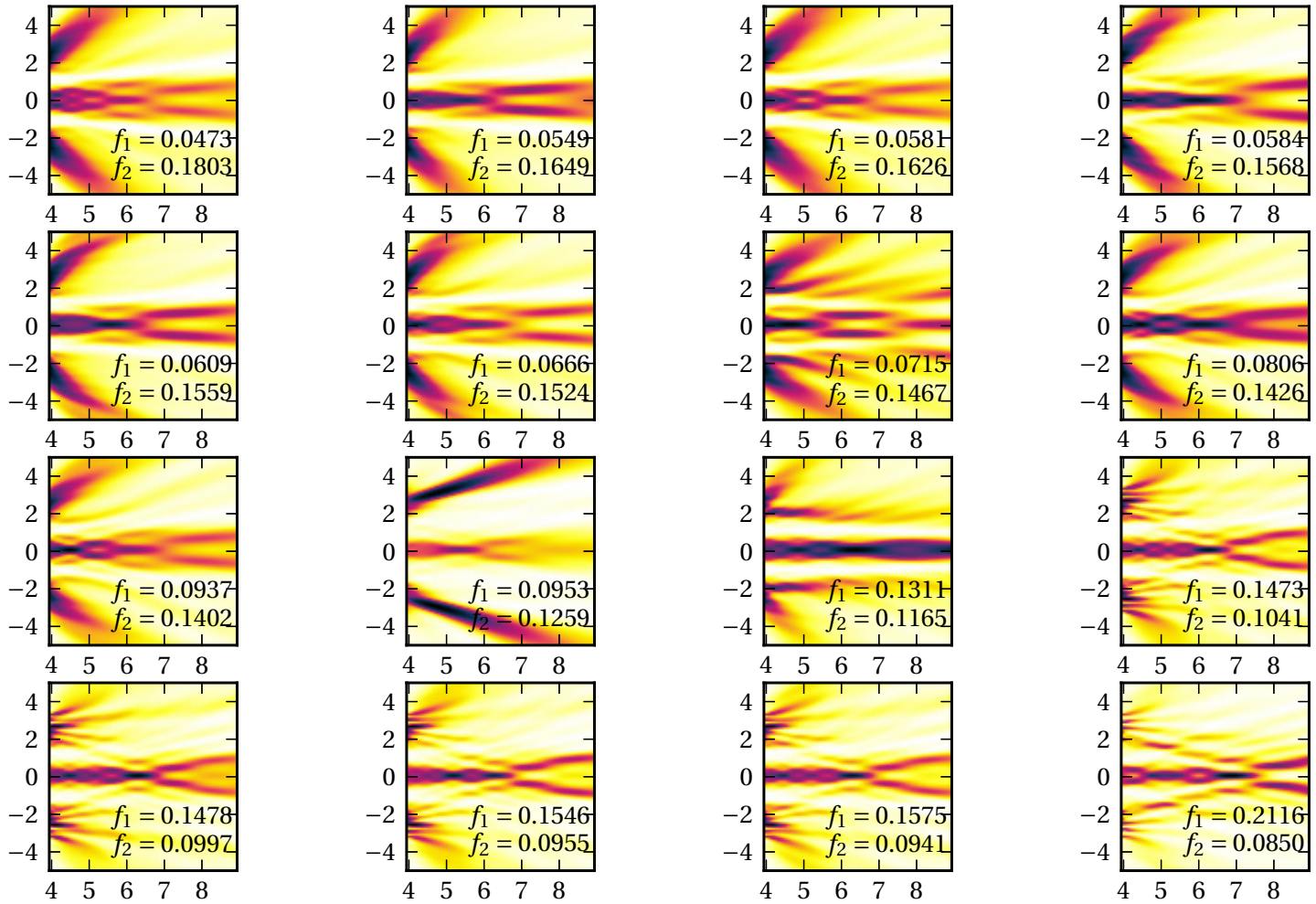

Figure 5.9 – Beam profiles corresponding to all configurations found on the sampled Pareto set for the wider grid (Fig. 5.8). Axis are in units of lattice constant Λ.

5.7.2 Self-collimation effect in photonic crystals

Photonic crystals are known to exhibit a phenomenon of self-collimation [146]. This collimation results from the periodic modulation of the refractive index in the direction perpendicular to the beam propagation axis, and can be exploited to create PhC lenses [92, 94]. To sum up, the focusing regime occurs at frequencies (or wavenumbers) between the corner of the first Brillouin zone ω_{BZ} and the so-called *self-collimation* frequency ω_{SC}. At this frequency, waves propagate in the photonic crystal in a diffraction-less way. Supposing a propagation along the x axis, the diffraction can be related to the second derivative of the band curves in the following way [124, 146]

$$\mathscr{D} = \frac{d^2\omega}{dk_x^2}, \tag{5.7.3}$$

where k_x is the x component of the wavevector $\mathbf{k}$. Focusing occurs in the anomalous diffraction regime ($\mathscr{D} > 0$). This corresponds to a situation where the wavefronts of the beam exiting the PhC are concave, thus leading to a focal point located behind the PhC. In the normal diffraction regime ($\mathscr{D} < 0$), the wavefronts are convex and no focusing is expected. Consequently, the self-collimation frequency can be identified as an inflection point in the transmission bands ($\mathscr{D} = 0$). In short, if the diffraction $\mathscr{D}$ is of opposite signs at both edges of a transmission band, there must be an inflection point somewhere in between where self-collimation occurs, and there should exist a focusing regime, that is a frequency range for which $\mathscr{D} < 0$.

5.7.3 Focal points in beam shaping computations

Let us investigate further the band structure (Fig. 5.10a) of the PhC geometry used in chapters 4 and 5. Let us also concentrate on wavevectors comprised between the Γ and X points, that is $0 < k_x < k_0$. This corresponds to propagation along the x axis. Looking at a snapshot of the second TM band, one can see that ($\mathscr{D} < 0$) at the Γ point and ($\mathscr{D} > 0$) at the X point. As expected, there exists an inflection point in between at a normalized frequency $k_0\Lambda = 1.727$ (Fig. 5.10b). This is the self-collimation frequency. One can expect focusing for normalized frequencies in the range $1.727 < k_0\Lambda < 2.361$. Somewhat coincidentally, all computations performed in chapters 4 and 5 used $k_0\Lambda = 1.76$ which falls in the focusing regime. This may explain the appearance of effective "focal points" in the output profiles shown in Fig. 5.9.

In order to mitigate the effect of the focusing effect on beam shaping computations, we performed another multiobjective run using the same basic geometry and beam widths, but a normalized frequency $k_0\Lambda = 1.25$, outside the focusing regime. Results are shown in Figs. 5.11 and 5.12. The output profiles can be found to be somewhat smoother in that case (smaller values of f_1), but at this point we do not find a guarantee that focal spots can be eliminated by getting out of the self-collimation regime. Of course, the Bloch modes expansion does not hold in the case of the irregular configurations optimized via metaheuristics algorithms, but this picture seems to give a qualitative guideline to get smoother output profiles and mitigate the presence of focal spots.

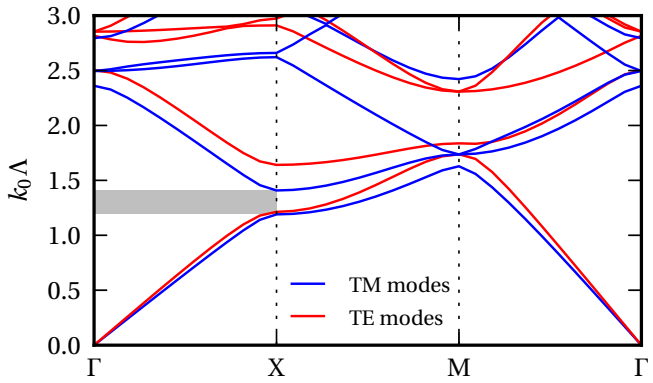

(a) Band structure along high symmetry points of the first Brillouin zone. The location of a partial bandgap in the Γ–X direction is shaded. The band structure is identical to that of Fig. 4.2.

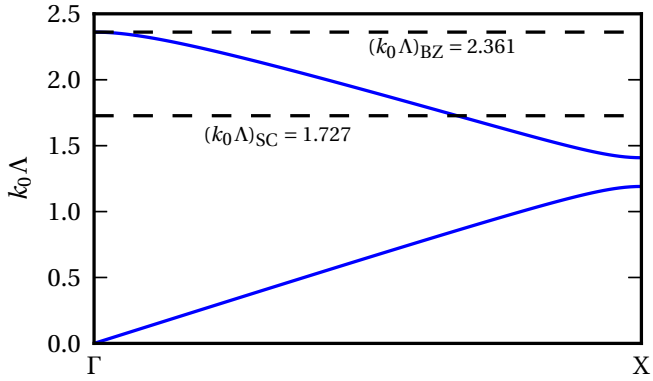

(b) Identification of an inflection point in the second TM transmission band. The location of the self-collimation frequency and the frequency at the Brillouin zone corner are indicated by dashed lines.

Figure 5.10 – Band structure for a square lattice of air holes of radius $r = 0.3\Lambda$ in a dielectric medium with refractive index $n = 2.76$. Eigenmodes were computed using the MIT PHOTONIC BANDS software package [73].

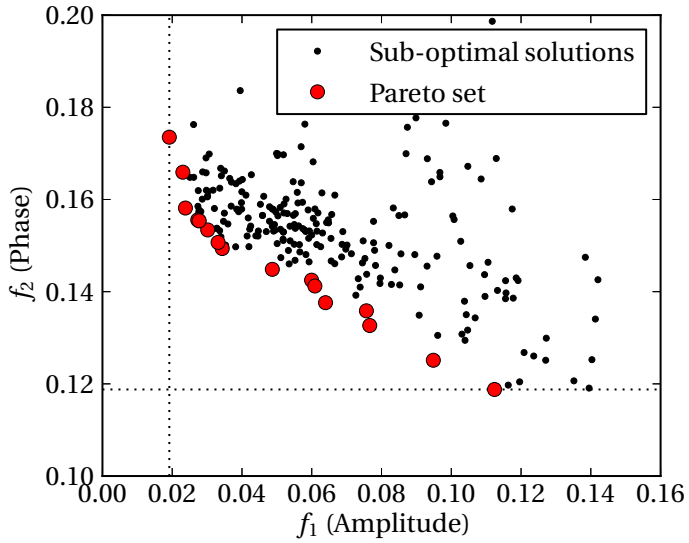

Figure 5.11 – Sampling of the Pareto front of the multiobjective problem for the wider grid with $k_0\Lambda = 1.25$.

It is also unclear why we get smoother profiles in the case of smaller beam widths, as found in chapters 4 and 5. We can speculate that this is partly due to the fact that a larger basic lattice has to be used for larger beams. This means the final lattice configurations are closer to a regular lattice, thus giving rise to long-range order effects, such as self-collimation. Nevertheless, those results highlight the importance of sampling many possible "optimal" solutions of the optimization problem before making a final decision on which output profile is the best for a given purpose.

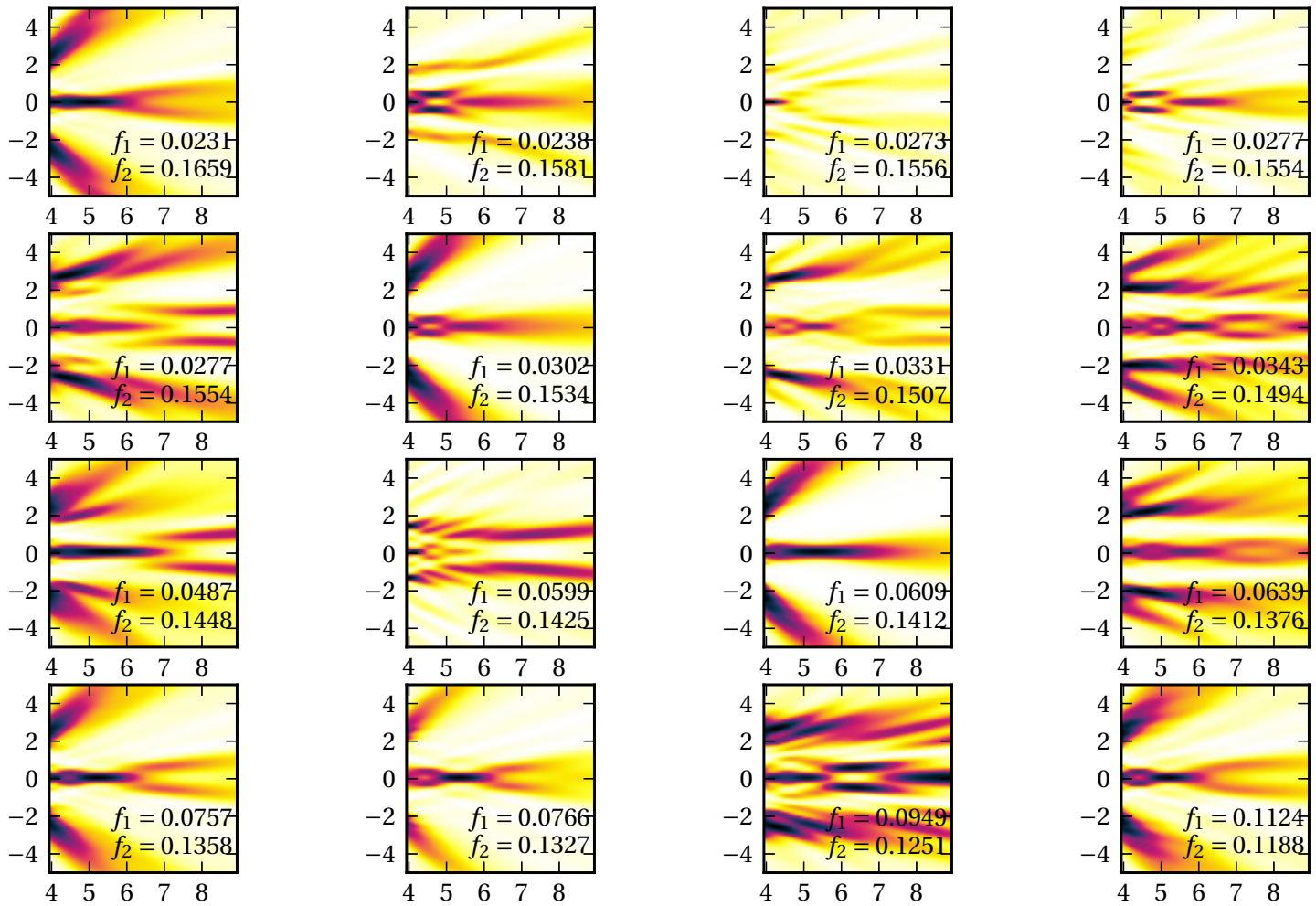

Figure 5.12 – Beam profiles corresponding to all configurations found on the sampled Pareto set with $k_0\Lambda = 1.25$ (Fig. 5.11). Axis are in units of lattice constant Λ.

5.8 Supplement III: Lensing using a finite rods-in-air type photonic crystals

In section 5.7.2 of this supplement, we described the phenomenon of self-collimation in PhCs. Self-collimation was subsequently deemed to be potentially detrimental to beam shaping devices in section 5.7.3. However, this effect could be beneficial if we consider applications other than beam shaping, for instance lensing. To illustrate this, this section numerically demonstrates the possibility of designing a convergent lens using a finite-sized PhC.

In order to obtain a focused TM-polarized beam, we use a rods-in-air photonic crystal. The refractive index of the rods is set to $n = 2$, and their radius is set to $r = 0.3\Lambda$. The band structure of this PhC geometry is shown in Fig. 5.13. According to the previous analysis (§5.7.2), one can expect focusing for normalized frequencies in the range $3.39 < k_0\Lambda < 4.18$. To verify this hypothesis, we performed 2D-GLMT computations at different normalized frequencies using a 31×12 ($N = 372$) finite crystal illuminated by a GB. The width of the incident GB was kept at a constant value of $w_0 = 3\Lambda$. The consequence of this is that the Rayleigh distance of the GB varies with the normalized frequency (compare Eqs. 5.7.1 and 5.7.2).

It should be noted that the output beam can not be expected to have a purely Gaussian shape. Therefore, we can only define arbitrary criteria for what constitutes focusing behavior. In the case of our computations, we define focusing as occurring if a *waist plane* can be observed after the output plane of the finite crystal. Specifically, we define the waist as the plane of maximal irradiance located after the output plane. If this plane coincides with the output plane, this means the output beam is divergent and no focusing occurs. The scattering computation shown in Fig. 5.14a is performed in the normal diffraction regime ($\mathscr{D} > 0$). As expected, no waist plane can be observed. At higher values of the normalized beam frequency, a waist plane can be observed as the output beam changes from divergent to convergent (see Fig. 5.14b). However, it should be noted that the first occurrence of self-collimation, or focusing, does not coincide exactly with the inflection point ($\mathscr{D} = 0$) shown in Fig. 5.13b. A similar observation was made in a recent publication [124]. The authors of this paper state that "there seems to be a trade-off between operating at the inflection point and as far away from the band edge as possible". In other words, the presence of an inflection point in a transmission band should not be seen as providing an exact prediction of the frequency range corresponding to the focusing regime, but rather as providing a design rule for PhC lenses.

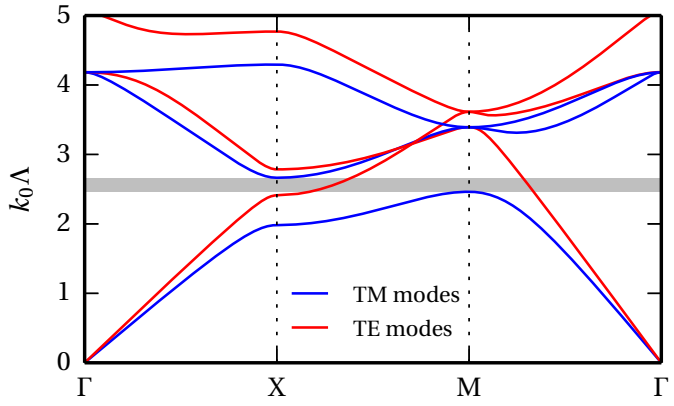

(a) Band structure along high symmetry points of the first Brillouin zone. The location of a bandgap between the first two TM propagation bands is shaded.

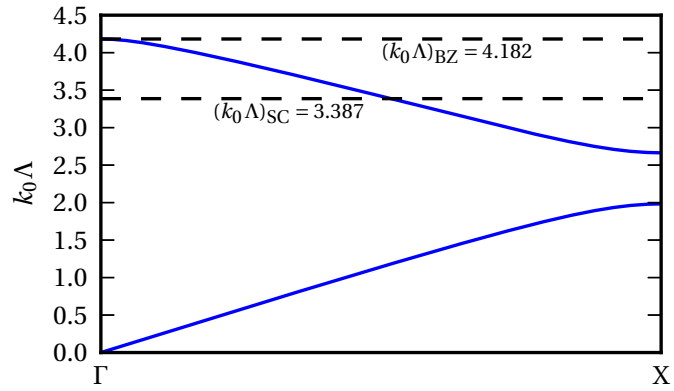

(b) Identification of an inflection point in the second TM transmission band. The location of the self-collimation frequency and the frequency at the Brillouin zone corner are indicated by dashed lines.

Figure 5.13 – Band structure for a square lattice of rods in air of radius $r = 0.3\Lambda$ and refractive index $n = 2.00$. Eigenmodes were computed using the MIT PHOTONIC BANDS software package [73].

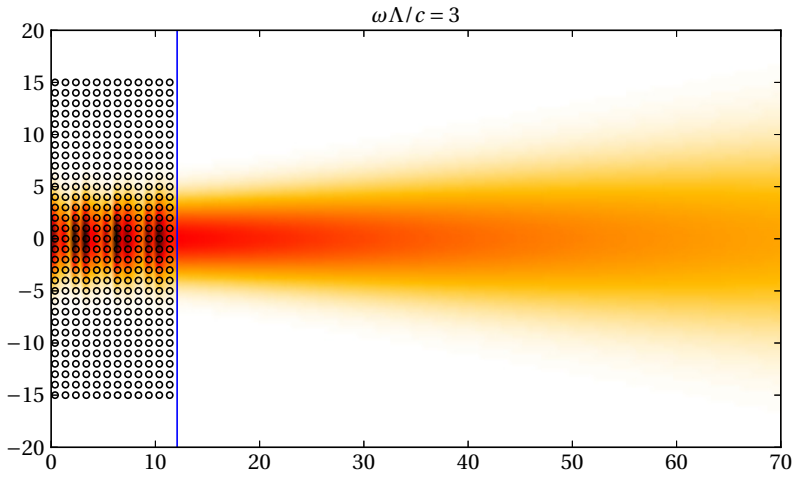

(a) $\mathscr{D} > 0$

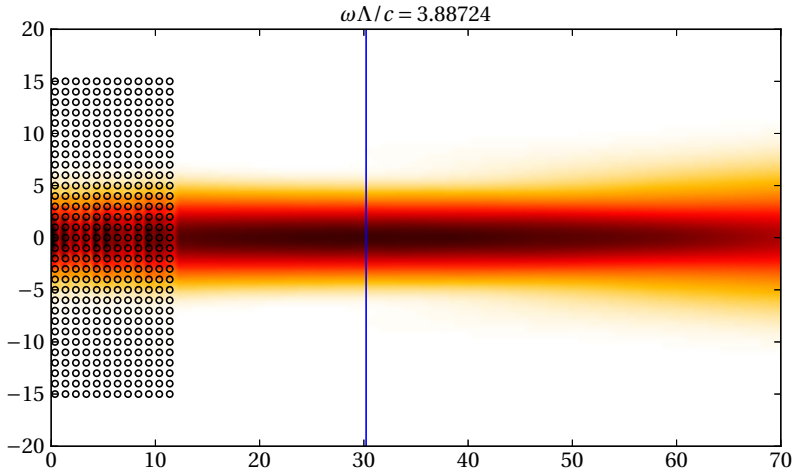

(b) $\mathscr{D} < 0$

Figure 5.14 – Transformation of a Gaussian beam by a rods-in-air type lattice in the second transmission band. Axis are in units of lattice constant Λ. The vertical line indicates the location of the transmitted beam waist plane.

5.9 Supplement IV: Remarks on the experimental realization of beam shaping devices

Electron-beam lithography [94] and deep UV lithography [161] and are two of the most commonly used microfabrication techniques for silicon-on-insulator optical devices. These techniques typically exhibit experimental deviations smaller than 10 nm. [94, 161]. Since these deviations are not taken into account in the optimization procedures used in this thesis, the goal of this supplement is to assess their impact on the functionality of the proposed devices. In other words, we examine the tolerance of optimized photonic lattice configurations to the limitations of fabrication processes.

To quantify this tolerance, we consider random variations in the position and radius of the individual scatterers of configurations found via metaheuristic algorithms. Let x_i be a length parameter describing a scatterer (for instance its position or diameter). We suppose Gaussian deviations from the mean geometric parameters, that is $x_i' = x_i + \delta x_i$, where is δx_i is a normally distributed random variable. The probability density function of δx_i is given by

$$f(\delta x_i; \mu_i, \sigma_i) = \frac{1}{\sigma_i \sqrt{2\pi}} \exp\left[\frac{(\delta x_i - \mu_i)^2}{2\sigma_i^2}\right]. \tag{5.9.1}$$

For the purpose of this study, we will center our attention the basic geometry shown in Fig. 5.5a, that is a 13×10 square grid of scatterers with mirror symmetry, resulting in 2^{70} possible configurations [46]. The geometric parameters of the grid as well as the incident beam are detailed in Table 5.1.

Consider the optimized configuration shown in Fig. 5.15a, obtained via PTS. To assess the tolerance of this configuration to fabrication imperfections, we compute the value of the objective function g_1 for various test configurations (an example is shown in Fig. 5.15b). First, we suppose Gaussian deviations from the mean position of every scatterer, with average values $\mu_i = 0$, while keeping the scatterers radii unchanged. We then consider a similar deviation of the radius of every scatterer, but keeping their positions unchanged. Every scatterer is randomly affected independently of each other, and all scatterers are affected in every test configuration. The result of those computations is shown in Fig. 5.16. One can see the increasing average values and standard deviations of g_1 as a function of the standard deviations σ_i used in computations.

It is possible to compare the results of those computations to typical experimental variations found in the literature [17]. For instance, the fabrication of corrugated Bragg gratings in a silicon ridge waveguide was recently reported, with typical deviations of the corrugation width on the order of 10 nm [161]. In this work, deep UV lithography is used to fabricate the devices [161]. Moreover, the fabrication of silicon integrated photonic lenses based on holes in a waveguide core was recently reported [94], with primitive hole matrices similar to those used in this thesis. In this work, electron-beam lithography was used to engrave the holes [94]. The experimental deviation from

17. For definiteness, we use the real-world values found in the last column of Table 5.1.

the mean of the holes radii was reported to be between 1 and 5 nm [94]. Based on those reports, we shall suppose a deviation from the mean between 1 and 10 nm for the holes positions, and 1 and 5 nm for the holes radii. Those ranges are indicated by shaded regions in Fig. 5.16. These results show that optimized designs are moderately tolerant to fabrication imperfections. Indeed, the maximal reported experimental deviations imply an increase of the objective function g_1 by a factor between 2 and 5.

Table 5.1 – Geometric and wave parameters used in beam shaping computations

Parameter	Value	Value at $\lambda = 1.55$ µm
Lattice constant	Λ	0.434 µm
Lattice depth	10Λ	4.342 µm
Lattice height	13Λ	5.644 µm
Wavelength	$\lambda = 2\pi\Lambda/1.76$	1.55 µm
Holes radius	$r = 0.3\Lambda$	0.130 µm
Width of incident beam	$w_0 = 2.5\Lambda$	1.085 µm
Effective index of waveguide core	n	2.76

It should be noted that the beam shaping elements proposed in this dissertation do not necessarily imply freely propagating input and output beams. Indeed, it is possible to create beams with a very small waist size using integrated input and output waveguides, as demonstrated experimentally by Xu *et al.* [171]. Moreover, the field emitted by a cleaved waveguide can be modeled by a Gaussian beam as proposed by Okamoto [106, p. 41]. In this reference, it is stated that the radiation pattern of an integrated waveguide with a width of 1.5 µm, refractive index $n = 3.5$ operating at $\lambda = 1.55$ µm can be approximated by a Gaussian beam with a width of $w_0 = 800$ nm [106, p. 46]. This is on the order of the input beam width given in Table 5.1. Consequently, the relatively small beam widths used in our computations could be viewed as being created by integrated waveguides and not as propagating in free space, save for a very short distance from the device input.

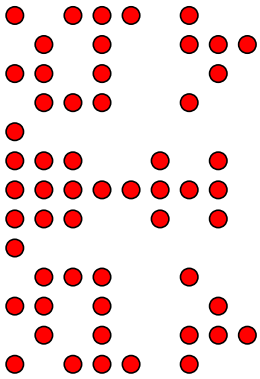

(a) Optimized configuration ($N = 56$)

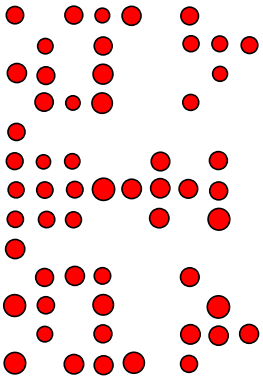

(b) Test configuration with perturbations

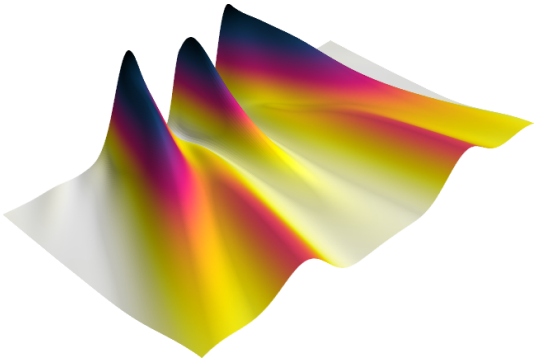

(c) Resulting profile ($g_1 \simeq 2\%$)

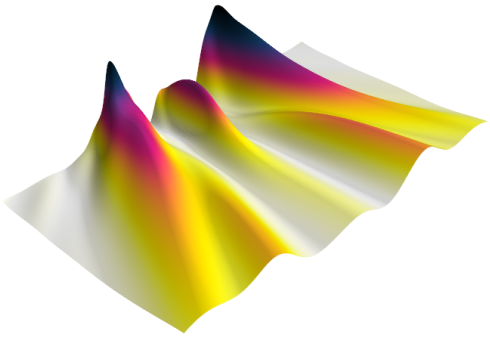

(d) Resulting profile, with perturbations ($g_1 \simeq 30\%$)

Figure 5.15 – Test configuration for tolerance assessment. (a) Lattice configuration optimized for the generation of a order 2 Hermite-Gauss beam profile. (b) Example test configuration with Gaussian deviations from the mean $\sigma_{X,Y} = \sigma_r = 3 \times 10^{-2} \Lambda$. (c–d) Resulting beam profiles and associated g_1 values.

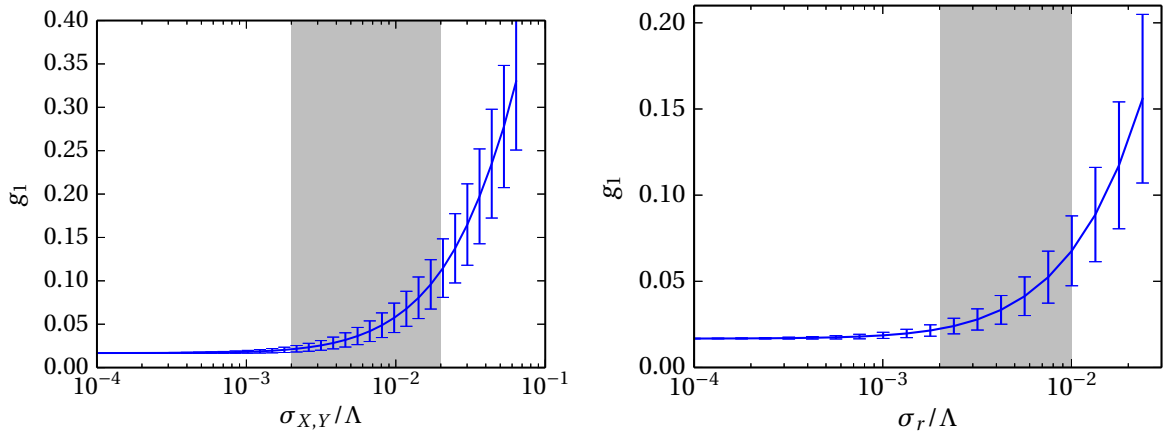

(a) Position perturbations

(b) Radius perturbations

Figure 5.16 – Tolerance of the configuration shown in Fig. 5.15a to fabrication imperfections. (a) The positions (X_i, Y_i) of individual scatterers are varied while their radii are kept unchanged. The shaded region corresponds to an experimental deviation between 1 and 10 nm for the holes positions, based on [161]. (b) The radii r_i of individual scatterers are varied while their positions are kept unchanged. Each data point represents a sample of 1000 randomized test configurations. The shaded region corresponds to an experimental deviation between 1 and 5 nm for the holes radii, based on [94]. The parameters of the lattice are drawn from Table 5.1, assuming an operating wavelength of 1.55 µm.

Chapter 6

Optimization of integrated polarization filters

Denis Gagnon, Joey Dumont, Jean-Luc Déziel and Louis J. Dubé

Département de physique, de génie physique et d'optique
Faculté des Sciences et de Génie, Université Laval, Québec G1V 0A6, Canada

Journal reference: Optics Letters, Vol. 39, pp. 5768–5771 (2014)

URL: http://dx.doi.org/10.1364/OL.39.005768
ePrint: http://arxiv.org/abs/1407.7401

Résumé

Cette étude porte sur la conception de filtres de polarisation intégrés basés sur des cristaux photoniques bidimensionnels possédant des défauts optimisés. En utilisant une grille de piliers diélectriques placés dans l'air pour la réalisation d'un filtre TE et une grille d'inclusions dans un substrat diélectrique pour la réalisation d'un filtre TM, nous sommes en mesure de maximiser le degré de polarisation du faisceau de sortie jusqu'à 98 %, tout en maintenant une efficacité de transmission supérieure à 75 %. Les designs proposés constituent non seulement des filtres logiques de polarisation, mais peuvent également être optimisés afin d'émettre un faisceau de sortie de profil arbitraire. Les filtres sont optimisés au moyen d'un algorithme d'optimisation récemment proposé (PTS) pour la conception d'éléments optiques intégrés.

Abstract

This study reports on the design of small footprint, integrated polarization filters based on engineered photonic lattices. Using a rods-in-air lattice as a basis for a TE filter and a holes-in-slab lattice for the analogous TM filter, we are able to maximize the degree of polarization of the output beams up to 98 % with a transmission efficiency greater than 75 %. The proposed designs allow not only for logical polarization filtering, but can also be tailored to output an arbitrary transverse beam profile. The lattice configurations are found using a recently proposed parallel tabu search (PTS) algorithm for combinatorial optimization problems in integrated photonics.

6.1 Introduction

Polarization is a physical dimension of light that can be exploited to increase the rate of transmission of information in optical communications [168]. For instance, polarization beam-splitters based on modal birefringence in integrated waveguides may enable transmission rates up to 400 Gbps in optical networks [113]. Integrated polarization manipulation is also critical to accelerating electrons using dielectric structures [16]. These examples are but a small sample of important applications that have moved the design of integrated elements dedicated to polarization management to the forefront of photonics research. Some existing solutions for tailoring the polarization of light at the microscale level include subwavelength gratings [20, 100], chains of coupled optical microspheres [26], Raman processes [170], metasurfaces [8] and photonic crystals [27, 114]. In parallel to these developments, various photonic crystal (PhC) inspired devices have also been proposed, such as near-field beam shapers [44, 46, 158], lenses [94, 130], waveguide bends [169] and waveguide couplers [3]. The design process of these nanophotonic devices is almost always based on the optimization of a primitive PhC lattice – or grid of scatterers – using *metaheuristics*, optimization algorithms based on empirical rules for exploring large solution spaces [149].

The aim of this Letter is to optimize small footprint integrated devices combining two function-

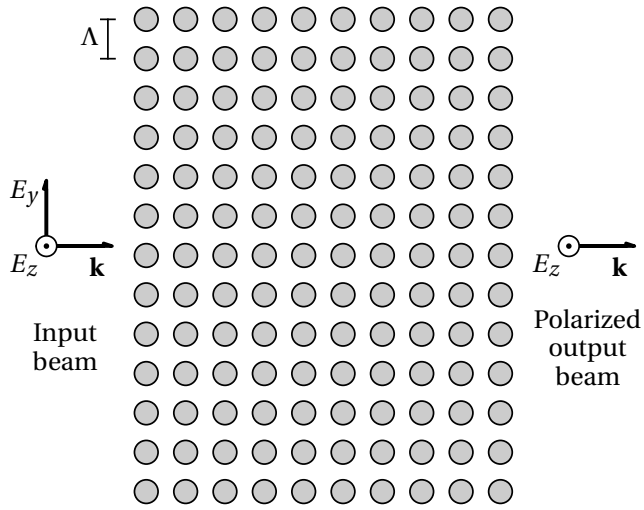

Figure 6.1 – Schematic representation of the basic photonic lattice configuration and the polarization optimization problem. In this example, the E_y component of the incident beam is filtered out, resulting in a TM polarized beam. For a TE polarized beam, replace (E_z, E_y) by (H_z, H_y). The final optimized design will consist of occupied or empty scattering sites.

alities: beam shaping and polarization filtering. We show that two basic scatterer grids can be used for this purpose, namely a rods-in-air (RIA) lattice for TE polarization filtering and a holes-in-slab (HIS) lattice for TM polarization filtering. This choice is motivated by the band structure of each basic photonic lattice. Moreover, the polarization filters proposed are experimentally feasible as RIA lattices can be fabricated routinely using electron beam lithography of amorphous silicon films [171], and HIS lattices can be produced by etching inclusions in a high refractive index membrane of semiconductor material [27].

Although polarization selective beam-splitters based on PhC bandgaps have been demonstrated in the past [114], our designs allow not only for logical polarization filtering, but are also specifically tailored to preserve the beam shape or to transform it to specification at the device output. Our approach consists in using a metaheuristic algorithm, *parallel tabu search* (PTS), to optimize a basic photonic lattice in order to achieve the required functionality [46], a polarized beam with a definite shape at the device output. This will be demonstrated by the generation of quasi-Gaussian polarized beams at the near-field of the device.

6.2 Configuration space and optimization problem

Before proceeding with the optimization problem, it is critical to choose an adequate configuration space, in other words a basic photonic lattice. In this Letter, we use a 10×13 lattice as shown in Fig. 6.1. This geometry defines two privileged directions, namely the direction parallel to the scatterers' axis (the z-axis) and the beam propagation axis (the x-axis). The configuration space is specified by the fact that we only allow individual scattering sites to be occupied or empty in the

final design, resulting in 2^{70} possible solutions taking a mirror symmetry into account. This basic lattice geometry was successfully used in a previous optimization study, for the conversion of a Gaussian beam to coherent Hermite-Gauss type beams [46].

To obtain a TM polarized output beam ($E_y = 0$), we choose the HIS design, whereas to obtain a TE polarized beam we adopt the RIA design. These choices are motivated by the band structure of both photonic lattices. As can be seen from Fig. 6.2, the HIS lattice exhibits a wider directional bandgap for the TE polarization in the $\Gamma - X$ direction. This implies that the TE component of the beam (E_y) is more strongly scattered, making the HIS lattice suitable for filtering this polarization out and favoring the TM polarization. For the device to operate near that bandgap, the radius of all air holes is set to $r = 0.3\Lambda$, where Λ is the lattice constant. We use an effective refractive index $n = 2.76$, corresponding to a thin silicon slab at $\lambda \sim 1.5\,\mu$m [22]. In contrast, we choose a RIA lattice for the TE polarizer with the rods refractive index set to $n = 3.3$. Similarly, this lattice exhibits a bandgap for the TM polarization, meaning that it strongly scatters the TM component of the beam (H_y). The incident beam wavenumber is set to $k_0 = 1.76/\Lambda$, with a half-width $w_0 = 2.5\Lambda$. Such a beam could in principle be generated using an integrated waveguide [171]. The value of k_0 is chosen to fall near the bandgap of both HIS and RIA lattices. Although the Bloch modes expansion yielding the band diagrams does not strictly hold for our final optimized configurations (as they are neither periodic nor infinite), this approach provides a useful design tool for polarization filters. Moreover, integrated polarization selective beam splitters based on PhCs have been reported to exhibit an effective bandgap despite only three rows of scatterers being present in the final design [27, 114].

Once the solution space has been defined, the next step is to formulate the optimization objectives. The problem consists in finding a lattice configuration which, when illuminated with a Gaussian input beam, produces a polarized beam that also matches a specific Gaussian profile in a given target plane, although in principle both the input and output profiles can be arbitrary [44, 46]. In two dimensions, this beam shaping problem can be formulated as the minimization of the following objective function [30, 44]

$$g_1 = \frac{\int ||\varphi_z(x_0, y)|^2 - |\bar{\varphi}_z(x_0, y)|^2| dy}{\int |\bar{\varphi}_z(x_0, y)|^2 dy}, \tag{6.2.1}$$

where x_0 is the location of the target plane, $\varphi_z(x_0, y)$ is the computed EM field on the target plane (either E_z for a TM polarizer or H_z for a TE polarizer) and $\bar{\varphi}_z(x_0, y)$ is the required beam profile at the device output. For a given configuration, the resulting beam profile $\varphi_z(x_0, y)$ can be computed using a two-dimensional generalized Lorenz-Mie theory (2D-GLMT). This computation method – the speed of which is crucial to the optimization procedure – is detailed in Refs. [33, 44, 103].

To obtain a polarized output beam, another objective function related to the degree of polarization $\mathscr{P}$ of the output beam must be optimized. We use the following definition [2]

$$\mathscr{P} = \frac{\int \langle S_x(x_0, y)\rangle_z dy}{\int \langle S_x(x_0, y)\rangle_z dy + \int \langle S_x(x_0, y)\rangle_y dy} = \frac{P_z}{P_{\text{tot}}}, \tag{6.2.2}$$

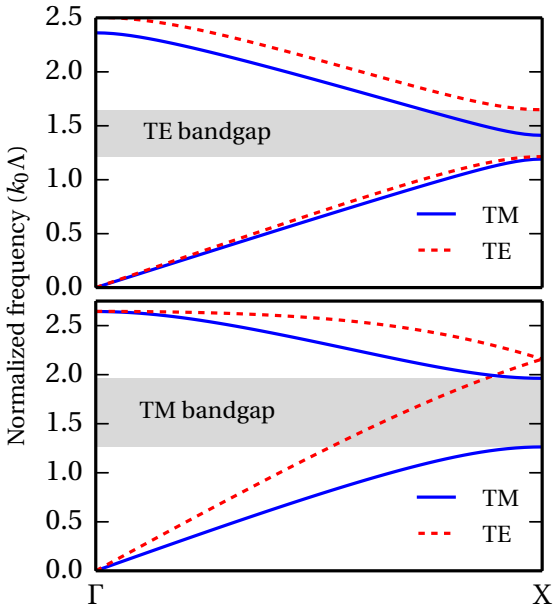

Figure 6.2 – Band structure for two different square lattices of cylinders (radius $r = 0.3\Lambda$). (Top) HIS configuration with refractive index of slab $n = 2.76$. (Bottom) RIA configuration with rods of refractive index $n = 3.3$ embedded in air. Eigenmodes were computed using the MIT PHOTONIC BANDS software package [73].

where $\langle S_x \rangle_{z,y}$ is the x component of the time-averaged Poynting vector, i. e. the power transmitted through the target plane ($x = x_0$). The (z, y) subscripts represent the contribution of each orthogonal polarization to the Poynting vector. The ratio $\mathscr{P}$ is therefore equal to the power carried by the polarized portion of the beam P_z divided by the total power contained in both polarizations P_{tot}. To obtain a perfectly TM (TE) polarized beam, the contribution of the E_z (H_z) component must be maximized at the target plane (maximum possible value of $\mathscr{P} = 1$). Since the device geometry does not mix polarizations, we suppose an equal incident power in both orthogonal field components, and attempt to maximize P_z. The flexibility of the 2D-GLMT approach makes the computation of the Poynting vector components a simple matter [103]. On a side note, since real structures either based on pillars or embedded in waveguides are not infinite in the $z-$direction, the modes are more accurately labeled as "quasi-TM" or "quasi-TE" because polarization mixing, however small, can indeed take place [27]. For the purpose of this work, we shall consider that no mixing occurs.

Another way of characterizing the polarization filters is by means of the ratio between the total power transmitted by the φ_z component of the field and the total power transmitted by the φ_y component. This ratio is computed from the Poynting vector components in the following way

$$R = \frac{\int \langle S_x(x_0, y) \rangle_z dy}{\int \langle S_x(x_0, y) \rangle_y dy} = \frac{P_z}{P_y}. \tag{6.2.3}$$

Finally, another quantity of interest is the power transmission efficiency η, simply defined as the ratio between the power incident in the φ_z component on the polarization filter and the output

power in the same field component [44]

$$\eta = \frac{\int \langle S_x(x_0, y)\rangle_z dy}{\int \langle S_x(x_{\text{in}}, y)\rangle_z dy}, \tag{6.2.4}$$

where x_{in} is the location of the input plane. Both R and η are useful indicators to measure the performance of the final optimized configurations.

To sum up, the optimization problem consists in minimizing the objective function g_1 while simultaneously maximizing the degree of polarization $\mathscr{P}$ over a 70 dimensional binary search space. This set of objectives constitutes a combinatorial *multiobjective optimization problem*. These problems are often tackled using *metaheuristics*, general optimization techniques which aim to provide well conditioned solutions in a reasonable amount of time [149]. Metaheuristics are sometimes called global optimization algorithms. Notable instances in photonics design include genetic algorithms (GAs) [44, 46, 94, 130, 158], differential evolution [79] and harmony search [3]. In a recent contribution, we have proposed the use of an alternative metaheuristic for combinatorial multiobjective optimization problems in photonics called *parallel tabu search* (PTS) [46]. The main feature of tabu search is that it uses an adaptive memory to escape from local minima in the solution space [53, 149]. Besides, it involves fewer adjustable parameters and relies less on stochastic operators than the more commonly used GA. The net benefit is to increase the convergence speed for the sort of optimization problems considered here [46].

6.3 Results and discussion

Using PTS, we have performed the optimization of the objectives functions $(g_1, \mathscr{P})$ in order to find lattice configurations suited for polarization filtering, i.e. the conversion of an non-polarized Gaussian beam to a polarized one. Since both objectives are not independent, the solution to this multiobjective problem is not a single configuration, but rather a set of compromises between the two objectives, the Pareto set of the problem [46, 149]. For demonstrative purposes, a Gaussian beam with a half-width $w_0 = 2.5\Lambda$ is required at the device output. However, the beam shaping procedure just described could allow for the generation of arbitrary shaped polarized beams. To obtain polarization filters exhibiting high profile accuracy and high transmission efficiency, we have only retained the Pareto solutions with $g_1 \leq 0.05$, that is an error on the output beam profile inferior to 5 %.

The two best lattice configurations found (in terms of $\mathscr{P}$) satisfying this condition are shown in Figs. 6.3 and 6.4. In both cases we are able to maximize the degree of polarization to values exceeding $\mathscr{P} = 0.980$. Alternatively, both configurations are characterized by $R \geq 48$, which means that the transmission of the preferred field component is at least 48 times higher than the filtered out component. Additionally the near-field beam shapes deviate from a Gaussian amplitude profile by less than 4.4 % and both configurations exhibit power transmission efficiencies above $\eta = 0.75$. For the TM polarization, we also found a configuration (not shown) characterized by $\eta = 0.81$, but in that

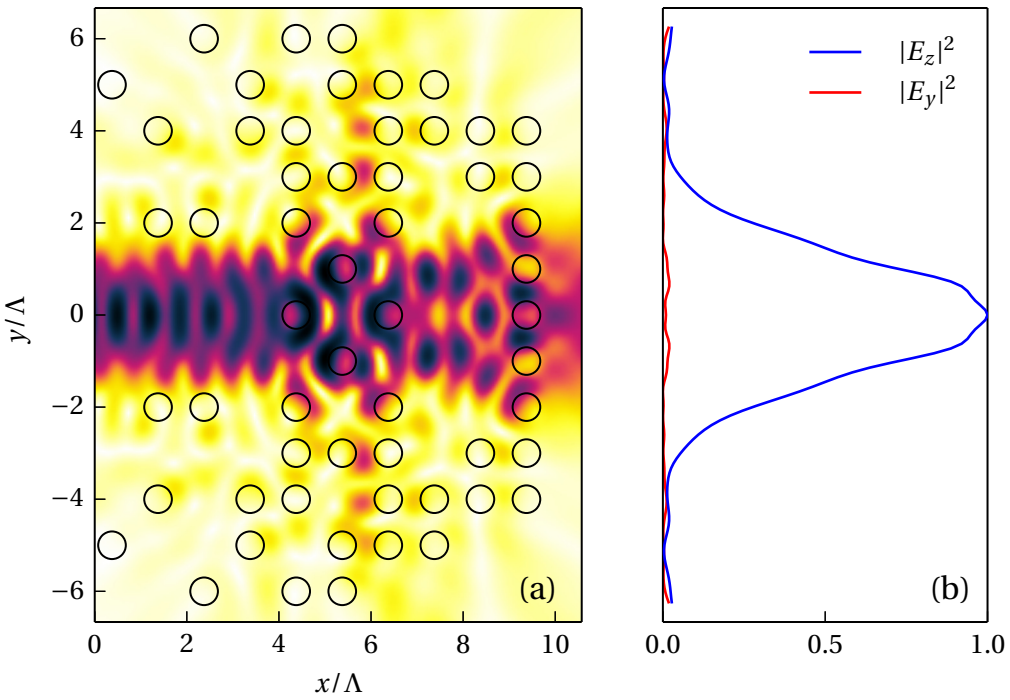

Figure 6.3 – Generation of a TM polarized Gaussian beam. (a) Optimized HIS configuration (57 scatterers) and $|E_z|$ field profile (arbitrary units). The target plane coincides with the upper limit of the x axis. (b) Comparison of orthogonal polarization components along target plane. This solution is characterized by $\mathscr{P} = 0.983$, $R = 59.8, g = 0.044, \eta = 0.759$.

case the output beams is slightly less polarized ($\mathscr{P} = 0.978$ and $R \simeq 43.9$). We have also performed optimization using triangular primitive lattices, but we found that this procedure resulted in lower values of $\mathscr{P}$. This may be related to the fact that square grids allows for nearly complete rows to be present in the design (see Figs. 6.3a and 6.4a), allowing the effective bandgap effect described earlier to take place.

In summary, we have proposed small footprint integrated designs allowing for simultaneous polarization filtering and amplitude beam shaping. The designs are based on two-dimensional photonic lattices exhibiting partial bandgaps, which facilitates the filtering behavior. Using an optimization procedure based on the tabu search algorithm, we are able to maximize the average degree of polarization of the output beam up to 98 % with a transmission efficiency over 75 % for the TM polarizer and 80 % for the TE polarizer. While the designs we presented allow for the generation of a Gaussian amplitude profile at the device near-field, the optimization procedure can be used for the generation of arbitrary shape beams, as shown in previous studies [44, 46, 158].

Future work includes the application of the algorithm to different beam shapes as well as a generalization to three dimensional lattices, thereby allowing for an integrated solution to generate, for instance, radially polarized beams. Noteworthy is the fact that we were not able to obtain TE

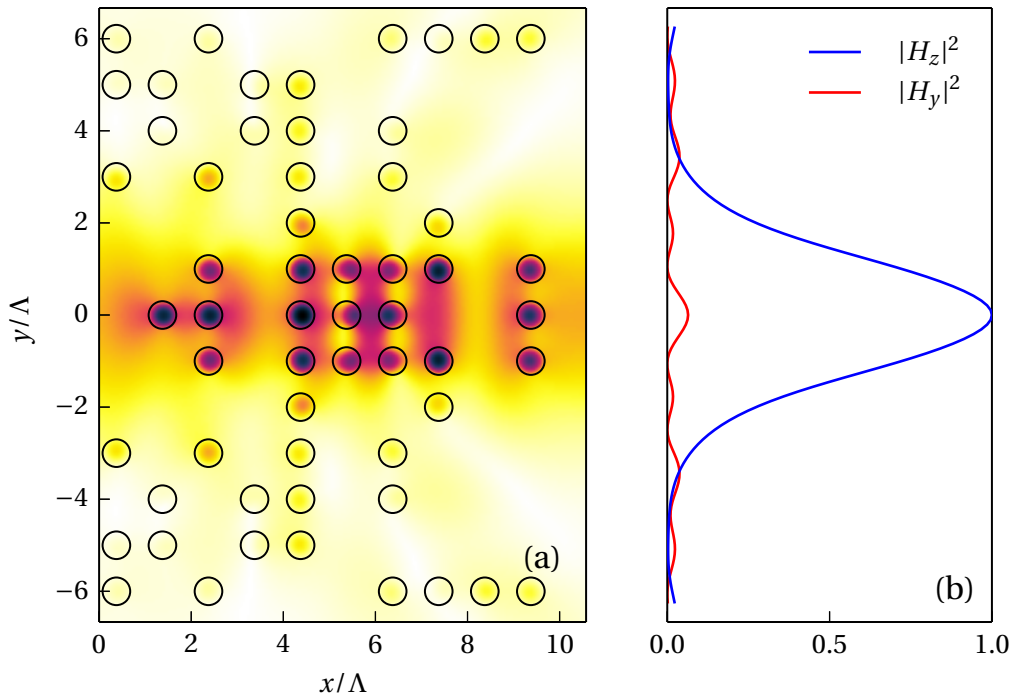

Figure 6.4 – Generation of a TE polarized Gaussian beam. (a) Optimized RIA configuration (58 scatterers) and $|H_z|$ field profile (arbitrary units). The target plane coincides with the upper limit of the x axis. (b) Comparison of orthogonal polarization components along target plane. This solution is characterized by $\mathscr{P} = 0.980$, $R = 48.0, g = 0.028, \eta = 0.890$.

polarized beams using the HIS design and TM beams using the RIA configuration. This confirms the usefulness of the bandgap analysis as a design guide. Nevertheless, using high-order bands (where there is no bandgap) to generate polarized beams may be possible. In fact, interesting effects in high-order transmission bands of PhCs, e.g. lensing, have recently been observed [92]. This could also be beneficial from an experimental standpoint, as the resulting polarization filters could accommodate wider beams.

6.4 Authors' contributions

DG designed the study, carried out the analysis, wrote the numerical codes, performed the computations and wrote the first version of the manuscript. JD suggested the definition of $\mathscr{P}$ used in the study. All authors have contributed to the analysis and have been instrumental in bringing the original manuscript to a publishable research contribution.

6.5 Supplement: Excerpts of supplemental material

6.5.1 Detailed Pareto fronts: optimization of efficiency

This appendix contains supplemental details about the multiobjective computations discussed in the accompanying article. The additional results are:

1. The Pareto fronts of the $(g_1, \mathscr{P})$ multiobjective optimization problem presented in the article.
2. The Pareto fronts of (g_1, η) and $(\eta, \mathscr{P})$ optimization problems. Indeed, computing the degree of polarization requires computing the Poynting vector components, as does the efficiency. It is therefore straightforward to add the power transmission efficiency η as an additional objective function, although we did not do so in the main contribution.
3. The fully three-dimensional Pareto front of the $(g_1, \mathscr{P}, \eta)$ beam shaping problem.
4. More beam profiles (Hermite-Gauss beams of order 1 and 2), both for the TE and TM polarization.

In short, we are faced with a three-objective problem that consists in minimizing the error on the output beam profile g_1 while maximizing the degree of polarization $\mathscr{P}$ and the transmission efficiency η simultaneously. To this end, we use the following objective function in PTS computations

$$f(v) = \frac{1}{g_1(v)} + \alpha_1 \mathscr{P}(v) + \alpha_2 \eta(v), \tag{6.5.1}$$

and proceed to solve multiple instances of the following problem

$$\max_{v \in \Upsilon} f(v), \tag{6.5.2}$$

using different values of the relative weights α_i. The case $\alpha_2 = 0$ corresponds to the objective function used in the main contribution. Since the solution space v is composed of 2^{70} solutions, a significant computation time is required to achieve a good sampling of the Pareto front of the beam shaping problem. The basic scatterer grids used in this section are also those of the main contribution, that is a holes-in-slab (HIS) configuration for the generation of TM-polarized beams and a rods-in-air (RIA) configuration for TE computations.

6.5.1.1 TM polarization

In this section, we present the detailed Pareto fronts of the optimization problem consisting in the generation of TM-polarized beams. Optimization runs for the generation of Gaussian and Hermite-Gauss beams of order 1 and 2 were performed. The resulting $(g_1, \eta), (g_1, \mathscr{P})$ and $(\eta, \mathscr{P})$ are shown in Fig. 6.5, while the $(g_1, \mathscr{P}, \eta)$ is presented in Fig. 6.6. It can be seen from these two figures that Pareto solutions of the two-objective problems are necessarily Pareto solutions of the three-objective problem, although the opposite is seldom true.

As a side note, these computations were obtained using a slightly different definition of $\mathscr{P}$ than that in the main contribution. This different version is [2]

$$\mathscr{Q} = \frac{1}{2y_0} \int_{-y_0}^{y_0} \frac{\langle S_x(x,y) \rangle_z - \langle S_x(x,y) \rangle_y}{\langle S_x(x,y) \rangle_z + \langle S_x(x,y) \rangle_y} dy, \tag{6.5.3}$$

where $\pm y_0$ are arbitrarily chosen integration bounds. For the simulations shown in Fig. 6.5 and 6.6, we used the value of $\mathscr{Q}$ to guide the optimization computations, but post-characterization of the solutions is done using the value of $\mathscr{P}$. The reason for this is that $\mathscr{Q}$ was the initial choice of objective function, but it was found that $\mathscr{P}$ produced better results since it prevented the beam profiles from exhibiting unpolarized side-lobes. Since the computations are time-consuming and there is a good correlation between $\mathscr{Q}$ and $\mathscr{P}$, we did not repeat all of them using $\mathscr{P}$. Nevertheless, the results in the main contribution and in the next section (§6.5.1.2) were carried out later using $\mathscr{P}$.

Two representative configurations located on the sampled Pareto front are detailed in Fig. 6.7. We have selected the Pareto solutions characterized by $g_1 \leq 0.1$ and the best possible value of $\mathscr{P}$. We find that values of $\mathscr{P} > 0.9$ can be achieved for the TM polarization. Although these values are slightly smaller than those characterizing the polarized Gaussian profiles presented in the main contribution, these results show that it is in principle possible to create polarization filters adapted for the generation of arbitrary profile beams, while maintaining a high transmission efficiency ($\eta > 0.85$).

6.5.1.2 TE polarization

In this section, we present the detailed Pareto fronts of the optimization problem consisting in the generation of TE-polarized beams (Figs. 6.8 and 6.9). The method used to sample the Pareto fronts is similar to that described in section 6.5.1.1, except that the objective function $\mathscr{P}$ used in the main contribution is used here as well.

Two representative configurations are also shown in Fig. 6.10. Interestingly, the configuration shown in the bottom panel of this figure (generation of a TE-polarized Hermite-Gauss beam of order 2) stands apart from the others in the $(g_1, \mathscr{P})$ Pareto front, as it is the only one characterized by a value of $g_1 < 0.1$, although the degree of polarization is also smaller.

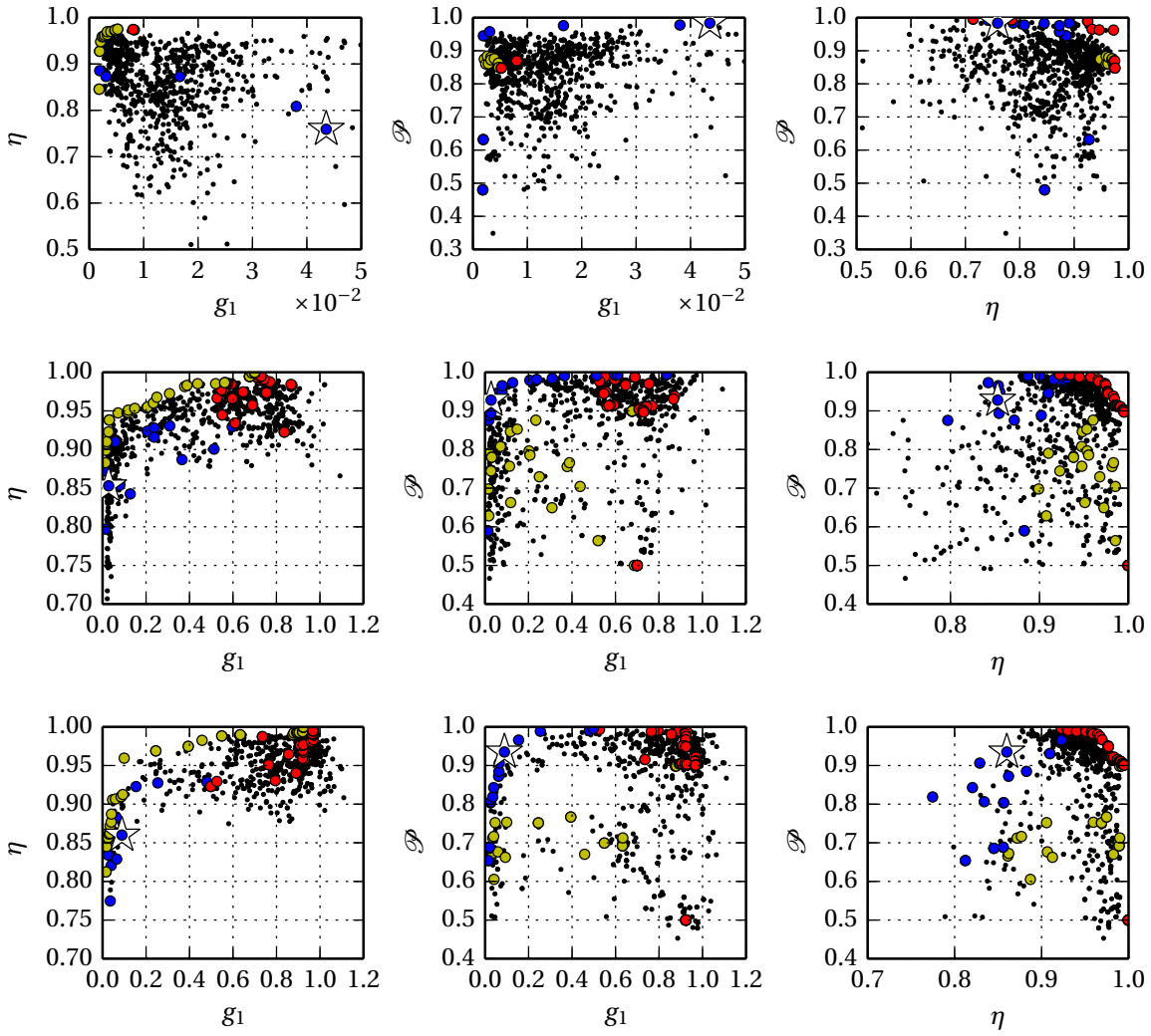

Figure 6.5 – Detailed Pareto fronts of three multiobjective beam shaping problems (TM polarization). (Top row) The output beam is set to a Gaussian beam profile. The configuration of Fig. 6.3 is marked by a star. (Middle row) The output beam is set to a Hermite-Gauss beam profile of order 1. The configuration of Fig. 6.7 is marked by a star. (Bottom row) The output beam is set to a Hermite-Gauss beam profile of order 2. The configuration of Fig. 6.7 is marked by a star. Color codes for the sampled Pareto fronts are as follows: Yellow (g_1, η), blue ($g_1, \mathscr{P}$), red ($\eta, \mathscr{P}$). Black markers indicate non-Pareto solutions.

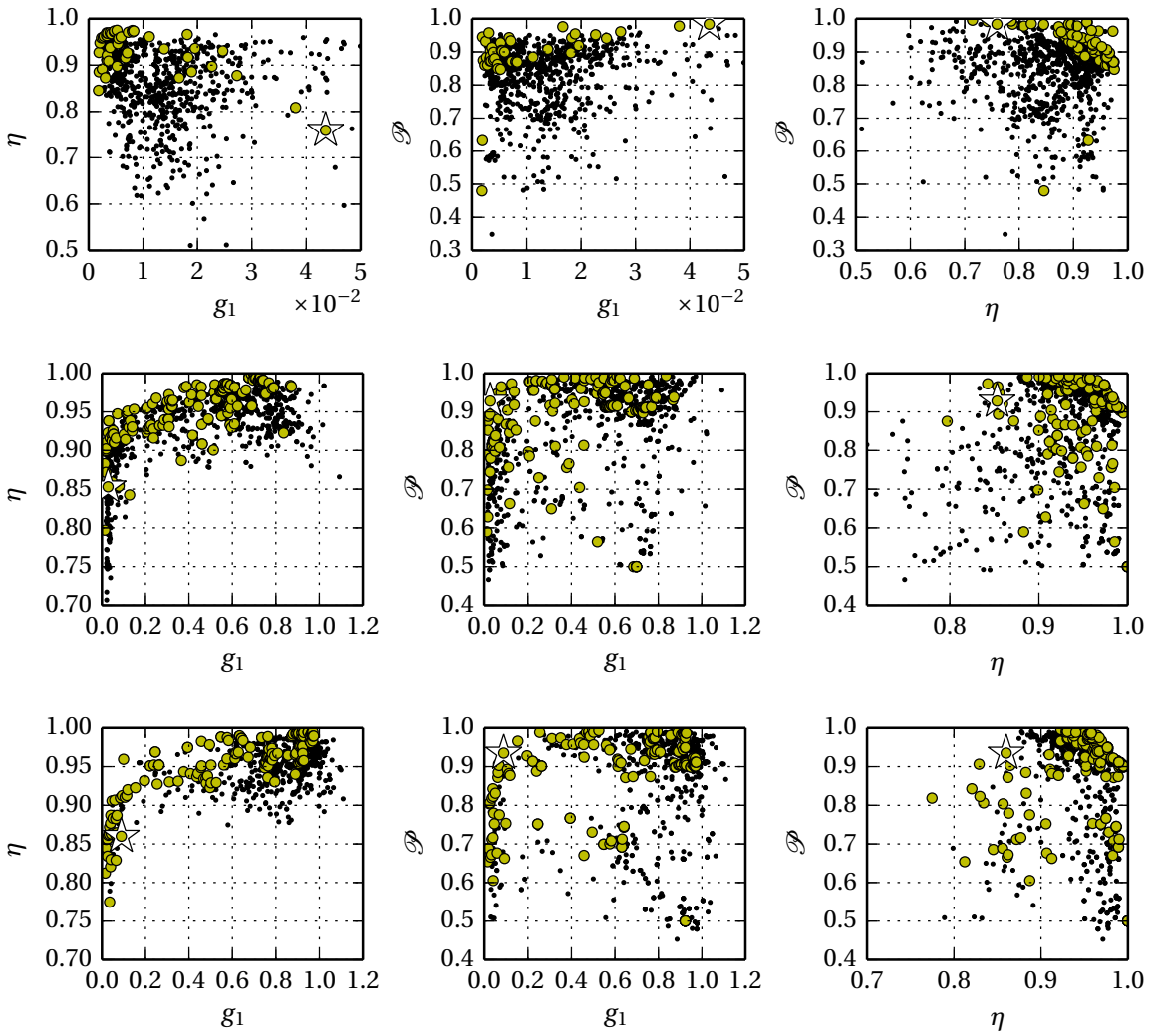

Figure 6.6 – Detailed Pareto fronts of the three-objective shaping problems (TM polarization). Each panel shows a projection of the three-dimensional front in a two-objective plane. (Top row) The output beam is set to a Gaussian beam profile. The configuration of Fig. 6.3 is marked by a star. (Middle row) The output beam is set to a Hermite-Gauss beam profile of order 1. The configuration of Fig. 6.7 is marked by a star. (Bottom row) The output beam is set to a Hermite-Gauss beam profile of order 2. The configuration of Fig. 6.7 is marked by a star.

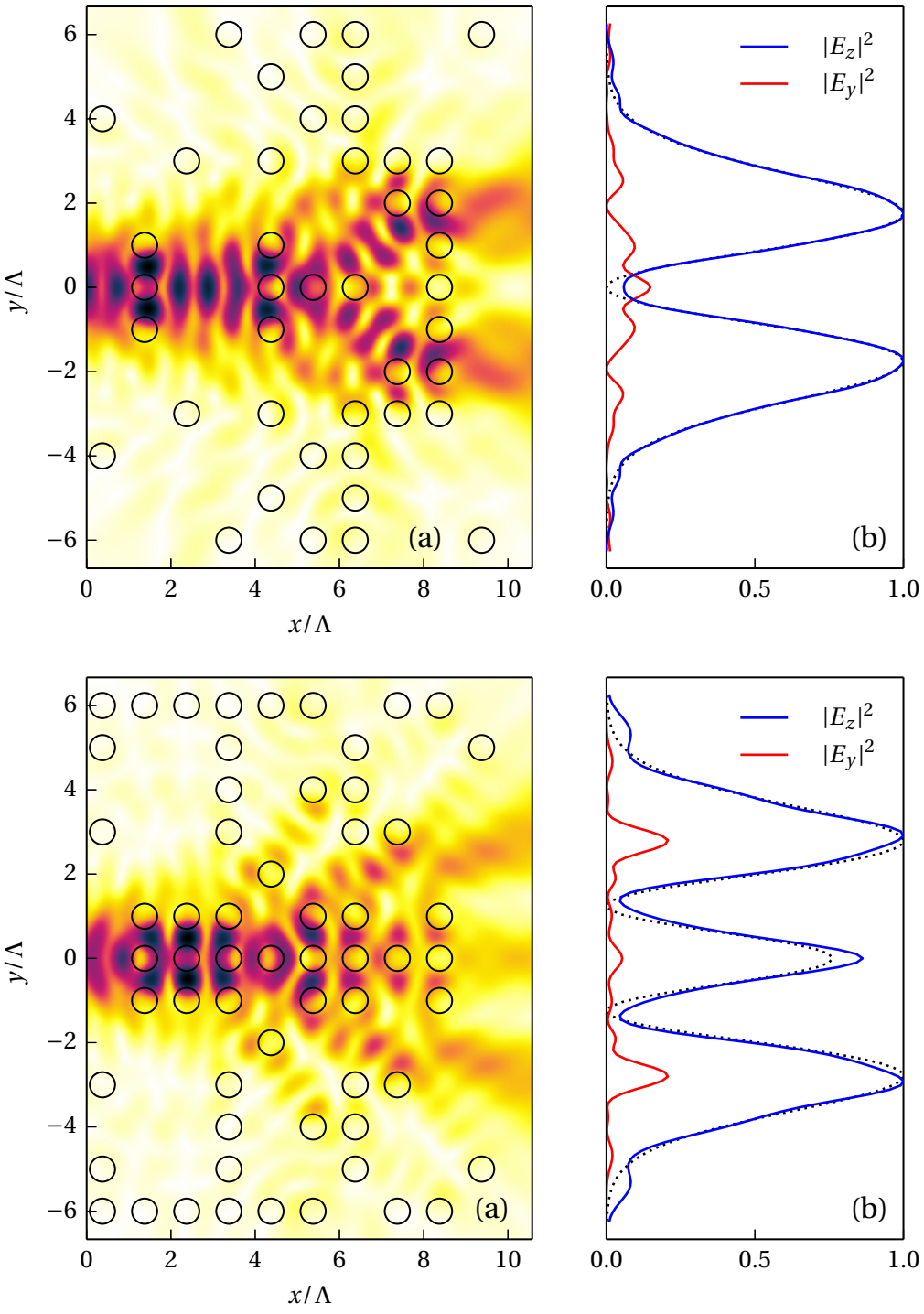

Figure 6.7 – Generation of TM polarized Hermite-Gauss beams of order 1 (Top row) and order 2 (Bottom row). (a) Optimized configurations and $|E_z|$ field profile (arbitrary units). The target plane coincides with the upper limit of the x axis. (b) Comparison of polarization components along target plane. The target profile is indicated by a dotted black line. Solution characteristics are: (Top row) $\mathscr{P} = 0.928, R = 12.89, g_1 = 0.028, \eta = 0.853, N = 43$ and (Bottom row) $\mathscr{P} = 0.935, R = 14.47, g_1 = 0.089, \eta = 0.860, N = 60$.

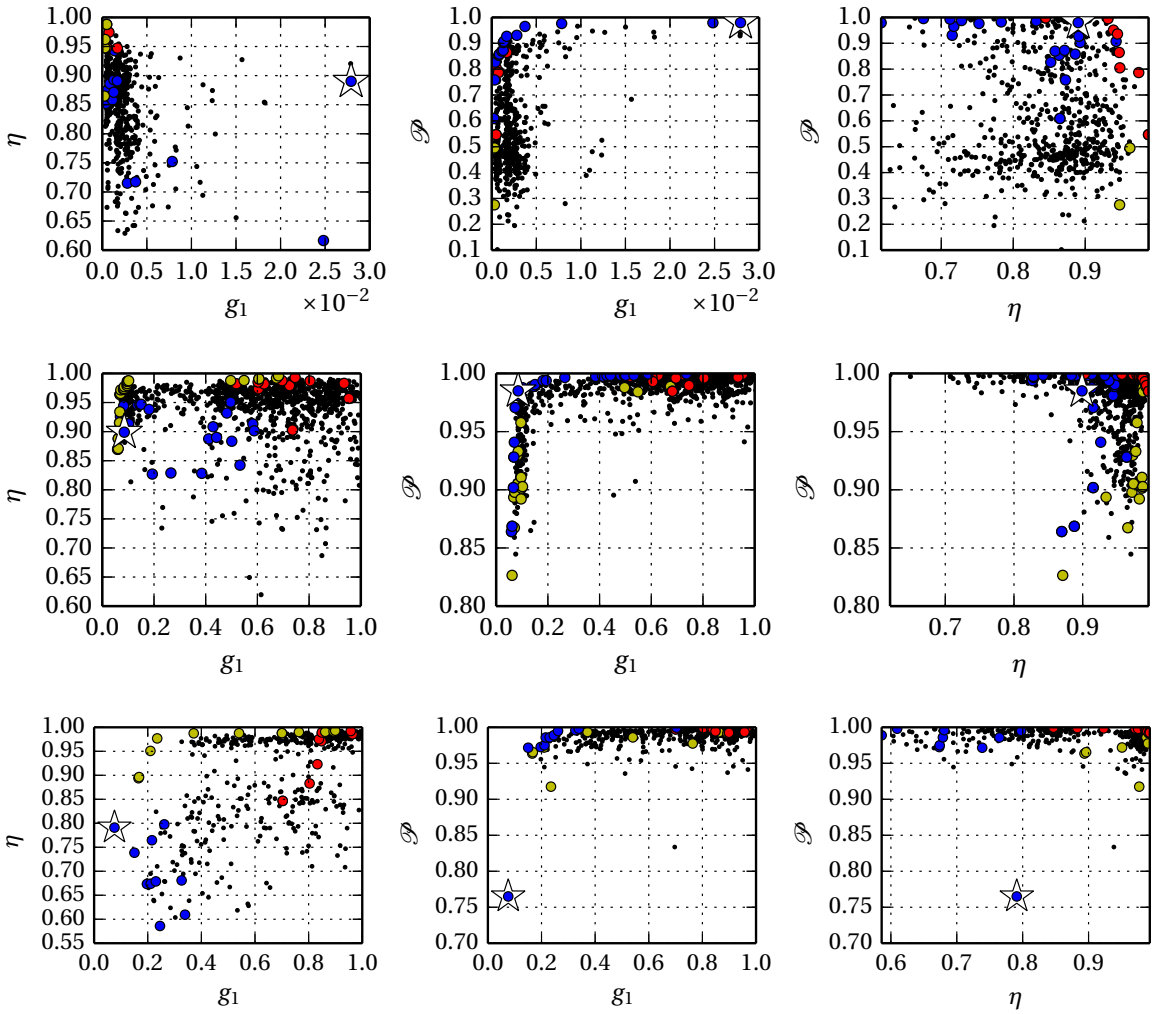

Figure 6.8 – Detailed Pareto fronts of three multiobjective beam shaping problems (TE polarization). (Top row) The output beam is set to a Gaussian beam profile. The configuration of Fig. 6.4 is marked by a star. (Middle row) The output beam is set to a Hermite-Gauss beam profile of order 1. The configuration of Fig. 6.10 is marked by a star. (Bottom row) The output beam is set to a Hermite-Gauss beam profile of order 2. The configuration of Fig. 6.10 is marked by a star. Color codes for the sampled Pareto fronts are as follows: Yellow (g_1,η), blue (g_1,$\mathscr{P}$), red (η,$\mathscr{P}$). Black markers indicate non-Pareto solutions.

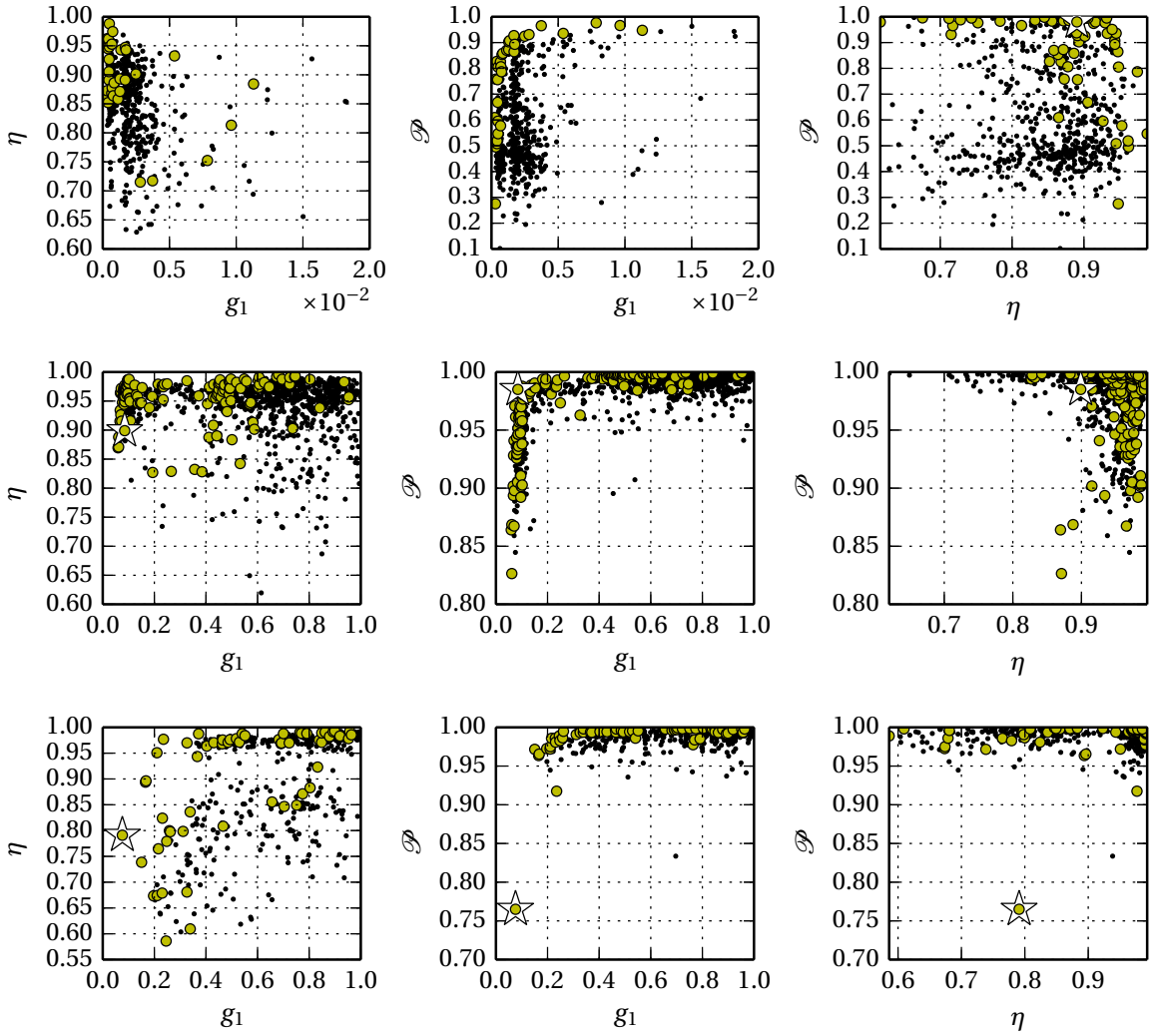

Figure 6.9 – Detailed Pareto fronts of the three-objective shaping problems (TE polarization). Each panel shows a projection of the three-dimensional front in a two-objective plane. (Top row) The output beam is set to a Gaussian beam profile. The configuration of Fig. 6.4 is marked by a star. (Middle row) The output beam is set to a Hermite-Gauss beam profile of order 1. The configuration of Fig. 6.10 is marked by a star. (Bottom row) The output beam is set to a Hermite-Gauss beam profile of order 2. The configuration of Fig. 6.10 is marked by a star.

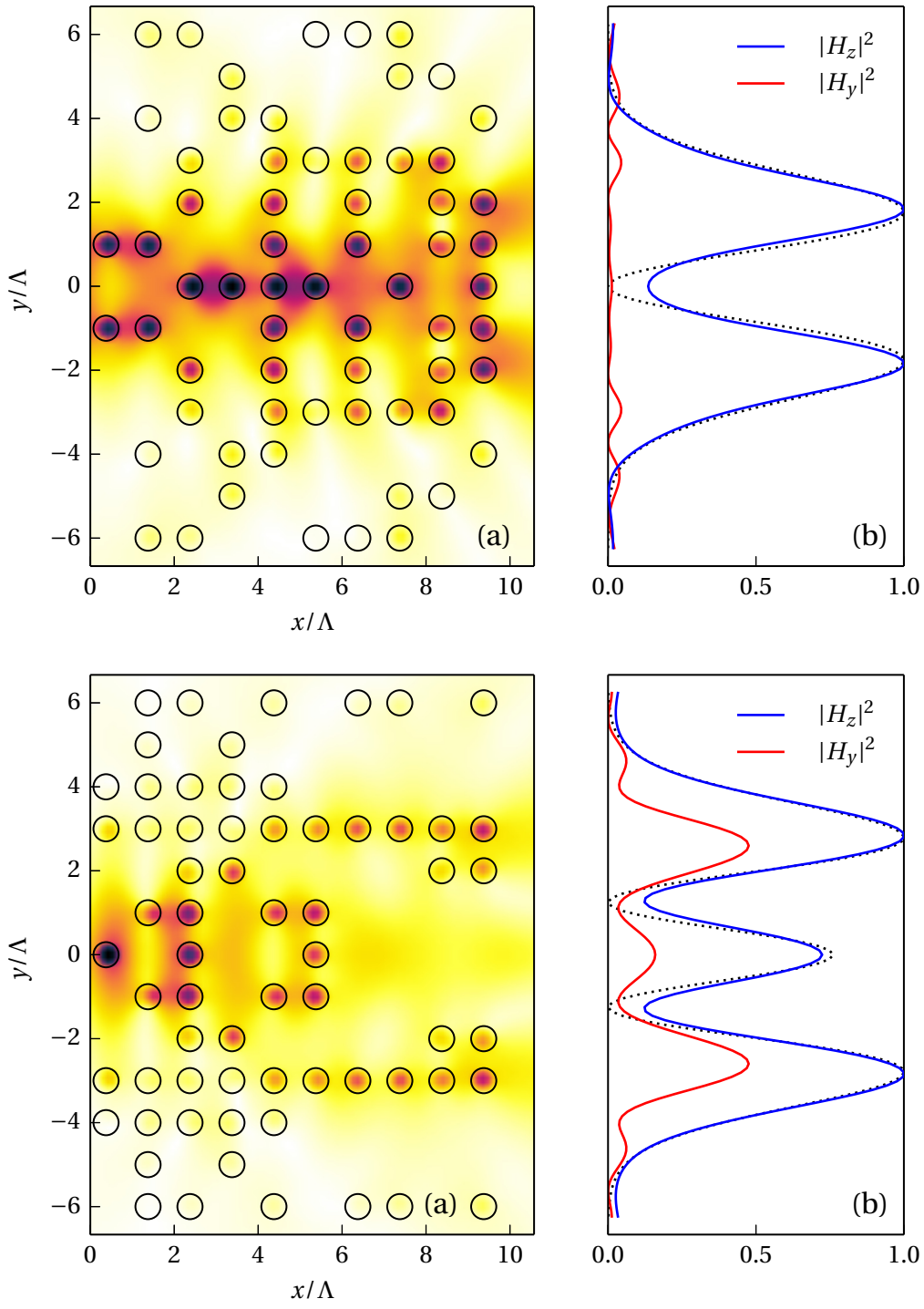

Figure 6.10 – Generation of TE polarized Hermite-Gauss beams of order 1 (Top row) and order 2 (Bottom row). (a) Optimized configurations and $|H_z|$ field profile (arbitrary units). The target plane coincides with the upper limit of the x axis. (b) Comparison of polarization components along target plane. The target profile is indicated by a dotted black line. Solution characteristics are: (Top row) $\mathscr{P} = 0.985, R = 63.54, g_1 = 0.085, \eta = 0.899, N = 64$ and (Bottom row) $\mathscr{P} = 0.765, R = 3.25, g_1 = 0.0759, \eta = 0.791, N = 65$.

Chapter 7

Ab initio investigation of lasing thresholds in photonic molecules

Denis Gagnon, Joey Dumont, Jean-Luc Déziel and Louis J. Dubé

Département de physique, de génie physique et d'optique
Faculté des Sciences et de Génie, Université Laval, Québec G1V 0A6, Canada

Journal reference: J. Opt. Soc. Am. B, Vol. 31, pp. 1867–1873 (2014)

URL: http://dx.doi.org/10.1364/JOSAB.31.001867
ePrint: http://arxiv.org/abs/1401.7305

Résumé

Cette publication présente une investigation des seuils lasers d'une molécule photonique typique composée de deux cylindres actifs couplés. Plus précisément, nous utilisons une récente théorie stationnaire du laser (SALT) afin d'évaluer la dépendence des seuils et des fréquences laser sur les paramètres du milieu de gain formant la molécule. La principale conclusion de cette étude est que l'ordre dans lequel les différents modes laser s'allument peut être modifié en choisissant une combinaison appropriée des paramètres du milieu de gain, soit sa largeur et sa fréquence centrale. Ce résultat est hors d'atteinte de l'approche traditionnelle des états quasi-liés. Nous quantifions également l'effet de la fréquence centrale de la transition laser sur les fréquences de résonances, un phénomène communément appelé « frequency pulling ».

Abstract

We investigate lasing thresholds in a representative photonic molecule composed of two coupled active cylinders of slightly different radii. Specifically, we use the recently formulated *steady-state ab initio laser theory* (SALT) to assess the effect of the underlying gain transition on lasing frequencies and thresholds. We find that the order in which modes lase can be modified by choosing suitable combinations of the gain center frequency and linewidth, a result that cannot be obtained using the conventional approach of quasi-bound modes. The impact of the gain transition center on the lasing frequencies, the frequency pulling effect, is also quantified.

7.1 Introduction

The study of light-matter interactions in photonic molecules (PMs), formed by coupling several optically active microcavities (atoms), has been the object of much work in recent years [13, 118]. Applications of microresonators and photonic molecules include optical communications [57], sensing [12, 112, 157, 159], quantum computing [69] and metrology [28]. Photonic atoms [54] and molecules [98] are also well suited for the fabrication of microlasers owing to their high quality factor, or photon recycling rate. These coupled systems also provide a test bed for a panoply of fundamental phenomena including optical bistability [70], coupled-resonator induced transparency [13], non-reciprocal light transmission [111] and exceptional points (EPs) [84, 126]. EPs are ubiquitous in parameter-dependent eigenvalue problems and can lead to surprising physical effects [60]. For instance, coupled edge-emitting lasers may turn off even as the pump power *increases* above threshold. This counter-intuitive behavior is achieved by pumping the cavities non-uniformly near an EP [84].

The lasing characteristics of microresonators are often obtained from the calculation of the cold-cavity (passive) modes. An alternative approach consists in introducing the threshold material gain in the laser eigenvalue problem [141, 142, 143]. This approach allows assessment of the effect

of the resonator geometry on lasing thresholds and emission directionality. However, to take into account the spectral properties of a given laser transition, for instance its position and linewidth, formulations such as the Maxwell-Bloch or Schrödinger-Bloch (for 2D systems) theory must be used [58, 147]. This is especially important in the case of nearly degenerate lasing frequencies, for instance near EPs. As we show in this work, the conventional wisdom of cold-cavity modes may not be sufficient in this case.

We will use the *steady-state ab initio laser theory* (SALT) [49, 152] to assess the effect of gain transition parameters on lasing frequencies and thresholds of a simple two-dimensional PM composed of two coupled active cylinders in the vicinity of a geometric EP. The term *ab initio* refers to the fact that this theory involves the solution of a set of self-consistent equations that explicitly take the gain medium parameters into account. In other words, SALT allows one to determine the steady-state solutions of the Schrödinger-Bloch equations [48, 58, 152]. The near-threshold behavior of the PM can be obtained by computing the threshold lasing modes (TLMs) as described in [49]. This choice of basis states permits to study the effect of the Lorentzian gain transition on thresholds when there are several modes competing for efficient gain extraction.

This paper is organized as follows. In Section 2, we describe the theoretical background behind our computations, including the main equations of SALT and the method used to compute the lasing states for an arbitrary number of cylinders. In Section 3, we compute the lasing states of a diatomic photonic molecule as a representative example. Our results show that the thresholds of closely spaced modes exhibit a non-trivial dependence on the parameters of the gain transition, specifically the gain center frequency and its linewidth. We also investigate how the lasing modes are subject to the frequency pulling effect, i.e. the effect of the gain center frequency on the spectrum of the PM laser. We summarize our findings in Section 4 and mention a number of possible improvements and extensions.

7.2 Theoretical background

The investigation of the lasing behavior of 2D cavities usually implies the computation of the eigenstates of the passive cavity. These states are governed by the Helmholtz equation

$$[\nabla^2 + \epsilon(\mathbf{r})k^2]\varphi(\mathbf{r}) = 0, \tag{7.2.1}$$

where an harmonic time dependence $\exp(-i\omega t)$ is assumed and $\epsilon(\mathbf{r})$ is the passive spatially varying refractive index. Both TM ($\varphi \equiv E_z$) and TE ($\varphi \equiv H_z$) polarized waves can be considered. By applying the usual Sommerfeld radiation condition, i.e. an outgoing wave component only, we obtain a set of leaky, or quasi-bound (QB) states characterized by complex eigenfrequencies $k_{\mathrm{QB}} = k' + ik''$ [18]. Since the radiation condition implies $k'' < 0$, QB states are non-orthogonal and exhibit exponential growth towards infinity [48, 152]. Despite this unrealistic behavior, QB states provide a useful measure of the photon lifetime in the cavity by means of the quality factor $Q = |k'/2k''|$. The Q-factor

18. Since $\omega = ck$, we will refer generically to both quantities as eigenfrequencies.

gives a *qualitative* indication of which cavity modes will lase first. Considering a gain transition with center located at frequency k_a, one will usually infer that the modes with eigenfrequencies close to k_a and sufficiently high Q-factor will lase first [138, 147].

7.2.1 Steady-state ab initio laser theory

Although the QB states are widely used, they can not describe the lasing behavior of microcavities or PMs in a completely accurate way since the gain medium parameters have no influence on the QB states described by (7.2.1). Dynamical theories, for instance the Schrödinger-Bloch model, have been used in the past decade to improved the treatment of lasing modes [58, 147]. In this respect, the recently developed SALT offers an alternative formulation as a stationary version of the Schrödinger-Bloch model. Since we are precisely interested in the steady-state lasing behavior of PMs, we shall use SALT in the remainder of this work.

The most important feature of SALT is the introduction of a new kind of eigenstate called a constant-flux (CF) state [48, 49, 58, 152]. The CF states satisfy the following equation

$$[\nabla^2 + \epsilon(\mathbf{r})K^2(k)]\varphi(\mathbf{r}) = 0, \qquad \mathbf{r} \in C, \tag{7.2.2a}$$

$$[\nabla^2 + \epsilon(\mathbf{r})k^2]\varphi(\mathbf{r}) = 0, \qquad \mathbf{r} \notin C, \tag{7.2.2b}$$

where C is the *cavity region*, defined as the union of all optically active regions. CF states are characterized by complex eigenfrequencies K inside C, but real frequencies k outside this region. Thus, they exhibit no exponential growth and are physically meaningful, contrary to the QB states [58].

The laser modes can be expanded in the basis of CF states to take into account effects such as non-linear coupling between modes (spatial hole-burning) and non-uniform pump profiles [49, 84]. For the purpose of this work, we restrict ourselves to the case of near-threshold behavior and spatially uniform pumping inside all cylinders composing of the PM. Under those conditions, the threshold lasing modes (TLMs) of the PM satisfy the following equation

$$\left\{\nabla^2 + \left[\epsilon(\mathbf{r}) + \frac{\gamma_a D_0 F(\mathbf{r})}{k - k_a + i\gamma_a}\right] k^2\right\}\varphi(\mathbf{r}) = 0, \tag{7.2.3}$$

where k_a is the gain center frequency, γ_a is the gain width and D_0 is associated to the "pump strength". Since we suppose uniform pumping of all cylinders forming the PM, $F(\mathbf{r}) = 1$ for $\mathbf{r} \in C$ and $F(\mathbf{r}) = 0$ for $\mathbf{r} \notin C$ (the cavity region and the cylinders coincide). The TLMs must satisfy an additional reality condition on D_0 [49]. For a given choice of exterior real frequency k, the value of D_0 is in general complex, but when it crosses the real axis at $k = k_\mu$, we obtain a pair of real numbers (k_μ, D_0^μ) defining the TLM lasing frequency and lasing threshold, respectively. The first lasing mode is therefore the TLM with the smallest threshold D_0^μ [49].

In the case of uniform pumping and a uniform dielectric constant $\epsilon(\mathbf{r}) = \epsilon_c$ inside all cylinders, each TLM can be associated with a single CF state. By comparing (7.2.2a) and (7.2.3), one obtains

the relation

$$\frac{\gamma_a D_0}{k - k_a + i\gamma_a} = \epsilon_c \left(\frac{K^2}{k^2} - 1 \right). \tag{7.2.4}$$

Simply stated, for a given combination of gain parameters (k_a, γ_a), each TLM of eigenvalue k_μ corresponds to a CF state of eigenvalue K_μ for which D_0 is purely real, according to (7.2.4).

7.2.2 2D Generalized Lorenz-Mie theory

While SALT allows for arbitrary pump profiles, we restrict our discussion to uniformly pumped dielectric cylinders. This pump uniformity permits the use of the 2D Generalized Lorenz-Mie theory (2D-GLMT) [19] – also called multipole method – to compute the eigenstates of the PM [4, 131]. This kind of theory can be used provided the cylinders composing the PM possess enough symmetry to use the method of separation of variables [56]. It can also be used for the computation of the scattering of arbitrary beams by a complex arrangement of dielectric cylinders [33, 44, 46]. Multipole-based methods can also be used for modal analysis of quantum dots [117]. For the sake of completeness, we review briefly the main equations of the application of 2D-GLMT for the computation of lasing states.

Consider an array of N cylindrical scatterers of radii u_n and relative permittivity ϵ_n. Let also $\mathbf{r}_n = (\rho_n, \theta_n)$ be the cylindrical coordinate system local to the n^{th} scatterer. For modeling purposes, we suppose that every cylinder is infinite along the axial z direction. The central hypothesis of 2D-GLMT is that the total field outside the scatterers can be expanded in a basis of cylindrical functions centered on each individual scatterer, that is

$$\varphi^E(\mathbf{r}) = \sum_{n=1}^{N} \sum_{l'=-\infty}^{\infty} b_{nl'} H_{l'}^{(+)}(k_0 \rho_n) e^{il'\theta_n}, \tag{7.2.5}$$

where $H_l^{(+)}$ is a Hankel function of the first kind. Inside the n^{th} scatterer, the field can be written as

$$\varphi_n^I(\mathbf{r}) = \sum_{l=-\infty}^{\infty} c_{nl} J_l(k_n \rho_n) e^{il\theta_n}, \tag{7.2.6}$$

where J_l is a Bessel function of the first kind.

In order to apply electromagnetic boundary conditions at the interface of the n^{th} scatterer, one must find an expression for $\varphi^E(\mathbf{r})$ outside the scatterers containing only cylindrical harmonics centered on the n^{th} scatterer, that is

$$\varphi_n^E(\mathbf{r}) = \sum_{l=-\infty}^{\infty} \left[a_{nl} J_l(k_0 \rho_n) + b_{nl} H_l^{(+)}(k_0 \rho_n) \right] e^{il\theta_n}. \tag{7.2.7}$$

19. We use the denomination GLMT in accordance with [56] to mean "theories dealing with the interaction between electromagnetic arbitrary shaped beams and a regular particle, allowing one to solve the problem by using the method of separation of variables". However, as a matter of historical precision, it could be argued that a theory, dealing specifically with the scattering by many cylinders, should be called "generalized Rayleigh theory" in honour of the first calculation of scattering by one single cylinder by Rayleigh [87].

This can be achieved via the application of Graf's addition theorem for cylindrical functions, allowing a translation from the frame of reference of scatterer n' to the frame of reference of scatterer n [1]. The theorem states that

$$H_{l'}^{(+)}(k_0\rho_{n'})e^{il'\theta_{n'}} = \sum_{l=-\infty}^{\infty} e^{i(l'-l)\phi_{nn'}} H_{l-l'}^{(+)}(k_0 R_{nn'}) J_l(k_0\rho_n)e^{il\theta_n}, \tag{7.2.8}$$

where $R_{nn'}$ is the center-to-center distance between scatterers n and n' and $\phi_{nn'}$ is the angular position of scatterer n' in the frame of reference of scatterer n. Substituting (7.2.8) in (7.2.5) yields

$$\varphi_n^E(\mathbf{r}) = \sum_{l=-\infty}^{\infty} b_{nl} H_l^{(+)}(k_0\rho_n)e^{il\theta_n} + \sum_{l=-\infty}^{\infty}\sum_{n'\neq n}\sum_{l'=-\infty}^{\infty} b_{n'l'} e^{i(l'-l)\phi_{nn'}} H_{l-l'}^{(+)}(k_0 R_{nn'}) J_l(k_0\rho_n)e^{il\theta_n}. \tag{7.2.9}$$

The comparison of (7.2.7) with (7.2.9) then yields the following relation between the $\{a_{nl}\}$ and $\{b_{nl}\}$ coefficients

$$a_{nl} = \sum_{n'\neq n}\sum_{l'=-\infty}^{\infty} e^{i(l'-l)\phi_{nn'}} H_{l-l'}^{(+)}(k_0 R_{nn'}) b_{n'l'}. \tag{7.2.10}$$

A further relation between the $\{a_{nl}\}$ and $\{b_{nl}\}$ coefficients is obtained by applying electromagnetic boundary conditions to (7.2.6) and (7.2.7) at $\rho_n = u_n$. This finally leads to the homogeneous equation for the coefficient vector $\mathbf{b}$, $\mathbf{T}(k_n, k_0)\mathbf{b} = 0$, whose non-trivial solutions are given by the condition

$$\det[\mathbf{T}(k_n, k_0)] = 0, \tag{7.2.11}$$

where k_n is the frequency inside the n^{th} cylinder and k_0 is the exterior frequency (both can be complex). One immediately recognizes the transfer matrix $\mathbf{T}$ as the inverse of the usual scattering matrix. $\mathbf{T}$ has a well defined structure; it is composed of blocks containing coupling coefficients between cylindrical harmonics centered on each circular scatterer. Its elements are given by

$$\mathbf{T}_{ll'}^{nn'}(k_n, k_0) = \delta_{nn'}\delta_{ll'} - (1-\delta_{nn'})e^{i(l'-l)\phi_{nn'}} H_{l-l'}^{(+)}(k_0 R_{nn'}) s_{nl}(k_n, k_0). \tag{7.2.12}$$

The s_{nl} factor results from the application of electromagnetic boundary conditions and is given by

$$s_{nl}(k_n, k_0) = -\frac{J_l'(k_0 u_n) - \Gamma_{nl} J_l(k_0 u_n)}{H_l^{(+)\prime}(k_0 u_n) - \Gamma_{nl} H_l^{(+)}(k_0 u_n)}, \tag{7.2.13}$$

where

$$\Gamma_{nl} = \xi_{n0}\frac{k_n J_l'(k_n u_n)}{k_0 J_l(k_n u_n)}, \tag{7.2.14}$$

and $\xi_{ij} = 1\left(\epsilon_j/\epsilon_i\right)$ for TM (TE) polarization. Prime symbols indicate differentiation with respect to the whole argument. In a typical implementation, $\mathbf{T}$ is composed of $N \times N$ blocks of dimension $2l_{\max}+1$, where $l_{\max}$ is chosen sufficiently large to ensure convergence of the cylindrical function expansions [20]. Its value is usually fixed by $l_{\max} \geq 3k\max_n\{u_n\}$. In the case of a diatomic photonic

20. A further technical aspect of the implementation should be noted. Although we have not encountered any instabilities in our calculations, it should be acknowledged that for high accuracy work, Eqns. (12) and (13) are not well suited (exponential decay or growth of $\mathbf{T}_{ll'}^{nn'}$ with the indices l and l'). This difficulty has been recognized before [143] and solved generally in [99].

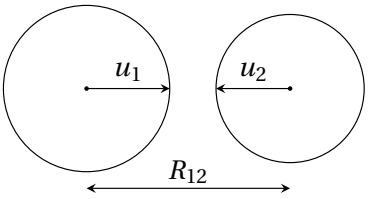

Figure 7.1 – Geometry of the diatomic photonic molecule used in this work. The cylinders radii are u_1 and u_2, with $u_2 = 0.8908\ u_1$. The center-to-center distance is $R_{12} = 2.448\ u_1$ and the relative permittivity of the cylinders is $\epsilon_c = 4$. This geometry is also used in Ref. [126].

molecule ($N = 2$), the matrix is of the form

$$\mathbf{T} = \begin{bmatrix} \mathbf{T}^{11} & \mathbf{T}^{12} \\ \mathbf{T}^{21} & \mathbf{T}^{22} \end{bmatrix}, \tag{7.2.15}$$

with the diagonal blocks equal to identity matrices and dense off-diagonal blocks, consistent with (7.2.12). More details on the Lorenz-Mie method can be found in [4, 33, 44, 56, 99, 103, 131].

The QB states of a PM can be computed by substituting $k_n \to k\sqrt{\epsilon_n}$ and $k_0 \to k\sqrt{\epsilon_0}$ in (7.2.11) and looking for solutions in the complex k-plane. As for the CF states, the appropriate substitution is $k_n \to K\sqrt{\epsilon_n}$ if the n^{th} cylinder is part of the cavity region C and $k_n \to k\sqrt{\epsilon_n}$ otherwise, with real k. The solutions are in this case located in the complex K-plane. We note that a countably infinite set of CF states can be computed for each different value of the real exterior frequency k.

7.3 Lasing states of a simple photonic molecule

As a proof of concept, we consider a diatomic PM composed of two coupled cylinders, and restrict the discussion to TM-polarized modes. More specifically, we consider the asymmetric PM as proposed in Ref. [126], shown in Fig. 7.1. The motivation behind this choice is two-fold. First, it allows us to calibrate the combination of 2D-GLMT and SALT against a previous calculation method, in this case the boundary element method [126]. Moreover, the proposed geometry exhibits an avoided crossing of QB states, resulting from the proximity of a EP of *geometrical nature*. EPs are generically defined as specific parametric combinations for which the eigenvalues of the non-Hermitian operator describing a coupled system *coalesce* [60, 84]. In the case of the asymmetric PM, the EP can be parametrically encircled by varying the inter-disk distance and the ratio between disk radii [126]. Therefore, this choice of geometry is also motivated by the interesting physics of EPs.

The PM is composed of two cylinders of radii u_1 and u_2, with $u_2 = 0.8908\ u_1$. The center-to-center distance is $R_{12} = 2.448\ u_1$ and the relative permittivity of the cylinders is $\epsilon_c = 4$ (see Fig. 7.1). The y axis is perpendicular to the line connecting the two cylinders, while the x axis is taken along R_{12}. The near-coalescent states located near $k'u_1 = 5.4$ are shown in Fig. 7.2, and the evolution of the associated complex eigenfrequencies is shown in Fig. 7.3a. The states are split in two symmetry

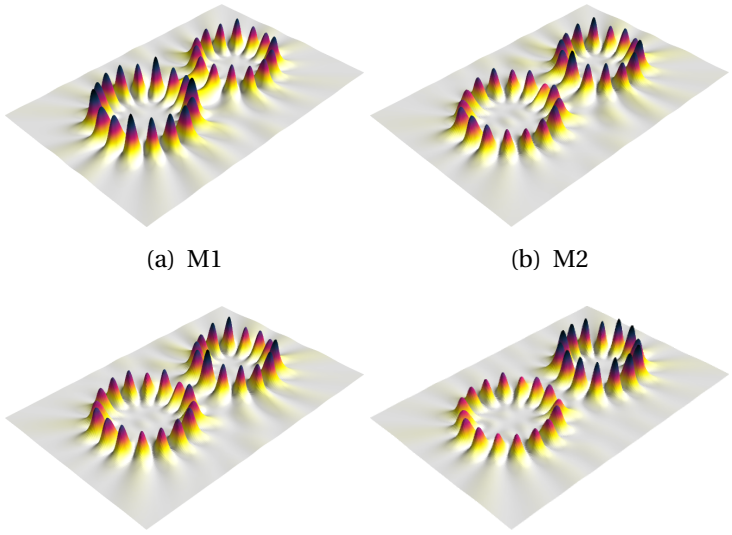

(a) M1 (b) M2

(c) M3 (d) M4

Figure 7.2 – Profile of four TM-polarized QB states of a diatomic photonic molecule composed of two cylinders of different diameters, as shown in Fig. 7.1. The z-coordinate is proportional to the intensity (arbitrary units).

classes with respect to the x axis, odd modes (M1 and M4) and even modes (M2 and M3). They result from the coupling between whispering-gallery modes of slightly different angular momenta of the uncoupled cylinders, creating doublet states [13, 136]. As a result of the proximity of the geometrical EP, the four QB states located near $k'u_1 = 5.4$ have closely spaced resonance frequencies [126]. Moreover, the Q-factors are all similar ($Q \sim 200$) and the four states compete for gain. The order in which the modes will lase is not obvious, especially if we consider a gain center with a frequency higher than that of M4. In other words, the conventional approach of considering only Q-factors does not allow a quantitative determination of the lowest threshold mode for nearly-degenerate states. Despite this close spacing of modes, we assume that the stationary inversion approximation – which is central to SALT – still holds for this geometry. Typical atomic relaxation rates for semi-conductor lasers show that this is indeed the case [50].

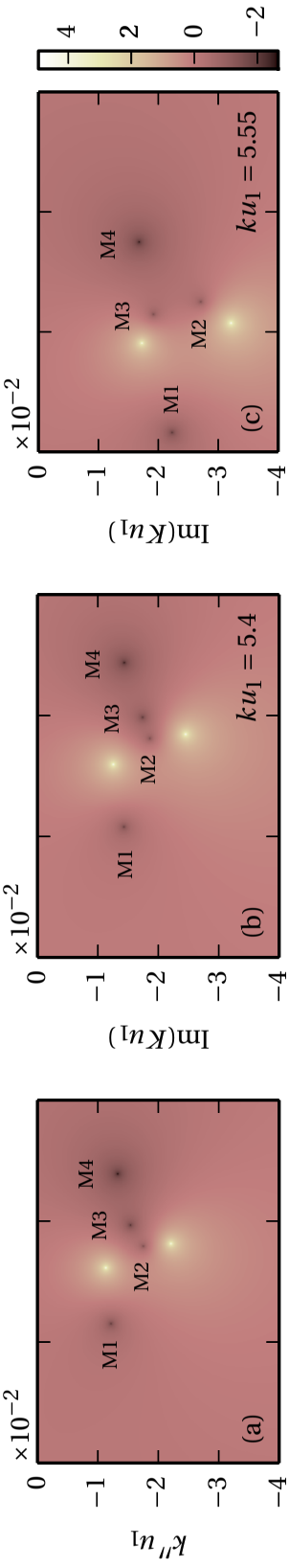

Figure 7.3 – (a) Map of $\log|\det[\mathbf{T}]|$ in the complex k plane for each of the four QB states of the photonic molecule. Eigenvalues correspond to the zeros of the function (dark spots) and are located at [M1: $k_{\mathrm{QB}} u_1 = 5.3830 - i0.0122$, M2: $k_{\mathrm{QB}} u_1 = 5.3958 - i0.01756$, M3: $k_{\mathrm{QB}} u_1 = 5.3993 - i0.0154$, M4: $k_{\mathrm{QB}} u_1 = 5.4078 - i0.0133$]. (b-c) Map of $\log|\det[\mathbf{T}]|$ in the complex K plane for two different values of the exterior frequency k (purely real). Each QB state can be associated to a unique CF state, allowing the use of the same labels for QB and CF states.

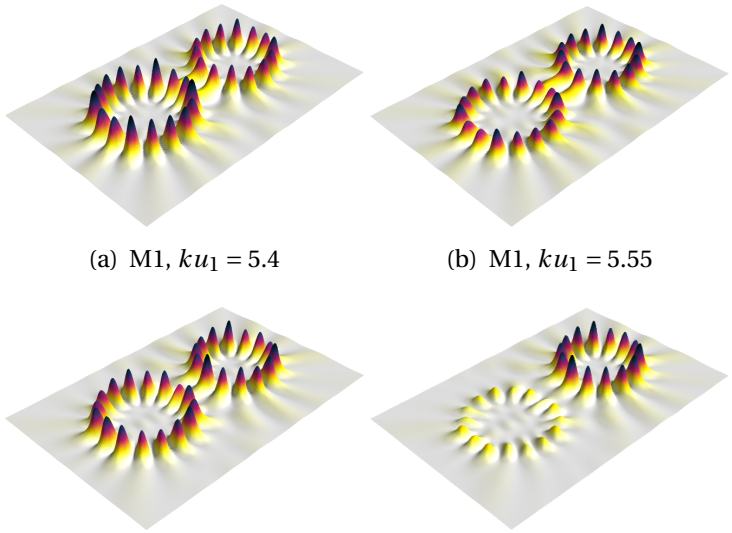

(a) M1, $ku_1 = 5.4$ (b) M1, $ku_1 = 5.55$

(c) M4, $ku_1 = 5.4$ (d) M4, $ku_1 = 5.55$

Figure 7.4 – Profile of two TM-polarized CF states of a diatomic photonic molecule, counterparts to the QB states M1 and M4 shown in Fig. 7.2. These profiles are computed for the same values of the exterior frequency used in Figs. 7.3b and 7.3c. The z-coordinate is proportional to the intensity (arbitrary units).

7.3.1 Influence of gain medium parameters

As stated previously, the computation of QB states cannot account for the influence of the gain center frequency and width on the lasing characteristics of a PM. However, if the exterior frequency k is chosen to be close to the frequency $\mathrm{Re}[k_{\mathrm{QB}}] = k'$ of a QB state, then this state can be associated to a single CF state and their intensity profiles look similar inside the active medium [48]. This correspondence can be seen by comparing the symmetries of the amplitude profiles between Figs. 7.2 and 7.4. For other values of the exterior frequency k, the intensity profiles may look somewhat different, but the one-to-one correspondence with the QB states still holds (see for instance Figs. 7.3 and 7.4).

Since we restrict ourselves to the case of uniform pumping, each QB state shown in Fig. 7.2 is also associated to a TLM, making it possible to keep the same labels and compute the associated TLMs to assess the influence of the gain medium parameters. To achieve this goal, one can devise the following procedure for computing the TLM associated to a single QB state

1. Compute the complex eigenfrequency $k_{\mathrm{QB}} = k' + ik''$ of the QB state.
2. Compute the complex eigenfrequency $K(k')$ of the corresponding CF state, using the fact that $K(k')$ and k_{QB} are usually close [48, 152], as seen in Figs. 7.3a and 7.3b for instance.
3. Compute the values of $K(k)$ in the real neighborhood of k'.
4. Using (7.2.4), map the values of $K(k)$ to values of $D_0(k)$. The TLM is characterized by the pair of values (k_μ, D_0^μ) for which D_0 becomes purely real. An example of this behavior is shown in Fig. 7.5.

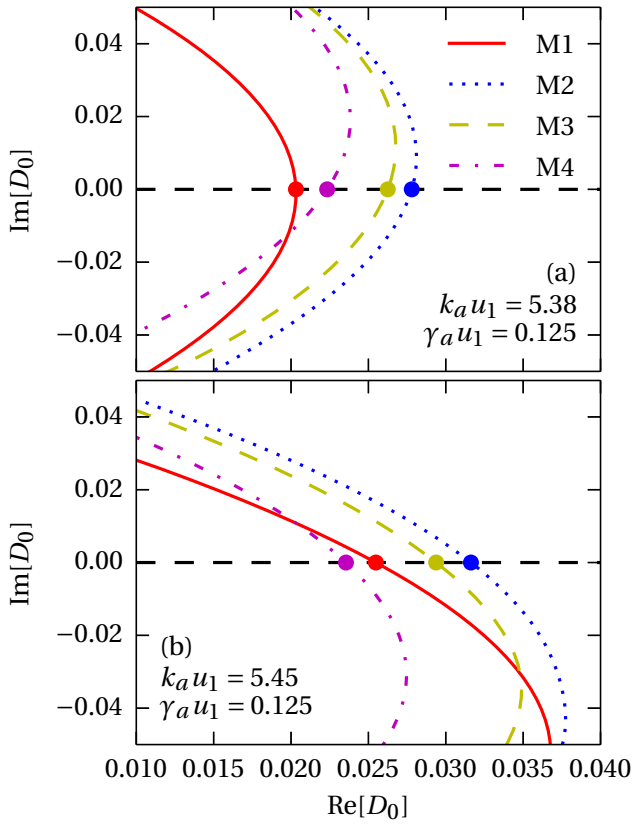

Figure 7.5 – Evolution of complex D_0 values of the four CF states shown in Fig. 7.3 for different values of the gain transition central frequency k_a. The threshold for each mode is given by D_0^μ when $\mathrm{Im}[D_0^\mu] = 0$, indicated by circles on the curves. Note the reversal of M1 and M4 as the first lasing mode when $k_a u_1$ is increased.

Once the values of $K(k)$ are computed using (7.2.11), it is *not* necessary to repeat steps 1–3 when varying the values of k_a and γ_a in step 4 as long as the cavity geometry and pump profile are unchanged.

Using this straightforward approach, the dependence of the lasing thresholds and lasing frequencies on the gain medium parameters can be readily investigated for each of the four modes depicted in Fig. 7.2. We find that the lowest thresholds modes are always M1 and M4 owing to their higher quality factor. Therefore, we restrict our discussion to these two modes. The dependence of the lasing thresholds D_0^1 and D_0^4 on k_a and γ_a is shown in Figs. 7.5–7.7. As expected, M1 is the first lasing mode when the gain center frequency k_a is smaller than the value of k' for that mode. However, as the value of k_a is increased, M1 can still lase first even if k_a is greater than the position of mode M4 (see Fig. 7.7). This is especially true for a large gain width γ_a as mode M1 is able to extract energy more efficiently from the gain transition in that case, while for a narrow gain transition M4 is favored.

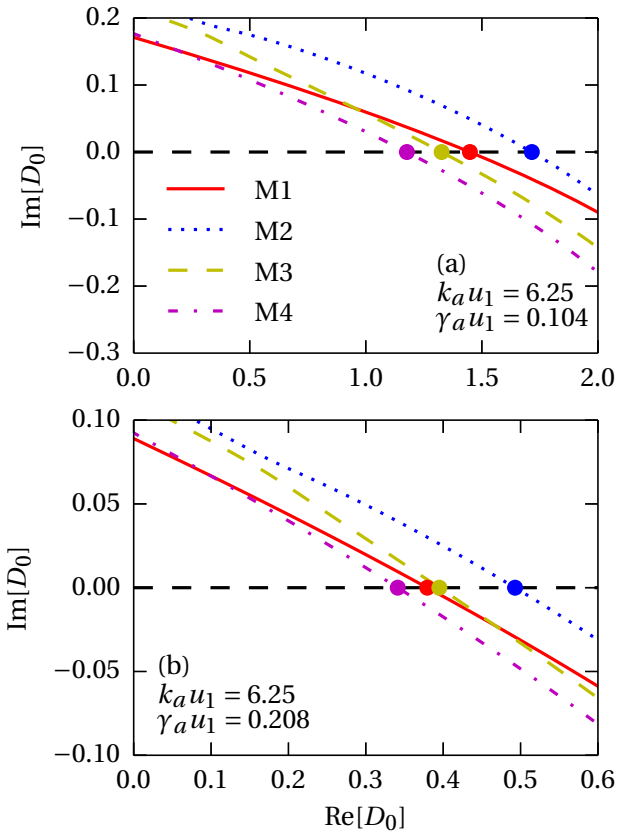

Figure 7.6 – Evolution of complex D_0 values of the four CF states shown in Fig. 7.3 for different values of the gain transition width γ_a. The threshold for each mode is given by D_0^μ when $\mathrm{Im}[D_0^\mu] = 0$, indicated by circles on the curves.

Interestingly, at the intersection of the two surfaces shown in Fig. 7.7, both modes have exactly the same threshold and lase concurrently. Although this lasing behavior is qualitatively consistent with the fact that M1 corresponds to the highest Q cold-cavity mode, the use of SALT is needed to obtain quantitative predictions of its dependence on k_a and γ_a.

It is also instructive to examine the evolution of lasing thresholds when the gain transition center frequency is far from the QB eigenfrequencies. The dependence of D_0^μ on the value of γ_a for a gain transition for large values of $|k - k_a|$ is shown in Fig. 7.6. Our numerical results show that the thresholds of modes approximately quadruple when the value of γ_a is reduced by half. Accordingly, one can derive the following expression for $\mathrm{Re}[D_0]$ from (7.2.4), under the conditions $\mathrm{Im}[D_0] = 0$ and $|k - k_a| \gg \gamma_a$

$$D_0 \simeq -2\epsilon_c \mathrm{Re}[K]\mathrm{Im}[K]\frac{(k-k_a)^2}{\gamma_a^2 k^2}. \tag{7.3.1}$$

This behavior ($D_0 \sim \gamma_a^{-2}$) is consistent with the observation that modes extract energy more efficiently from a broad lasing transition.

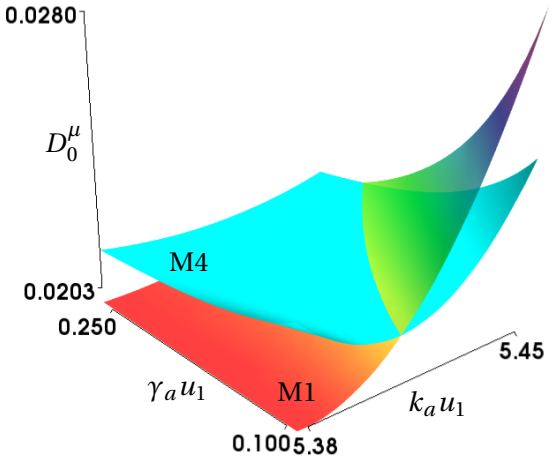

Figure 7.7 – Evolution of lasing thresholds of modes M1 and M4 as a function of the gain center frequency k_a and gain width γ_a. The thresholds of modes M2 and M3 are higher for this range of parameters (not shown).

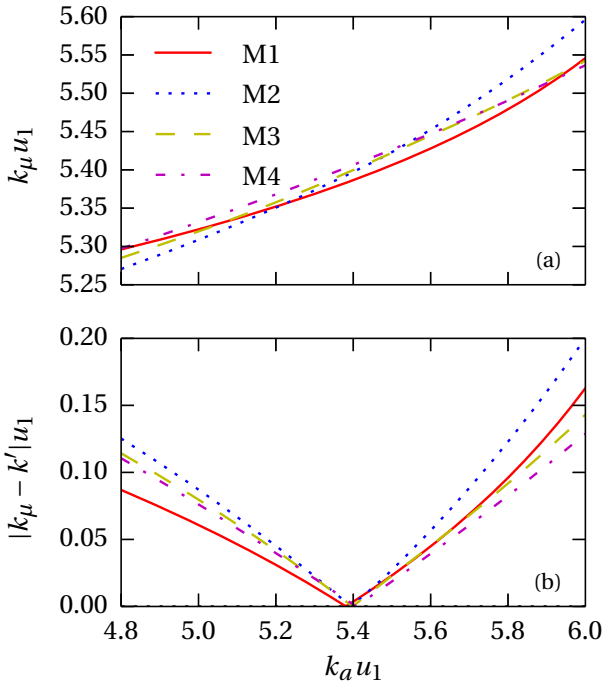

Figure 7.8 – Frequency pulling effect in a simple photonic molecule for $\gamma_a u_1 = 5.4 \times 10^{-2}$. (a) Evolution of the lasing frequency of each TLM as a function of the gain center frequency k_a. (b) Magnitude of the line-pulling effect.

Next, we assess the influence of the gain center frequency k_a on the lasing frequencies of individual modes. The exact lasing frequency of a mode is always shifted by a small amount from the cold-cavity resonance frequency towards the gain center frequency, an effect known as frequency pulling [49, 138]. Since the studied PM geometry exhibits closely spaced lasing modes, this small shift may be of the order of magnitude of the mode spacing. As shown in Fig. 7.8a, the order of the lasing frequencies k_μ can be altered by changing the gain center frequency. For instance, for $k_a u_1 \simeq 5.4$, the lasing frequencies are in the order of the QB eigenfrequencies $(1,2,3,4)$, whereas for $k_a u_1 \simeq 6.0$, the order is $(4,3,1,2)$. This can be explained by the fact that lower Q modes are pulled more strongly. As seen in Fig. 7.8b, mode M2 is generally the most strongly pulled mode. However, for large values of k_a, mode M1 is also subject to strong pulling since it is the mode located further away from the gain center frequency. This result shows that in the case where there are closely spaced cold cavity modes of similar Q-factor, for instance in the vicinity of an EP, the spectral characteristics of the PM laser may be strongly affected by the gain transition parameters.

7.4 Summary and outlook

In summary, we have used the threshold lasing modes of SALT to obtain accurate quantitative predictions of the lasing thresholds and frequencies of a simple diatomic PM composed of two coupled cylinders. These predictions were obtained from the computation of threshold lasing modes using 2D-GLMT. This combination of SALT and 2D-GLMT is general and not limited to diatomic photonic molecules. For instance, it can readily be applied to the computation of modes of random lasers for an arbitrary number of active scattering centers [4].

We found that the lasing thresholds of closely spaced modes of the diatomic PM are strongly influenced by the gain center frequency k_a and its linewidth γ_a. More specifically the order in which modes lase can be changed by a suitable combination of those gain medium parameters. We also highlighted the frequency pulling effect, and found that lower Q modes are usually subject to stronger pulling. These results show the importance of using *ab initio* theories to take the gain medium characteristics into account in microcavities research. Future work includes an extension to non-uniformly pumped PMs, which precludes however the use of the generalized Lorenz-Mie approach. Although this kind of computations may be achieved via a finite-element method [84], we have recently developed a versatile scattering approach [108] that also allows for inhomogeneous pumping and arbitrary 2D geometries. The generalization to 3D geometries is more challenging, although approaches based on solving the underlying differential equations directly have recently been proposed [34]. By combining these various numerical schemes with SALT, the path is laid out to investigate, engineer and harness the lasing properties of PMs for ultra-low threshold and directional single-mode emission.

7.5 Authors' contributions

DG designed the study, carried out the analysis, wrote the numerical codes, performed the computations and wrote the first version of the manuscript. All authors have contributed to the analysis and have been instrumental in bringing the original manuscript to a publishable research contribution.

7.6 Supplement I: Far-field emission profiles

In the main contribution, we have used SALT to highlight the fact that the lasing thresholds of PM lasers may be strongly affected by the underlying gain medium parameters, specifically the gain transition frequency and linewidth. In this supplement, we address a related issue, that is the importance of using SALT to characterize the emission directionality of PMs. Specifically, we illustrate how the emission profile of CF states of PMs can differ from that of QB states. Characterizing far-field emission is an important topic, as directionally emitting microresonators have been the subject of intense research in the last decade [54, 58, 61, 74, 81, 110, 125, 126, 144, 160].

The far-field emission profile of the QB/CF states of a PM can be readily computed using 2D-GLMT. According to the Sommerfeld radiation condition, the field at $\rho \to \infty$ satisfies

$$\lim_{\rho\to\infty} \varphi^E(\rho,\theta) = \varphi^E(\theta)\frac{e^{ik_0\rho}}{\sqrt{k_0\rho}}, \tag{7.6.1}$$

where $\varphi^E(\theta)$ is the far-field distribution, independent of ρ. Applying the asymptotic expansion of cylindrical functions to (7.2.5), one obtains the following expression (derived in supplement A.1.4)

$$\varphi^E(\theta) = \sqrt{\frac{2}{\pi}}e^{i\pi/4}\sum_n \sum_{l,l'=-\infty}^{\infty} b_{nl'}J_{l-l'}(k_0R_n)\exp\left[il\left(\theta-\frac{\pi}{2}\right)+i(l'-l)\phi_n\right], \tag{7.6.2}$$

where (R_n,ϕ_n) is the location of scatterer n in the "global" frame of reference.

As a representative example, we consider a triangular PM composed of three circular photonic atoms of identical relative permittivity $\epsilon = 4$ and radii r_1 arranged on the vertices of an equilateral triangle of side $R_{12} = 2.5r_1$ (see Fig. 7.9). The signature of four QB states of this geometry, as well as the associated CF states, is shown in Fig. 7.10. The QB states are located in the frequency range $5.36 \le k'r_1 \le 5.42$. For a value of the real exterior frequency $k = 5.5$, the eigenfrequencies of the CF states (in the complex K plane) are shifted towards lower frequencies as well, as can be seen from Fig. 7.10b. This situation where the real exterior frequency k is shifted from k' can occur if the central frequency of the gain transition is shifted as well.

In the main contribution, we have shown how shifts in the exterior frequency may affect the lasing thresholds and frequencies of the PM. It was found that the computation of the CF states – a central feature of SALT – is necessary to precisely determine which of the modes will lase first. Another important characteristic of PM lasers which can be affected by such a shift is the emission profile.

To illustrate this, we single out the eigenmode indicated by a white circle in Fig. 7.10. As can be seen in Fig. 7.11, the near-field profile of both the corresponding QB and CF states is rather similar, with the exception that the field of the CF state does not grow exponentially outside the PM. However, the strongest far-field emission direction of CF states does not correspond to that of the QB states. Indeed, the privileged directions are aligned with the triangle vertices in the case of the QB state, whereas they are aligned with the triangle edges in the case of the CF states. Moreover, the CF state far-field profile exhibits three sharper peaks, while there are six peaks in the QB state profile.

This numerical example shows the importance of using SALT for adequate characterization of directional emission. It also hints at using the gain medium as an additional control parameter to harness the emission directionality of microcavities. Pump shape engineering was also proposed as a control knob for directional emission; this is further discussed in section 8.3.

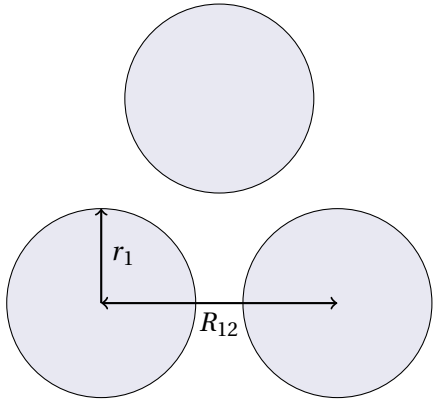

Figure 7.9 – Three identical coupled cylinders arranged on the vertices of an equilateral triangle ($\epsilon_c = 4, R_{12} = 2.5r_1$). This geometry is used to demonstrate the different emission profiles that can be obtained using SALT.

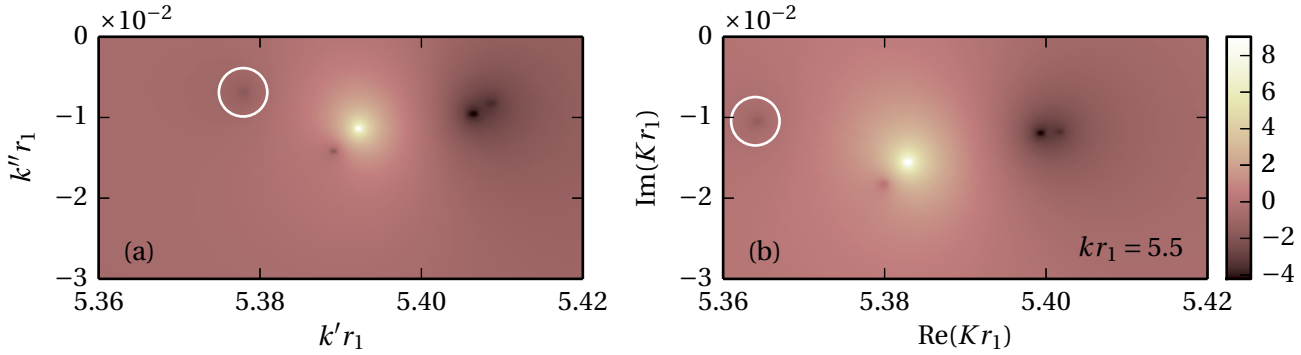

Figure 7.10 – Map of $\log|\det[\mathbf{T}]|$ in the complex k plane (QB states, left panel) and the complex $K(k)$ plane (CF states, right panel). The signature of four eigenmodes of the triatomic PM can be seen as zeros of the determinant of the transfer matrix.

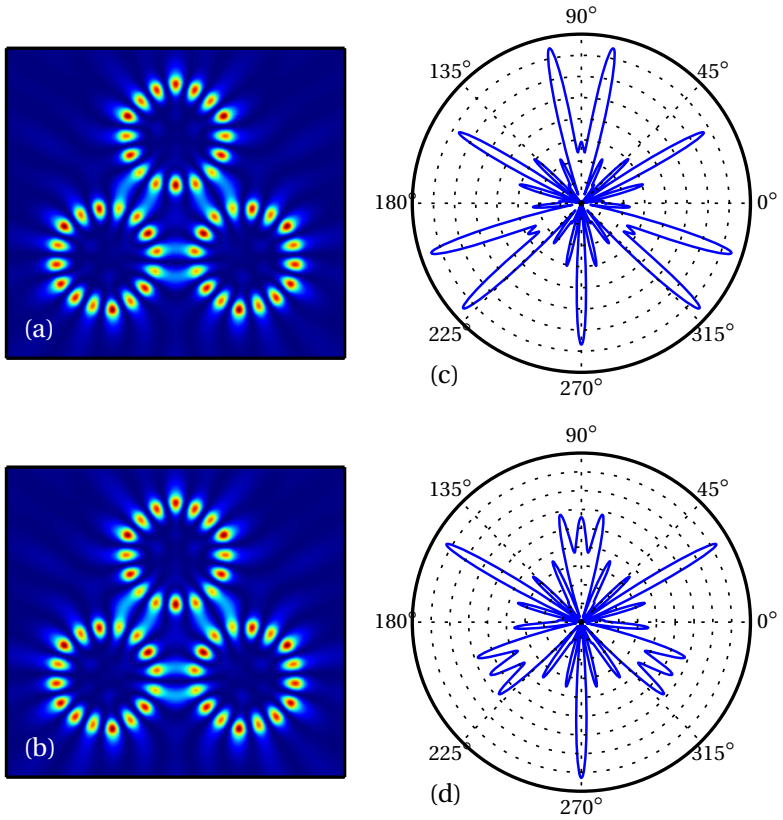

Figure 7.11 – Emission profiles of a photonic molecule. (a) Amplitude profile of a QB state of a triangular PM. (b) Profile of the corresponding CF state. The position of this eigenstate is indicated by a white circle in Fig. 7.10 (c-d) Comparison of the far-field profile $|\varphi^E(\theta)|$ for each of the two kind of eigenstates. Arbitrary intensity units.

7.7 Supplement II: Numerical computation of the eigenmodes

This supplement contains a summary of the numerical method used to compute the eigenmodes (QB and CF states) of an array of coupled cylinders. As stated in the main contribution, the computation of eigenmodes is a non-linear eigenvalue problem of the following form

$$\mathbf{T}(k)\mathbf{b} = 0, \tag{7.7.1}$$

where $\mathbf{T}$ is a square complex matrix. A non-linear eigenvalue problem consists in finding the eigenvalues k and eigenvectors $\mathbf{b}$ satisfying this equation. The theory of linear systems prescribes that non-trivial solutions to this matrix equation exist if and only if

$$\det[\mathbf{T}(k)] = 0. \tag{7.7.2}$$

This class of problems is termed "non-linear" since $\mathbf{T}$ depends non-linearly on k. The usual linear problem is a special case of the non-linear one if one defines [122]

$$\mathbf{T}(k) = \mathbf{A} - k\mathbf{I}, \tag{7.7.3}$$

where $\mathbf{I}$ is the identity matrix and $\mathbf{A}$ is a constant matrix. Nonlinear eigenvalue problems frequently arise in the computation of cavity resonances using various numerical schemes, for instance the well-established boundary element method [41, 59, 165].

While solvers are readily available for linear eigenvalue problems, algorithms for solving the non-linear eigenvalue problem are more complicated. It is possible to solve the non-linear eigenvalue problem either using Newton's method, or using linearization methods that reduce the problem to a sequence of linear ones, as described in [59, 122].

In this work, we use Newton's method to find the eigenmodes, as described in [41, 122]. The goal is to find roots of (7.7.2) numerically. One iteration of Newton's method can be written as

$$k_{n+1} = k_n - \frac{\det[\mathbf{T}(k_n)]}{\det[\mathbf{T}(k_n)]'}, \tag{7.7.4}$$

where k_0 is an initial guess for the eigenvalue (complex wavenumber) and prime symbols indicate the derivative with respect to k. The derivative can be computed using Jacobi's identity [90]

$$\det[\mathbf{T}]' = \det[\mathbf{T}]\mathrm{Tr}\left[\mathbf{T}^{-1}\mathbf{T}'\right], \tag{7.7.5}$$

where $\mathbf{T}'$ is the element-wise derivative of $\mathbf{T}$ with respect to k. This allows one to rewrite one step of Newton's method as

$$k_{n+1} = k_n - \frac{1}{\mathrm{Tr}[\mathbf{T}^{-1}(k_n)\mathbf{T}'(k_n)]}. \tag{7.7.6}$$

The procedure corresponding to this Newton's method is detailed in algorithm 7.7.1. Newton's method is known to converge quadratically to the roots of the determinant if one is located sufficiently close to the said roots. To ensure convergence, the initial guesses for the eigenvalues k_0

must be chosen carefully. In this work, we obtain those initial guesses by evaluating the value of $\det[\mathbf{T}(k)]$ in a region of interest of the complex k plane on a rectangular grid (see for instance Figs. 7.3 and 7.10). Points of this grid corresponding to a change in sign of the function are subsequently used as initial guesses for Newton's method.

Once the roots of (7.7.2) have been found using this algorithm, one simply uses a singular value decomposition routine to obtain the null eigenvector $\mathbf{b}$, which can be used to reconstruct the electromagnetic field profile of the eigenmode using Eq. (7.2.5). This method is general for QB and CF states and is not limited to 2D-GLMT computations. Indeed, it can also be used in conjunction with other methods using transfer matrices, for instance the boundary element method for cavity resonances [41, 59, 165].

Algorithm 7.7.1 : Newton-Raphson procedure for finding roots of $\det|\mathbf{T}|$

Input : Initial guess k_0, step δk, tolerance ε, maximum number of iterations $n_{\max}$

$k := k_0$;
$n := 0$;
while $n < n_{\max}$ **do**
  // Compute one Newton-Raphson step
  $\mathbf{T}_0 := \mathbf{T}(k)$;
  $\mathbf{T}_1 := \mathbf{T}(k+\delta k)$; // $\mathbf{T}_1$ and $\mathbf{T}_2$ are used to compute numerical derivative
  $\mathbf{T}_2 := \mathbf{T}(k+i\delta k)$;
  $\Delta\mathbf{T} := \frac{\mathbf{T}_1 - i\mathbf{T}_2 + (i-1)\mathbf{T}_0}{2\delta k}$; // Numerical derivative
  $\Delta k := -\mathrm{Tr}[\mathbf{T}_0^{-1}\Delta\mathbf{T}]^{-1}$; // Newton-Raphson step
  // Check if error tolerance is reached
  if $\Delta k < \varepsilon$ **then**
    break;
  else
    continue;
  end
  // Apply Newton-Raphson step
  $k := k + \Delta k$;
  $n := n + 1$;
end

Output : Final value k

Chapter 8

Conclusion and outlooks

In recent years, several advances in optics and photonics have involved complex photonic media such as photonic crystals [27], metamaterials [24] and cavity resonators [153]. In this thesis, we have presented the 2D Generalized-Mie theory (2D-GLMT), a method of choice for the modeling of photonic complexes based on coupled cylinders. We have privileged two applications of the theory, namely the design of integrated beam shapers and the modeling of coupled resonators. This has resulted in several research contributions which are summarized in section 8.1. Although they were not necessary to our work, alternative numerical methods that can deal with 3D, asymmetric and inhomogeneous photonic complexes are discussed in section 8.2 We conclude in section 8.3 with a brief discussion of random lasers, another potential application of 2D-GLMT and optimization algorithms.

8.1 Summary of contributions

In chapter 2, we have presented the electromagnetic theory behind 2D-GLMT, which is targeted at computing wave scattering by arrays of coupled cylinders. Specifically, we have considered focused Gaussian beams incident on the arrays and have shown how to compute the scattered wavefunction using 2D-GLMT. Throughout this dissertation, various arrangements of coupled cylinders have been used, up to hundreds of them in beam shaping computations.

Eigenmode computations are an another important application of 2D-GLMT discussed in chapter 2. Furthermore, we have described the recently formulated *steady-state ab initio laser theory* (SALT) in section 2.2. SALT is a stationary formulation of the Maxwell-Bloch equations that allows to model complex active geometries such as coupled resonators and random lasers. Although most of our research contributions have been centered on passive optical media, SALT was thoroughly used for the modeling of active media in chapter 7.

In chapter 3, we have presented metaheuristics, optimization algorithms which are central to the beam shaping computations carried out in this thesis. The reason is that these computations in-

volve solving a combinatorial optimization problem, for which there exists a finite (albeit large) number of solutions. The goal of this chapter is to give guidelines concerning two kinds of metaheuristics that can be useful for combinatorial optimization in optics and photonics. One of those is the canonical genetic algorithm (GA), a stochastic, population-based algorithm which is commonly used in the photonics research community. The other algorithm, tabu search (TS) is less usual and consists in exploring the solution space of an optimization problem using deterministic rules and a *memory* of past visited configurations.

Chapters 4 to 6 of this thesis have been concerned with designing integrated optical elements using 2D-GLMT in conjunction with metaheuristic algorithms. Our first publication using this combination of numerical tools has been presented in chapter 4. Its objective was the design of an integrated optical element dedicated to laser beam shaping, the conversion of an input beam into an output beam of predefined amplitude profile. To achieve this goal, we have proposed the use of a 2D photonic lattice engineered using a canonical GA. We have presented lattice configurations tailored for the generation of Hermite-Gauss beams of order 1 and 2. The tolerance of the configurations to variations in parameters of the input beam, more specifically its depth of field and wavelength, were also quantified. Overall, this contribution shows the potential of engineered photonic crystal lattices for the design of small footprint optical elements dedicated to beam shaping.

In chapter 5, we have extended the approach presented in chapter 4 by considering the generation of beams of controlled amplitude *and* phase profile. The control of the phase profile allows the generation of beams with a larger field depth, in other words exhibiting a better collimation. Once again, the proposed beam shapers are based on an optimized 2D photonic lattice. Whereas the amplitude-only beam shaping problem has been tackled using the GA, the amplitude and phase beam shaping problem is a *multiobjective* one. Since multiobjective optimization requires a more exhaustive search, we have proposed to use a parallel implementation of tabu search (PTS) instead of the canonical GA. After assessing the performance of PTS, we have shown that the algorithm is suited not only to the handling of multiple objective functions, but also to larger solution spaces. In summary, this contribution shows that PTS represents a robust alternative to the canonical GA for combinatorial and multiobjective optimization problem in photonics design. This has been achieved using the incoherent beam shaping problem as a benchmark. The study has subsequently been extended to coherent beam shaping using this improved performance.

A third contribution on beam shaping has been presented in chapter 6. In this study, we once again have considered a multiobjective beam shaping problem, as in chapter 5. However, we have replaced the objective function related to the phase front of the output beam by an objective function related to its degree of polarization. Using PTS optimization, we have shown that it is possible to use a basic lattice configuration consisting of holes in a waveguide core to filter out the TE polarization component of the incident beam. Similarly, we have found that a rods-in-air configuration is more suited to filtering out the TM polarization. This contribution shows the possibility to create integrated polarization filters using the structures studied in chapters 4 and 5. Since polarization

is a physical dimension of light that can be used to carry information, the proposed devices could find applications in the field of optical communications.

The final contribution presented in chapter 7 differs slightly from the beam shaping computations of the preceding chapters. In this work, we have presented a study of the lasing thresholds of a photonic molecule (PM) composed of two coupled active cylinders. More specifically, we have used the 2D-GLMT approach combined with SALT for the computation of the resonances of this very simple cylinder array. The goal of this contribution is to show that the lasing thresholds, spectral characteristics and emission profile of coupled resonators exhibit a non-trivial dependence on the parameters of the underlying laser transition, a conclusion that can not be obtained using the more usual approach of quasi-bound modes. This conclusion was reached via the computation of the threshold lasing modes (TLMs) of the PM, a new kind of eigenstate central to the SALT theory.

8.2 Alternative numerical schemes

Numerical schemes for the solution of Maxwell's equations can be classified in two broad categories. The first category of methods are based on the expansion of the electromagnetic field in a basis of functions suited to the problem geometry. In other words, these methods exploit a physical symmetry of the problem. The second category of methods are based on some kind of spatial and temporal discretization of the problem, necessary in the absence of useful geometrical symmetries.

The 2D-GLMT approach, based on cylindrical function expansions, falls into the first category. For the purposes of this dissertation, this algorithm was particularly appealing because it does not require any spatial discretization Other arguments in favor of the use of 2D-GLMT for the modeling of photonic complexes are its numerical stability (especially considering the improvement proposed in section 2.3.6) and its relative speed. However, despite these advantages, the method as presented in section 2.3 is inherently limited to homogeneous coupled cylinders, in other words to piecewise continuous refractive index distributions separated by circular interfaces contained in a 2D plane. Although these limitations were acceptable for our purposes, they are an impediment when considering either (a) 3D geometries, (b) asymmetric scatterers or (c) inhomogeneous refractive indices. In this section, we enumerate some research areas where one or more of these three conditions preclude the use of 2D-GLMT and summarize which alternative numerical schemes may be of use in these cases.

This dissertation was mainly concerned with 2D photonic-crystal-like geometries which can be easily fabricated using electron beam lithography, for instance. Although 2D structures lend themselves better to the introduction of lattice defects than 3D structures, many interesting effects have been observed in the latter. For instance, researchers have recently demonstrated flat lensing using a 3D woodpile PhC [92]. Photonic bandgap switching is another recently proposed application of 3D PhCs [123]. This is achieved using an "inverse-opal" geometry, consisting of closely packed

arrangements of spherical voids surrounded by dielectric material [7]. In the case of a periodic 3D crystal, the bandgap analysis can still be performed using the plane wave expansion method [7, 73]. However, it is often necessary to consider finite, photonic-crystal-like structures as was done in this thesis. In that case, the method of choice encountered in the literature is the finite-difference time-domain (FDTD) approach, a systematic fully vectorial method based on a spatial and temporal discretization of the problem [7, 27, 92, 148]. Generalized Lorenz-Mie approaches can also be used to compute the scattering of arbitrary shaped beams by arrangements of spheres, using spherical instead of cylindrical harmonics expansions [55]. This numerical method could be used for the modeling of PMs composed of coupled spherical resonators. However, as with the 2D version, it is limited to individually homogeneous spheres.

Asymmetric resonant cavities (ARCs), consisting of deformed circular resonators, are another research topic related to the PM lasers discussed in this dissertation [54, 58, 81, 82, 101, 132, 137, 147]. As mentioned earlier, the achievement of directionally emitting compact laser sources is one of the main goals of ARCs [54]. Several numerical methods for the computation of eigenmodes of deformed cavities are available in the scientific literature. One of these is the boundary element method (BEM), which is based on the Green's function of the Helmholtz equation [41, 165]. This method is especially suited to asymmetric but homogeneous cavities, in which case the Helmholtz equation can be recast in a boundary integral equation. A discrete form of this integral equation is then solved numerically to obtain the eigenfrequencies and the eigenmodes of the ARC, similar to the approach described in section 2.3.5.

Throughout this dissertation, we have solely considered photonic complexes composed of homogeneous cylinders, in other words piecewise continuous refractive index distributions. However, inhomogeneous and partially pumped resonators have been the object of many recent publications [5, 10, 11, 34, 66, 84]. This corresponds to a dielectric distribution $\epsilon(\mathbf{r})$ that varies inside a single resonator, possibly following a smooth function. As discussed in section 8.3, pumping a laser in a non-uniform way is another method to tune its emission profile or lasing threshold. The numerical modeling of inhomogeneous or partially pumped optical media represents an additional challenge since the spatial discretization of inhomogeneous regions is unavoidable. This not only precludes the use of 2D-GLMT, but also that of BEM. One method that is able to deal with asymmetric boundaries and inhomogeneous refractive indices consists in computing the characteristic modes of the cavity via a numerically constructed scattering matrix [108]. This method, like 2D-GLMT and BEM, naturally takes the Sommerfeld radiation condition into account, allowing one to avoid the use of artificial boundary conditions provided by perfectly matched layers, for instance. However, it is more suited for the computation of eigenfrequencies since reconstructing the field using this scattering matrix method turns out to be numerically unstable [109].

It is important to note that the development of algorithms designed to deal with partially pumped media has closely paralleled that of SALT. For instance, Esterhazy *et al.* have recently developed a high-order finite-element method (FEM) for the discretization of non-uniform pump profiles

[34, 84]. Their algorithm is designed to solve directly the differential equations of SALT for arbitrary refractive index distributions, completely eschewing the CF states presented in section 2.2.2. Although efficient mostly for symmetrical or low-dimensional resonators, the computation of the CF states for inhomogeneous and/or 3D geometries turns out to be numerically expensive [34]. This high-order FEM algorithm is perhaps the most promising approach to obtain stationary solutions of the Maxwell-Bloch equations for active, inhomogeneous and complex photonic media. Indeed, besides not being limited by symmetry considerations, it yields full-vectorial solutions that include the lasing frequencies, thresholds and field patterns.

In retrospect, the 2D-GLMT approach used in this dissertation was particularly appealing because of its speed, which in turn has been instrumental in solving the beam shaping problem in a reasonable amount of time. Indeed, since the use of metaheuristics to solve optimization problems often necessitates numerous objective function evaluations, it is profitable to use a fast algorithm to carry out these repeated evaluations. Moreover, the speed of 2D-GLMT has been useful to our contributions on PM lasers since it has allowed us to characterize the impact of gain medium parameters in an exhaustive way for a simple, symmetrical geometry. To further characterize 3D, inhomogeneous or asymmetric photonic complexes, however, alternative numerical schemes compatible with SALT – such as FDTD and FEM – may be preferable.

8.3 Modes of random lasers and pump engineering

A laser is often understood as being composed of a cavity resonator, an active medium and a mechanism allowing the pumping of the lasing transitions. Laser action takes place when the photon generation rate exceeds the losses of the cavity resonator [138]. Scattering in a laser cavity is often seen as detrimental because it leads to additional losses, and thus an increased threshold. However, lasing in strongly scattering active media is also possible and leads to what is commonly called a *random laser* [19]. In a random laser, there is no well-defined resonator since the feedback for laser oscillation is provided by multiple scattering by wavelength-scale obstacles rather than by repeated round-trips in a conventional resonator of dimensions much larger than the wavelength [19]. Although the scattering of photons in such a laser is inherently random, it is also coherent, which means interference effects occur. Thus, a random laser does not possess mirrors, but it possesses modes owing to coherent feedback [166].

Random lasers may well find applications such as tumor detection [166] and optical trapping [120]. They are appealing structures because of their potentially very small size, low-cost and ease of fabrication [19]. Indeed, the realization of random lasers using optically pumped active “powders” has been demonstrated experimentally [19]. It is also possible to fabricate disordered lasers in a more controlled way using photonic-crystal-like structures. This was recently achieved via the etching of cylindrical inclusions in a GaAs planar waveguide, optically activated by layers of InAs quantum dots [120].

This recent interest in random lasers has given rise to a number of possible modeling tools designed to harness the modal characteristics of strongly scattering random media. The potential of 2D-GLMT for the computation of modes of random lasers was first proposed in [4]. In this section, we consider the computation of the constant-flux (CF) states of a large array of active cylinders via 2D-GLMT. The goal of this exercise is to illustrate the main difficulties associated to the computation of modes of random lasers and state some interesting research outlooks.

Using Ref. [39] as a guideline, we assume that an array of identical, non-overlapping rods are uniformly distributed within a circle of radius R_{out} with a predefined surface filling factor. For the purpose of illustration, we consider one realization of an array with $R_{\text{out}} = 40$, normalized with respect to the radius of individual rods ($r = 1$). We set the filling factor to 0.2, which translates to an array containing 320 active scatterers. The relative permittivity of the cylinders is set to $\epsilon_c = 4$. The geometry of the resulting array is shown in Fig. 8.1. This arrangement of cylinders provides a useful, albeit simplified, model of a 2D random laser.

The method for computing CF states described in section 7.7 can be applied to find those of the random array with little modification. The main difficulty lies in the much greater computation time for the determinant $\det[\mathbf{T}]$ of the transfer matrix describing the laser. Moreover, the number of states in a given wavenumber interval is also greater, as seen in Fig. 8.2a. Using a sufficiently fine sampling of the complex K plane, we are able to obtain estimates for the position of a number of CF states (see Fig. 8.2b). These estimates can subsequently be refined using the procedure described in section 7.7. The field distribution of one of these CF states is shown in Fig. 8.2c. For this value of the surface filling factor, the scattering strength of the system is modest and the CF state intensity extends to the whole surface of the random laser. If scattering is stronger, the eigenmodes of the system can become *localized*, meaning the strength of the scattering effectively creates a closed cavity which results in spatial confinement of the mode. This is called the strong scattering, or Anderson-localized regime [167].

The computation of the field distribution with this fine resolution takes several hours due to the large number of cylindrical harmonics that contribute to the total wavefunction at a given point in space. Moreover, stocking the transfer matrices associated to this geometry implies important memory requirements. For these reasons, we have not yet performed random laser computations in the strong scattering regime since this requires considering higher filling factors, and consequently important computational resources.

A research topic strongly related to the study of random lasers is the engineering of pump profiles in complex laser resonators. In all computations presented in this thesis, including the CF state shown in Fig. 8.2c, we have been concerned with *uniform pumping*, meaning that all scatterers composing the laser were supposed active. Another case of uniform pumping frequently encountered in the literature is a random laser composed of passive inclusions in a uniform active medium. *Partial pumping*, on the other hand, implies only a subset of the scatterers (or back-

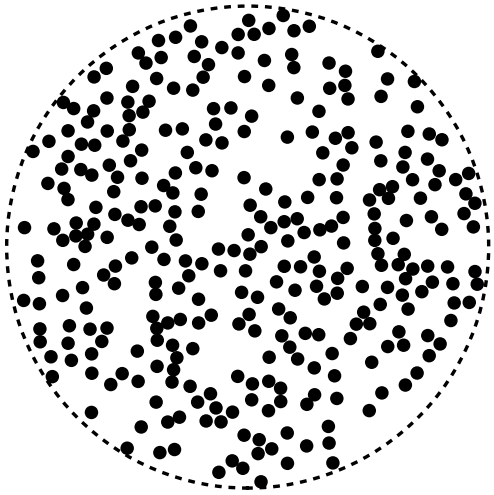

Figure 8.1 – Possible realization of a random laser composed of 320 identical active cylinders of permittivity $\epsilon_c = 4$.

ground medium) are pumped. Partially pumped lasers have been the object of several numerical and experimental studies in recent years [4, 5, 10, 11, 66, 85]. This stems from the fact that partial (or non-uniform) pumping allows to control not only the modal output profile of a laser, but also its lasing threshold and spectral properties [5]. Liertzer *et al.* have shown how to turn on and off a coupled cavity laser by engineering the pump shape, even though the lasing threshold is reached [84]. In the case of random lasers, pump shape engineering yields an additional control parameter to harness emission characteristics without having to engineer the shape of the laser cavity itself, which remains random [5]. For instance, Bachelard *et al.* have demonstrated how to favor certain lasing modes by optimizing the spatial pump profile in real-time [10, 11].

A great deal of research concerning random lasers remains to be made. As stated by Andreasen *et al.*, the theory of partially pumped lasers is not yet full-fledged [5]. Another unanswered question is the link between modes of random lasers and statistical models based on random matrix theory [4]. In summary, the tools used in this thesis (2D-GLMT and SALT), as well as those described in section 8.2, constitute a framework of choice for the study of complex, disordered and random photonic media, a field that has witnessed considerable growth in the past decade [19, 120, 151, 166, 167].

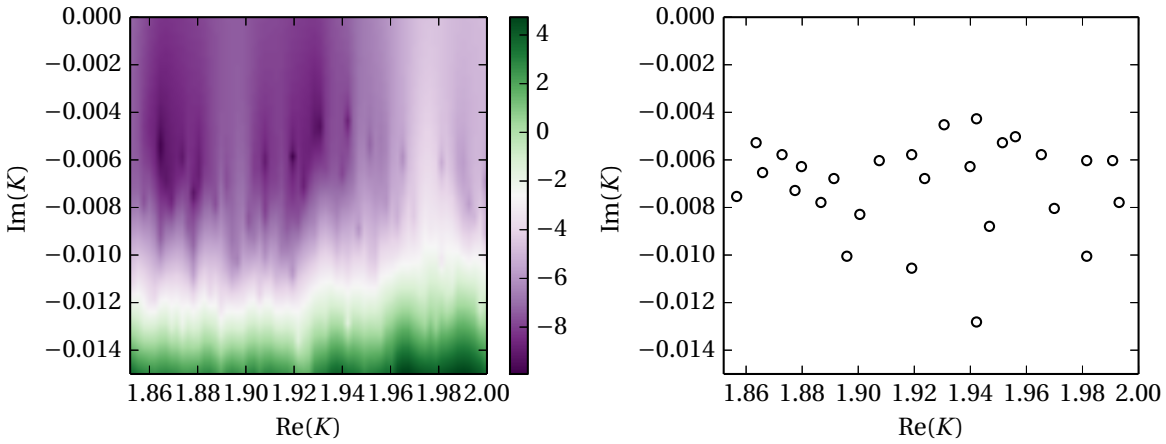

(a) $\log|\det[\mathbf{T}]|$

(b) CF state position predictors

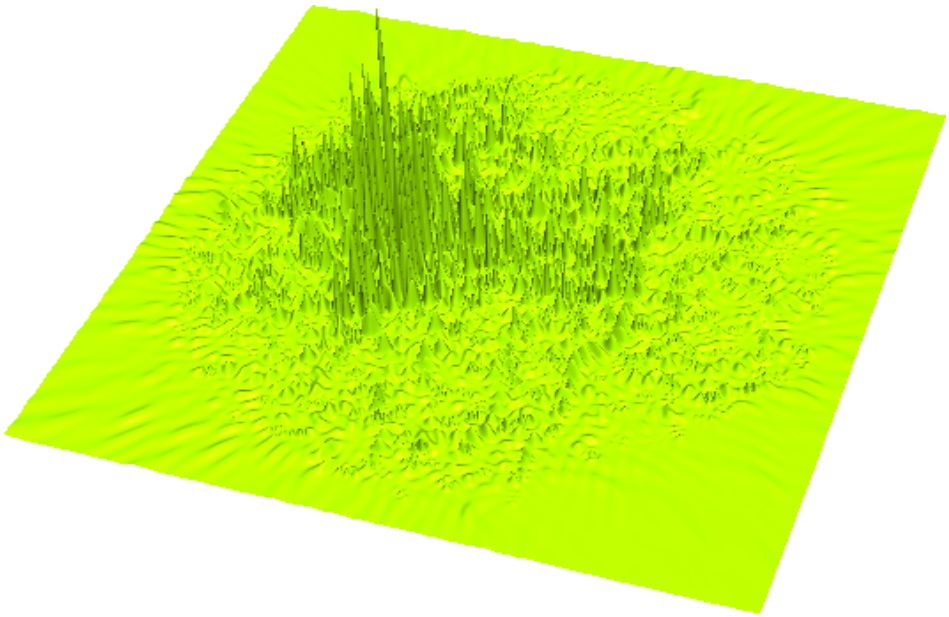

(c) CF state ($K = 1.9420 - 0.004i$)

Figure 8.2 – Determination of CF states for the geometry shown in Fig. 8.1. (a) Evolution of $\log|\det[\mathbf{T}]|$ in the complex $K(k = 2)$ plane. (b) Predictors of the position of various CF states of the random laser. These correspond to local minima in the surface defined by $\log|\det[\mathbf{T}]|$. (c) Intensity distribution $|\varphi|^2$ of a single CF state with $K = 1.9420 - 0.004i$. The z coordinate is proportional to the intensity.

Appendix A

Various algebraic results

A.1 Two-dimensional generalized Lorenz-Mie theory

This section contains various algebraic results, mainly the computation of the spatial derivatives of field expressions of the 2D-GLMT.

A.1.1 Computation of spatial derivatives

Let $\mathbf{r}_n = (\rho_n, \theta_n)$ be the cylindrical coordinate system whose center is located at $\mathbf{R}_n = (X_n, Y_n)$, which implies $\rho_n^2 = (x - X_n)^2 + (y - Y_n)^2$. Field expansions of the following form are ubiquitous in the formulation of 2D-GLMT

$$h_l(\rho_n, \theta_n) = \mathscr{F}_l(k\rho_n) e^{il\theta_n}, \tag{A.1.1}$$

where $\mathscr{F}_l$ denotes $J_l, Y_l, H_l^{(+)}, H_l^{(-)}$ or any linear combination of these functions. The Cartesian derivatives of this function are given by

$$\frac{\partial h_l}{\partial x} = e^{il\theta_n} \left\{ il\mathscr{F}_l(k\rho_n) \frac{\partial \theta_n}{\partial x} + k\mathscr{F}_l'(k\rho_n) \frac{\partial \rho_n}{\partial x} \right\}, \tag{A.1.2a}$$

$$\frac{\partial h_l}{\partial y} = e^{il\theta_n} \left\{ il\mathscr{F}_l(k\rho_n) \frac{\partial \theta_n}{\partial y} + k\mathscr{F}_l'(k\rho_n) \frac{\partial \rho_n}{\partial y} \right\}, \tag{A.1.2b}$$

where prime symbols denote differentiation with respect to the whole argument. Using the following definition of θ_n

$$\theta_n = \tan^{-1}\left(\frac{y - Y_n}{x - X_n} \right), \tag{A.1.3}$$

we obtain

$$\frac{\partial \theta_n}{\partial x} = -\frac{1}{1 + \left(\frac{y - Y_n}{x - X_n} \right)^2} \frac{y - Y_n}{(x - X_n)^2} = -\frac{y - Y_n}{\rho_n^2}, \tag{A.1.4a}$$

$$\frac{\partial \theta_n}{\partial y} = -\frac{1}{1 + \left(\frac{y - Y_n}{x - X_n} \right)^2} \frac{1}{x - X_n} = \frac{x - X_n}{\rho_n^2}. \tag{A.1.4b}$$

We can also compute the derivatives of ρ_n

$$\frac{\partial \rho_n}{\partial x} = \frac{y - Y_n}{\rho_n}, \tag{A.1.5a}$$

$$\frac{\partial \rho_n}{\partial y} = \frac{x - X_n}{\rho_n}. \tag{A.1.5b}$$

Inserting (A.1.4) and (A.1.5) into (A.1.2), we obtain

$$\frac{\partial h_l}{\partial x} = \frac{e^{il\theta_n}}{\rho_n}\left\{-\frac{y - Y_n}{\rho_n} il\mathscr{F}_l(k\rho_n) + k(x - X_n)\mathscr{F}_l'(k\rho_n)\right\}, \tag{A.1.6a}$$

$$\frac{\partial h_l}{\partial y} = \frac{e^{il\theta_n}}{\rho_n}\left\{\frac{x - X_n}{\rho_n} il\mathscr{F}_l(k\rho_n) + k(y - Y_n)\mathscr{F}_l'(k\rho_n)\right\}. \tag{A.1.6b}$$

Also useful are the derivatives of the incident excitation with respect to Cartesian coordinates. For a plane wave incident from the negative x-axis, we have

$$h^0(x, y) = e^{ikx}, \tag{A.1.7}$$

which implies

$$\frac{\partial h^0}{\partial x} = ike^{ikx} \quad , \quad \frac{\partial h^0}{\partial y} = 0. \tag{A.1.8}$$

For an incident complex-source beam (CSB), we have

$$h^0(x, y) = H_0^{(+)}(kr_s), \tag{A.1.9}$$

where $r_s = \sqrt{y^2 + (x - ix_R)^2}$. Using equation (9.1.28) from Ref. [1], we obtain

$$\frac{\partial h^0}{\partial x} = -kH_1^{(+)}(kr_s)\frac{\partial r_s}{\partial x} = -k\left(\frac{x - ix_R}{r_s}\right)H_1^{(+)}(kr_s), \tag{A.1.10a}$$

$$\frac{\partial h^0}{\partial y} = -kH_1^{(+)}(kr_s)\frac{\partial r_s}{\partial y} = -\frac{ky}{r_s}H_1^{(+)}(kr_s). \tag{A.1.10b}$$

A.1.2 Longitudinal field components

The general solution method of 2D-GLMT involves uncoupling both polarizations of the electromagnetic field and solving either for E_z or H_z. However, it is sometimes useful to have access to the in-plane vector components of the field. In this section, we give useful expressions for these longitudinal components.

A.1.2.1 TM polarization

In the case of TM polarization, the longitudinal field is the magnetic field $\mathbf{H}$, given by

$$\mathbf{H} = -\frac{i}{k}\nabla \times \mathbf{E} = -\frac{i}{k}\left[\frac{\partial E_z}{\partial y}\hat{\mathbf{e}}_x - \frac{\partial E_z}{\partial x}\hat{\mathbf{e}}_y\right]. \tag{A.1.11}$$

Let E_z be expanded in the following way

$$E_z = \sum_{l=-\infty}^{\infty} b_{nl} H_l^{(+)}(k\rho_n) e^{il\theta_n}. \tag{A.1.12}$$

Using (A.1.6), we obtain the following longitudinal components

$$H_x = -\frac{i}{k} \sum_{l=-\infty}^{\infty} b_{nl} \frac{e^{il\theta_n}}{\rho_n} \left\{ \frac{x - X_n}{\rho_n} il H_l^{(+)}(k\rho_n) + k(y - Y_n) H_l^{(+)\prime}(k\rho_n) \right\}, \tag{A.1.13a}$$

$$H_y = -\frac{i}{k} \sum_{l=-\infty}^{\infty} b_{nl} \frac{e^{il\theta_n}}{\rho_n} \left\{ \frac{y - Y_n}{\rho_n} il H_l^{(+)}(k\rho_n) - k(x - X_n) H_l^{(+)\prime}(k\rho_n) \right\}. \tag{A.1.13b}$$

The longitudinal field components of a TM-polarized incident CSB can also be computed from (A.1.10)

$$H_x^0 = \frac{iy}{r_s} H_1^{(+)}(kr_s), \tag{A.1.14a}$$

$$H_y^0 = -i \left(\frac{x - ix_{\mathrm{R}}}{r_s} \right) H_1^{(+)}(kr_s). \tag{A.1.14b}$$

A.1.2.2 TE polarization

In the case of TE polarization, the longitudinal field is the electric field **E**, given by

$$\mathbf{E} = \frac{i}{n^2 k} \nabla \times \mathbf{H} = \frac{i}{n^2 k} \left[\frac{\partial H_z}{\partial y} \hat{\mathbf{e}}_x - \frac{\partial H_z}{\partial x} \hat{\mathbf{e}}_y \right]. \tag{A.1.15}$$

Let H_z be expanded in the following way

$$H_z = \sum_{l=-\infty}^{\infty} b_{nl} H_l^{(+)}(k\rho_n) e^{il\theta_n}. \tag{A.1.16}$$

Using (A.1.6), we obtain the following longitudinal components

$$E_x = \frac{i}{n^2 k} \sum_{l=-\infty}^{\infty} b_{nl} \frac{e^{il\theta_n}}{\rho_n} \left\{ \frac{x - X_n}{\rho_n} il H_l^{(+)}(k\rho_n) + k(y - Y_n) H_l^{(+)\prime}(k\rho_n) \right\}, \tag{A.1.17a}$$

$$E_y = \frac{i}{n^2 k} \sum_{l=-\infty}^{\infty} b_{nl} \frac{e^{il\theta_n}}{\rho_n} \left\{ \frac{y - Y_n}{\rho_n} il H_l^{(+)}(k\rho_n) - k(x - X_n) H_l^{(+)\prime}(k\rho_n) \right\}. \tag{A.1.17b}$$

The longitudinal field components of a TM-polarized incident CSB can also be computed from (A.1.10)

$$E_x^0 = -\frac{i}{n^2} \frac{y}{r_s} H_1^{(+)}(kr_s), \tag{A.1.18a}$$

$$E_y^0 = \frac{i}{n^2} \left(\frac{x - ix_{\mathrm{R}}}{r_s} \right) H_1^{(+)}(kr_s). \tag{A.1.18b}$$

A.1.3 Time-averaged Poynting vector

The time-averaged Poynting vector measures the average power density flowing through a surface. It is defined as [21]

$$\langle \mathbf{S} \rangle = \frac{1}{2} \mathrm{Re}[\mathbf{E} \times \mathbf{H}^*]. \tag{A.1.19}$$

In this subsection, we derive an expression for $\langle \mathbf{S} \rangle$ in TM polarization, and give the result for TE, the derivation being similar.

A.1.3.1 TM polarization

The cross product can be expressed as a determinant

$$\mathbf{E} \times \mathbf{H}^* = \begin{vmatrix} \hat{\mathbf{e}}_x & \hat{\mathbf{e}}_y & \hat{\mathbf{e}}_z \\ 0 & 0 & E_z \\ H_x^* & H_y^* & 0 \end{vmatrix} = -E_z H_y^* \hat{\mathbf{e}}_x + E_z H_x^* \hat{\mathbf{e}}_y. \tag{A.1.20}$$

Using (A.1.11), and substituting (A.1.20) into (A.1.19) we obtain

$$\langle S_x \rangle = -\frac{1}{2k} \mathrm{Im}\left[E_z E_{zx}^*\right], \tag{A.1.21a}$$

$$\langle S_y \rangle = -\frac{1}{2k} \mathrm{Re}\left[E_z E_{zy}^*\right], \tag{A.1.21b}$$

where the second subscript indicates partial differentiation. We can further split the fields in real and imaginary parts, using the notation $U \equiv U' + iU''$, which yields

$$\begin{aligned} \langle S_x \rangle &= -\frac{1}{2k} \mathrm{Im}\left[E_z' E_{zx}' + E_z'' E_{zx}'' + i E_{zx}' E_z'' - i E_z' E_{zx}''\right] \\ &= \frac{1}{2k}\left[E_z' E_{zx}'' - E_{zx}' E_z''\right], \end{aligned} \tag{A.1.22a}$$

and similarly

$$\langle S_y \rangle = \frac{1}{2k}\left[E_z' E_{zy}'' - E_{zy}' E_z''\right]. \tag{A.1.22b}$$

A.1.3.2 TE polarization

The computation for the orthogonal polarization is similar, and we only state the result here. The main difference is the appearance of the refractive index in the final expressions, due to a similar occurrence in (A.1.15).

$$\langle S_x \rangle = \frac{1}{2k} \mathrm{Re}\left[\frac{1}{n^2}\right]\left(H_z' H_{zx}'' - H_{zx}' H_z''\right), \tag{A.1.23a}$$

$$\langle S_y \rangle = \frac{1}{2k} \mathrm{Re}\left[\frac{1}{n^2}\right]\left(H_z' H_{zy}'' - H_{zy}' H_z''\right). \tag{A.1.23b}$$

21. In the Heaviside-Lorentz system of units, this definition lacks a factor of c [71]. We drop this factor for convenience as we are mostly interested in computing the ratio between the incident and transmitted power, meaning this c factor cancels out.

A.1.4 Derivation of far-field expressions

It is straightforward to compute the far-field emission profiles of resonators based on the 2D-GLMT equations. To achieve this, the field expansions centered on individual scatterers can be recast in a global frame of reference as proposed in Ref. [103]. The starting point is the equation for the scattered wavefunction (2.3.5b), which reads

$$\varphi_s(\mathbf{r}) = \sum_{n=1}^{N} \sum_{l'=-\infty}^{\infty} b_{nl'} H_{l'}^{(+)}(k_0\rho_n) e^{il'\theta_n}. \tag{A.1.24}$$

Using Graf's addition formula, one can displace the $H_{l'}^{(+)}(k_0\rho_n)e^{il'\theta_n}$ function in a "global" frame of reference, say $\mathbf{r} = (\rho,\theta)$. The addition formula gives

$$H_{l'}^{(+)}(k_0\rho_n)e^{il'\theta_n} = \sum_{l=-\infty}^{\infty} H_{l'+l}^{(+)}(k_0\rho) J_l(k_0 R_n) e^{i(l'+l)\theta} e^{-il\phi_n}, \tag{A.1.25}$$

where R_n is the distance between the center of the cylinder n and the origin of the global coordinate system, and ϕ_n is the angular position of cylinder n in that same frame of reference. Inserting (A.1.25) in (A.1.24) yields

$$\varphi_s(\rho,\theta) = \sum_{n=1}^{N} \sum_{l,l'=-\infty}^{\infty} b_{nl'} H_{l'+l}^{(+)}(k_0\rho) J_l(k_0 R_n) e^{i(l'+l)\theta} e^{-il\phi_n}. \tag{A.1.26}$$

The substitution $l \leftarrow l - l'$ can then be made since indices run to infinity. This yields

$$\varphi_s(\rho,\theta) = \sum_{n=1}^{N} \sum_{l,l'=-\infty}^{\infty} b_{nl'} H_{l}^{(+)}(k_0\rho) J_{l-l'}(k_0 R_n) e^{il\theta} e^{i(l'-l)\phi_n}. \tag{A.1.27}$$

Using the Sommerfeld radiation condition, the field at $\rho \to \infty$ can be written as

$$\varphi_s(\rho,\theta) = \varphi_s(\theta) \frac{e^{ik_0\rho}}{\sqrt{k_0\rho}}. \tag{A.1.28}$$

Using the asymptotic expansion of cylindrical functions

$$\lim_{|z|\to\infty} H_l^{(+)}(z) \sim \sqrt{\frac{2}{\pi z}} \exp\left[i\left(z - \frac{l\pi}{2} - \frac{\pi}{4}\right)\right], \tag{A.1.29}$$

in (A.1.27), one finally obtains the following far-field distribution

$$\varphi_s(\theta) = \sqrt{\frac{2}{\pi}} e^{i\pi/4} \sum_{n} \sum_{l,l'=-\infty}^{\infty} b_{nl'} J_{l-l'}(k_0 R_n) \exp\left[il\left(\theta - \frac{\pi}{2}\right) + i(l'-l)\phi_n\right], \tag{A.1.30}$$

where (R_n,ϕ_n) is the location of scatterer n in the "global" frame of reference.

Bibliography

[1] M. Abramowitz and I. A. Stegun, *Handbook of Mathematical Functions*, Dover Publications, June 1970.

[2] A. Al-Qasimi, O. Korotkova, D. James, and E. Wolf, *Definitions of the degree of polarization of a light beam*, Opt. Lett., 32 (2007), pp. 1015–1016.

[3] I. Andonegui, A. Blanco, I. Calvo, and A. J. Garcia-Adeva, *Inverse design of novel nanophotonic structures*, in ICTON Conf. Proc., IEEE, June 2013, pp. 1–7.

[4] J. Andreasen, A. A. Asatryan, L. C. Botten, M. A. Byrne, H. Cao, L. Ge, L. Labonté, P. Sebbah, A. D. Stone, H. E. Türeci, and C. Vanneste, *Modes of random lasers*, Adv. Opt. Photon., 3 (2011), pp. 88–127.

[5] J. Andreasen, N. Bachelard, S. B. N. Bhaktha, H. Cao, P. Sebbah, and C. Vanneste, *Partially pumped random lasers*, Int. J. Mod. Phys. B, 28 (2014), pp. 1430001+.

[6] A. M. Armani, R. P. Kulkarni, S. E. Fraser, R. C. Flagan, and K. J. Vahala, *Label-free, single-molecule detection with optical microcavities*, Science, 317 (2007), pp. 783–787.

[7] D. P. Aryal, K. L. Tsakmakidis, and O. Hess, *Tutorials in Complex Photonics Media*, SPIE, 2009, ch. 8, pp. 179–228.

[8] O. Avayu, O. Eisenbach, R. Ditcovski, and T. Ellenbogen, *Optical metasurfaces for polarization-controlled beam shaping*, Opt. Lett., 39 (2014), pp. 3892–3895.

[9] T. Baba, *Slow light in photonic crystals*, Nat. Photon., 2 (2008), pp. 465–473.

[10] N. Bachelard, J. Andreasen, S. Gigan, and P. Sebbah, *Taming random lasers through active spatial control of the pump*, Phys. Rev. Lett., 109 (2012), pp. 033903+.

[11] N. Bachelard, S. Gigan, X. Noblin, and P. Sebbah, *Adaptive pumping for spectral control of random lasers*, Nat. Phys., 10 (2014), pp. 426–431.

[12] S. V. Boriskina, *Spectrally engineered photonic molecules as optical sensors with enhanced sensitivity: a proposal and numerical analysis*, J. Opt. Soc. Am. B, 23 (2006), pp. 1565–1573.

[13] ——, *Photonic Microresonator Research and Applications*, Springer, 2010, ch. 16, pp. 393–421.

[14] S. BOXWELL, S. G. FOX, AND J. F. ROMAN, *Design and optimization of optical components using genetic algorithms*, Opt. Eng., 43 (2004), pp. 1643+.

[15] R. W. BOYD, *Wave-Equation Description of Nonlinear Optical Interactions*, Elsevier, 2003, ch. 2, pp. 67–127.

[16] J. BREUER AND P. HOMMELHOFF, *Laser-Based acceleration of nonrelativistic electrons at a dielectric structure*, Phys. Rev. Lett., 111 (2013), pp. 134803+.

[17] B. R. BROWN AND A. W. LOHMANN, *Complex spatial filtering with binary masks*, Appl. Opt., 5 (1966), pp. 967–969.

[18] M. CAI, O. PAINTER, K. J. VAHALA, AND P. C. SERCEL, *Fiber-coupled microsphere laser*, Opt. Lett., 25 (2000), pp. 1430–1432.

[19] H. CAO, *Lasing in Random Media – Tutorials in Complex Photonics Media*, SPIE, 2009, ch. 11, pp. 301–358.

[20] K.-W. CHIEN AND H.-P. D. SHIEH, *Design and fabrication of an integrated polarized light guide for Liquid-Crystal-display illumination*, Appl. Opt., 43 (2004), pp. 1830+.

[21] S.-C. C. CHU AND H. L. FANG, *Genetic algorithms vs. tabu search in timetable scheduling*, in Third International Conference on Knowledge-Based Intelligent Information Engineering Systems, IEEE, Dec. 1999, pp. 492–495.

[22] A. CHUTINAN AND S. NODA, *Waveguides and waveguide bends in two-dimensional photonic crystal slabs*, Phys. Rev. B, 62 (2000), pp. 4488–4492.

[23] T. G. CRAINIC, M. TOULOUSE, AND M. GENDREAU, *Toward a taxonomy of parallel tabu search heuristics*, INFORMS J. Comput., 9 (1997), pp. 61–72.

[24] Y. CUI, Y. HE, Y. JIN, F. DING, L. YANG, Y. YE, S. ZHONG, Y. LIN, AND S. HE, *Plasmonic and metamaterial structures as electromagnetic absorbers*, Laser Photon. Rev., 8 (2014), pp. 495–520.

[25] L. DAL NEGRO AND S. V. BORISKINA, *Deterministic aperiodic nanostructures for photonics and plasmonics applications*, Laser Photon. Rev., 6 (2012), pp. 178–218.

[26] A. DARAFSHEH, N. MOJAVERIAN, N. I. LIMBEROPOULOS, K. W. ALLEN, A. LUPU, AND V. N. ASTRATOV, *Formation of polarized beams in chains of dielectric spheres and cylinders*, Opt. Lett., 38 (2013), pp. 4208–4211.

[27] R. M. DE LA RUE AND C. SEASSAL, *Photonic crystal devices: some basics and selected topics*, Laser Photon. Rev., 6 (2012), pp. 564–597.

[28] P. DEL'HAYE, A. SCHLIESSER, O. ARCIZET, T. WILKEN, R. HOLZWARTH, AND T. J. KIPPENBERG, *Optical frequency comb generation from a monolithic microresonator*, Nature, 450 (2007), pp. 1214–1217.

[29] E. A. DESLOGE, *Relation between equations in the international, electrostatic, electromagnetic, Gaussian, and Heaviside-Lorentz systems*, Am. J. Phys., 62 (1994), pp. 601–609.

[30] F. DICKEY AND S. HOLSWADE, *Laser Beam Shaping Applications*, Taylor & Francis, 2005, ch. 8, pp. 269–305.

[31] M. DUOCASTELLA AND C. B. ARNOLD, *Bessel and annular beams for materials processing*, Laser Photon. Rev., 6 (2012), pp. 607–621.

[32] M. EHRGOTT, *Multicriteria Optimization*, Springer-Verlag, 2005.

[33] A. Z. ELSHERBENI AND A. A. KISHK, *Modeling of cylindrical objects by circular dielectric and conducting cylinders*, IEEE Trans. Antennas Propag., 40 (1992), pp. 96–99.

[34] S. ESTERHAZY, D. LIU, M. LIERTZER, A. CERJAN, L. GE, K. G. MAKRIS, A. D. STONE, J. M. MELENK, S. G. JOHNSON, AND S. ROTTER, *Scalable numerical approach for the steady-state ab initio laser theory*, Phys. Rev. A, 90 (2014), p. 023816.

[35] N. C. EVANS AND D. L. SHEALY, *Design and optimization of an irradiance Profile-Shaping system with a genetic algorithm method*, Appl. Opt., 37 (1998), pp. 5216–5221.

[36] D. FELBACQ, G. TAYEB, AND D. MAYSTRE, *Scattering by a random set of parallel cylinders*, J. Opt. Soc. Am. A, 11 (1994), pp. 2526–2538.

[37] L. FELSEN, *Complex rays*, Philips Res. Repts, 30 (1975), pp. 187–195.

[38] L. H. FRANDSEN, P. I. BOREL, Y. X. ZHUANG, A. HARPØTH, M. THORHAUGE, M. KRISTENSEN, W. BOGAERTS, P. DUMON, R. BAETS, V. WIAUX, J. WOUTERS, AND S. BECKX, *Ultralow-loss 3-dB photonic crystal waveguide splitter*, Opt. Lett., 29 (2004), pp. 1623–1625.

[39] G. FUJII, T. MATSUMOTO, T. TAKAHASHI, AND T. UETA, *A study on the effect of filling factor for laser action in dielectric random media*, Appl. Phys. A, 107 (2012), pp. 35–42.

[40] C. GAGNÉ, J. BEAULIEU, M. PARIZEAU, AND S. THIBAULT, *Human-competitive lens system design with evolution strategies*, Appl. Soft Comput., 8 (2008), pp. 1439–1452.

[41] D. GAGNON, *Modélisation ondulatoire de structures optiques résonantes: application aux microcavités diélectriques bidimensionnelles*, Master's thesis, Université Laval, 2011.

[42] D. GAGNON, J. DUMONT, J.-L. DÉZIEL, AND L. J. DUBÉ, *Ab initio investigation of lasing thresholds in photonic molecules*, J. Opt. Soc. Am. B, 31 (2014), pp. 1867–1873.

[43] ——, *Optimization of integrated polarization filters*, Opt. Lett., 39 (2014), pp. 5768–5771.

[44] D. GAGNON, J. DUMONT, AND L. J. DUBÉ, *Beam shaping using genetically optimized two-dimensional photonic crystals*, J. Opt. Soc. Am. A, 29 (2012), pp. 2673–2678.

[45] ——, *Coherent beam shaping using two-dimensional photonic crystals*, in ICTON Conf. Proc., IEEE, July 2013.

[46] ——, *Multiobjective optimization in integrated photonics design*, Opt. Lett., 38 (2013), pp. 2181–2184.

[47] B. GAYRAL, J. M. GÉRARD, A. LEMAÎTRE, C. DUPUIS, L. MANIN, AND J. L. PELOUARD, *High-Q wet-etched GaAs microdisks containing InAs quantum boxes*, Appl. Phys. Lett., 75 (1999), pp. 1908–1910.

[48] L. GE, *Steady-state Ab Initio Laser Theory and its Applications in Random and Complex Media*, PhD thesis, Yale University, 2010.

[49] L. GE, Y. D. CHONG, AND A. D. STONE, *Steady-state ab initio laser theory: Generalizations and analytic results*, Phys. Rev. A, 82 (2010), pp. 063824+.

[50] L. GE, R. J. TANDY, A. D. STONE, AND H. E. TÜRECI, *Quantitative verification of ab initio self-consistent laser theory*, Opt. Express, 16 (2008), pp. 16895–16902.

[51] F. GLOVER, *Tabu Search–Part I*, ORSA J. Comput., 1 (1989), pp. 190–206.

[52] F. GLOVER, J. P. KELLY, AND M. LAGUNA, *Genetic algorithms and tabu search: Hybrids for optimization*, Comp. Oper. Res., 22 (1995), pp. 111–134.

[53] F. W. GLOVER AND M. LAGUNA, *Tabu Search*, Springer, 1997.

[54] C. GMACHL, F. CAPASSO, E. E. NARIMANOV, J. U. NÖCKEL, A. D. STONE, J. FAIST, D. L. SIVCO, AND A. Y. CHO, *High-power directional emission from microlasers with chaotic resonators*, Science, 280 (1998), pp. 1556–1564.

[55] G. GOUESBET AND G. GREHAN, *Generalized Lorenz-Mie theory for assemblies of spheres and aggregates*, J. Opt. A: Pure Appl. Opt., 1 (1999), pp. 706–712.

[56] G. GOUESBET AND J. A. LOCK, *List of problems for future research in generalized Lorenz–Mie theories and related topics, review and prospectus [Invited]*, Appl. Opt., 52 (2013), pp. 897–916.

[57] G. GRIFFEL AND S. ARNOLD, *Synthesis of variable optical filters using meso-optical ring resonator arrays*, in LEOS Conf. Proc., 1997, pp. 165+.

[58] T. HARAYAMA AND S. SHINOHARA, *Two-dimensional microcavity lasers*, Laser Photon. Rev., 5 (2011), pp. 247–271.

[59] P. HEIDER, *Computation of scattering resonances for dielectric resonators*, Comput. Math. Appl., 60 (2010), pp. 1620–1632.

[60] W. D. HEISS, *The physics of exceptional points*, J. Phys. A: Math. Theor., 45 (2012), pp. 444016+.

[61] M. HENTSCHEL, *Optical microcavities as Quantum-Chaotic model systems: Openness makes the difference!*, Adv. Solid State Phys., 48 (2009), pp. 293–304.

[62] R. M. HERMAN AND T. A. WIGGINS, *Production and uses of diffractionless beams*, J. Opt. Soc. Am. A, 8 (1991), pp. 932–942.

[63] A. HERTZ, *Méta-heuristiques.* Notes de cours, École Polytechnique de Montréal.

[64] M. HEUCK, P. T. KRISTENSEN, Y. ELESIN, AND J. MØRK, *Improved switching using Fano resonances in photonic crystal structures*, Opt. Lett., 38 (2013), pp. 2466+.

[65] E. HEYMAN AND L. B. FELSEN, *Gaussian beam and pulsed-beam dynamics: complex-source and complex-spectrum formulations within and beyond paraxial asymptotics*, J. Opt. Soc. Am. A, 18 (2001), pp. 1588–1611.

[66] T. HISCH, M. LIERTZER, D. POGANY, F. MINTERT, AND S. ROTTER, *Pump-controlled directional light emission from random lasers*, Phys. Rev. Lett., 111 (2013), p. 023902.

[67] A. HOFLER, B. TERZIĆ, M. KRAMER, A. ZVEZDIN, V. MOROZOV, Y. ROBLIN, F. LIN, AND C. JARVIS, *Innovative applications of genetic algorithms to problems in accelerator physics*, Phys. Rev. Spec. Top. Accel Beams, 16 (2013), pp. 010101+.

[68] C. HOLDSWORTH, R. D. STEWART, M. KIM, J. LIAO, AND M. H. PHILLIPS, *Investigation of effective decision criteria for multiobjective optimization in IMRT*, Med. Phys., 38 (2011), pp. 2964–2974.

[69] A. IMAMOGLU, *Quantum Computation Using Quantum Dot Spins and Microcavities*, Wiley, 2005, ch. 14, pp. 217–227.

[70] S. ISHII, A. NAKAGAWA, AND T. BABA, *Modal characteristics and bistability in twin microdisk photonic molecule lasers*, IEEE J. Sel. Top. Quant., 12 (2006), pp. 71–77.

[71] J. D. JACKSON, *Classical Electrodynamics*, Wiley, 1962.

[72] C. JIN, N. JOHNSON, H. CHONG, A. JUGESSUR, S. DAY, D. GALLAGHER, AND R. DE LA RUE, *Transmission of photonic crystal coupled-resonator waveguide (PhCCRW) structure enhanced via mode matching*, Opt. Express, 13 (2005), pp. 2295–2302.

[73] S. G. JOHNSON AND J. D. JOANNOPOULOS, *Block-iterative frequency-domain methods for Maxwell's equations in a planewave basis*, Opt. Express, 8 (2001), pp. 173–190.

[74] M.-W. KIM, C.-H. YI, S. RIM, C.-M. KIM, J.-H. KIM, AND K.-R. OH, *Directional single mode emission in a microcavity laser*, Opt. Express, 20 (2012), pp. 13651–13656.

[75] D. E. KNUTH, *Structured programming with go to statements*, Comput. Serv., 6 (1974), pp. 261–301.

[76] H. KURT, *Limited-diffraction light propagation with axicon-shape photonic crystals*, J. Opt. Soc. Am. B, 26 (2009), pp. 981–986.

[77] H. KURT AND M. TURDUEV, *Generation of a two-dimensional limited-diffraction beam with self-healing ability by annular-type photonic crystals*, J. Opt. Soc. Am. B, 29 (2012), pp. 1245–1256.

[78] H. Laabs and B. Ozygus, *Excitation of Hermite Gaussian modes in end-pumped solid-state lasers via off-axis pumping*, Opt. Laser Technol., 28 (1996), pp. 213–214.

[79] J. Lavelle and C. O'Sullivan, *Beam shaping using gaussian beam modes*, J. Opt. Soc. Am. A, 27 (2010), pp. 350–357.

[80] M. Lebental, J. S. Lauret, J. Zyss, C. Schmit, and E. Bogomolny, *Directional emission of stadium-shaped microlasers*, Phys. Rev. A, 75 (2007), pp. 033806+.

[81] S. Y. Lee and K. An, *Directional emission through dynamical tunneling in a deformed microcavity*, Phys. Rev. A, 83 (2011), pp. 023827+.

[82] S. Y. Lee, M. S. Kurdoglyan, S. Rim, and C. M. Kim, *Resonance patterns in a stadium-shaped microcavity*, Phys. Rev. A, 70 (2004), pp. 023809+.

[83] L. Li, H. Lin, S. Qiao, Y. Zou, S. Danto, K. Richardson, J. D. Musgraves, N. Lu, and J. Hu, *Integrated flexible chalcogenide glass photonic devices*, Nat. Photon., 8 (2014), pp. 643–649.

[84] M. Liertzer, L. Ge, A. Cerjan, A. D. Stone, H. E. Türeci, and S. Rotter, *Pump-Induced exceptional points in lasers*, Phys. Rev. Lett., 108 (2012), pp. 173901+.

[85] S. F. Liew, B. Redding, L. Ge, G. S. Solomon, and H. Cao, *Active control of emission directionality of semiconductor microdisk lasers*, Appl. Phys. Lett., 104 (2014), pp. 231108+.

[86] B. E. Little, S. T. Chu, H. A. Haus, J. Foresi, and J. P. Laine, *Microring resonator channel dropping filters*, J. Lightwave Technol., 15 (1997), pp. 998–1005.

[87] Lord Rayleigh, *On the electromagnetic theory of light*, Philos. Mag., 12 (1881), pp. 81–101.

[88] ——, *The dispersal of light by a dielectric cylinder*, Philos. Mag., 36 (1918), pp. 365–376.

[89] B. Luk'yanchuk, N. I. Zheludev, S. A. Maier, N. J. Halas, P. Nordlander, H. Giessen, and C. T. Chong, *The Fano resonance in plasmonic nanostructures and metamaterials*, Nat. Mater., 9 (2010), pp. 707–715.

[90] J. Magnus and H. Neudecker, *Matrix Differential Calculus with Applications in Statistics and Econometrics*, Wiley, 1999.

[91] R. Mahillo-Isla, M. Gonzalez-Morales, and C. Dehesa-Martinez, *Regularization of complex beams*, in 12th International Conference on Mathematical Methods in Electromagnetic Theory, 2008, pp. 242–244.

[92] L. Maigyte, V. Purlys, J. Trull, M. Peckus, C. Cojocaru, D. Gailevicius, M. Malinauskas, and K. Staliunas, *Flat lensing in the visible frequency range by woodpile photonic crystals*, Opt. Lett., 38 (2013), pp. 2376–2378.

[93] D. Marcuse, *Gaussian approximation of the fundamental modes of graded-index fibers*, J. Opt. Soc. Am., 68 (1978), pp. 103–109.

[94] J. MARQUES-HUESO, L. SANCHIS, B. CLUZEL, F. DE FORNEL, AND J. P. MARTÍNEZ-PASTOR, *Properties of silicon integrated photonic lenses: bandwidth, chromatic aberration, and polarization dependence*, Opt. Eng., 52 (2013), pp. 091710+.

[95] M. W. MCCALL AND G. DEWAR, *Negative Refraction – Tutorials in Complex Photonics Media*, SPIE, 2009, ch. 1, pp. 1–32.

[96] B. MIN, L. YANG, AND K. VAHALA, *Perturbative analytic theory of an ultrahigh-Q toroidal microcavity*, Phys. Rev. A, 76 (2007), pp. 013823+.

[97] G. MOLINA-TERRIZA, J. P. TORRES, AND L. TORNER, *Twisted photons*, Nat. Phys., 3 (2007), p. 305.

[98] A. NAKAGAWA, S. ISHII, AND T. BABA, *Photonic molecule laser composed of GaInAsP microdisks*, Appl. Phys. Lett., 86 (2005), pp. 041112+.

[99] D. M. NATAROV, R. SAULEAU, M. MARCINIAK, AND A. I. NOSICH, *Effect of periodicity in the resonant scattering of light by finite sparse configurations of many silver nanowires*, Plasmonics, 9 (2014), pp. 389–407.

[100] N. NGUYEN-HUU, Y.-L. LO, Y.-B. CHEN, AND T.-Y. YANG, *Realization of integrated polarizer and color filters based on subwavelength metallic gratings using a hybrid numerical scheme*, Appl. Opt., 50 (2011), pp. 415–426.

[101] J. U. NÖCKEL, *Resonances in nonintegrable open systems*, PhD thesis, Yale University, 1997.

[102] M. A. NOGINOV, G. DEWAR, M. W. MCCALL, AND N. I. ZHELUDEV, *Tutorials in Complex Photonic Media*, SPIE, Dec. 2009.

[103] S. NOJIMA, *Theoretical analysis of feedback mechanisms of two-dimensional finite-sized photonic-crystal lasers*, J. Appl. Phys., 98 (2005), pp. 043102+.

[104] G. NORDIN, S. KIM, J. CAI, AND J. JIANG, *Hybrid integration of conventional waveguide and photonic crystal structures*, Opt. Express, 10 (2002), pp. 1334–1341.

[105] T. OGUZER, A. ALTINTAS, AND A. I. NOSICH, *Accurate simulation of reflector antennas by the complex source-dual series approach*, IEEE Trans. Antennas Propag., 43 (1995), pp. 793–801.

[106] K. OKAMOTO, *Fundamentals of Optical Waveguides (2nd edition)*, Academic Press, 2006.

[107] N. OLIVIER, D. DÉBARRE, P. MAHOU, AND E. BEAUREPAIRE, *Third-harmonic generation microscopy with Bessel beams: a numerical study*, Opt. Express, 20 (2012), pp. 24886–24902.

[108] G. PAINCHAUD-APRIL, J. DUMONT, D. GAGNON, AND L. J. DUBÉ, *S and Q matrices reloaded: Applications to open, inhomogeneous, and complex cavities*, in ICTON Conf. Proc, IEEE, July 2013.

[109] G. PAINCHAUD-APRIL, J. DUMONT, D. GAGNON, AND L. J. DUBÉ, *Scattering method for resonances in dielectric microcavities.* In preparation, 2014.

[110] G. PAINCHAUD-APRIL, J. POIRIER, D. GAGNON, AND L. J. DUBÉ, *Phase space engineering in optical microcavities I: Preserving near-field uniformity while inducing far-field directionality*, in ICTON Conf. Proc, IEEE, June 2010.

[111] B. PENG, S. K. OZDEMIR, F. LEI, F. MONIFI, M. GIANFREDA, G. L. LONG, S. FAN, F. NORI, C. M. BENDER, AND L. YANG, *Parity-time-symmetric whispering-gallery microcavities*, Nat. Phys., 10 (2014), pp. 394–398.

[112] C. PENG, Z. LI, AND A. XU, *Optical gyroscope based on a coupled resonator with the all-optical analogous property of electromagnetically induced transparency*, Opt. Express, 15 (2007), pp. 3864–3875.

[113] D. PEREZ-GALACHO, R. ZHANG, A. ORTEGA-MONUX, R. HALIR, C. ALONSO-RAMOS, P. RUNGE, K. JANIAK, G. ZHOU, H. G. BACH, A. G. STEFFAN, AND I. MOLINA-FERNANDEZ, *Integrated polarization beam splitter for 100/400 GE polarization multiplexed coherent optical communications*, J. Lightwave Technol., 32 (2014), pp. 361–368.

[114] P. POTTIER, S. MASTROIACOVO, AND R. M. DE LA RUE, *Power and polarization beam-splitters, mirrors, and integrated interferometers based on air-hole photonic crystals and lateral large index-contrast waveguides*, Opt. Express, 14 (2006), pp. 5617–5633.

[115] W. H. PRESS, B. P. FLANNERY, S. A. TEUKOLSKY, AND W. T. VETTERLING, *Numerical Recipes in C: The Art of Scientific Computing (3rd Edition)*, Cambridge University Press, Oct. 2007.

[116] M. QIU, *Effective index method for heterostructure-slab-waveguide-based two-dimensional photonic crystals*, Appl. Phys. Lett., 81 (2002), pp. 1163–1165.

[117] S. M. RAEIS-ZADEH AND S. SAFAVI-NAEINI, *Multipole-based modal analysis of gate-defined quantum dots in graphene*, Eur. Phys. J. B, 86 (2013), pp. 1–7.

[118] Y. P. RAKOVICH AND J. F. DONEGAN, *Photonic atoms and molecules*, Laser Photon. Rev., 4 (2010), pp. 179–191.

[119] O. RASOGA AND D. DRAGOMAN, *Engineered beam shaping effect in anisotropic photonic crystals*, Appl. Opt., 49 (2010), pp. 2161–2167.

[120] F. RIBOLI, N. CASELLI, S. VIGNOLINI, F. INTONTI, K. VYNCK, P. BARTHELEMY, A. GERARDINO, L. BALET, L. H. LI, A. FIORE, M. GURIOLI, AND D. S. WIERSMA, *Engineering of light confinement in strongly scattering disordered media*, Nat. Mater., 13 (2014), pp. 720–725.

[121] A. RICKMAN, *The commercialization of silicon photonics*, Nat. Photon., 8 (2014), pp. 579–582.

[122] A. RUHE, *Algorithms for the nonlinear eigenvalue problem*, SIAM J. Numer. Anal., 10 (1973), pp. 674–689.

[123] T. RUHL, P. SPAHN, C. HERMANN, C. JAMOIS, AND O. HESS, *Double-Inverse-opal photonic crystals: The route to photonic bandgap switching*, Adv. Funct. Mater., 16 (2006), pp. 885–890.

[124] R. C. RUMPF AND J. J. PAZOS, *Optimization of planar self-collimating photonic crystals*, J. Opt. Soc. Am. A, 30 (2013), pp. 1297–1304.

[125] J.-W. RYU AND M. HENTSCHEL, *Designing coupled microcavity lasers for high-Q modes with unidirectional light emission*, Opt. Lett., 36 (2011), pp. 1116–1118.

[126] J. W. RYU, S. Y. LEE, AND S. W. KIM, *Coupled nonidentical microdisks: Avoided crossing of energy levels and unidirectional far-field emission*, Phys. Rev. A, 79 (2009), pp. 053858+.

[127] B. SALEH AND M. TEICH, *Fundamentals of Photonics*, Wiley, 2007.

[128] D. P. SAN-ROMAN-ALERIGI, T. K. NG, Y. ZHANG, A. BEN SLIMANE, M. ALSUNAIDI, AND B. S. OOI, *Generation of J_0-Bessel-Gauss beam by a heterogeneous refractive index map*, J. Opt. Soc. Am. A, 29 (2012), pp. 1252–1258.

[129] P. A. SANCHEZ-SERRANO, D. WONG-CAMPOS, S. LOPEZ-AGUAYO, AND J. C. GUTIÉRREZ-VEGA, *Engineering of nondiffracting beams with genetic algorithms*, Opt. Lett., 37 (2012), pp. 5040–5042.

[130] L. SANCHIS, A. H. KANSSON, D. L. ZANÓN, J. B. ABAD, AND J. S. DEHESA, *Integrated optical devices design by genetic algorithm*, Appl. Phys. Lett., 84 (2004), pp. 4460–4462.

[131] H. G. SCHWEFEL AND C. G. POULTON, *An improved method for calculating resonances of multiple dielectric disks arbitrarily positioned in the plane*, Opt. Express, 17 (2009), pp. 13178–13186.

[132] H. G. SCHWEFEL, H. E. TÜRECI, A. D. STONE, AND R. K. CHANG, *Progress in Asymmetric Resonant Cavities: Using shape as a design parameter in dielectric microcavity lasers*, World Scientific, 2004, ch. 9, pp. 415–492.

[133] A. SENGUPTA, R. SEDAGHAT, AND Z. ZENG, *Multi-objective efficient design space exploration and architectural synthesis of an application specific processor (ASP)*, Microprocess. Microsyst., 35 (2011), pp. 392–404.

[134] I. V. SHADRIVOV, A. A. SUKHORUKOV, AND Y. S. KIVSHAR, *Beam shaping by a periodic structure with negative refraction*, Appl. Phys. Lett., 82 (2003), pp. 3820–3822.

[135] A. SHAPIRA, R. SHILOH, I. JUWILER, AND A. ARIE, *Two-dimensional nonlinear beam shaping*, Opt. Lett., 37 (2012), pp. 2136–2138.

[136] J.-B. SHIM AND J. WIERSIG, *Semiclassical evaluation of frequency splittings in coupled optical microdisks*, Opt. Express, 21 (2013), pp. 24240–24253.

[137] F.-J. SHU, C.-L. ZOU, AND F.-W. SUN, *An optimization method of asymmetric resonant cavities for unidirectional emission*, J. Lightwave Technol., 31 (2013), pp. 2994–2998.

[138] A. E. SIEGMAN, *Lasers*, University Science Books, 1986.

[139] S. N. SIVANANDAM AND S. N. DEEPA, *Introduction to Genetic Algorithms*, Springer-Verlag, Berlin, 2008.

[140] M. SKOROBOGATIY AND J. YANG, *Fundamentals of Photonic Crystal Guiding*, Cambridge University Press, 2009.

[141] E. I. SMOTROVA, V. O. BYELOBROV, T. M. BENSON, J. CTYROKY, R. SAULEAU, AND A. I. NOSICH, *Optical theorem helps understand thresholds of lasing in microcavities with active regions*, IEEE J. Quantum Elec., 47 (2011), pp. 20–30.

[142] E. I. SMOTROVA AND A. I. NOSICH, *Optical coupling of an active microdisk to a passive one: effect on the lasing thresholds of the whispering-gallery supermodes*, Opt. Lett., 38 (2013), pp. 2059–2061.

[143] E. I. SMOTROVA, A. I. NOSICH, T. M. BENSON, AND P. SEWELL, *Optical coupling of whispering-gallery modes of two identical microdisks and its effect on photonic molecule lasing*, IEEE J. Sel. Top. Quant., 12 (2006), pp. 78–85.

[144] Q. SONG AND H. CAO, *Highly directional output from long-lived resonances in optical microcavity*, Opt. Lett., 36 (2011), pp. 103–105.

[145] M. SRINIVAS AND L. M. PATNAIK, *Adaptive probabilities of crossover and mutation in genetic algorithms*, IEEE T. Sys. Man. Cyb., 24 (1994), pp. 656–667.

[146] K. STALIUNAS AND R. HERRERO, *Nondiffractive propagation of light in photonic crystals*, Phys. Rev. E, 73 (2006), pp. 016601+.

[147] S. SUNADA, T. HARAYAMA, AND K. S. IKEDA, *Multimode lasing in two-dimensional fully chaotic cavity lasers*, Phys. Rev. E, 71 (2005), p. 046209.

[148] A. TAFLOVE AND S. C. HAGNESS, *Computational Electrodynamics: The Finite-Difference Time-Domain Method, Third Edition*, Artech House, May 2005.

[149] E. TALBI, *Metaheuristics: From Design to Implementation*, Wiley, 2009.

[150] Y. TANG, Z. WANG, W. K. WONG, J. KURTHS, AND J. A. FANG, *Multiobjective synchronization of coupled systems*, Chaos, 21 (2011), pp. 025114+.

[151] H. E. TÜRECI, L. GE, S. ROTTER, AND A. D. STONE, *Strong interactions in multimode random lasers*, Science, 320 (2008), pp. 643–646.

[152] H. E. TÜRECI, A. D. STONE, AND B. COLLIER, *Self-consistent multimode lasing theory for complex or random lasing media*, Phys. Rev. A, 74 (2006), pp. 043822+.

[153] K. J. VAHALA, *Optical microcavities*, Nature, 424 (2003), pp. 839–846.

[154] F. VANIER, M. ROCHETTE, N. GODBOUT, AND Y.-A. PETER, *Raman lasing in As_2S_3 high-Q whispering gallery mode resonators*, Opt. Lett., 38 (2013), pp. 4966–4969.

[155] Z. V. VARDENY, A. NAHATA, AND A. AGRAWAL, *Optics of photonic quasicrystals*, Nat. Photon., 7 (2013), pp. 177–187.

[156] F. VOLLMER, *Taking detection to the limit*, B.I.F. Futura, 20 (2005), pp. 239–244.

[157] F. VOLLMER AND S. ARNOLD, *Whispering-gallery-mode biosensing: Label-free detection down to single molecules*, Nat. Methods, 5 (2008), pp. 591–596.

[158] A. VUKOVIC, P. SEWELL, AND T. M. BENSON, *Strategies for global optimization in photonics design*, J. Opt. Soc. Am. A, 27 (2010), pp. 2156–2168.

[159] C. WANG AND C. P. SEARCH, *Nonlinearly enhanced refractive index sensing in coupled optical microresonators*, Opt. Lett., 39 (2014), pp. 26–29.

[160] Q. J. WANG, C. YAN, N. YU, J. UNTERHINNINGHOFEN, J. WIERSIG, C. PFLÜGL, L. DIEHL, T. EDAMURA, M. YAMANISHI, H. KAN, AND F. CAPASSO, *Whispering-gallery mode resonators for highly unidirectional laser action*, PNAS, 107 (2010), pp. 22407–22412.

[161] X. WANG, W. SHI, H. YUN, S. GRIST, N. A. F. JAEGER, AND L. CHROSTOWSKI, *Narrow-band waveguide bragg gratings on SOI wafers with CMOS-compatible fabrication process*, Opt. Express, 20 (2012), pp. 15547–15558.

[162] D. S. WEILE AND E. MICHIELSSEN, *Genetic algorithm optimization applied to electromagnetics: a review*, IEEE Trans. Antennas Propag., 45 (1997), pp. 343–353.

[163] E. W. WEISSTEIN, *Jacobi-Anger Expansion. From MathWorld—A Wolfram Web Resource*. http://mathworld.wolfram.com/Jacobi-AngerExpansion.html. Last visited on 23/04/2013.

[164] D. WHITLEY, *A genetic algorithm tutorial*, Stat. Comput., 4 (1994), pp. 65–85.

[165] J. WIERSIG, *Boundary element method for resonances in dielectric microcavities*, J. Opt. A: Pure Appl. Opt., 5 (2003), pp. 53–60.

[166] D. S. WIERSMA, *The physics and applications of random lasers*, Nat. Phys., 4 (2008), pp. 359–367.

[167] ——, *Disordered photonics*, Nat. Photon., 7 (2013), pp. 188–196.

[168] P. J. WINZER, *Making spatial multiplexing a reality*, Nat. Photon., 8 (2014), pp. 345–348.

[169] P. F. XING, P. I. BOREL, L. H. FRANDSEN, A. HARPØTH, AND M. KRISTENSEN, *Optimization of bandwidth in 60° photonic crystal waveguide bends*, Opt. Commun., 248 (2005), pp. 179–184.

[170] X. XIONG, C.-L. ZOU, X.-F. REN, AND G.-C. GUO, *Integrated polarization rotator/converter by stimulated raman adiabatic passage*, Opt. Express, 21 (2013), pp. 17097–17107.

[171] T. XU, N. ZHU, M. Y. C. XU, L. WOSINSKI, J. S. AITCHISON, AND H. E. RUDA, *Pillar-array based optical sensor*, Opt. Express, 18 (2010), pp. 5420–5425.

[172] E. YABLONOVITCH, *Inhibited spontaneous emission in Solid-State physics and electronics*, Phys. Rev. Lett., 58 (1987), pp. 2059–2062.

Index